Imperial College of Science, Technology and Medicine
National Heart and Lung Institute

Analysis of cardiac electrogram morphology and its relationship with the underlying substrate using biological models and in silico tools

Shengzhe Li

Submitted in part fulfilment of the requirements for the degree of
Doctor of Philosophy in Clinical Research and
the Diploma of Imperial College London, June 2025

Abstract

The extracellular contact electrogram is a valuable tool for understanding the relationship between the electrical activity and the structural characteristics of the myocardium. Commonly used in the cardiac catheterisation laboratory, it provides important information on the electrical behaviour and conduction properties of the heart. Although the morphology of the electrogram can reveal important insights into conduction abnormalities and electrophysiological disturbances, its interpretation remains challenging due to the complex relationship between the electrical signals of the heart and its underlying structural and functional properties. The central hypothesis of this thesis is that the left ventricular electrogram morphology is affected by the underlying substrates and that these electrical activities can be effectively modelled using in-silico simulations.

To test this hypothesis, several biological models were characterised. Unipolar electrograms were recorded from rat and human biomimetic myocardial slices, neonatal rat ventricular myocytes, and ex-vivo porcine whole hearts. These electrograms were analysed using custom-developed signal processing and feature extraction tools to examine their morphological characteristics. In parallel, fluorescence microscopy was used to observe structural and functional changes, which were then quantified and correlated with electrogram features. This analysis revealed significant correlations between electrogram morphology and the underlying myocardial substrates, illustrating how conditions such as heart failure can alter both the structural and functional underlying myocardial substrates of the heart, ultimately affecting the electrogram.

In addition to the experimental work, computational models were developed to further explore the link between myocardial substrates and electrogram morphology. A multi-domain computational model and a continuum model of action potential propagation were used, incorporating gap junction remodelling to simulate the effects of structural changes on the electrogram. These simulations, performed using the spectral/hp element method, successfully demonstrated the feasibility of integrating substrate-related effects into numerical models of electrogram behaviour.

Acknowledgements

I would like to express my deepest gratitude to everyone who has supported me throughout the process of completing this thesis and the work therein.

First, I would like to thank my primary supervisors, Prof. Prapa Kanagaratnam, Dr. Rasheda Chowdhury, Prof. Liliang Wang, and Dr. Chris Cantwell, for their continuous guidance, expertise, and encouragement. Prof. Liliang, I would not have been able to start my PhD journey without your support, thank you for both your financial and emotional support over the past three years. Prof. Prapa, I deeply appreciate your belief in me, especially as someone from an engineering background with little initial medical knowledge. Dr. Rasheda, I am incredibly grateful for entrusting me with this project and patiently teaching me, from the basics of anatomy to electrophysiological and biological analysis. Dr. Chris, I will forever be thankful for the time you devoted to this project, the many productive discussions, and the genuine care you have shown me throughout this process.

I am also deeply grateful to the members of the group, Dr. Konstantinos Ntagiantas, Dimitrios Panagopoulos, and Danya Agha Jaffar for their thoughtful suggestions and for taking the time to train me and share their knowledge.

A special thank you goes to Ursula Herbort-Brand, Dr. Jose Sanchez Alonso-Mardones, and Prof. Julia Gorelik for their invaluable contributions and support during my research. Their assistance has been pivotal in helping me overcome various challenges.

I would like to express my heartfelt appreciation to my parents, whose unwavering support and understanding kept me motivated throughout this journey. Your belief in me has been a constant source of strength.

To all of you, thank you once again for your encouragement and for believing in my work.

Statement of Originality

I declare that this submission is my own work, unless specifically acknowledged in the text.

Copyright Dedication

The copyright of this thesis rests with the author. Unless otherwise indicated, its contents are licensed under a Creative Commons Attribution-Non Commercial 4.0 International Licence (CC BY-NC).

Under this licence, you may copy and redistribute the material in any medium or format. You may also create and distribute modified versions of the work. This is on the condition that: you credit the author and do not use it, or any derivative works, for a commercial purpose.

When reusing or sharing this work, ensure you make the licence terms clear to others by naming the licence and linking to the licence text. Where a work has been adapted, you should indicate that the work has been changed and describe those changes.

Please seek permission from the copyright holder for uses of this work that are not included in this licence or permitted under UK Copyright Law.

'Success consists of going from failure to failure without loss of enthusiasm.'

Winston Churchill

Papers

1. **Li, Shengzhe**, Danya Agha-Jaffar, Dimitrios Panagopoulos, Konstantinos Ntagiantas, Ariana JF Hawkins, Liliang Wang, Prapa Kanagaratnam, Rasheda A. Chowdhury, and Chris D. Cantwell. "Comparison of a Discrete-cell and Dontinuum Model of Two-dimensional Ventricular Tissues Under Modulation of Cx43." In 2023 Computing in Cardiology (CinC), vol. 50, pp. 1-4. IEEE, 2023.

2. **Li, Shengzhe**, Jamie A. Kay, Danya Agha-Jaffar, Cindy SY Gao, Justin Perkins, Simos Koutsoftidis, Emm Mic Drakakis, Liliang Wang, Prapa Kanagaratnam, Chris D. Cantwell, and Rasheda A. Chowdhury. "Successful Stimulation of Myocardial Ganglionic Plexi by Tau-20 in the Absence of Cardiac Damage." Frontiers in Physiology 16 (2025): 1536362.

3. Liu, Xiaochuan, Ming Ming, Lihua Du, Huiyuan Xu, Chenyu **Li, Shengzhe** Li, Denis J. Politis, Di Zhang, Heli Liu, and Xuefeng Chen. "An Automated Mechanical Property Testing System Based on Electric Field Assistance and Non-Contact Signal Measurement." IEEE Transactions on Instrumentation and Measurement (2025).

4. **Li, Shengzhe**, Fasai Wutthiphakdee, Nga Man Ting, Cindy SY Gao, Danya Agha-Jaffar, Liliang Wang, Prapa Kanagaratnam, Chris D. Cantwell, and Rasheda A. Chowdhury. "The Relationship Between Scar and the Underlying Myocardial remodelling and the Effects of Remodelling on the Cardiac Electrogram Morphology." in preparation.

5. **Li, Shengzhe**, Joshua DeCoteau, Cindy SY Gao, Danya Agha-Jaffar, Liliang Wang, Prapa Kanagaratnam, Chris D. Cantwell, and Rasheda A. Chowdhury. "A Feature Extraction Tool for Cardiac Electrogram Recorded by Multi-electrodes Array." in preparation.

6. **Li, Shengzhe**, Dimitrios Panagopoulos, Konstantinos Ntagiantas, Danya Agha-Jaffar, Liliang Wang, Prapa Kanagaratnam, Chris D. Cantwell, Norman Qureshi and Rasheda A. Chowdhury. "Novel Features of the Contact Electrogram Correlate with Location of Scar in Ex Vivo Rat and Human Myocardial Slices." in preparation.

Abstract

1. **Li, Shengzhe**, Fasai Wutthiphakdee, Danya Agha-Jaffar, Joe Brook, Dimitrios Panagopoulos, Cindy S Y Gao, Gabrielle Johnston, Mubassher Husain, Norman A Qureshi, Liliang Wang, Chris D Cantwell, Prapa Kanagaratnam, and Rasheda A Chowdhury. "Correlation between gap junction remodelling and the contact electrogram in human hearts" Heart Rhythm Congress 2024, Birmingham, UK, October 2024

Contents

Abstract **i**

Acknowledgements **iii**

Statement of Originality **v**

1 Introduction **1**

1.1 Heart and cardiac electrophysiology 1

1.1.1 Human heart structure 1

1.1.2 Electrical conduction 3

1.1.3 Action potential and ion channels 5

1.1.4 Gap junctions 7

1.1.5 Electrophysiological Effects of Cx43 Changes 8

1.2 Arrhythemias 10

1.3 Electrogram and electrogram morphology 11

1.4 Existing Models of Cardiac Electrophysiology 18

1.4.1 Biological models 18

1.4.2 Computational models 19

1.4.3 Hybrid and translational models 19

1.5 Simulation of cardiac electrophysiological activities 20

1.5.1 Action potential model 20

1.5.2 Continuum and discrete propagation models 23

1.6 Outline of thesis 24

2 Materials and Methods **28**

2.1 Introduction 28

2.2 Materials 29

2.2.1 Cell culture 30

2.2.2 Collection and preparation of rat heart tissue samples 33

2.2.3 Collection and preparation of human heart tissue 35

2.2.4 Langendorff hearts 39

2.2.5 Pharmacological Modulators 41

2.3 Microelectrode array recordings 41

2.4 Langendorff 43

2.5 Immunofluorescence 47

2.5.1 The principles of Immunofluorescence 48

2.5.2 Immunofluorescence protocol 49

2.6 Microscopy 50

2.6.1 Second-harmonic generation microscopy 51

2.6.2 Microscopy protocol 51

2.7 Numerical simulations 53

2.7.1 Mathematical models of Cardiac Electrophysiology 53

2.7.2 Simulation protocol 59

2.8 Statistic analysis 60

3 Development of Cardiac Electrogram Feature Extraction tool 61

3.1 Introduction 61

3.1.1 Cardiac electrophysiology signal processing 62

3.1.2 Electrogram morphology 63

3.2 Methods 64

3.2.1 Features of electrogram 64

3.2.2 Preprocessing of electrogram 65

3.2.3 Time-domain feature extraction 66

3.2.4 Frequency-domain feature extraction 71

3.2.5 Time-frequency feature extraction 74

3.2.6 Entropy 76

3.2.7 Statistic analysis 77

3.3 Results 78

3.3.1 quantification of electrogram features 78

3.3.2 Validation of the accuracy 79

3.3.3 Comparison between different models 86

3.4 Discussion 90

3.5 Limitations 93

3.6 Conclusion 93

4 Effects of Structural remodelling on Cardiac Electrogram Morphology 95

4.1 Introduction . . . 95

4.1.1 Development and the rule of scar . . . 96

4.1.2 Structural remodelling affects cardiac electrophysiology . . . 96

4.2 Methods . . . 97

4.2.1 Microelectrode array recording . . . 97

4.2.2 Microscope and image processing . . . 99

4.2.3 Data analysis . . . 103

4.3 Results . . . 104

4.3.1 Collagen development in rat models . . . 104

4.3.2 Collagen development human donor samples and human failing samples . 106

4.3.3 Collocation of EGM features and locations of collagen in rat model . . . 108

4.3.4 Collocation of EGM features and locations of collagen in human model . 115

4.4 Discussion . . . 126

4.4.1 Collagen index . . . 126

4.4.2 BDM limitations . . . 126

4.4.3 The effects of collagen on EGM features . . . 128

4.4.4 Differences between rat models and human models . . . 130

4.5 Limitations . . . 130

4.6 Conclusion . . . 131

5 Effects of Functional remodelling on Cardiac Electrogram Morphology 132

5.1 Introduction . . . 132

5.1.1 Neuronal cells affect cardiac electropgyology 132

5.1.2 Gap junctional remodelling 134

5.1.3 Fast sodium ion channel remodelling 135

5.2 Methods 136

5.2.1 Cell culture 136

5.2.2 Microelectrode array recording 136

5.2.3 Immunofluoresence 138

5.2.4 Microscope and imaging processing 138

5.2.5 Data analysis 145

5.3 Results 146

5.3.1 The effects of SNs on EGM features of NRVMs 146

5.3.2 Gap junctional remodelling and its relationship between scar in human donor and human failing samples 150

5.3.3 Characterisation of EGM feature modifications correlating to gap junctional remodelling 152

5.3.4 $Na_v1.5$ ion channel remodelling and its relationship between scar in human donor and human failing samples 171

5.3.5 Characterisation of EGM feature modifications correlating to $Na_v1.5$ ion channel remodelling 172

5.4 Discussion 182

5.4.1 The effects of SNs on NRVMs and its EGM features 182

5.4.2 The effects of gap junctional remodelling on EGM features in human donor and human failing samples 184

5.4.3 The effects of $Na_v1.5$ channel remodelling on EGM features in human donor and human failing samples . . . 187

5.5 Limitations . . . 190

5.6 Conclusion . . . 191

6 Analysis of EGM morphology of the ex-vivo porcine hearts with pharmacological modifications 192

6.1 Introduction . . . 192

6.2 Methods . . . 194

6.3 Results . . . 196

6.4 Discussion . . . 202

6.5 Limitations . . . 204

6.6 Conclusion . . . 205

7 Development of Numerical Simulation of Cardiac Electrophysiology with remodelling 206

7.1 Introduction . . . 206

7.2 Methods . . . 207

7.2.1 Digital cell monolayer generation . . . 207

7.2.2 Simulation setup . . . 208

7.3 Results . . . 209

7.3.1 Feature extraction of simulated data . . . 209

7.3.2 Comparison between continuum model and discrete model . . . 211

7.4 Discussion . . . 213

7.4.1 The accuracy of different models . . . 214

7.4.2 The accuracy of the novel discrete model 214

7.5 Limitations 215

7.6 Conclusion 215

8 Conclusion **217**

8.1 Summary of Key findings 217

8.1.1 Development of electrogram morphology analysis tool 218

8.1.2 Electrogram Morphology effects due to underlying substrate changes in BMS and cell models 219

8.1.3 Electrogram Morphology effects due to functional changes in ex vivo porcine heart model 222

8.1.4 Development of in-silico simulations 223

8.2 Clinical relevance of findings 224

8.3 Future directions 225

Bibliography **227**

List of Tables

2.1 The number of NRVMs and SNs to be added. 32

2.2 Clinical characteristics of heart failure patients 37

2.3 Characteristics of donors for rejected heart transplants 38

2.4 Langendorff experiment: Date of heart collection, duration of the experiment, and source of the hearts. 41

3.1 List of time domain features. 71

3.2 List of frequency domain features. 73

3.3 List of time frequency features. 76

3.4 List of features related to entropy. 77

5.1 A semi-quantitative scoring system is used for assessing the connexin43 distribution. 142

6.2 EGM Features for all the porcine hearts at baseline and after pharmacological modulations. 200

6.1 P values of the comparisons between all the features of baseline EGMs and pharmacological modulated EGMs. 201

6.3 P values of the comparisons between all the features of different pharmacological modulated EGMs. 202

List of Figures

1.1 The structure of the human heart and the blood flow direction. 2

1.2 The cardiac electrophysiological system. 4

1.3 Ventricular myocyte AP demonstrating voltage changes during each phase. . . . 7

1.4 (A) Connexins expression in mammalian myocardium. (B) conduction velocities in different regions. 8

1.5 Visual description of the different fundamental components of a single ECG heartbeat. 13

1.6 Types of human cardiac fibrosis in explanted hearts can be visualised using light microscopy, with collagen-dense areas stained red using picrosirius red. 16

1.7 Activation induced at site A of an infarcted myocardium propagates following the indicated zig-zag route due to the complex distribution of myocardial bundles. 17

2.1 Overview of the methodology used by this study towards the development of both biological models and computational model. 29

2.2 Heart and carotid artery ganglion were dissected from the neonatal rat and NRVMS and SNs were isolated following different protocol. 31

2.3 (A) Co-cultured NRVMs and 10% SNs cells on day 2 under 20x microscope. (B) Micro Electrode Array dish. 33

2.4 (A) Apex of the failing heart from a patient diagnosed with DCM. (B) A healthy donor heart meets all the requirement and was transported to the laboratory. . . 36

2.5 (A) The high precision vibrating microtome used for producing tissue slices. (B) A block from human left ventricle was mounted on the specimen holder using Histoacryl® during slicing. (C) A BMS placed on top of the electrode matrix of a micro-electrode array dish. 39

2.6 (A) Raw recordings from all the electrodes from pure NRVMs, stimulation voltage is 2000mv, direction is from East and stimulation frequency is 1 Hz. (B) Raw recordings from all the electrodes from pure NRVMs, stimulation voltage is 2000mv, direction is from East and stimulation frequency is 1 Hz. 42

2.7 (A) Zoomed in raw recordings from one electrode from a human failing heart BMS. (B) Raw recordings from one electrode from a human failing heart BMS. . 43

2.8 The Langendorff apparatus, pump, and aortic cannula feeding into a porcine heart. 45

2.9 The 16 locations on the epicardium surface that EGM was recorded from. 46

2.10 Image of the HD grid from Abbott Medical. 47

2.11 An example of a reference image of the HD grid catheter position on a porcine heart. 47

2.12 Illustration of the mechanism of immunofluorescence 49

3.1 Time points detected from the simulated EGM for time-domain feature extraction. 68

3.2 Stimulation removal process. (A) Original EGMs. (B) EGMs after stimulation removal process. 78

3.3 Example of the feature extraction of one EGM. (A) The point detection including Q, R, S and end point. (B) Time-domain features of a single EGM. (C) Frequency- domain features of a single EGM. (D) Time-Frequency features of a single EGM. 79

3.4 Comparison between features (from one human donor BMS) extracted manually and by using GUI. 80

3.5 Time domain features inter-user variability detection using a BMS from human failing heart. 81

3.6 Frequency domain features inter-user repeatability test using a BMS from human failing heart. 82

3.7 Time frequency features inter-user repeatability test using a BMS from human failing heart. 83

3.8 Time domain features inter-user variability detection using a BMS from human donor heart. 84

3.9 Frequency domain features inter-user repeatability test using a BMS from human donor heart. 85

3.10 Time frequency features inter-user repeatability test using a BMS from human donor heart. 86

3.11 Comparison between time domain features extracted from human donor BMS and human failing BMS. 88

3.12 Comparison between frequency domain features and Shannon entropy extracted from human donor BMS and human failing BMS. 89

3.13 Comparison between time frequency features extracted from human donor BMS and human failing BMS. 90

4.1 Examples of the raw EGMs recorded from rat BMS. (A) Control rat. (B) Myocardial fibrosis rat. 98

4.2 [Examples of the raw EGMs recorded from human BMS. (A) Donor heart. (B) Failing heart. 99

4.3 Colocalisation and Quantification of collagen in a rat healthy BMS. (A) SHG image of the BMS. Slice channel (top left); Collagen channel (top right); Merged image (bottom left); processed collagen channel (bottom right). (B) Colocalisation of collagen and micro electrodes. 100

4.4 Colocalisation and Quantification of collagen in a rat myocardial fibrosis BMS. (A) SHG image of the BMS. Slice channel (top left); Collagen channel (top right); Merged image (bottom left); processed collagen channel (bottom right). (B) Colocalisation of collagen and micro electrodes. 101

4.5 Colocalisation and Quantification of collagen in a human donor BMS. (A) SHG image of the BMS. Slice channel (top left); Collagen channel (top right); Merged image (bottom left); processed collagen channel (bottom right). (B) Colocalisation of collagen and micro electrodes. 102

4.6 Colocalisation and Quantification of collagen in a human failing BMS. (A) SHG image of the BMS. Slice channel (top left); Collagen channel (top right); Merged image (bottom left); processed collagen channel (bottom right). (B) Colocalisation of collagen and micro electrodes. 103

4.7 Development of collagen in rat models and it's effects on electrical propagation and conduction velocity. (A) Higher CI was calculated from myocardial fibrosis heart BMS. (B) The conduction velocity map, activation map and compress of conduction directions of a healthy heart BMS. (C) The conduction velocity map, activation map and compress of conduction directions of a myocardial fibrosis heart BMS. 105

4.8 Development of collagen in human models and it's effects on electrical propagation and conduction velocity(A) Higher CI was calculated from human failing heart BMS. (B) The conduction velocity map, activation map and compress of conduction directions of a human donor BMS. (C) The conduction velocity map, activation map and compress of conduction directions of a human failing BMS. . 107

4.9 Comparison between time domain features of EGM recorded from healthy rat heart BMS and myocardial fibrosis heart BMS. 109

4.10 Comparison between frequency domain features of EGM recorded from healthy rat heart BMS and myocardial fibrosis heart BMS. 110

4.11 Comparison between time frequency features of EGM recorded from healthy rat heart BMS and myocardial fibrosis heart BMS. 111

4.12 Collagen Index with relation to time domain features of the EGMs of rat heart BMS. . . . 112

4.13 Collagen Index with relation to frequency domain features of the EGMs of rat heart BMS. . . . 113

4.14 Collagen Index with relation to time frequency features features of the EGMs of rat heart BMS. . . . 114

4.15 Comparison between time domain features of EGM recorded from human donor BMS and human failing BMS. . . . 116

4.16 Comparison between frequency domain features and Shannon entropy of EGM recorded from human donor BMS and human failing BMS. . . . 117

4.17 Comparison between time frequency features of EGM recorded from human donor BMS and human failing BMS. . . . 118

4.18 Collagen Index with relation to time domain features of the EGMs of human heart BMS. . . . 119

4.19 Collagen Index with relation to frequency domain features and Shannon entropy of the EGMs of human heart BMS. . . . 120

4.20 Collagen Index with relation to time frequency features of the EGMs of human heart BMS. . . . 121

4.21 Collagen Index with relation to frequency domain features of the EGMs of human donor heart BMS. . . . 122

4.22 Collagen Index with relation to frequency domain features and Shannon entropy of the EGMs of human failing heart BMS. . . . 123

4.23 Collagen Index with relation to time frequency features of the EGMs of human donor heart BMS. . . . 124

4.24 Collagen Index with relation to time frequency features of the EGMs of human failing heart BMS. . . . 124

4.25 Comparison between electrode level and slice level collocations. . . . 125

5.1 Examples of the raw EGMs recorded from cells. (A) Pure NRVMs. (B) NRVMs/SNs. 137

5.2 Example images of Cx 43 staining. (A) Zoomed in scar area from a donor heart sample. (B) Zoomed in remote area from a donor heart sample. (C) The whole image of a donor heart sample. 140

5.3 Example images of the Cy3 channel from a Cx43 immunolabelled human left ventricle after adjusting brightness (A) Thresholding and binarising (B) Pixel counting is shown on the bottom row. (C) The process of locating an en-face gap junction. (D) The marking of an area of Cx43 labelling at the en-face gap junction for pixel counting. 141

5.4 Example images showing the scoring system and Cx43 distribution. The dashed double-ended arrows indicate the longitudinal fibre orientation. 142

5.5 Example Widefield microscope images of $Na_v1.5$ ion channel. (A) Separated channels of a image of a small area (250 μm*250 μm). (B) Merged images of a large area (2 mm*2 mm) from a donor heart. 143

5.6 Example Confocal microscope images of $Na_v1.5$ ion channel. (A) Image acquired using Widefield microscopy, including an example depicting t-tubules. (B) Tailed large area images (3842.6μm*3842.6μm) from a donor heart. (C) Tailed large area images (3842.6μm*3842.6μm) from a failing heart. 144

5.7 Example images illustrating the image processing steps for measuring $Na_v1.5$ ion channel expression levels. (A) Representative image of a heart sample slice under the 488/Scar (green channel) and the Alexa Fluor 680 (red channel), along with the resultant image after autofluorescence signal subtraction. (B) Representative images demonstrating the effect of applying a fixed threshold to the processed images for pixel counting. 145

5.8 Conductance of NRVMs under all culture conditions. (A) Representative conduction maps of NRVMs-only. (B) Representative conduction maps of NRVMs + 10% SNs. (C) Conduction velocity. 147

5.9 Co-culture with SNs alters time domain EGM Features of NRVMs. Histograms and dot plots compare (A) EGM duration (B) R-S interval (C) Voltage amplitude between NRVMs-only controls and co-cultured NRVMs. 148

5.10 Cx43 expression of NRVMs under all culture condition. (A)Double immunofluorescence staining of Cx43 and SNs in NRVMs + 10% SNs condition. (B) Double immunofluorescence staining of Cx43 and SNs in NRVMs-only condition. (C) Expression of Cx43. 149

5.11 Cell morphology of NRVMs under all culture conditions. (A) Double immunofluorescence staining of WGA and SNs in NRVMs + 10%SN condition. (B) Double immunofluorescence staining of WGA and TOH in NRVMs-only condition. (C) Cell diameters. 150

5.12 Gap junction remodelling characteristics with relation to heart types. (A) Cx43 expression. (B) Cx43 heterogeneity. (C) Cx43 lateralisation. 151

5.13 Gap junction remodelling characteristics with relation to scar. (A) Cx43 expression. (B) Cx43 heterogeneity. (C) Cx43 lateralisation. 152

5.14 Cx43 expression with relation to time domain features of the EGMs of human hearts. 153

5.15 Cx43 expression with relation to frequency domain features and Shannon entropy of the EGMs of human hearts. 154

5.16 Cx43 expression with relation to time frequency features of the EGMs of human hearts. 155

5.17 Homogeneity of Cx43 with relation to time domain features of the EGMs of human hearts. 156

5.18 Homogeneity of Cx43 with relation to frequency domain features and Shannon entropy of the EGMs of human hearts. 157

5.19 Homogeneity of Cx43 with relation to time frequency features of the EGMs of human hearts. 158

5.20 Lateralisation of Cx43 with relation to time domain features of the EGMs of human hearts. 159

5.21 Lateralisation of Cx43 with relation to frequency domain features and Shannon entropy of the EGMs of human hearts. 160

5.22 Lateralisation of Cx43 with relation to time frequency features of the EGMs of human hearts. 161

5.23 Cx43 expression with relation to frequency domain features of the EGMs of human donor hearts. 162

5.24 Cx43 expression with relation to frequency domain features of the EGMs of human failing hearts. 163

5.25 Cx43 expression with relation to time frequency features of the EGMs of human donor hearts. 164

5.26 Cx43 expression with relation to time frequency features of the EGMs of human failing hearts. 164

5.27 Homogeneity of Cx43 with relation to frequency domain features of the EGMs of human donor hearts. 165

5.28 Homogeneity of Cx43 with relation to frequency domain features of the EGMs of human failing hearts. 166

5.29 Homogeneity of Cx43 with relation to time frequency features of the EGMs of human donor hearts. 167

5.30 Homogeneity of Cx43 with relation to time frequency features of the EGMs of human failing hearts. 167

5.31 Lateralisation of Cx43 with relation to frequency domain features of the EGMs of human donor hearts. 168

5.32 Lateralisation of Cx43 with relation to frequency domain features of the EGMs of human failing hearts. 169

5.33 Lateralisation of Cx43 with relation to time frequency features of the EGMs of human donor hearts. 170

5.34 Lateralisation of Cx43 with relation to time frequency features of the EGMs of human failing hearts. 170

5.35 $Na_v1.5$ ion channel remodelling characteristics with relation to heart types. (A) $Na_v1.5$ ion channel expression. (B) $Na_v1.5$ ion channel heterogeneity. 171

5.36 $Na_v1.5$ ion channel remodelling characteristics with relation to scar. (A) $Na_v1.5$ ion channel expression. (B) $Na_v1.5$ ion channel heterogeneity. 172

5.37 $Na_v1.5$ ion channel expression with relation to time domain features of the EGMs of human hearts. 174

5.38 $Na_v1.5$ ion channel expression with relation to frequency domain features and Shannon entropy of the EGMs of human hearts. 175

5.39 $Na_v1.5$ ion channel expression with relation to time frequency features of the EGMs of human hearts. 176

5.40 Homogeneity of $Na_v1.5$ ion channel with relation to time domain features of the EGMs of human hearts. 178

5.41 Homogeneity of $Na_v1.5$ ion channel with relation to frequency domain features and Shannon entropy of the EGMs of human hearts. 179

5.42 Homogeneity of $Na_v1.5$ ion channel with relation to time frequency features of the EGMs of human hearts. 180

5.43 $Na_v1.5$ ion channel expression with relation to the features of the EGMs of human donor hearts. 181

5.44 $Na_v1.5$ ion channel expression with relation to the features of the EGMs of human failing hearts. 181

5.45 Homogeneity of $Na_v1.5$ ion channel with relation to the features of the EGMs of human donor hearts. 182

5.46 Homogeneity of $Na_v1.5$ ion channel with relation to the features of the EGMs of human failing hearts. 182

6.1 Example EGMs with pacing cycle length of 600 ms. (A) Baseline. (B) After administering Lidocaine. (C) After administering Carbenoxolone . (D) After administering Pinacidil. 196

6.2 Comparison between time domain features of EGM recorded from Langendorff porcine hearts at baseline and after pharmacological modifications. 197

6.3 Comparison between frequency domain features and Shannon Entropy of EGM recorded from Langendorff porcine hearts at baseline and after pharmacological modifications. 198

6.4 Comparison between time frequency features of EGM recorded from Langendorff porcine hearts at baseline and after pharmacological modifications. 199

7.1 (A) Cells seeded in a 1.2 mm $\times$ 1.2 mm domain. (B) Cells in the "growing" process. (C) Final grown monolayer. 208

7.2 File format conversion process. 208

7.3 (A) A healthy 1.2 mm $\times$ 1.2 mm monolayer with electrodes. (B) Monolayer with an abnormal gap junction area, 9 electrodes are located in the abnormal area, the conductivity of the gap junctions within the abnormal area was set to 1/5 of it from the normal area. 209

7.4 (A) EGMs recorded from the simulation with the discrete model and healthy monolayer. (B) EGMs recorded from the simulation with the discrete model and the monolayer with abnormal gap junction area. 210

7.5 Simulated EGMs in relation with the locations of the electrodes. 210

7.6 Simulated propagation in healthy monolayer and the monolayer with abnormal gap junction area. (A) The continuum model. (B) The discrete model. 212

7.7 Comparison between time domain features of EGMs recorded from the simulations. (A) EGM duration. (B) EGM voltage. (C) conduction velocity. 213

Chapter 1

Introduction

1.1 Heart and cardiac electrophysiology

1.1.1 Human heart structure

A human heart has four chambers: left atrium, right atrium, left ventricle, and right ventricle. These chambers are filled with blood and the function of the heart is to pump blood in a consistent direction through the heart and through the body. Deoxygenated blood first arrives at the right atrium from the superior and inferior vena cava. The blood is then pumped into the right ventricle through the tricuspid valve. Subsequently, the blood leaves the heart from the pulmonary artery and enters the lung, where the blood is oxygenated, and then returns to the left atrium via the pulmonary veins. Next, the blood is pumped into the left ventricle through the mitral valve. From the left ventricle, the blood is pumped into the aorta for systemic circulation, delivering oxygen to the body. The blood flow and the structure of the human heart is shown in Figure 1.1 The mechanism is that the heart is made of muscles that could contract and relax and this is coordinated by electrical signals[1].

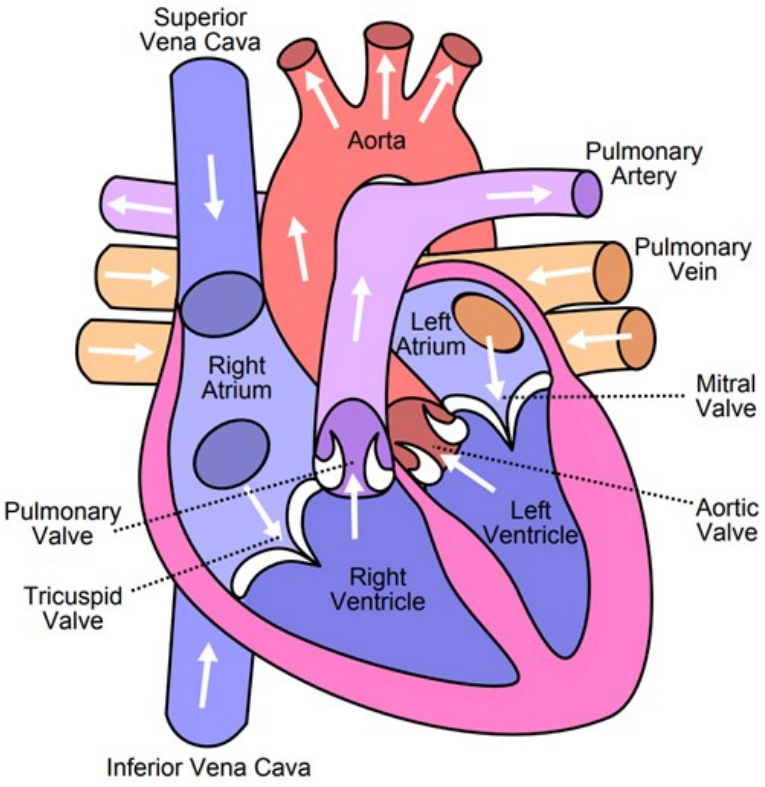


Figure 1.1: The structure of the human heart and the blood flow direction[1].

The cellular composition of the heart comprises several major cell populations, including cardiomyocytes, fibroblasts, endothelial cells, and smooth muscle cells. Cardiomyocytes, the contractile muscle cells, account for the majority of cardiac volume and are essential for generating the force of contraction[2]. In contrast, non-cardiomyocytes outnumber cardiomyocytes, with fibroblasts and endothelial cells being particularly abundant. Fibroblasts are the predominant non-cardiomyocyte population and play a central role in synthesising and maintaining the extracellular matrix, thereby providing structural integrity and mechanical support[2, 3]. Endothelial cells form the inner lining of the cardiac vasculature and regulate vascular tone, permeability, and blood flow. Smooth muscle cells, localised within the vascular walls, contribute to vascular contractility and blood pressure regulation. In addition, the heart contains diverse supporting cell types, including immune cells, pericytes, and others, which collectively contribute to cardiac homeostasis, repair, and overall function[2].

1.1.2 Electrical conduction

The contractile activity of the heart is governed by propagating electrochemical waves. Local myocardial excitation triggers the depolarisation of adjacent cardiomyocytes via gap junctions, resulting in spatially coordinated contraction[4]. However, the presence of non-conductive connective tissue (e.g., fibrous annuli) creates discontinuous propagation pathways, leading to anisotropic wavefront progression.

The electrophysiological cascade originates in the sino-atrial (SA) node, a cluster of autorhythmic pacemaker cells in the right atrial wall that exhibits spontaneous phase-4 depolarisation at 60–100 bpm. From the SA node, the depolarisation wave spreads radially through the atria via preferential conduction pathways (e.g., Bachmann's bundle), inducing synchronised atrial systole and ventricular filling. The impulse then converges at the atrioventricular (AV) node, where delayed conduction ($\simeq$ 100 ms) ensures sequential atrial-ventricular activation[4]. Subsequent rapid transmission occurs through the His-Purkinje system (bundle of His $\rightarrow$ left/right bundle branches $\rightarrow$ Purkinje fibres), achieving near-instantaneous (<80 ms) ventricular myocardium depolarisation. This coordinated sequence, termed sinus rhythm, represents the normative electrophysiological state in healthy hearts[4]. The cardiac electrophysiological system is shown in Figure 1.2.

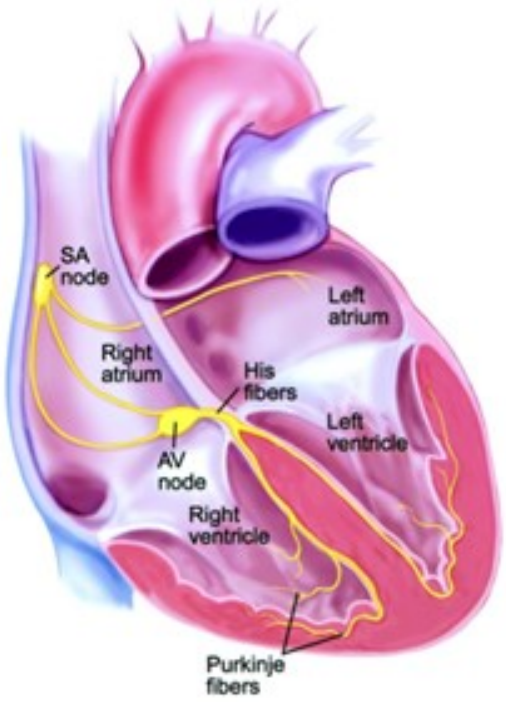


Figure 1.2: The cardiac electrophysiological system[4].

The work of Schram et al. demonstrated that regional specialisation of cardiac electrical function is primarily governed by the differential expression of ion channels throughout the heart. Key regions, including the sinoatrial node, atria, atrioventricular node, His-Purkinje system, and ventricles, exhibit different ion channel profiles that underpin their unique electrophysiological properties. For example, the sinoatrial node depends on hyperpolarisation-activated cyclic nucleotide-gated (HCN) channels for pacemaking, whereas the atria and ventricles differ markedly in both the action potential morphology and the ionic current composition. The atria exhibit faster repolarisation and a reduced inward rectifier potassium current (I_{K1}) compared to the ventricles, along with region-specific currents such as the ultra-rapid delayed rectifier potassium current (I_{Kur}), which is absent in ventricular tissue. These features contribute to their greater susceptibility to arrhythmias such as atrial fibrillation. Ventricular myocytes, on the contrary, display stronger I_{K1}, larger sodium currents (I_{Na}) and well-defined transmural heterogeneity in repolarising currents, such as I_{to}, I_{Kr} and I_{Ks} - giving rise to region-specific action potentials across the epicardial, endocardial, and midmyocardial layers. This complex spatial variation plays a crucial role in maintaining coordinated contraction and electrical stability. Understanding these molecular and functional distinctions is essential not only for elucidating

normal cardiac physiology, but also for advancing our knowledge of arrhythmogenic mechanisms and guiding the development of targeted antiarrhythmic therapies[5].

1.1.3 Action potential and ion channels

The action potential (AP) is the potential difference change between an individual cell and its environment[4]. The electrical wave in the heart is the macro performance of the propagating AP (from one cell to its neighbour cells). The extracellular space is isolated from the intracellular space by the lipid bilayer membrane, but the ions (mainly Na^+, Ca^{2+}, K^+, and Cl^-) could flow into and out of the cell via a series of membranal proteins which are selective to one or a few ions and most of them can be activated and inactivated under specific transmembrane properties (Some of them are also sensitive to other features such as time)[4]. These proteins are known as ion channels, ion exchangers, and ion pumps[4]. An AP contains a series of ions' changes, and the whole process normally lasts around 300 ms in the ventricles. During this time, the transmembrane potential rapidly increases, then slightly decreases, and remains stable for a short time followed by a sudden drop. The voltage varies from around -90 mV to 30 mV. The AP process is generally divided into five steps[6].

Phase 4 is the resting phase. In this phase, ventricular cardiomyocytes maintain a stable resting membrane potential (approximately -80 mV), primarily sustained by the inward rectifier potassium current (I_{K1})-mediated K^+ efflux, which strongly conducts outward current at negative membrane potentials and anchors the potential near the K^+ equilibrium potential. During this phase, the voltage-gated Na^+ channels (I_{Na}) and Ca^{2+} channels ($I_{CaT/F}$) remain closed. Unlike sinoatrial nodal pacemaker cells, ventricular myocytes lack both the hyperpolarisation-activated funny current (I_f) and the T-type Ca^{2+} current (I_{CaT}), thus exhibiting no spontaneous depolarisation. The resting membrane potential is principally governed by the K^+ concentration gradient according to the Nernst equation, with minor contributions from the background Na^+ current (I_{Na})[6].

Phase 0 is the rapid depolarisation step. In this stage, the electrical wavefront is traveling through the tissue. At the begining of this stage, the local circuit currents ("gap junction

coupling" via connexin 43) depolarise ventricular myocytes passively and when the potential reaches the threshold (-70 mV) potential of the fast Na^+ channels, the channel is activated. Once the fast Na^+ ion channels are opened, there is a rapid influx of Na^+ ions (I_{Na}), which results in a fast rise of the transmembrane potential (depolarisation). The transmembrane potential reaches a positive value in a short time (generally 20 – 30 mv in 0.6 ms) and the fast Na^+ ion channels are inactivated. This rapid change in the potential triggers the activations of a series of other ion channels[6]. For some voltage gated ion channels, the threshold potentials are similar between different models. However, for some other ion channels, there is a huge gap in the threshold potentials.

Phase 1 is a rapid repolarisation step. The transmembrane potential experiences a sudden drop in this phase due to the opening of the transient outward K^+ channels. This causes a fast outflow of K^+ ions (I_K). The potential repolarises to -20 – 0 mV at the end of phase 1[6].

Phase 2 is a stable stage called the plateau. Although there is no significant change in the transmembrane potential, there are several ion channels opening in this phase. The transient outward K^+ channels are still opening in phase 2. Apart from that, the delayed rectifier K^+ channels and the L-type Ca^{2+} channels are activated. The delayed rectifier K^+ channels also allow K+ ions to flow out and the Ca^{2+} ions can flow into the cell through the L-type Ca^{2+} channels. As a result, the influx of Ca^{2+} ions (I_{CaL}) balances the outflow of K^+ ions[6].

Phase 3 is the repolarisation step. At the beginning of this phase, the L-type Ca^{2+} channels are closed and several other K^+ channels such as the inward rectifier K^+ channels are activated. The rapid outflow of K^+ ions leads to a sudden decrease in the transmembrane potential which arrives at around -80 mV. The repolarisation phase takes longer than the depolarisation phase. After repolarisation, the cell changes back to the resting stage. During the late phase of repolarisation (membrane potential between -60 to -90 mV), ventricular cardiomyocytes may potentially be re-excited under specific conditions, although this is highly unlikely in healthy tissue. In normal physiology, the rapid outward K^+ currents (I_{Kr}, I_{Ks}) dominate this phase, driving repolarisation while sodium channels ($Na_{v1.5}$) remain largely inactivated until the membrane potential recovers beyond -70 mV, making successful re-excitation difficult

without extremely strong stimuli (e.g., defibrillation-level energy). However, under pathological conditions such as prolonged action potential duration (APD, as seen in heart failure or ischemia), impaired sodium channel inactivation, or drug-induced channel dysfunction, partial recovery of sodium channels at membrane potentials around -70 mV may permit abnormal depolarisation, manifesting as early afterdepolarisations (EADs) or localised re-excitation.[6, 7].

The typical AP of ventricular myocytes is shown in Figure 1.3. But the real AP in different regions are slightly different from each other due to the variations of function.

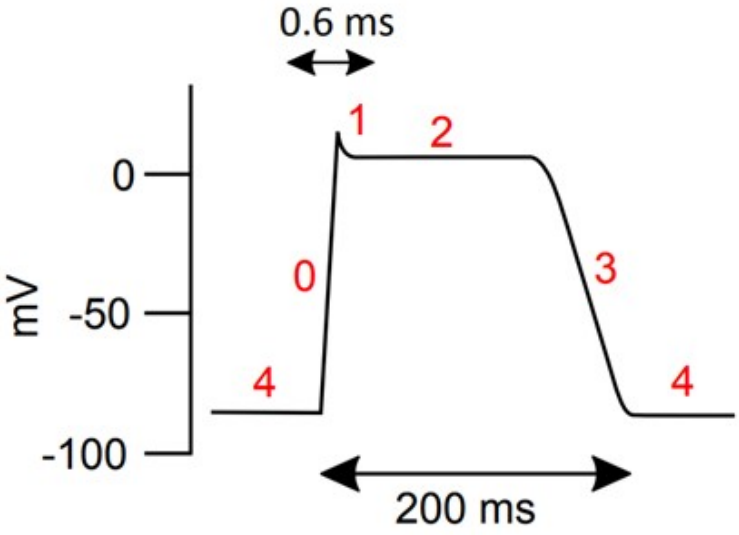


Figure 1.3: Ventricular myocyte AP demonstrating voltage changes during each phase[8].

1.1.4 Gap junctions

The healthy human cardiac myocytes are rod-shaped (100 – 150 μm in length, 10 – 20 μm in width), and gap junctions are located in the intercalated discs, an area at the ends of the cells[9]. Gap junctions allow passage of electrical activity between adjacent cells and is the basis of electrical wave propagation[10]. Gap junctions contain two hexametric channels known as connexon hemichannels (CxHcs) or connexons, these two connexons exist in the membranes of two adjacent myocytes. A full gap junction is formed by two connexons docking together[11]. Thousands of gap junctions are situated together in a gap junctional plaque. Multiple of these plaques are situated together in the intercalated disc[12]. One connexon is formed by six

connexins, a rob-shaped protein. 21 different kinds of connexins have been identified in the human species by analysing genes[11], which is shown in Figure 1.4. Three types of cardiac connexins, Cx40, Cx43, and Cx45 are expressed in mammalian hearts[13]. Different connexins are expressed in different regions of the heart as each of them has different properties such as pore size, conductions and charge permeability. Therefore, their combinations give the connexons and gap junctions different conductions, which is shown in Figure 1.4.

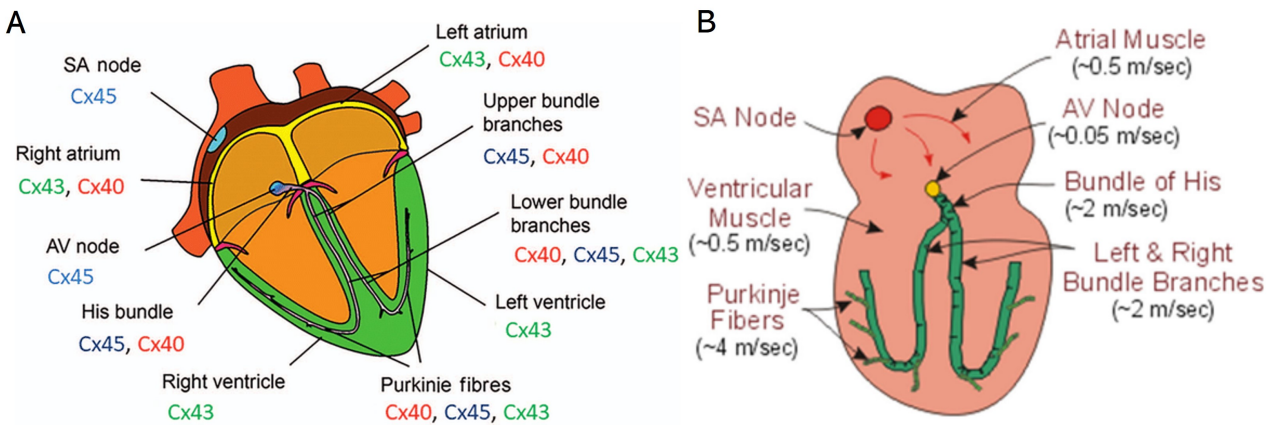


Figure 1.4: (A) Connexins expression in mammalian myocardium. (B) conduction velocities in different regions. As the protein expression varies in different regions, the functions (such as conduction) of the gap junctions also have differences[14, 15].

A myocyte is generally coupled to around 8 – 14 of its neighbour cells by gap junctions, which allows the electrical impulse to propagate at the microscopic level and extend to the macroscopic level[16]. The residence of the gap junction (0.1–10 $M\Omega \cdot cm^2$) is higher than the cytoplasmic resistance (0.1–1 $\Omega \cdot cm$), hence electrical delay has always been obtained in the experiments[17]. Due to the coupling directions and the conduction delay, the electrical propagation in cardiac tissues is discontinuous and anisotropic[18, 19].

1.1.5 Electrophysiological Effects of Cx43 Changes

Connexin43 (Cx43) is the principal gap junction protein in the mammalian heart and plays a central role in maintaining normal cardiac electrophysiology. It is predominantly located at the intercalated discs, where it assembles into gap junction channels that facilitate the intercellular

transfer of ions and small metabolites, thereby lowering electrical resistance between neighbouring cardiomyocytes[20, 21]. This intercellular coupling is fundamental for the rapid propagation of action potentials and the synchronisation of myocardial contraction. Outside the heart, Cx43 is also expressed in the central nervous system and in vascular tissues, where it contributes to diverse processes including astrocytic potassium buffering, intercellular signalling, and vascular tone regulation[22, 23].

Alterations in Cx43 expression, phosphorylation, and distribution have been shown to markedly influence cardiac electrophysiological behaviour. A reduction in Cx43 abundance, frequently observed in conditions such as ischaemic heart disease, dilated cardiomyopathy, and hypertrophy, has been consistently associated with impaired cell-to-cell coupling and slowing of conduction velocity[24, 25]. Similarly, abnormal phosphorylation or redistribution of Cx43 away from the intercalated disc results in heterogeneous conduction and promotes re-entrant arrhythmias[26, 15]. Evidence from murine models further supports this, as targeted deletion or conditional knockdown of Cx43 leads to conduction slowing and a heightened risk of ventricular arrhythmias[27, 28]. Even partial loss, as seen in heterozygous Cx43-null mice, increases susceptibility to inducible ventricular tachycardia[29]. Conversely, interventions that stabilise Cx43 expression or preserve gap junctional communication have been shown experimentally to maintain conduction safety and reduce arrhythmic risk[30, 31].

Although Cx43 does not directly generate ionic currents such as sodium or potassium fluxes, its regulation of intercellular resistance has a critical influence on impulse propagation across the myocardium. Impaired coupling can also alter refractoriness and increase repolarisation heterogeneity, thereby intensifying the arrhythmogenic substrate[17]. Moreover, coupling between cardiomyocytes and non-myocytes, particularly fibroblasts, through Cx43 channels has been demonstrated to depolarise myocyte resting membrane potential and reduce excitability, thereby contributing further to the development of arrhythmia[17]. Collectively, these findings identify Cx43 as a pivotal determinant of cardiac conduction and emphasise its importance in the electrical remodelling that underlies many forms of heart disease.

1.2 Arrhythemias

The population affected by cardiac arrhythmias, especially atrial fibrillation (AF) is growing, and their average age is getting younger in recent decades[32]. Based on data provided by Framingham Heart Study, the prevalence of AF increased threefold from 1966 to 2016. The Global Burden of Disease Project estimated that 46.3 million people worldwide were living with AF in 2016[33]. Cardiac arrhythmias are abnormal muscle contractions and can further lead to cardiac arrest in the worst scenario[32, 34]. Cardiac arrhythmias are caused by irregular electrical conductions such as circus excitation and re-entry triggered by slow conduction, unidirectional conduction block, and a refractory core around which an AP can circulate. Scars, ion channels and gap junctions play key roles in these irregular electrical conductions[35].

Heart failure (HF) and cardiac arrhythmias, particularly AF and ventricular arrhythmias (VAs), are closely intertwined through complex electrical, structural, and neurohormonal mechanisms, forming a vicious cycle that exacerbates disease progression and worsens clinical outcomes[36]. This bidirectional relationship means that HF predisposes patients to arrhythmias, while arrhythmias further deteriorate cardiac function, accelerating HF progression[37].

HF induces gap junctional remodelling, disrupting normal electrical conduction[6]. Downregulation of Cx43 leads to slow and heterogeneous conduction, creating a substrate for re-entrant arrhythmias such as AF and ventricular tachycardia (VT)[38]. HF also alters ion channel expression leading to prolonged APD and increased arrhythmia susceptibility. For example, one of the main reasons for the conduction failure is the reduction of membrane excitability. This reduction is attributed to the reduced availability of Na^+ Channels, which leads to the weakening of I_{Na}. When the flow speed of Na+ ions is reduced to a level, conduction can not be further maintained and failure occurs[39]. Reduced potassium currents (I_K) can delay repolarisation, prolong the QT interval, and increase the risk of Torsades de Pointes. Calcium handling dysfunction, manifested by $SERCA2a$ downregulation and $RyR2$ hyperphosphorylation, leads to intracellular calcium overload and the generation of EADs and delayed afterdepolarisations (DADs).

Apart from ion channels and gap junctions, collagen/ scar also has a significant influence on the electrical wave propagation in the heart[40]. Because heart cells are non-renewable, the forming of scar tissues is a normal phenomenon of replacing dead myocardium and repairing cardiac tissue damage. Cardiac scar tissue, or myocardial scar tissue, develops as part of the healing response following myocardial injury, such as infarction. It is not merely inert or "dead" tissue, but rather a dynamic structure with ongoing cellular and metabolic activity[41]. The scar is primarily composed of a collagen-rich extracellular matrix, predominantly type I and type III collagen, which together account for approximately 97% of its composition. Collagen provides essential structural integrity and plays a critical role in wound repair and remodelling[42]. The cellular constituents of scar tissue include myofibroblasts—fibroblasts that differentiate under stress conditions and are characterised by the expression of α-smooth muscle actin (α-SMA)—which are central to matrix deposition and remodelling[43]. In addition, a subset of cardiomyocytes may persist within the scar, and other non-cardiomyocyte populations, including immune cells, further contribute to its cellular composition and function.

There is a huge difference between the electrical conductivities in scar tissues and healthy cardiac tissues[41, 44]. Therefore, the locations, sizes, and structures of scars may also lead to abnormal electrical conductions. The pathological changes in scars and ion channels, and gap junction remodelling occur simultaneously in the heart experiencing arrhythmias[6]. It is important to investigate the impacts of the individual feature and their combinations on the AP propagation.

1.3 Electrogram and electrogram morphology

An electrogram (EGM) is a recording of electrical activity of organs by placement of electrodes in direct contract with the tissue. As the electrical wavefront propagation is the foundation of heart activity, EGMs are widely used in research, clinical diagnoses, and during treatment[45].

Unipolar and bipolar EGMs capture the summation of electrical activity from cardiac tissue in the area surrounding intracardiac catheter electrodes. Unipolar EGMs measure the difference

in electrical potential between a recording electrode, placed on the heart tissue, and a reference electrode, positioned far from the area of interest. The recording electrode connects to the positive input of a differential amplifier, while the reference electrode is connected to the negative input, enabling the amplifier to detect the signal. In contrast, bipolar EGMs measure the potential difference between two closely spaced electrodes, providing a more localised view of the electrical activity[46]. While bipolar EGMs are particularly useful for determining the local activation time (LAT) in specific regions of the heart, unipolar signals offer a more accurate representation of the activation time due to their ability to capture electrical changes across a wider area[47].

EGMs and APs are closely related: EGMs represent recordings of the electrical activity within the heart, whereas APs correspond to the cellular-level electrical events that initiate myocardial contraction. A standard electrocardiogram (ECG) is typically characterised by three principal components: the P wave, QRS complex, and T wave. The P wave reflects atrial depolarisation initiated by the SA node. This is followed by an isoelectric segment corresponding to the AV nodal conduction delay after atrial depolarisation is complete. Ventricular depolarisation then begins at the apex, generating the QRS complex, during which atrial repolarisation occurs simultaneously but is obscured. Another isoelectric segment follows, marking the completion of ventricular depolarisation. Ventricular repolarisation subsequently originates at the apex, giving rise to the T wave. Once ventricular repolarisation is complete, the ECG waveform returns to the baseline. A representative ECG waveform is illustrated in Figure 1.5[48]. In this study, the analysis focuses on EGMs recorded from the LV. As a result, the P wave is absent because atrial electrical activity is not captured in these recordings.

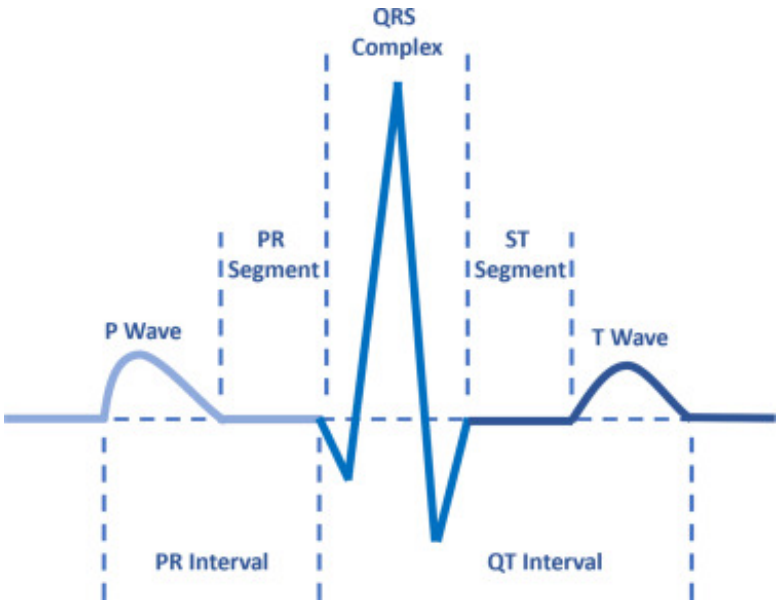


Figure 1.5: Visual description of the different fundamental components of a single ECG heartbeat.[48].

The activation time, which marks the point of maximal depolarisation, is traditionally defined as the moment when the AP reaches its maximum positive slope, signifying the peak of the depolarisation rate. This point coincides with the peak Na+ current, which plays a central role in the depolarisation process. Studies exploring the relationship between the slope of the AP, the unipolar EGM, and the timing of the peak Na+ current have found that the maximum positive slope of the AP, the maximum negative slope of the unipolar EGM, and the peak Na+ current all occur simultaneously. This alignment helps to clearly define the activation time from both the intracellular and extracellular perspectives[49].

The connection between the AP, the unipolar EGM, and Na+ current provides valuable information on the timing and propagation of electrical events in the heart. By combining unipolar and bipolar EGM measurements, clinicians can achieve a more comprehensive understanding of the heart's electrical activity, which is essential for diagnosing arrhythmias and improving the precision of electrophysiological assessments and treatments.

One of the primary advantages of using unipolar EGMs is their ability to accurately measure the activation time of the underlying tissue. The morphology of unipolar EGMs is also easily interpretable, as it reflects the progression of a wavefront across the electrode. In addition to

activation time, unipolar EGMs can be used to identify repolarisation events in the cardiac tissue. A key metric in this regard is the activation-recovery interval, which represents the time between the maximum negative slope of the recorded EGM and the maximum positive derivative that occurs just before the peak of the repolarisation wave. This interval has been shown to correlate with the duration of the cellular AP, offering valuable insights into the electrical properties of the heart[50, 51]. In vitro studies have also suggested that a similar time period, referred to as field potential duration (FPD), can be recorded between the minimum deflection of the EGM and the peak of the T-wave. FPD is thought to be equivalent to APD90, the time at which 90% repolarisation occurred, providing further confirmation of its relevance to AP duration[52, 53].

However, unipolar EGMs also have unavoidable limitations. One is that they can be influenced by far-field electrical activity from regions of the heart distant from the electrode. This interference makes the interpretation of the unipolar EGM morphology more complex, particularly when analysing signals from the atria. In these cases, far-field signals from larger depolarising events, such as ventricular depolarisation, can contaminate the EGM signal, complicating the analysis[54]. Despite these challenges, the ability of unipolar EGMs to provide both activation and repolarisation information makes them a powerful tool in electrophysiological studies, provided their limitations are considered and accounted for in the analysis.

Extracellular EGMs, which are recorded invasively from the heart, provide valuable information on the electrical function of the myocardium. In a healthy heart, the morphology of the unipolar EGM is relatively simple, reflecting normal electrical conduction. However, in pathological conditions, the EGM typically becomes more complex. This complexity is often characterised by multiple components and prolonged durations, which are indicative of abnormal conduction or arrhythmic activity within the myocardium[55]. Changes in EGM morphology may result from several factors, including areas of non-conductive tissue, such as scars or regions of fibrosis, which disrupt normal conduction pathways. These areas can lead to fragmented or altered waveforms in the EGM. Furthermore, abnormal conduction patterns, such as those caused by reentrant circuits, can also contribute to the irregularities observed in the EGM. Consequently, alterations in EGM morphology are often associated with either functional abnormalities in

electrical conduction or the presence of non-conductive regions within the heart. Understanding these changes is essential for diagnosing arrhythmias, assessing myocardial viability, and informing therapeutic approaches, such as ablation or pacing interventions[56].

A key tissue-related factor that influences the morphology of EGMs is anisotropy[55]. Cardiac tissue is anatomically and electrically anisotropic due to the arrangement of muscle fibres, which are aligned in specific orientations. This anisotropy arises from the combined effects of the structural properties of individual cells and the electrical coupling between them, facilitated by gap junctions. As a result, electrical impulse propagation occurs more rapidly along the direction of the fibres, while it is significantly slower in the perpendicular direction. At sites where the activation front runs parallel to the fibre orientation, the unipolar extracellular EGM typically exhibits a biphasic deflection at the point where the activation passes[55]. However, when the activation wavefront propagates orthogonally to the fibre orientation, the EGM morphology becomes more complex. In these instances, the electrical signals may show more intricate patterns, reflecting the altered direction of wavefront propagation[57]. Furthermore, sudden changes in fibre orientation, such as in areas of fiber disorganisation, can lead to discontinuous conduction and a more complex EGM configuration, which has been observed in various pathological conditions[58].

Another important structural factor influencing both electrophysiology and EGM morphology is fibrosis. Fibrosis refers to the abnormal accumulation of fibrous connective tissue, often as part of a reparative or reactive process[41]. The presence of collagen, a key component of the extracellular matrix, is used to quantify fibrosis. Depending on the degree and type of fibrosis, the tissue can exhibit different patterns, ranging from focal, compact scars to patchy, and diffuse forms[41]. The different forms of fibrosis can be classified as follows: Interstitial fibrosis: This type involves the accumulation of collagen between groups of myocytes, disrupting the normal myocardial architecture without completely separating muscle fibres; Diffuse fibrosis: Characterised by collagen interspersed between the myocardial fibres, this form of fibrosis leads to a more widespread distribution of fibrous tissue throughout the myocardium; Patchy fibrosis: In this form, collagen separates myocardial strands over relatively long distances, creating irregularly distributed areas of fibrous tissue that affect the continuity of the myocardial network;

Compact fibrosis: This type is marked by the formation of large, collagen-dense areas that are completely devoid of myocytes, resulting in significant disruptions of the myocardial tissue and conduction pathways. The different types of fibrosis are shown in Figure 1.6. This fibrotic tissue disrupts the normal myocardial structure, creating barriers that affect the propagation of action potentials. The presence of fibrosis forces excitation waves to take anisotropic, often circuitous paths, which can contribute to the formation of reentrant circuits responsible for abnormal electrical activity[59]. Fibrosis can also lead to areas of conduction block and serve as anchor sites for reentrant activation[60], the propagation of the electrical wave is shown in Figure 1.7. While the precise role of fibrosis in the generation and maintenance of abnormal electrical conduction remains unclear[41], scar tissue is believed to be a key contributor to complex fractionated atrial electrograms (CFAE)[61, 62, 63]. Although CFAE-targeted catheter ablation, which aims to target scar tissue, has been explored as a treatment, its success has been limited, and the effectiveness of this method remains a topic of debate[41].

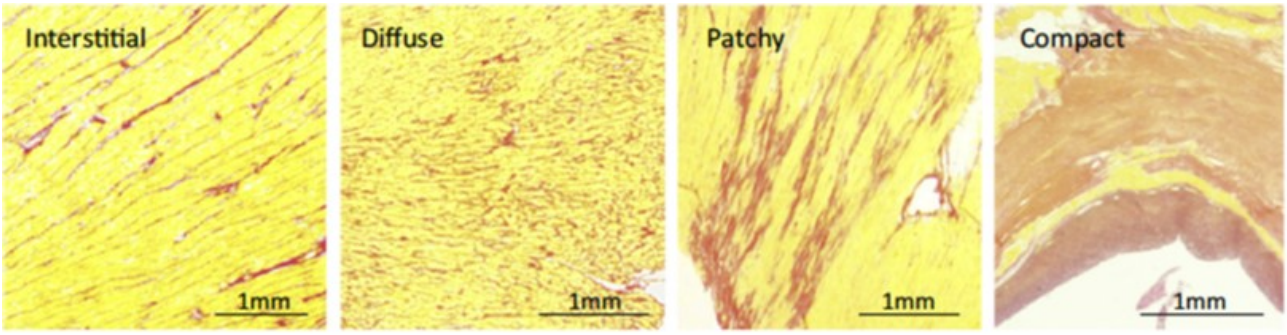


Figure 1.6: Types of human cardiac fibrosis in explanted hearts can be visualised using light microscopy, with collagen-dense areas stained red using picrosirius red[41].

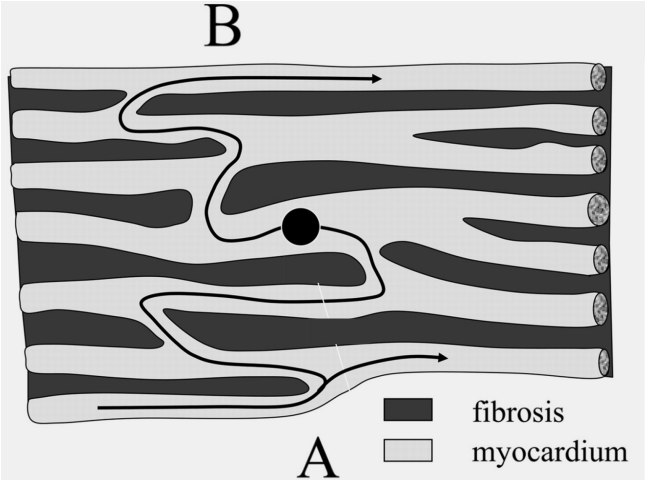


Figure 1.7: Activation induced at site A of an infarcted myocardium propagates following the indicated zig-zag route due to the complex distribution of myocardial bundles[55].

Structural remodelling in cardiac diseases often involves changes in cellular morphology, increased collagen deposition, and the disorganisation of myocardial fibres[55]. Collagen accumulation, which is closely related to fibrosis, plays a significant role in the remodelling process[64, 65]. This increased collagen deposition disrupts the coherence of myocardial wavefronts and electrically isolates cardiomyocytes, further compromising the propagation of electrical signals and contributing to the pathophysiology of arrhythmias[41].

Functional changes that lead to modified EGM morphology often involve abnormalities in ion channels and gap junctions[41, 53]. Gap junctions are crucial for the propagation of APs as they electrically couple neighbouring cells[17, 6]. These protein complexes facilitate cell-to-cell communication by allowing the exchange of ions and the transfer of small molecules (up to 1 kDa) between adjacent cells. By directly linking the cytoplasm of neighbouring cells, gap junctions ensure the coordinated conduction of electrical signals throughout the myocardium[15, 66]. Any alterations in the function or expression of gap junctions can disrupt this process, leading to abnormal electrical conduction and subsequent changes in the EGM morphology, which may contribute to arrhythmias and other cardiac dysfunctions[67]. Ion channel remodelling may affect the formation of AP hence modify the EGM morphology[6].

1.4 Existing Models of Cardiac Electrophysiology

Research in cardiac electrophysiology relies heavily on experimental and computational models that allow systematic investigation of conduction, repolarisation, and arrhythmogenic mechanisms. The complexity of the human heart precludes direct interrogation at sufficient resolution, and thus the development of reliable models has been central to advancing mechanistic understanding. These models can broadly be categorised into biological preparations, in silico simulations, and integrative hybrid frameworks, each with distinct advantages and limitations.

1.4.1 Biological models

Biological models have provided the foundation for much of our current understanding of cardiac electrophysiology. Small-animal models, particularly murine and rat hearts, are widely used owing to their genetic tractability and accessibility[68]. They have enabled the study of ion channel mutations, gap junction regulation, and arrhythmogenic remodelling. However, significant interspecies differences in repolarisation, conduction velocity, and action potential morphology limit their direct translational value to humans. Larger-animal models, such as canine, ovine, and porcine hearts, provide closer structural and electrophysiological similarity to the human myocardium[**?**, 69]. These preparations have been extensively used in arrhythmia research, particularly in mapping studies of atrial fibrillation and ventricular tachycardia.

Ex vivo models, including Langendorff-perfused hearts and thin myocardial slices, have proven particularly valuable for studying conduction and EGM morphology under controlled conditions[70, 71]. Thin-slice preparations preserve native architecture, anisotropy, and cell–cell coupling, while enabling optical mapping and multi-electrode array (MEA) recordings. They provide a balance between structural fidelity and experimental control, making them attractive for probing the relationship between microstructure and electrophysiological readouts. Nevertheless, such preparations are limited by viability over time, lack of neurohumoral regulation, and difficulty in reproducing chronic remodelling processes.

1.4.2 Computational models

Computational, or in silico, approaches have emerged as indispensable tools for probing cardiac electrophysiology. At the cellular level, models of action potentials—such as those by Hodgkin and Huxley[72], Noble[73], Luo and Rudy[74], and more recently the O'Hara–Rudy model[75]—have described ionic currents and excitation–contraction coupling with increasing fidelity. Tissue- and organ-level simulations, incorporating bidomain or monodomain formulations, allow the study of conduction, arrhythmia dynamics, and therapy optimisation[76, 77].

These models enable controlled manipulation of parameters such as ion channel conductance, gap junction density, or fibre orientation, providing mechanistic insights that are often unattainable experimentally. However, limitations remain in terms of computational expense, assumptions regarding tissue homogeneity, and difficulties in faithfully replicating complex structural remodelling observed in diseased hearts.

1.4.3 Hybrid and translational models

More recently, hybrid frameworks have emerged that integrate experimental and computational approaches. These involve validating in silico models against high-resolution biological data, enabling iterative refinement of both systems[69]. Such approaches are particularly promising in linking structural remodelling, gap junctional reomodellings, and EGM morphology. For example, optical mapping of experimental models has been combined with computational reconstructions to investigate anisotropic conduction and arrhythmia initiation[78].

Despite substantial progress, gaps remain in correlating microstructural and molecular alterations with clinically measurable signals such as EGM. While clinical studies have demonstrated the diagnostic utility of EGM morphology in identifying arrhythmogenic substrates [61, 79], there is still a need for models that can systematically relate structure and function to recorded signals. This is the niche addressed in the present thesis: developing and integrating biological and computational models capable of quantifying how structural and functional remodelling influence EGM morphology.

1.5 Simulation of cardiac electrophysiological activities

In order to investigate the mechanism of heart activities and cardiac arrhythmia, it is necessary to find out which factors can influence the AP and its propagation[80]. Based on the knowledge of the biological processes of AP generation and propagation, an accurate in- silico model of AP propagation could precisely simulate the propagation of electrical waves through cardiac tissues without noise[81]. It can bring convenience to the research on the mechanisms of heart activities and cardiac arrhythmias. An AP propagation model contains two parts: the reaction process and the diffusion process. The reaction process describes the AP progress in every cell and the diffusion process is how the electrical wave travels through cells[82]. Therefore, large numbers of experiments are required to investigate the functions and locations of ion channels, and gap junctions[83]. The parameters of the model should also be calibrated by comparing the simulation results and the experimental data[84].

1.5.1 Action potential model

AP models are used to simulate the change of the transmembrane potential over time after the cell is stimulated. Alan Hodgkin and Andrew Huxley developed a model for the nerve AP based on ion channels theory in 1952[80]. Although it is relatively simple compared to the cardiac cell models developed later, the mathematical description of ion channels in it is used in most of the models. The model for ion channels is developed from changes in entropy, which is calculated by Boltzmann's equation:

$$S = k_B . \ln W. \tag{1.1}$$

where S is entropy ($J.K^{-1}$), W is the number of ways of arranging a distribution of microstates of a system and kB is Boltzmann's constant.

The relationship between the change of energy and the change of entropy is described as:

$$\Delta q = T\Delta S. \tag{1.2}$$

where T is temperature.

The energy change when the ion flows from the high ion concentration environment to the low ion concentration environment is:

$$\Delta q = T\Delta S = k_B \mathrm{T}(\ln[Y^+]_o - \ln[Y^+]_i) = k_B \mathrm{T} \ln \frac{[Y^+]_o}{\ln[Y^+]_i}, \tag{1.3}$$

where $[Y^+]_0$ is the low ion concentration and $[Y^+]_i$ is the high concentration. The unit of Δq is J.ion^{-1}. The equation could be further driven to the form as:

$$\Delta Q = RT \ln \frac{[Y^+]_o}{[Y^+]_i}, \tag{1.4}$$

The unit of ΔQ is $J.mol^{-1}$, hence R = $\mathrm{k_B N_A} \approx 8.4$ (J. mol^{-1}K^{-1}) which is known as universal gas constant.

In order to calculate the potential change, ΔQ is replaced by z$\mathrm{F}\Delta\Phi$ where z is the number of charges in one ion, F is Faraday's constant, and $\Delta\Phi$ is the change in potential.

Therefore, the potential change can be described as:

$$\Delta\phi = E_Y = \frac{RT}{zF} \ln \frac{[Y^+]_o}{\ln[Y^+]_i}, \tag{1.5}$$

where E_Y is the "Nernst" potential of ionY^+.

The current flow through the channel could be calculated from the Nernst potential:

$$\bar{\iota}_Y = \bar{g}_Y(V - E_Y). \tag{1.6}$$

where $\bar{g}_Y$ is the channel conductance.

It is believed that the activation and the deactivation of the channel are controlled by the channel gate. A first-order differential equation is introduced to describe the gate states transition[80]:

$$\frac{dy}{dt} = \alpha_y(1-y) - \beta_y.y. \tag{1.7}$$

where α_y is the opening rate and β_y is the closing rate. y is generally used to describe the fraction of gates opening, hence the fraction of gates that are closed is 1-y. And the solution of the equation is:

$$y = \frac{\alpha_y}{\alpha_y + \beta_y} + Ae^{-(\alpha_y+\beta_y)t}. \tag{1.8}$$

Furthermore, it has been discovered that the initial current obtained from the experiments (squid experiments) is smaller than the calculated data, so another parameter that represents the number of gates is added to the model:

$$i_Y = \bar{\imath}_Y y^\gamma = y^\gamma \bar{g}_Y(V - E_Y). \tag{1.9}$$

where γ is the number of the gate.

The cable equation is applied to the modelling of the AP, by ignoring the axial current changing rate, the relationship between current flow through the ion channels and the transmembrane potential is described in Hodgkin and Huxley's model as:

$$\frac{dV}{dt} = -(i_{Na} + i_k + i_L)/C_m. \tag{1.10}$$

Where i_L is the current flow through leakage channels, i_{Na} is the current flow through the

sodium channel, i_K is the current flow through the potassium channel and Cm is the capacitance of the membrane. These equations formed the first model of the nerve AP[80].

Based on this, a range of cardiac AP models for different mammals has been developed, including models for mice[85], rabbits[86], guinea pig[87], goats[88], and canines[89]. The Priebe-Beuckelman model (PB model, 1998) is the first AP model for human ventricular cells. It is developed based on the Luo-Rudy (LR1) model which is a model for guinea pig ventricular cells. A range of models of human cardiac cells from different regions (atria, ventricle, nodes, etc.) of the heart has been developed in the past decades.

1.5.2 Continuum and discrete propagation models

The AP propagations between the cells are proved to be discontinuous due to the exitance of gap junctions and membranes. Continuum models still have been developed by applying continuum approximations. The most widely used approach to build continuum models is the bidomain or monodomain approach[69, 77, 90]. In this approach, Ohm's law is driven into a set of partial differential equations. The extracellular and intracellular domain are coupled at all meshed points in finite element analysis, so the discrete propagation is averaged.

The bio-domain equations represent the homogenisation of the cardiac tissue, all discrete features are averaged over the volume. The basic equations are:

$$\nabla\overline{\sigma}_l\nabla\phi_i = \beta I_m \nabla\overline{\sigma_e}\nabla\emptyset_e = -\beta I_m - I_e I_m = C_m\frac{\partial V_m}{\partial t} + I_{ion}(V_m,\gamma) - I_{trans}. \tag{1.11}$$

Where σ_i is the intracellular conductivity tensor and σ_e is the extracellular conductivity tensor, β is the surface to the volume ratio, I_{trans} is the transmembrane current, I_e is the extracellular current[69]. These equations combine with the boundary conditions could form the propagation model of the AP. Even though the continuum approximations inevitably introduce errors in the simulation results, the simulation could still be applied in some specific research.

The discrete models are more complex than the continuum models because the traditional

cable theory cannot be used to represent this type of conduction. The real shape of the cells, anisotropic in conductions, spaces, and other features has been included in discrete models in recent research and the error between simulation results and experimental data is getting smaller. However, these complexities of the models bring long calculation time which is not suitable for all research.

1.6 Outline of thesis

The central hypothesis of this work is that LV EGM morphology is determined by the underlying structural (collagen) and functional (nerve, Cx43 and $Na_v1.5$ ion channel) substrates of the myocardium, and such electrical activities can be simulated using the in-silico model.

In order to address the main hypothesis, the thesis has the following sub-hypotheses and related aims:

1. Development of an in silico tool that can extract features from EGM recordings collected from different experiments.

2. Validation of the structural change of LV (collagen) and its corelation with the morphology of EGM using rat and human models.

3. Validation of the functional changes of LV (nerve, Cx43 and $Na_v1.5$ ion channel) and their correlation with the morphology of EGM using rat and human models.

4. Characterisation of the ex-vivo intact heart EGM morphology changes with functional changes that are achieved by pharmacological modifications.

5. Development of in silico simulation models that can include the influence of underlying substrates on LV electrical activities.

The structure of the thesis is as follows:

Chapter 1 introduces the foundational concepts of cardiac electrophysiology and arrhythmias, discussing the physiological and pathological factors that influence the electrical activity of

the heart. The chapter also highlights the role of EGMs in the analysis of arrhythmic events, providing a detailed overview of the features that can be derived from EGM recordings, such as fractionation, voltage, and dominant frequency. Additionally, this chapter addresses the challenges involved in linking EGM morphology to underlying structural and functional changes in the heart and presents an overview of existing computational models used to study LV electrical activity. The goal is to establish the context for the study and introduce the objectives of the thesis.

Chapter 2 outlines the experimental and computational methods employed in this research. It describes the biological models used, including LV tissue slices from rat and human hearts, as well as ex-vivo porcine hearts and neonatal rat ventricular myocytes. The chapter explains the protocols for the preparation of the samples, EGM recording, slides staining and how pharmacological interventions were applied to alter functional properties of the ex-vivo hearts. The computational methods, including the development of the EGM feature extraction tool using Python and the simulation models created with Nektar++, are also detailed. This chapter provides a comprehensive overview of the materials and techniques that underlie the study, ensuring clarity and transparency in the research methodology.

In Chapter 3, the focus is on the development and validation of the EGM feature extraction tool. This chapter explains the various data processing techniques and algorithms implemented to extract key features from EGM recordings. The chapter also presents the validation process of the tool, comparing its results with those obtained through manual extraction methods. The aim is to provide a reliable and efficient tool for EGM analysis, enabling researchers to process large datasets and perform consistent feature extraction across different experimental conditions.

Chapter 4 investigates the structural changes in the LV myocardium, particularly focusing on collagen deposition and its effects on EGM morphology. Using tissue slices from rat and human hearts, this chapter explores how alterations in collagen expression and distribution are associated with changes in EGM characteristics. This chapter provides a deeper understanding of the relationship between structural remodelling and its impact on the heart electrical activity,

which is a key to understanding arrhythmic processes.

Chapter 5 focuses on functional changes within the LV and their impact on the EGM morphology. This chapter explores how changes in Neurons expression, gap junction remodelling (especially Cx43), and ion channel remodelling (such as Na_v 1.5) affect the electrical properties of the heart. The chapter uses neonatal rat ventricular myocytes and ex-vivo human heart slices to study how these functional alterations correlate with observed changes in EGM features. The aim is to establish a clearer link between cellular and molecular-level changes and macroscopic electrical disturbances, advancing our understanding of arrhythmogenesis.

Chapter 6 examines the effects of pharmacological modulators (as functional changes) on the EGM morphology using ex-vivo porcine heart models. By applying different drugs that modulate ion channels and other cardiac functions, this chapter investigates how pharmacological interventions alter the electrical activity of the heart. The chapter compares baseline EGM recordings with those taken after drug administration to assess whether the effects observed in isolated tissue models are also seen in whole-heart preparations. This chapter serves to bridge the gap between small tissue and whole-heart models.

Chapter 7 presents the development and application of in-silico models to simulate LV electrical activity. These models integrate a functional change identified in previous chapters and simulate how it affects the heart's electrical conduction. The chapter compares two types of simulation models: the continuum propagation model and the discrete-cell model. By analysing these models, the research explores their respective strengths and limitations in capturing the complexity of the electrical behaviour of the LV. This chapter highlights the value of computational modelling in understanding the dynamics of electrical activity in the heart and its relevance for studying arrhythmias.

Chapter 8 concludes the thesis by summarising the key findings of the study and discussing their clinical implications. The chapter reflects on how the study has advanced our understanding of the structural and functional changes in the LV and their effects on EGM morphology. It also discusses the potential for using these findings to improve diagnostic and therapeutic strategies for arrhythmias. Finally, the chapter outlines potential directions for future research, including

further refinement of in-silico models and the application of these tools to personalised medicine in the treatment of arrhythmias.

Chapter 2

Materials and Methods

2.1 Introduction

This chapter provides a general description of all the materials and biological and computational techniques used in this study. Materials include fresh human donor hearts, human failing hearts, porcine hearts, rat hearts, neonatal rat ventricular myocytes (NRVM), neuron cells and the consumable materials for the experiment.

Methods include EGM acquisitions from in vitro and ex vivo models, for ex vivo models, on which ion channel and gap junction modulator are applied, immunofluorescence and microscopy. Computational modelling and simulation are also included. Detailed materials and methods will be introduced in the relevant chapters.

The biological methodology is developed to provide the necessary data to investigate how the structural and function changes stated in Chapter 1 influence the electrophysiology of the models and have been further imported into the computational model for the simulation. The computational methodology is developed to build an in-silico model to simulate the electrical behaviour of the models using biological acquired data. A schematic representation of the methods is shown in Figure 2.1.

The animal experiments conducted in this study adhered to the guidelines established by Im-

perial College London, Royal Veterinary College and complying with the Animal Scientific Procedures Act (ASPA) of 11 October 1986 and Directive 2010/63/EU.

The experimental work was approved by the Imperial College London Ethical Review Board and was carried out under the Project License PCA5EE967.

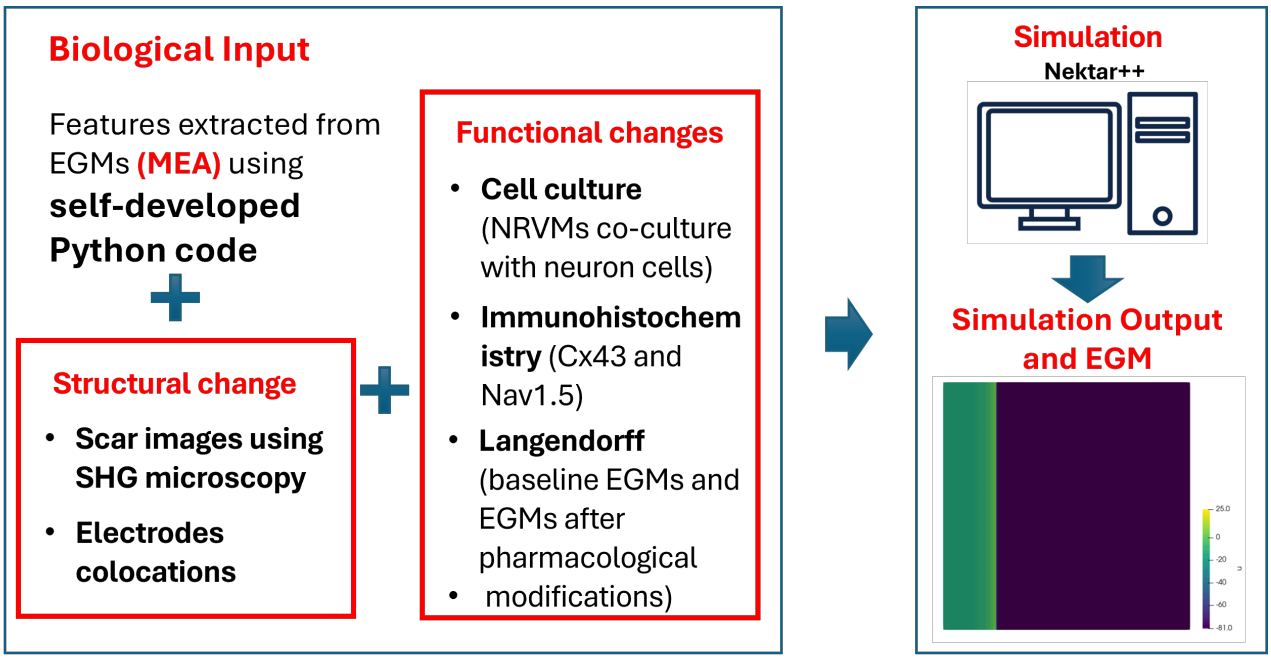


Figure 2.1: Overview of the methodology used by this study towards the development of both biological models and computational model. The EGMs were recorded from cells, rat heart slices and human heart slices using microelectrode array and ex-vivo porcine hearts using HD Grid catheter. Features were extracted from the EGMs using a self-developed python code and then been analysed. The structural change of the slices was analysed using SHG microscopy images in association with an in-house electrode collocation and scar quantification code. The functional changes were analysed using immunofluorescence, microscopy and pharmacological modifications on ex-vivo hearts. The EGM features were then correlated with these changes and some in-silico simulations were carried out.

2.2 Materials

In this section, the materials used in this study and the preparation processes are introduced.

NRVMs and sympathetic neurons (SNs) cells were used to study the influence of neuro on the electrical activities at the cellular level due to the fact that the concentration and distribution of NEVMs and neuron cells are easy to control, and hence the results can be easily compared.

Blocks of fresh human left ventricles (both donor hearts and failing hearts) and fresh rat ventricles were acquired and cut to record electrograms. The prepared slices were called biomemetic myocardial slices (BMS). The BMS were then fixed and imaged to study the collagen contributions.

An adjacent block from all human left ventricles was also saved for studying ion-channel remodelling using immunohistochemistry and imaging.

Electrograms were also recorded from porcine and human ex-vivo Langendorff models using commercial and in-house made catheters.

All biological data recorded were analysed using a validated python code made in house and used to develop the in-silico model.

2.2.1 Cell culture

All cell culture work was performed in laminar flow safety cabinets to maintain sterile conditions. Neonatal Mouse and Rat Heart Dissociation Kit (Miltenyi Biotec Inc.) was used to isolate NRVM from neonatal rat pups. The rats were anaesthetised with 5% isoflurane-95% O_2 and killed by cervical dislocation, after which the hearts were quickly extracted. The ventricles were dissected into 1 mm^3 after the vessels and atria were carefully removed. The enzyme A, enzyme D and buffer Y were mixed with buffer x, then the cut ventricles were incubated three times with the enzymes at 37°C for 15 minutes each time. The sample was centrifuged at 1000 rpm for 5 min after passing a 70um pre-separation filter. The cell pellet was re-suspended in M199 10% cell culture medium which contains 10% Neonatal Calf Serum (NCS, BioSerum) , 0.5% penicillin-streptomycin (Sigma, USA), 0.1% L-glutamine (Sigma, USA), and 0.5% vitamin B12.

The isolated rat carotid artery ganglion was placed under a microscope (Leica, Germany), and the ganglion was carefully removed from the artery using fine forceps. The cleaned ganglion was then centrifuged (200 rpm x 2 min). After that, 1-1.5 mL of trypsin was added for digestion at 37°C for 30 minutes. The sample was re-suspended with 1-2 mL of final medium (Roswell Park

Memorial Institute medium supplemented with 0.5% horse serum, 0.5% penicillin-streptomycin, and 1 mM nerve growth factor) followed by another round of centrifugation. The experimental workflow is shown in Figure 2.2.

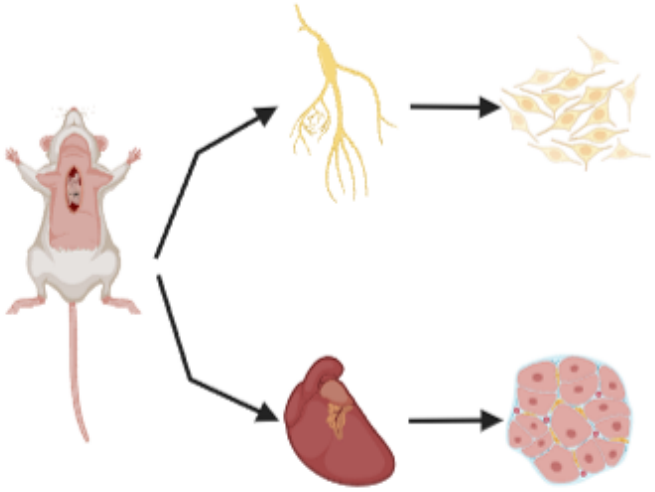


Figure 2.2: Heart and carotid artery ganglion were dissected from the neonatal rat and NRVMS and SNs were isolated following different protocol. Pure NRVMs, NRVMs + 5% SNs and NRVMS + 10% SNs were then cultured for 4 days.

Pure NRVM and NRVM co-culture with SNs were cultured four days. Cells were plated on the Micro-electrode array (MEA) dishes (Figure 2.3) on day 1. In details, 70ul of collagen (SIGMA, USA) were added to the centre of each MEA dish and the dishes were then washed and dried under UV light for 1 hour. The cell suspension was centrifuged at 1000 rpm for 5 min. Then, the supernatant was removed and the cells were resuspended in the different concentration (0%, 5% and 10%) of SNs suspension or an equivalent amount of 10% M199. The total amount of cells in each dish was controlled to 250,000. Stratified cell co-culture ratios, including controls and experimental groups, are shown in Table 2.1. The dishes with pure NRVMs were placed in a humidified incubator (1% CO_2 at 37°C), while the dishes containing both NRVM and SNs were placed in a humidified incubator (5% CO_2 at 37°C) for 30 minutes. After the incubation, the total amount of solutions in each MEA plate was toped up to 1ml with 10% M199. The plates were then placed back into the incubators for 24 hours. The medium in the dishes was changed on day 2 and day 3 cell culture to provide a clean and nutritious environment for the cells. On day 2, 1ml of 5% M199 medium (with 5% neonatal serum, 0.5% penicillin,

0.1% L-glutamine, and 0.5% vitamin B12) was added to each dish after 10% M199 medium was removed. The dishes were then shaken vertically and horizontally (2minutes each) and the medium was removed to remove dead and unattached cells. The dishes were put back to the neonatal/neuronal incubators to continue incubation after topping up another 1 ml of 5% M199 medium per dish. Day 2 culture protocol was repeated on day 3, but without shaking step. EGMs were recorded and the cells were fixed for further staining after the EGM measurement on day 4. The M199 medium in the MEA dish was changed to warmed (37°C) 1mL of Hank's buffered saline solution (HBSS, Thermo Fisher Scientific, USA) and put back to the incubator for 30 minutes for stabilisation before the recording and the dish was kept at 37°C while recording. The detailed electrical signal acquisition method will be introduced later in section 2.3.

	NRVMs	SNs	M199
100% NRVMs + 0% SNs	250000	0	none
95% NRVMs + 5% SNs	237500	12500	top up to same amount of 100% NRVMs
90% NRVMs + 10% SNs	225000	25000	top up to same amount of 100% NRVMs

Table 2.1: The number of NRVMs and SNs to be added. Cell suspension volumes were determined by dividing the desired number of cells by the premeasured concentrations, with the total volume of M199 medium maintained at a fixed value.

Cultures were monitored daily using an epifluorescence microscope (Leica, Germany) to assess cell morphology, density and health conditions (Figure 2.3).

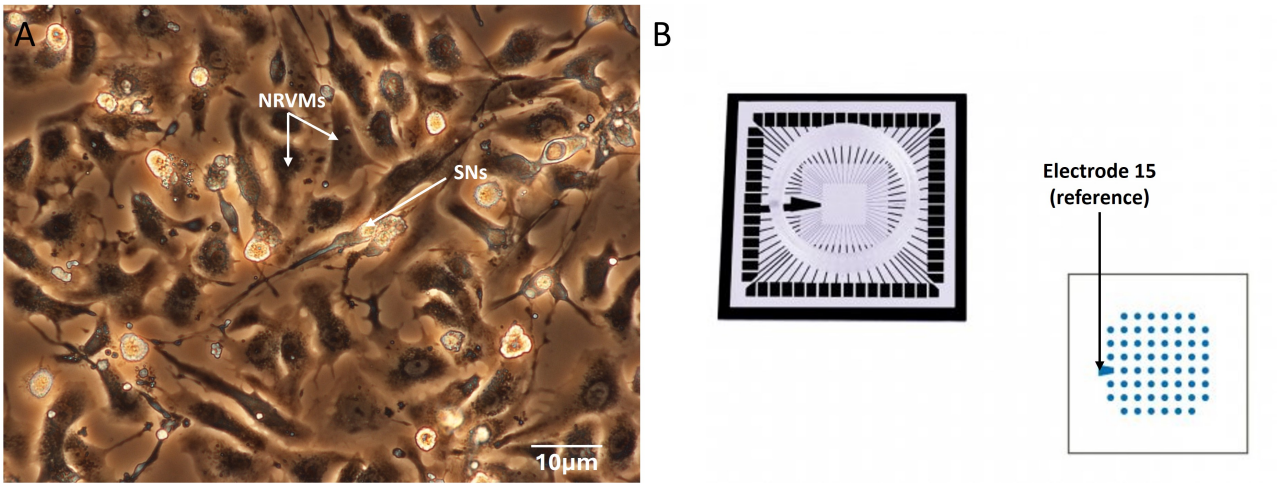


Figure 2.3: (A) Co-cultured NRVMs and 10% SNs cells on day 2 under 20x microscope. (B) Micro Electrode Array dish. There are 60 gold electrodes on the dish organised on an 8 x 8 matrix (electrodes missing on the corners) with an inter-electrode space of 700µm and electrode diameter of 100µm, No. 15 electrode is reference.

2.2.2 Collection and preparation of rat heart tissue samples

Rat left ventricular transmural tissue samples were prepared from angiotensin-II infusion hypertension-induced myocardial fibrosis model (N = 4) and healthy model (N = 4). 16 weeks old female Sprague-Dawley rats weighting 250-350g were used to prepare both models.

For the angiotensin-II infusion hypertension-induced myocardial fibrosis model, all rats underwent a 7 day period of acclimatisation before the procedure. Rats were anesthetised with 5% isoflurane in an induction chamber and immediately transferred to a Bain coaxial circuit in a preparation room, where isoflurane concentrations were maintained at 1.5–2% in 95% O_2. The abdomen of the rats was shaved and cleaned, and local anesthetic (0.5% bupivacaine) was injected midline in the subcostal region. Additional analgesics (buprenorphine 0.05 mg/kg and carprofen 5 mg/kg) and 1 ml of 0.9% saline were also administered. The rat was then transferred to the operating table and maintained under deep anesthesia, the state of anesthesia was confirmed by testing if the toe pinch reflex is absence and monitoring respiratory rate during the procedure. A small 2–3 cm incision was made in the midline of the upper abdomen. Blunt dissection was used to separate the subcutaneous tissue. The abdominal wall was lifted to avoid injury to the internal organs and incised to access the peritoneal cavity. An osmotic minipump

(2ml4, Azlet, CA, USA) was placed in the right iliac fossa, which was preloaded under sterile conditions to deliver angiotensin-II in a rate of 500 ng/kg/min. The incision in the muscle layer was closed with 4-0 Ethibond sutures (Ethicon, UK), and the skin layer was closed with 4-0 Vicryl sutures(Ethicon, UK).

After surgery, animals were placed in a plexiglass box with constant temperature of 30°C. When animals were fully mobile and alert, they were transferred into individual ventilated cages with non-abrasive substrate, wet food and oral analgesics (Carprofen 0.1ml/100ml water) for 72 hours. Animals were checked twice daily for signs of distress and further administered subcutaneous analgesia (Bupivacaine 0.5%). Once they had gained weight, they were rehoused to their previous cages. Animals were further monitored daily until the end of the study protocol or until the humane endpoint defined in the project license was reached. The fibrosis maturation period was a total of 30 days.

Rats from control group and myocardial fibrosis induced model were anaesthetised with 5% isoflurane-95% O2 and killed by cervical dislocation and hearts were harvested within 30 seconds of circulatory arrest. Heart and lung were immediately immersed in ice-cold high potassium/BDM cutting Tyrodes solution (140 mM $NaCl$, 6 mM KCl, 10 mM glucose, 10 mM HEPES, 1 mM $MgCl_2$, 1.8 mM $CaCl_2$, 3g/L 2.3 butanedione monoxime (BDM), pH 7.4) . After transferring the heart to the laboratory, it was dissected. The attached lung was first removed followed by the removal of the atria. The left ventricle was then flattened and isolated.

The tissue was mounted on a specimen holder of a high precision vibrating microtome (7000smz, Campden Instruments Ltd., UK) with endocardium down using tissue adhesive Histoacryl® (catalogue No.: 1050044; B.Braun Surgical S.A., Spain). The holder and the mounted sample were magnetically attracted to a water bath and submerged in ice-cold oxygenated (100% O_2) cutting Tyrode's solution. The water bath was fixed on the vibrating microtome and the sample was cut into BMS with 300µm thickness. Ceramic blade (7550/1/CC, Campden Instruments Ltd., UK) was used to slice the sample with the advancement speed of 0.01 mm/s-0.03 mm/s, according to the softness of the samples, the amplitude 2 mm and the vibration frequency was 80Hz.

Slices were incubated in oxygenated ice-cold cutting Tyrode's solution for at least 30 min before being placed in the center of the MEA dish and EGM recordings were acquired in oxygenated warm (40°C) recording Tyrodes' solution (140 mM $NaCl$, 6 mM KCl, 10 mM glucose, 10 mM HEPES, 1 mM $MgCl_2$, 1 mM $CaCl_2$, 3g/L 2.3 butanedione monoxime (BDM), pH 7.4).

2.2.3 Collection and preparation of human heart tissue

Samples from rejected human donor and explanted failing hearts were used for the study included in this thesis. The Royal Brompton and Harefield Hospitals Cardiovascular Research Centre Biobank provided failing human heart tissue samples for this study (NRES ethics number for biobank samples: 09/H0504/104+5; Biobank authorisation number: NP001-06-2015) alongside project specific ethics allowing collection of donor hearts via NHS Blood and Transplant (REC reference 16/LO/1568). Both sources were with informed consent either from the patient or their next of kin. All human tissue on this study was processed and stored in accordance with the Human Tissue Act 2004 (c30).

Human failing hearts were all collected from the theatres in Harefield hospital by trained research tissue collectors. The apex of the failing heart was dissected immediately by the surgeon after the after explantation. The apex (Figure 2.4) was then immersed in ice-cold cardioplegia solution (The cardioplegia used was Sterile Concentrate for 78 Cardioplegia Infusion, Martindale Pharmaceuticals Ltd, UK) and transported to the laboratory with in 2 hours. Human donor hearts (Figure 2.4) were the hearts have been rejected for transplantation due to different reasons such as age, organ size and functions. These hearts were then offered for research. Interest in the heart will be registered if following requirements are meet: 1. the ejection fraction (EF) of the heart is higher than 40%; 2. The donor does not carry pathogens in group 3 and group 4; 3. The transport time is less than 7 hours. Once the heart met all the requirements and was allocated to the College, the retrival team were required to flush and store the heart with ice-cold cardiopiegia.

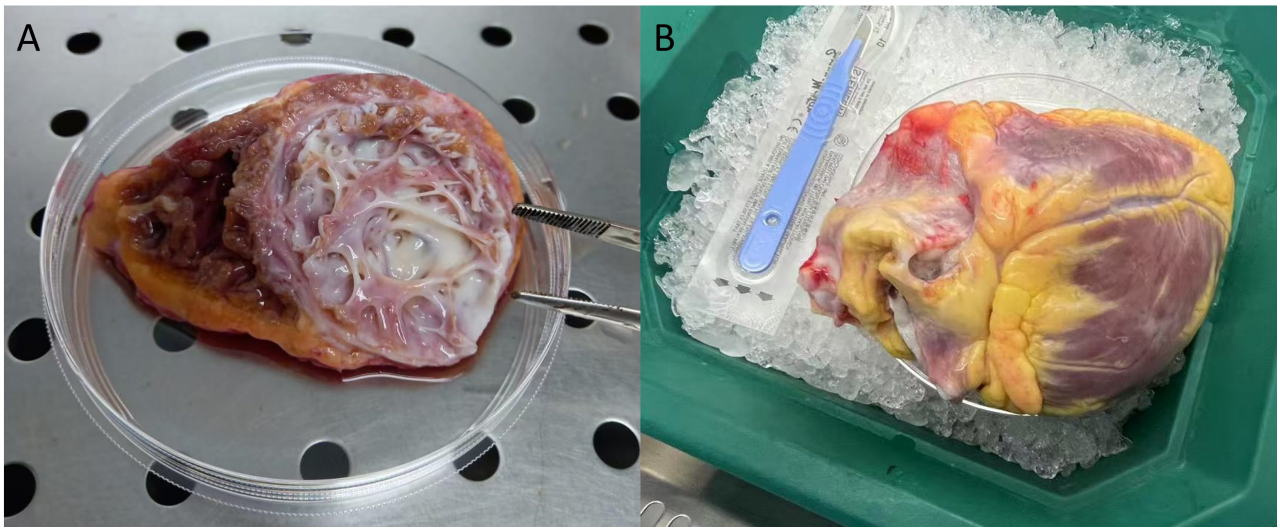


Figure 2.4: (A) Apex of the failing heart from a patient diagnosed with DCM. (B) A healthy donor heart meets all the requirement and was transported to the laboratory.

34 human failing hearts and 12 human donor hearts were collected during the period of this study and data has been recorded from 11 failing hearts and 7 donor hearts. No EGM has been recorded from the slices prepared from the rest hearts due to different reasons such as long transportation time and poor quality of the samples.

For human failing hearts, the patients' demographics, indications for anti-arrhythmia treatment, the diagnosed heart failure subtype and the presence of a device implant are shown in Table 2.2. For human donor hearts, the reason for rejecting the donor sample as a transplant, alongside the donor's history for alcohol consumption, smoking and the demographics are shown in Table 2.3. Only the information of the hearts from which EGM data is collected is included.

Patient No.	Age	Gender	HF Phenotype	Heart failure Arrhythmia (Anti-arrhythmic drugs)	Device implantation
1	34	F	RCM	Unknown	Yes (CRT-D)
2	23	M	ARVC	Unknown	No
3	48	M	ICM	No	No
4	16	M	DCM	No	No
5	38	M	ICM	No	No
6	38	M	DCM	Yes (Amiodarone)	Yes (LVAD+ICD)
7	52	M	ARVC	Unknown	No
8	61	M	DCM	Yes (Digoxin)	Yes (LVAD)
9	58	M	ICM	No	No
10	49	M	DCM	Yes (Amiodarone)	Yes (LVAD)
11	51	M	DCM	Yes (Amiodarone)	Yes (LVAD)

Table 2.2: Clinical characteristics of heart failure patients

Abbreviations: RCM=Restrictive cardiomyopathy; ARVC=Arrhythmogenic right ventricular cardiomyopathy; DCM=Dilated cardiomyopathy; ICM=Ischemic cardiomyopathy; LVAD=Left ventricular assist device; CRT-D=Cardiac resynchronisation therapy defibrillator; ICD=Implantable cardioverter-defibrillator.

Donor No.	Age	Gender	HTN History	Cardiac History	Smoking	Alcohol	Notes
1	22	F	No	No	No	Non-drinker	Cause of death: cerebral hypoxia. Rejection reason: cardiac function.
2	34	F	No	No	No	Non-drinker	Rejection: medical history + blood group. Death: brain tumor.
3	72	F	No	No	No	Light (1-2 U/day)	Rejection: age. Death: intracranial hemorrhage.
4	43	M	No	No	Yes (10 cig/day)	Heavy (7-9 U/day)	Rejection: function. Death: intracranial hemorrhage.
5	48	F	No	No	No	Very heavy ($\geq 9U/day$)	Death: hypoxic brain injury. Rejection: function.
6	37	F	No	No	No	Occasional ($\leq 1U/day$)	Death: brain tumor. Rejection: not mentioned.
7	41	M	No	No	No	Light (1-2 U/day)	Death: intracranial hemorrhage. Rejection: history.
8	59	F	No	No	No	Light (1-2 U/day)	Death: intracranial hemorrhage. Rejection: age.
9	53	M	No	No	No	Light (1-2 U/day)	Death: intracranial hemorrhage. Rejection: history.

Table 2.3: Characteristics of donors for rejected heart transplants
Abbreviations: HTN=Hypertension; U=Alcohol units; cig=Cigarettes

A 1 cm*1 cm*1 cm block from the left ventricle of each heart were dissected immidiatelly after the heart was taken out from cardioplrgia. The block was then mounted on the specimen holder of the vibrating microtome with epicardium down using tissue adhesive Histoacryl. The slicing protocol is same as that for rat left ventricle tissue, which is shown in Figure 2.5.

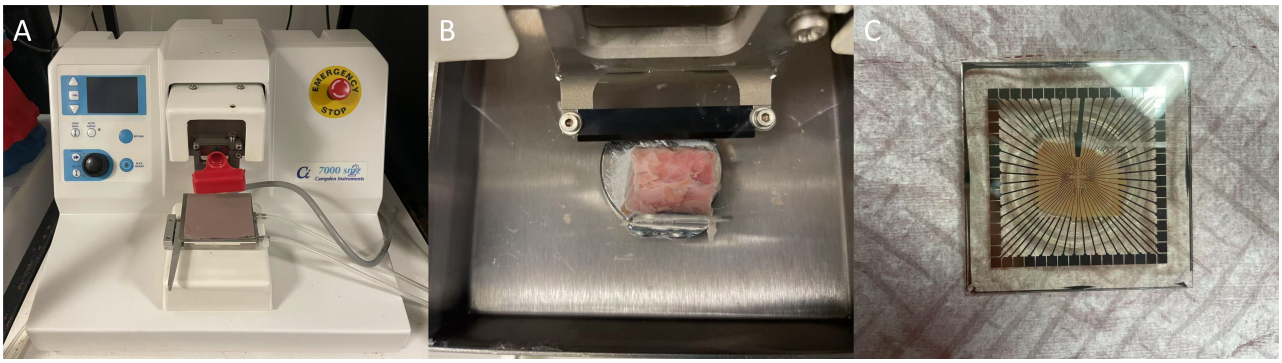


Figure 2.5: (A) The high precision vibrating microtome used for producing tissue slices. (B) A block from human left ventricle was mounted on the specimen holder using Histoacryl® during slicing. The tissue is submerged in a waterbath full of cold and oxygenated cutting Tyrode's solution. (C) A BMS placed on top of the electrode matrix of a micro-electrode array dish, the dish was perfused with warm recording Tyrode's solution during the recording.

An adjacent block (1cm* 1cm* 1cm) was taken from the left ventricle of each heart used for MEA recording for immunohistochemistry. The block was wraped with parafilm and aluminum film (Heathrow Scientific, UK) and then been frozen using dry-ice before saved in -80°C freezer.

Slides were prepared from frozen samples using a cryostat (OTF5000, Bright, UK) at -30°C. First, the frozen human left ventricle tissue block was mounted onto the specimen holder using OCT compound (Cryo-M-Bed embedding compound, Bright, UK) with the epicardium face down. The micrometre dial was set to 10µm to obtain ultrathin sections facilitating efficient antibody penetration and clear imaging of tissue. Slices were then cut parallel to epicardium, placed onto super-frost microscope slides (VWR laboratories, USA) and stored at -80°C.

2.2.4 Langendorff hearts

Isolated human and porcine hearts were used in the study of this thesis to develop the EGM feature extraction code, analyse functional abnormalities on EGM morphology and test the

electrodes distribution of catheters, which were further put into the in-silico simulation model. Comparing to the cell model and slice model, analysis of ex vivo human and porcine hearts is the closest translational step to the conditions observed clinically.

Porcine heart explanations were carried out in the RVC. Four healthy 4-5-month-old white female pigs weighing 70-80 kg were rested for at least a week before the heart extraction to provide a stable heart for the study. Ketamine (20mg/kg) and Midazolam (0.5mg/kg) were injected intramuscularly (IM) for the purpose of premedication. Propofol (2-4mg/kg) was used to induce anaesthesia via a 22 gauge intravenous catheter which was placed in the auricular vein (Carestastion 650, GE Healthcare, UK). Anaesthesia was maintained using inhaled sevoflurane (SevoFlo, Zoeitis, UK). Fentanyl (0.2mcg/kg/min) was applied via infusion to achieve analgesia after an initial loading dose of 2mcg/kg. Multiple vital signs were monitored to ensure welfare and the quality of the heart. In detail, the blood pressure was measured using a catheter (Leadercath, Vygon, UK) which was placed in the femoral artery. Body temperature, electrocardiogram, capnography etc. were measured using a multiparameter monitor (Carestation 650, GE Healthcare, UK). An overdose of 0.7mL/kg pentobarbital was applied to perform euthanasia at the end of the heart retrieval. The procedure was similar to our previous studies[91, 92].

All hearts were perfused retrogradely via the aorta with cardioplegia solution mixed with Heparin (12500I.U./L, Panpharma, France) before removal from the chest. All the hearts had a minimum of 3 cm of the ascending aorta remaining after extraction to allow cannulation for the Langendorff system. The extracted hearts were stored in ice-cold cardioplegia solution for transportation. The maximum cold ischaemic time was 90 minutes.

10 porcine hearts and 1 human donor heart have been used, the detailed information is shown in Table 2.4.

Number of heart	Duration of experiment (minutes)	Date of experiment	Type of heart
1	150	20/10/2022	Porcine
2	180	07/11/2022	Porcine
3	200	02/02/2023	Porcine
4	120	24/02/2023	Porcine
5	170	31/03/2023	Porcine
6	280	28/06/2023	Porcine
7	150	26/10/2023	Porcine
8	200	17/01/2024	Porcine
9	240	01/03/2024	Porcine
10	170	18/03/2024	Human
11	180	27/03/2024	Porcine

Table 2.4: Langendorff experiment: Date of heart collection, duration of the experiment, and source of the hearts.

2.2.5 Pharmacological Modulators

In ex vivo heart models, Carbenoxolone was used (C4790-5G, Sigma, USA) to reduce gap junction coupling, Lidocaine (L1026-1VL, Sigma, USA) was used to block voltage-gated Na+ channels (SCN10A, SCN9A, SCN5A) and Pinacidil (P154-1G, Sigma, USA) was applied to enhance I_{KATP} channel activity.

2.3 Microelectrode array recordings

The electrophysiological properties of cultured cells and BMS were recorded using the USB-MEA60-Inv MEA system (MultiChannel Systems, Germany)[53]. The MEA dish contains 60 gold electrodes organised on an 8 x 8 matrix (electrodes missing on the corners) with an inter-electrode space of 700µm and electrode diameter of 100µm. Biphasic stimulus (2ms duration;120% of the threshold; voltage:500-2500mV) was generated using the STG stimulus generator programmed by MC Stimulus II software (version 3.4.4, MultiChannel Systems). Stimulus with low voltage (500mv for cell monolayer, 1000mv for BMS) and low frequency (1Hz) was delivered to the cell monolayer and BMS for several minutes via electrodes on south, north and east sides of the matrix before recording in order to obtain stable EGMs. After stabilisation,

the voltage of the stimulus was increased (1000mv for cells, 1500mv - 2000mv for BMS from human donor heart and rat heart and 2000mv - 2500mv for BMS from human failing heart according to the condition of the heart). The EGMs were recorded for 10 seconds immediately after the increase of the voltage from all four pacing directions with 4 pacing frequencies (1Hz to 4 Hz). Unipolar extracellular EGMs were recorded at a sampling frequency of 25kHz. The raw recording from cells and BMS is shown in Figure 2.6 and Figure 2.7. The pacing direction doesn't have significant influence on the EGM features of cultured cell monolayers, so the data obtained from the north stimulation are usually used for subsequent analysis, if no data was obtained from north stimulation, If no EGM is obtained from the north stimulation, the data obtained from the south and west stimulation are used in sequence. However, Fibre orientation has a significant impact on the electrical conduction of BMS, the conduction of transverse stimulation is relatively slower than that of longitudinal stimulation, which can further influence other EGM features. Therefore, when positioning the BMS on the MEA dish, care was taken to align the tissue such that the myocardial fibre orientation corresponded with at least one of the available stimulation directions. Data obtained from one longitudinal stimulation were subsequently used for data analysis and signal processing. In cases where no EGM was recorded under longitudinal stimulation, the dataset from that particular BMS was excluded from further analysis.

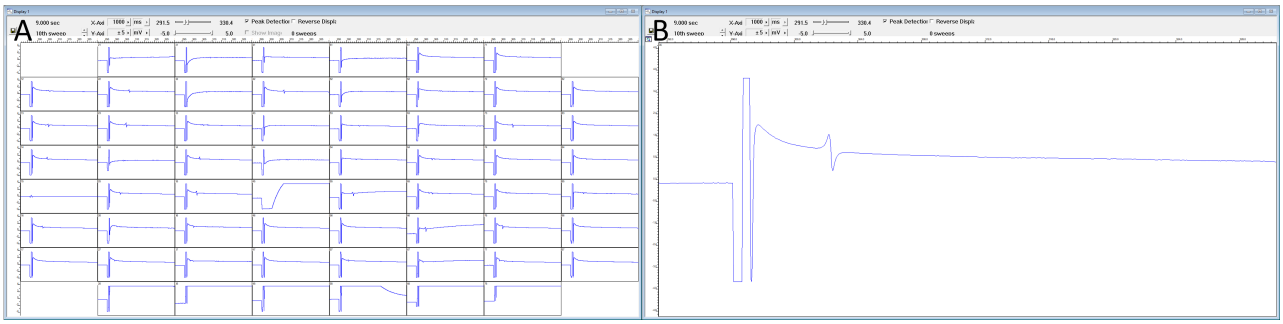


Figure 2.6: (A) Raw recordings from all the electrodes from pure NRVMs, stimulation voltage is 2000mv, direction is from East and stimulation frequency is 1 Hz. (B) Raw recordings from all the electrodes from pure NRVMs, stimulation voltage is 2000mv, direction is from East and stimulation frequency is 1 Hz.

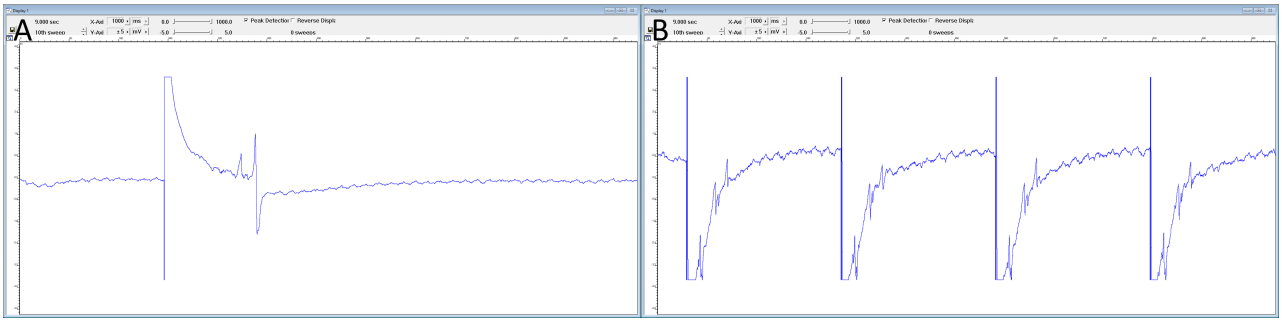


Figure 2.7: (A) Zoomed in raw recordings from one electrode from a human failing heart BMS, stimulation voltage is 2000mv, direction is from East and stimulation frequency is 1 Hz. (B) Raw recordings from one electrode from a human failing heart BMS, stimulation voltage is 2000mv, direction is from North and stimulation frequency is 4 Hz.

The MEA system is able to record the electrophysiological properties in details with such high sampling rate but this technique has its limitations. Because of the high sensitivity of the electrodes, different types of noise from the environment are also captured even the system has filters implanted. The properties of the EGMs can be easily influenced by these noises. Another limitation that can not be ignored is that impurities may attach on the electrode and therefore bring negative influence to the accuracy of the recording. Even impurities is unlikely to be seen in cell model, hydrolysis occurs in the solution when the simulation is applied. Bubbles formed by hydrolysis bring same impact to the recording.

The BMS was photographed and then fixed with 4% Paraformaldehyde (PFA) under room temperature for 20 minutes and then saved in Phosphate Buffered Saline (PBS) (Gibco, USA) supplemented with 1% azide. All BMSs were saved in a 4°C fridge before been brought to the microscope for collagen imaging. The cells were fixed with cold methanol (-20°C) for 5 minutes after the recording and stained immediately.

2.4 Langendorff

A custom-built Langendorff apparatus was constructed to keep the hearts alive for around 3-5 hours[91]. The apparatus consisted of a water heater to warm the solution, a two-layer 5L solution reservoir (custom supply from Radnoti Ltd.), heating water was pumped into the

outer layer to heat up the solution, an oxygen supply to oxygenate the physiological solution to maximal saturation, a heating coil (custom supply from Radnoti Ltd.) to keep the physiological solution at the optimal temperature of 37±0.5°C, a bubble trap (custom supply from Radnoti Ltd.) to remove the air bubbles in the solution to prevent potential damage to the hearts and a high flow peristaltic pump (Cole Parmer, UK) to circulate the solution around the system at a constant rate (90 rpm). The physiological solution was oxygenated warm Tyrode's solution (10 moL/L: $NaCl$, 130; KCl, 4.05;$MgCl_2$, 1.0; $NaHCO_3$, 20; NaH_2PO_4, 1.0; glucose, 5.5; and $CaCl_2$, 1.35; pH = 7.4). The heart was crenulated on the aorta. Tyrode's solution was perfused through the aortic cannula to flash the cardioplegia solution, warm the heart and provide necessary glucose and ions for the heart to maintain the electrical activities and contractions while it beats. The solution chambers were connected to the aortic cannula and oxygenatedTyrode's solution was perfused into the coronary arteries in a retrograde manner, thereby maintaining the metabolic, electrical, and contractile activity of the porcine hearts. The perfusate exited the coronary circulation into the right atrium and was subsequently expelled from the heart. On restarting, the heart was cardioverted using a Lifepak 20e defibrillator (Physio-Control, Inc., USA). ECG was recorded on Labchart (AD-Instruments, UK) to monitor the condition of the heart. During stabilisation, the heart was paced from the basal region of the left ventricle with 40mA current using a clinical stimulator (Micropace EP Inc., USA). Different Protocols was carried out once the heart was stabilised (sinus rhythm was consistently obtained for 15 minutes). The Langendorff setup is shown in Figure 2.8.

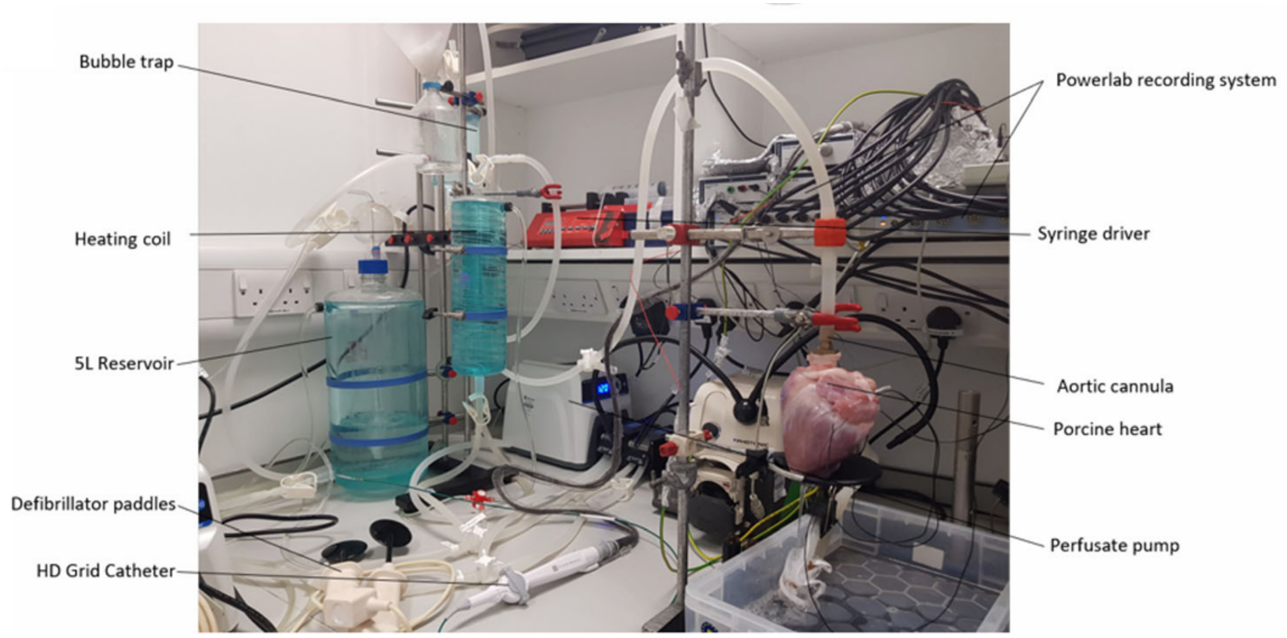


Figure 2.8: The Langendorff apparatus, pump, and aortic cannula feeding into a porcine heart.

EGM was recorded from the surface of the LV and the LA over 16 areas under steady pacing at 2-5 A of pacing frequencies 1Hz, 2Hz, 3Hz and 4Hz. Positions 1 to 12 were collected from the LV and positions 13-16 were collected from the LA. The positations are shown in Figure 2.9. EGMs were recorded for 10 seconds at each position and each pacing frequency.

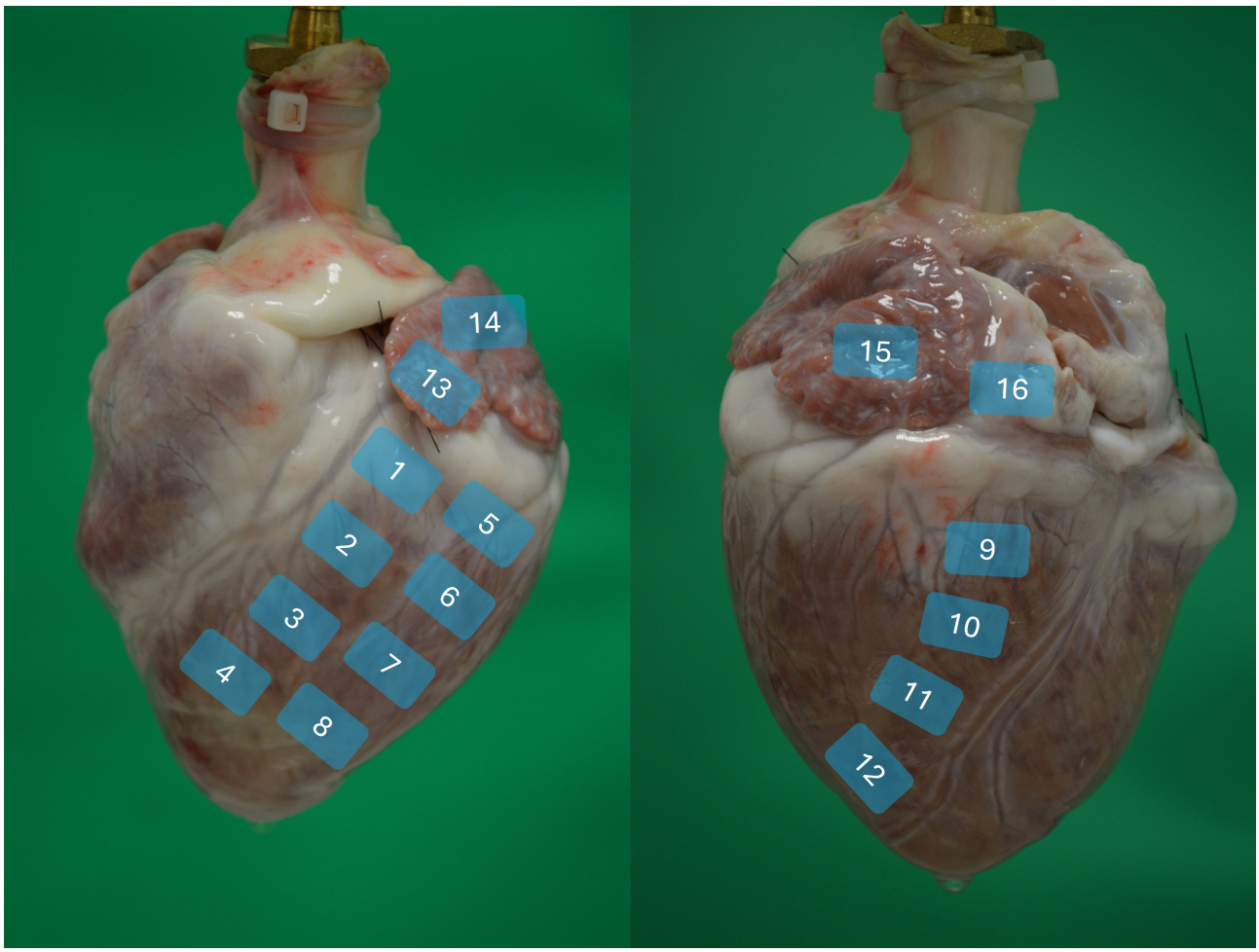


Figure 2.9: The 16 locations on the epicardium surface that EGM was recorded from. Locations 1 to 4 are on anterior LV, locations 5 to 8 are on medial LV, locations 9 to 12 are on This is broken down into LV, location 13 is underneath the LA appendage, location 14 and 15 are on the LA appendage and location 16 are on the posterior wall.

One commercial recording systems were used to acquire the data. The commercial system includes a HD Grid catheter (Abbott, USA) and a PowerLab (AD-Instruments, UK).

Baseline EGM was first recorded from all the 16 locations and pharmacological modulators were added. The modulated EGM was then recorded from the same locations. The Tyrode's solution in the Langendorff system was emptied to a circulating volume of 2 L. The determined dose of drug was prepared in 3 L of Tyrode's solution and injected into the Langendorff system at a rate of 50 ml/min for 30 minutes through the reservoir, with a total circulating volume of 5 L. For Carbenoxolone, a total of 1 mM was administered (equivalent to a maximum dose of 30.735 mg). For Lidocaine, a total of 0.32 mM was administered (equivalent to half of the maximum dose of 200 mg). For Pinacidil, a total of 0.05 mM was administered (equivalent

to half of the maximum dose of 13.1 mg). EGMs from 16 locations was recorded after the pharmacological modulation. The HD grid catheter and an example of recording process are shown in Figure 2.10 and Figure 2.11.



Figure 2.10: Image of the HD grid from Abbott Medical. The 16 electrodes on the 4×4 square grid are visible.

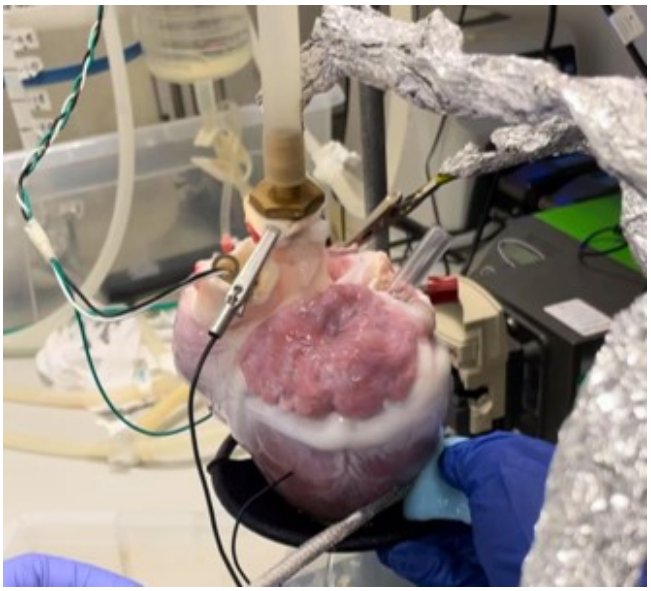


Figure 2.11: An example of a reference image of the HD grid catheter position on a porcine heart.

At the end of the live experiments, the heart was fixed with Tyrode's solution-buffered formalin solution and stored in a 4℃ cold room.

2.5 Immunofluorescence

In this section, the mechanisum of immunofluorescence and its protocol are introduced.

2.5.1 The principles of Immunofluorescence

Immunofluorescence is a technique used to investigate the location and distribution of targeted proteins. The background mechanism of this technique is the specific antibody-antigen interactions. In general, two antibodies are used: primary antibody and secondary antibody. Primary antibody has the ability to bind to the specific protein, monoclonal antibodies (mAb) and polyclonal antibodies (pAb) are two types of primary antibodies. The former can recognise a single epitope on an antigen, while the latter can specifically bind to different binding sites on the same target antigen. In order to obtain this antibody, a peptide sequence from the protein was injected into animal whose immune system recognises the forgign protein and the response against it. B-lymphocytes secrete antibodies that only target that peptide sequence during the reaction. Serum of the animal is taken after certain time and the antibody is purified from it. Secondary antibodies are antibodies that can bind to specific primary antibodies, their main function is to detect the presence of antibodies and amplify the signal of primary antibodies. Primary antibodies can specifically bind to target proteins, but usually require labels to be detected. Therefore, detectable secondary antibodies with labels (in this study, label is fluorescent marker) are used to bind to primary antibodies. In this way, when the primary antibody binds to the substrate and the secondary antibody binds to the primary antibody, the targeted protein can be detected by looking the labels[93, 94].

The choice of the host animal species of the primary antibody is very important. To avoid cross-reaction between the anti-immunoglobulin secondary antibody and endogenous immunoglobulins in the sample, the origin species of the selected primary antibody should be different from the species of the sample. It is also important to choose the corresponding secondary antibody against the species of the primary antibody. For example, if the primary antibody is a mouse monoclonal antibody, the secondary antibody should be an anti-mouse secondary antibody (goat anti-mouse or rabbit anti-mouse, etc.). The binding of antibodies to the sample is shown in Figure 2.12.

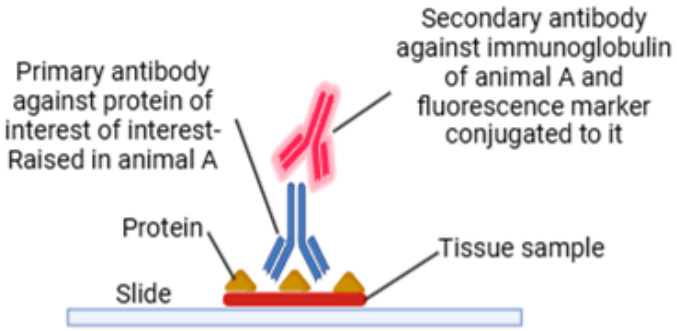


Figure 2.12: Illustration of the mechanism of immunofluorescence

The secondary antibodies can be visualised under a microscope using an epifluorescence filter or by confocal microscopy because they are conjugated to florescent markers. The location and distribution of targeted proteins can be captured after the staining due to the specific binding between protein and antibodies.

This technique also has limitations. Poor penetrance of antibodies into tissue can lead to potential false-negatives. Non-specific antibody binding also brings unexpected background noise.

2.5.2 Immunofluorescence protocol

For cell model, Cx 43, SNs and membrane were immunolabeled after the measurement of EGM. First, cell samples were washed twice with PBS and then they were fixed with 100% methanol at -20°C for 5 minutes. The cells were washed with PBS and permeabilised by 0.1% Triton X-100. After blocking in blocking buffer (5% BSA in PBS) for 30 minutes, the cell samples were divided into two groups. One group of cells was incubated overnight at room temperature with primary anti-Cx43 mouse antibody (MAB3067, Sigma-Aldrich, USA) (diluted 1:1000) for Cx43 and anti-Tyrosine Hydroxylase (TOH) (AB152, Sigma-Aldrich, USA) rabbit antibodies (diluted 1:200) for SNs. Cells were washed with PBS 3 times, followed by the incubation of Goat anti-mouse Cy3 (AP181-C, Sigma-Aldrich, USA) (diluted 1:500) and Goat anti-rabbit

IgG 488 (Invitrogen, USA) (diluted 1:200) secondary antibodies for 45 minutes. Another group was analysed for cell morphology using WGA (W32466, Invitrogen, USA) and TOH antibodies, for membrane staining, the wheat germ agglutinin (WGA) was conjugated to Alexa Fluor 647, so the cells were only incubated for 1 hour under room temperature.All the dilutions were done with 1% BSA solution in PBS. After the staining of secondary antibody and WGA, the cells were washed with PBS three times. The cells were mounted the MEA dish using VECTASHIELD Antifade Mounting Medium with DAPI (H-1000, Vectorlabs, USA). A round (17mm) coverslip was then carefully placed onto the slide, avoiding air bubbles.

For human heart model, connexin 43, $Na_v1.5$ ion channel and WGA were immunolabeled. All the stainings were carried out on the prepared slides introduced in section 2.2.3. Primary antibodies used were mouse anti-connexin43, rabbit anti-$Na_v1.5$ (SCN5A, Alomone, Israel) and WGA conjugated to Alexa Fluor 647. The secondary antibody used was a goat anti-mouse antibody conjugated with Cy3. All antibody dilutions were done with 1% BSA solution in PBS. The frozen human left ventricle slides were fixed for five minutes with pre-cooled methanol (-20°C) to prevent protein degradation. After fixing, slides were blocked with 1% BSA in PBS for 30 minutes which was then followed by an overnight incubation at RT with mouse anti-connexin43 antibody (diluted 1:1000), followed by a 3-hour incubation at RT with WGA (40µg/mL). The slides were then incubated for 45 minutes at RT with goat anti-mouse antibody (2µg/mL), following this, slides were mounted using Vectashield mounting medium (H-1200) to stain the nuclei. A coverslip was then carefully placed onto the slide, avoiding air bubbles, and then sealed with nail varnish.

All dishes slides were saved in a 4℃ fridge before been brought to the microscope.

2.6 Microscopy

In this section, the principles of second-harmonic generation microscopy, how its applied to image collagen in this study and the other microscpe protocols used are introduced.

2.6.1 Second-harmonic generation microscopy

Second-harmonic generation (SHG) is the optical phenomenon that occurs when molecules with non-symmetric structures are exploded to the light with sufficiently strong electric field. The anisotropy of such non-symmetric structure can result in oscillating field at twice the frequency, which is the second harmonic[95].

In this study, how collagen as a structural change influence the electrophysiological properties of BMS is investigated. Collagen is the most important extracellular structural protein of vertebrates[96]. Due to the fact that cardiomyocytes can not regenerate, fibrosis occurs during reparative or reactive cardiac processes to provide necessary mechanical supports which allows heart to keep beating. Fibrosis is achieved through the production of collagen[41]. However, collagen is not conductive, which means it has a great influence on the conduction of electrical signals in the heart. Hence, how to investigate the location and distribution of collagen in the myocardium is important. It is found that the collagen molecule is non-symmetric and is arranged in a triple helix.Therefore, SHG microscopy is widely applied on imaging the collagen.

2.6.2 Microscopy protocol

Three microscopes were used in the study of this thesis.

For cell model, Cx43 and co-cultured SNs were imaged using a Zeiss Axio Observer inverted microscope at Imperial College London. The imaging parameters were set as follows: DAPI exposure time was 10 ms; Alexa Fluor 488 channel (SNs) exposure time was 170 ms; and Alexa Fluor 568 (Cx43) channel exposure time was 400 ms. A 40x objective was used for partial images, while a 20x objective was used for overall images. The overall image was a tiled display of 25 images (5x5 array) with 10% overlap, which was post-processed to eliminate the overlap. A Leica Stellaris 8 inverted confocal microscope (Imperial College London) was used to examine the morphological changes in the NRVM under neuronal cell co-culture, and fluorescence images were processed using LAS X microscopy software to enhance resolution. Imaging parameters were normalised to the following settings: DAPI: smart gain of 102%, smart intensity of 1.00%,

pinhole of 1.00 AU, zoom of 1; 488 channels: smart gain of 123%, smart intensity of 1.00%, pinhole of 1.00 AU, zoom of 1; 647 channels: smart gain of 200%, smart intensity of 1.00%, pinhole of 1.00 AU, zoom of 1. Picture-taking z-step is set to 0.4µm with total Z-Stack distance of 6µm in order to image the whole cell monolayer. The images were further processed using FIJI to enhance the identification and analysis of the complex cellular morphology of NRVMs and changes in Cx43 density in the two different culture models.

For rat and human BMS models, fixed BMS was placed on a 35mm-uncoated imaging dish with low walls (catalogue No.: 80131, ibidi, Germany). The slice was immersed in PBS (keep the slice wet under high power laser) and a 19mm coverslip was placed on the top of the slice. A metal nut was put on the coverslip in order to keep the slice flat. The collagen was imaged using a Leica SP5 inverted confocal microscope with a multiphoton laser. A Spectraphysics Mai Tai 690-1020 DeepSee multiphoton (MP) laser was installed to this microscope and was used for SHG. The MP laser was turned to 860nm and simultaneous dual imaging was applied to capture collagen I (SHG) and cytoplasmic detail (autofluorescence). Images were captured using the Leica Application Suite Advanced Fluorescence (LAS AF) software. Z-Wide (each z step was set to 15µm) was applied to image all the collagen within the whole BMS.A 10x objective was used to take images of the whole BMS in series and all the images were tiled together. The imaging parameters were set as follows: Smart gain: 815.0V; Smart Offset: -0.5%; Scan Field Rotate: 0.0 and Phrase: -25.00.

For the immunofluorescence slides, the same Zeiss Axio Observer inverted microscope used for cell imaging was used to image slides with Cx43 staining. The image setting were as follow: DAPI exposure time was 10 ms; Alexa Fluor 488 channel (scar autofluorescence) exposure time was 200 ms; and Alexa Fluor 568 (Cx43) channel exposure time was 500 ms. A 20x objective was used all images. A Leica Stellaris 8 inverted confocal microscope was used to image $Na_v1.5$ ion channel. The image setting were as follow: smart gain of 150%, smart intensity of 1.00%, pinhole of 1.00 AU, zoom of 1; 488 channels (scar autofluorescence): smart gain of 150%, smart intensity of 1.00%, pinhole of 1.00 AU, zoom of 1; 647 channels (Nav1.5 sodium channel and WGA): smart gain of 200%, smart intensity of 1.00%, pinhole of 1.00 AU, zoom of 1. Because the surface of the sample was not flat and numbers of cells on the surface were damaged, so in

order to image the first intact cells layer, picture-taking z-step was set to 0.5µm, and the total Z-Stack distance was set to 10µm.

The SHG images were further processed using an validated in-house made python code and all the images were imported to FIJI for data processing. The detailed processing methods and parameters will be introduced in each chapter.

2.7 Numerical simulations

In this section, the simulation methods and tools used in this study is introduced.

2.7.1 Mathematical models of Cardiac Electrophysiology

The spectral/hp element method has the ability to calculate an approximate numerical solution to partial dierential equations. The following description of the framework and method is adapted from Karniadakis, Sherwin[97] and Cantwell et al[98]. For one dimension, each cell was considered as an individual subdomain that is coupled to the other cells through current continuity conditions imposed at interfaces. The extracellular space was considered as a signal continuous domain. The cable equation introduced in chapter 1 was rewriten into a format that spectral/hp element method can solve.

$$p\left(C_m\frac{\partial V_m}{\partial t}+I_{\text{ion}}\right)=\frac{1}{r_i+r_e}\nabla^2 V_m. \tag{2.1}$$

By applying an implicit backwards Euler scheme for the time derivative and rearranging the form in to Helmholtz form, the equation is changed to

$$\nabla^2 V_m^{n+1}-\lambda V_m^{n+1}+f=0, \tag{2.2}$$

$$f = \lambda \left(V_m^n - \frac{\Delta t}{C_m} I_{\text{ion}} \right), \tag{2.3}$$

where $\lambda = \frac{pC_m(r_i+r_e)}{\Delta t}$. The ionic current was considered as linear ohmic, which change the equation to

$$f = \lambda \left(1 - \frac{\Delta t}{R_m C_m} \right) V_m^n. \tag{2.4}$$

It was considered that the current in each space is conserved to obtain the potential and current owing across the membrane lead to all changes of intracellular or extracellular current, which gives

$$I_i = -\frac{1}{r_i} \frac{\partial V_i}{\partial x}, \tag{2.5}$$

$$I_e = -\frac{1}{r_e} \frac{\partial V_e}{\partial x}, \tag{2.6}$$

$$\frac{\partial I_i}{\partial x} + \frac{\partial I_e}{\partial x} = 0. \tag{2.7}$$

and the relationship between the potentials in intracellular and extracellular domains can be given:

$$-\frac{1}{r_i} \nabla^2 V_i - \frac{1}{r_e} \nabla^2 V_e = 0. \tag{2.8}$$

By adding transmembrane potential $V_m = V_i - V_e$, the equation 2.8 can be rewritten to:

$$\nabla^2 V_e + f = 0, \tag{2.9}$$

$$f = \frac{r_e}{r_e + r_i} \nabla^2 V_m. \tag{2.10}$$

Gap junction was an important fector in this study and was considered as a resistor,

$$-\frac{1}{r_i} \frac{\partial V_i^-}{\partial x} = I_{\mathrm{GJ}}, \tag{2.11}$$

$$I_{\mathrm{GJ}} = \frac{V_i^+ - V_i^-}{R_g}, \tag{2.12}$$

where + and - represents the solution at two sides of the interface which is the same point in Cartesian space. R_g is the resistance of the gap junction.

The equations can be finally rearranged into the form of finding V_m and V_e:

$$\nabla^2 V_m^{n+1} - \lambda V_m^{n+1} = \lambda \left(\frac{\Delta t}{C_m R_m} - 1 \right) V_m^n, \tag{2.13}$$

$$\nabla^2 V_e^{n+1} = -\frac{r_e}{r_i + r_e} \nabla^2 V_m^{n+1}. \tag{2.14}$$

The equations for one-dimension is numerically similar to the general two-domain equation because the extracellular and intracellular spaces were considered at the same location and were connected at every point through the membrane equations. But when it was changed to three dimension, the intracellular and extracellular spaces were considered as distinct sub-domains ($\Omega^{(i)}$). The numerical domain was the union of these sub-domains $\Omega = \cup_i \Omega^{(i)}$.

Three interfaces were considered in the three dimensional model: 1. the membrane interface shared by intracellular subdomain and the extracellular subdomain; 2. the gap junction interface shared by two intracellular subdomains; 3. the external boundary. For the first two interface equations can be writen as:

$$\partial\Omega_{\text{membrane}} = \Omega^{(i)} \cap \Omega^{(j)}, \tag{2.15}$$

Where i and j are intracellular/extracellular sub-domains, and:

$$\partial\Omega_{\text{GJ}} = \Omega^{(i)} \cap \Omega^{(j)}, \tag{2.16}$$

where i and j are both intracellular sub-domains.

Each sub-domain was assumed to be a volume conductor which does not have any current source. Laplace's equation can be given by using a quasi-static approximation:

$$\nabla\sigma^{(i)}\nabla V^{(i)} = 0. \tag{2.17}$$

where $\sigma^{(i)}$ is the scalar conductivity of sub-domain $\Omega^{(i)}$, $V^{(i)}$ is the electrostatic potential.

The equation can be changed to a new form by pre-multiplying by a test function σ and integrating over the sub-domain:

$$(v^{(i)}, \nabla\sigma^{(i)}\nabla V^{(i)})_{\Omega^{(i)}} = 0. \tag{2.18}$$

σ equals to 0 and the equation can be rearranged by applying the divergence theorem:

$$(\nabla v, \sigma\nabla V_{\Omega}) - \langle v, \sigma\nabla V \cdot \mathbf{n}\rangle = 0, \tag{2.19}$$

where

$$\langle v, \sigma\nabla V \cdot \mathbf{n}\rangle = \int_{\partial\Omega} v(\mathbf{x})\sigma\nabla V(\mathbf{x}) \cdot \mathbf{n}\mathrm{d}\mathbf{x}. \tag{2.20}$$

The current can be written in the form:

Interacellular,

$$-\sigma \nabla V \cdot \mathbf{n} = I_m, \tag{2.21}$$

extracellular,

$$-\sigma \nabla V \cdot \mathbf{n} = -I_m, \tag{2.22}$$

and

$$I_m = C_m \frac{\partial V_m}{\partial t} + I_{\text{ion}}(V_m, t). \tag{2.23}$$

where I_m is the membrane current, C_m is the capacitance, V_m is the trans-membrane voltage and I_{ion} is the current calculated from the cell action potential numerical model.

Between two cells and the gap junction in the interface of them equations can be given:

Cell1:

$$-\sigma \nabla V \cdot \mathbf{n} = I_{12}, \tag{2.24}$$

Cell2:

$$-\sigma \nabla V \cdot \mathbf{n} = -I_{12}, \tag{2.25}$$

$$I_{12} = C_{12} \frac{\partial w}{\partial t} + I_{\text{GJ}}, \tag{2.26}$$

$$I_{\mathrm{GJ}} = \frac{w}{R_{\mathrm{GJ}}}. \tag{2.27}$$

where I_{12} is the current, C_{12} is the capacitance, w is the potential difference across the gap junction interface and R_{GJ} is the resistance of the gap junction.

On a membrane interface, the time derivative can be discretised using finite dfference:

$$-\sigma \nabla V \cdot \mathbf{n} = \frac{C_m}{\Delta t}\left[\left(V_i^{n+1} - V_e^{n+1}\right) - \left(V_i^n - V_e^n\right)\right] + I_{\mathrm{ion}}. \tag{2.28}$$

The time derivative of the gap junction can be discretised as follow:

$$-\sigma \nabla V \cdot \mathbf{n} = \frac{C_{12}}{\Delta t}\left[\left(V_1^{n+1} - V_2^{n+1}\right) - \left(V_1^n - V_2^n\right)\right] + \frac{1}{R_{\mathrm{GJ}}}(V_1^{n+1} - V_2^{n+1}). \tag{2.29}$$

Combining all the numerical derivation the discrete form of the equations for the global solution can be written as:

$$\mathrm{L}\hat{\mathrm{V}}_g + \Gamma_{\mathrm{LHS}}\mathrm{M}\hat{\mathrm{V}}_g = \Gamma_{\mathrm{RHS}}\mathrm{M}\hat{\mathrm{V}}_{\mathrm{prev,g}} + \hat{\mathrm{f}}. \tag{2.30}$$

where L is the Laplacian matrix, M is the mass matrix and Γ is the flux conditions between sub-domains.

The Laplacian matrix L is:

$$\begin{bmatrix} \sigma^{(i,e)} l_{1,1} & \sigma^{(i,e)} l_{1,2} & \cdots & \sigma^{(i,e)} l_{1,N} \\ \sigma^{(i,e)} l_{2,1} & \sigma^{(i,e)} l_{2,2} & \cdots & \sigma^{(i,e)} l_{2,N} \\ \vdots & \vdots & \ddots & \vdots \\ \sigma^{(i,e)} l_{N,1} & \sigma^{(i,e)} l_{N,2} & \cdots & \sigma^{(i,e)} l_{N,N} \end{bmatrix} \hat{\mathbf{V}}_g. \tag{2.31}$$

If the interface is a membrane, $\Gamma_{\mathrm{LHS}}\mathrm{M}\hat{\mathrm{V}}_g$ is:

$$\begin{bmatrix} \frac{C_m}{\Delta t}m_{i,i} & -\frac{C_m}{\Delta t}m_{i,j} \\ -\frac{C_m}{\Delta t}m_{j,i} & \frac{C_m}{\Delta t}m_{j,j} \end{bmatrix} \begin{bmatrix} \hat{V}_g^i \\ \\ \hat{V}_g^j \end{bmatrix}. \tag{2.32}$$

$\hat{\mathbf{f}}_{\mathrm{membrane}}$ can be calcualted using:

$$\hat{\mathbf{f}}_{\mathrm{membrane}} = \hat{\mathbf{f}} + \begin{bmatrix} -I_{\mathrm{ion}} \\ \\ I_{\mathrm{ion}} \end{bmatrix}, \tag{2.33}$$

For gap junction interface, the left hand side can be given:

$$\begin{bmatrix} (\frac{C_{12}}{\Delta t} + \frac{1}{R_g})m_{i,i} & -(\frac{C_{12}}{\Delta t} + \frac{1}{R_g})m_{i,j} \\ \\ -(\frac{C_{12}}{\Delta t} + \frac{1}{R_g})m_{j,i} & (\frac{C_{12}}{\Delta t} + \frac{1}{R_g})m_{j,j} \end{bmatrix} \begin{bmatrix} \hat{V}_g^i \\ \hat{V}_g^j \end{bmatrix}, \tag{2.34}$$

And the right hand side can be given:

$$\begin{bmatrix} \frac{C_{12}}{\Delta t}m_{i,i} & -\frac{C_{12}}{\Delta t}m_{i,j} \\ -\frac{C_{12}}{\Delta t}m_{j,i} & \frac{C_{12}}{\Delta t}m_{j,j} \end{bmatrix} \begin{bmatrix} \hat{V}^i_{\mathrm{prev,g}} \\ \hat{V}^j_{\mathrm{prev,g}} \end{bmatrix}. \tag{2.35}$$

2.7.2 Simulation protocol

CardiacEPSolver, part of Nektar++ (version 5.2 and 5.3), a high order spectral/hp element framework was used to carry out all the simulations. A continuum model and a multi-domain discrete-cell model of action potential propagations were applied in the simulations.

All the domains used for continuum model were generated by Gmsh (Version 4.6.0), and converted using NekMesh into the native Nekter++ file format. The Ten Tusscher human LV

ion-channel model was applied[99]. Different electrodes distributions were also added in the simulations.

Human left ventricular myocardium monolayers with different sizes were created using Virtual Cardiac Tissue Model (VCT) [100] for simulation with the discrete propagation model. VCT allows virtual cells to be seeded on fibers, leading to similar anisotropy to that observed in vivo. The same cell ion-channel model and electrodes distributions were applied as the ones chosen for continuum model simulation in the discrete-cell model simulations.

Different gap junction resistances (from 0 Ω: non resistance to $\infty\Omega$: non conduction) were used in different simulation. The details of domain generation, conversion and simulations parameters will be introduced in chapter 7.

2.8 Statistic analysis

Statistical analysis was carried out using GraphPad Prism software (version 10.0, GraphPad Software, USA).

Normality was assessed using the Shapiro–Wilk test if sample size is smaller than 50 and Kolmogorov-Smirnov test was used if sample size is larger than 50. Data sets with normally distributed variables were statistically tested using parametric analyses. Non-parametrical statistical test was applied when at least one data set assessed failed the normality tests.

An unpaired t-test was implemented to compare the means of two independent sample populations with normally distributed populations, for data sets with at least one group showing non-normal distribution Mann–Whitney test was applied.

One-way analysis of variance (ANOVA) for unpaired data was applied to compare means of three or more groups. The comparison of MEA recordings with different structural changes and functional changes was validated with linear regression analysis (confidence interval: 95%). All numerical data are presented as mean $\pm$ SEM and p-value of < 0.05 was considered as significant.

Chapter 3

Development of Cardiac Electrogram Feature Extraction tool

3.1 Introduction

A numbers of features of the ECG have been used in clinical practice to access potential cardiac diseases and monitor the condition of patients during surgery. Similar features can also be used to analyse the electrophysiological properties of EGM recordings. However, the features applied clincially are provided by the commercial software and only several time-domain features were analysed. Frequency domain and time-frequency domain features play important roles in signal analysis in some other research such as electromagnetism, solid mechanics and kinematics, etc. These characteristics may be potentially important factors in the study of cardiac electrophysiology. Therefore, a software that can extract multiple features from recordings from typical cardiac electrophysiological models is urgently needed. This chapter introduces the features of EGM recordings considered for analysis, the development of algorithms for a user friendly feature extraction tool, and the validation of the reliability of the tool and the accuracy of extracted features.

The development of the feature extraction tool was based on the method presented by Dr. Tzortzis[101]. Dr. Tzortzis developed the code using MATLAB (R2016b, MathWorks, USA).

The new code was developed using Python (Version 3.7, Python Software Foundation, USA) which is faster. All the algorithms used to calculate the time domain features were developed by the author and the development of the GUI and data analysis was carried out with the help of Cindy Gao and Joshua DeCoteau.

3.1.1 Cardiac electrophysiology signal processing

Digital signal processing (DSP) refers to the numerical data processing methods applied to signals provided by different types of sensors [102]. The processing steps are in general as follows: first, the analogue input signal, continuous in time and amplitude is converted to a voltage-based electrical analogue signal by a transducer. Next, filtering is applied , which aims to limit the frequency range of the analogue signal before sampling, and also helps to limit any signal distortion. After filtering, the signal is converted into digital data with discrete time and amplitude. The digital data can be exported for other analysis. DSP has been widely used in clinical cardiac research and treatment (ECG monitor, mapping catheter, and imaging) in recent years[103].

Due to the fact that AF affects more and more people, the importance of DPS increases every year. It is important to obtain viable cardiac singles from all electrodes on the catheter in the presence of noise. In addition, the processed signal presented to nurses and physicians should be reliable and simple so that they can use the signal to determine whether the electrophysiological properties of the detected area are abnormal. In that case, the filters are important because there are numerous necessary instruments in the EP laboratory, resulting in different types of noise affecting the recording. If a wide range of frequency are filtered out, some important EGM information may be lost, while narrow filtered frequency range can lead to low signal-to-noise ratio (SNR). The setup of the laboratory also needs to be considered, including the electrical isolation of the patient and placement of amplifiers close to the signal source.

The quality of the signal has a significant impact on feature extraction. However, high and low frequency noise is inevitable[104]. Passive, active, and digital filters are normally applied in combination to enhance certain portions of the frequency spectrum while rejecting unwanted

components of the signal. Passive filtering is carried out by resistors, capacitors, and inductors, and active filtering is carried out by operational amplifiers. Digital filters are a combination of hardware filter and software filter. Research on ECG noise filtering has been carried out for years and a number of effective methods are employed by the instrument companies. Different cut-off frequencies are applied depending on the components of the signal derived from various parts of the cardiac tissue, such as His bundle, pulmonary veins, and Purkinje-fibre area. However, the same methods can not be simply used on cardiac EGM because the signal properties and the sources of the noise are different. Although there have been studies on the removal of EGM noise in recent years, there is still no effective general method. Clinically, bipolar EGM is more widely used than unipolar EGM because it naturally rejects noise which appears the same on both signals[104]. However, unipolar EGM can provide more information, which is preferred in research.

3.1.2 Electrogram morphology

Analysis of cardiac EGM morphology is used to identify arrhythmia activation patterns. Some time-domain and spectral analysis algorithms are integrated into most of the clinical electro-anatomical mapping systems. Physicians use these processed signals and features to map the heart and locate ablation locations.

Nademanee et al.[63] proposed a time-domain method, the interval confidence level (ICL) in 2006 to quantify the complex fractionated atrial electrograms recorded during AF. This algorithm is used by the CARTO mapping system (Abbott, USA). In detail, a noise threshold is chosen to remove components of the signal with high frequencies. The maximum value and minimum value of the filtered signal are calculated. The resting time is also preset based on the duration interval. If the period between two peaks in the real recording is lower than the predefined time, these peaks are excluded from all the analysis and plots. Another more advanced algorithm, used in the EnSite NavX mapping system (Abbott, USA), applies a new peak detection method. This algorithm calculates the mean value of all the R-peak intervals. The peaks are ignored if the period between two consecutive peaks is greater than the calculated mean

value. Some research indicates that the output of these algorithms is accurate[63, 105, 106] but some studies also show that accuracy need to be improved[107, 108].

Frequency-domain features are also used to support clinical decision-making. The dominant frequency (DF) is calculated by decomposing the recorded EGM into a sum of sinusoidal waves of different frequencies using the Fourier transform. DF is the frequency that contains the highest energy in the frequency spectrum and is used to identify the fast-firing locations in the atria[108, 109, 110]. Regularity index (RI) is the ratio of the power of the DF ($\pm$ 0.75 Hz) to the power of the other harmonics. RI is normally calculated to verify the reliability of DF. Although these features are already widely used in ablation threapies, research suggests that their accuracy needs to be further improved[111]. During cardiac therapies, DF can be used to assess tachycardia, but for atrial fibrillation and other types of arrhythmias, DF is insufficient for accurate diagnosis due to low sampling rates, noise, and other factors.

The correlation between EGM morphology features and abnormal electrical activity is not well understood. More features are needed to improve the differentiation of healthy and abnormal signals, and a new tool is needed to extract these features.

This chapter introduces the development of the feature extraction algorithms used in this study for processing the EGM recordings from different experiments and simulations. The extracted features were further used to correlate with the structural change and functional changes in Chapters 4,5 and 6. The reliability and precision of the extracted features were also assessed by comparing the data extracted by different users and comparing the features extracted from different modality of EGM recordings.

3.2 Methods

3.2.1 Features of electrogram

The feature extraction codes were written in Python (Version 3.7, Python Software Foundation, USA) and a graphical user interface (GUI) was also created to make the tool more user friendly.

The tool is able to extract 18 time domain features, 8 frequency domain features and 7 time frequency features. For the MEA experiments, the features of the EGMs recorded by the centre 36 electrodes were analysed because the remaining electrodes were used to deliver stimulation. For Langendorff recordings, EGMs recorded by all electrodes were analysed.

3.2.2 Preprocessing of electrogram

The EGM recordings include stimulation artefact because an electrical impulse was applied to all the experiments. In order to eliminate its impact of the stimulation artefact as well as noise, on the accuracy of feature extraction, some pre-processing steps were applied.

Due to the fact that the EGMs recorded from BMS and ex vivo Langendorff hearts are complex, applying filters will affect the extraction of time domain features (the key time point may be advanced or delayed). Hence, no filter was applied when extracting time-domain features.

For frequency domain features, a Chebyshev type I bandpass filter (50Hz-250Hz) was first applied to remove high-frequency noise. After that a 50 Hz notch filter was applied to eliminate mains electrical interference. Lastly, the filtered signal was filtered by a 20Hz low-pass 2nd order Butterworth filter. All three filters were applied to serve the purpose of optimising the EGM and enhancing the periodic EGMs recorded at 1-5Hz stimulation. The combination of filters was shown to diminish the effects of changing the morphology of EGM[112].

The stimulation carried out in different experiments has different amplitudes and waveforms, so the stimulation removal methods for different types of recording were different. For MEA recordings, the stimulation amplitude was stable, but when the stimulation was stopped, the data did not return to the baseline instantly, but gradually decayed to the baseline over a period of time. The recovery time was generally around 100ms to 200ms, an interval in which the EGM was likely to occur. Hence, the stimulation artefact can not be completely removed, as it will also remove part of or the whole EGM. In that case, the stimulation was removed, but the decaying curve was preserved. To be more specific, the maximum amplitude of the entire recording period (10 s) was detected and a threshold of 80% of this value was set. All

maxima greater than this threshold were identified as stimulation points. In case some R points were accidentally included, the next maxima will not be detected if the distance between two adjacent maxima is less than 200ms (the highest pacing rate is 4 Hz, so the minimum interval between two stimulations is 250ms). It should be noted that the stimulation was set to last for 1ms at the peak, but the real stimulation period is around 15ms due to the slow electrode response. That stimulation period also needs to be removed. For Langendorff recording, the electrodes on the catheter have a much faster response speed, so the stimulation recovery was instant and the recording immediately changed back to baseline. Therefore, only a very short period of time needed to be removed in case the stimulation was not completely removed. That time length was further added back to ensure the accuracy of the time domain features. However, the amplitude of the stimulation was not stable as in the MEA experiment because it is from an external pacing system and the pacing point is far from the recording locations to ensure that the pacing will not influence the recording. Therefore, the threshold was set to 60% of the maximum value and a 200 ms detection interval was also applied.

The mean value subtraction and stimulation removal preprocessing steps were applied to the extraction of all types of feature while the filtering step was not applied to the time-domain feature extraction.

The concepts of the features were previously proposed by members of the group. All the Python algorithms were developed by the author.

3.2.3 Time-domain feature extraction

All individual MEA recordings had a duration of 10 seconds, which means the total number of EGMs in the entire recording is at least 10 (1Hz) and at most 40 (4Hz). It was found that all EGMs within a recording had similar morphology, therefore most of the time domain features were extracted from one EGM from the whole recording.

The time domain features were calculated from the QRS complex, T wave and end point of the EGM. The Q point is the start point of the EGM, the R peak is the highest peak of the

EGM, the S peak is the lowest point of the EGM and the T wave is the the small wave after the QRS complex. The amplitude of the EGM is the voltage difference between the R peak and the S peak. It is calculated by subtracting the voltage of the S peak from the voltage of the R peak. The amplitudes of all EGMs in a single recording were detected and the average of the EGM amplitudes was calculated. The variance of the EGM amplitude was calculated because it is related to the vulnerability of arrhythmias[113, 114]. The Q point is the EGM onset, which is defined as the point where the slope of the curve suddenly rises before the R peak and after the simulation. It was detected as the point where the first derivative of the recording changes to positive from 0 or negative within the prescribed range. The end point is the EGM offset, which is defined as the point where the slope of the curve suddenly changes after the S peak and before the next stimulation. It was detected as the point where the first derivative of the recording changed to 0 within the prescribed range. QR interval was the time difference between the Q point and the R peak; RS interval was the time difference between the R peak and the S peak; QS interval was the time difference between the Q point and the S peak; the S end interval was the time difference between the S peak and the EGM offset, and the EGM duration was defined as the time difference between the Q point and the EGM offset. The width of R and the width of S were also detected by finding the time difference between the R peak, the point $(-dV/dt)_{max}$ and the S peak. These two widths were used to calculate the R width to EGM duration ratio and the S width to EGM duration ratio. The example of some time domain features and time points are shown in Figure 3.1.

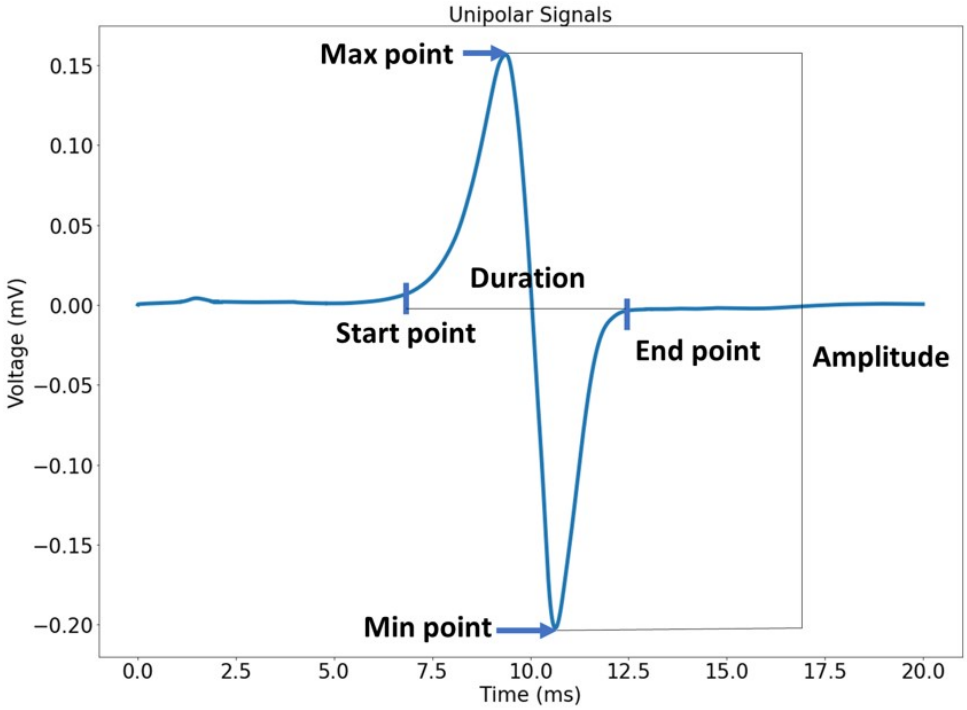


Figure 3.1: Time points detected from the simulated EGM for time-domain feature extraction.

Apart form the intervals, conduction velocity (CV) is another important feature needed to be considered. In order to calculate CV, the activation time which is the time difference between the end time of stimulation and the $(-dV/dt)_{max}$ time need to be calculated. The stimulation end time is the beginning of the data after stimulation removal, and the $(-dV/dt)_{max}$ time was detected by finding the local minimum of the first derivative of the recording between the R peak and the S peak. The activation map can be plotted by calculating the activation time gradient from all electrodes. CV is a vector, capturing the speed and direction of the wavefront. The propagation direction can be recognised from the activation map and the conduction speed between two electrodes can be obtained by dividing the electrode distance by the difference in the activation time between the two electrodes. The conduction velocity of one electrode was defined by calculating the square root of the sum of the squares of the CVs between the two electrodes in the direction of propagation (lateral, longitudinal).

In details, an activation map is a spatial distribution of activation times $T(\mathbf{x})$ (time from the end of the stimulation to $(-dV/dt)_{max}$ time) across the mapped surface. After assigning activation times to each recording site, data were lightly smoothed (thin-plate spline interpo-

lation or low-order polynomial) to reduce point noise while preserving wavefront curvature. Isochrones—lines of equal activation time—were then drawn at fixed intervals. The density of isochrones qualitatively reflects local conduction speed, with closer isochrones indicating slower conduction. Local conduction velocity (CV) was obtained from the spatial gradient of the activation-time field. If $T(\mathbf{x})$ denotes activation time at position $\mathbf{x} = (x, y)$, then the local CV magnitude is given by

$$c(\mathbf{x}) = \frac{1}{\|\nabla T(\mathbf{x})\|}, \tag{3.1}$$

and the propagation direction (unit vector) is

$$\mathbf{n}(\mathbf{x}) = -\frac{\nabla T(\mathbf{x})}{\|\nabla T(\mathbf{x})\|}. \tag{3.2}$$

Thus, the CV vector field is defined as

$$\mathbf{v}(\mathbf{x}) = c(\mathbf{x})\,\mathbf{n}(\mathbf{x}) = -\frac{\nabla T(\mathbf{x})}{\|\nabla T(\mathbf{x})\|^2}. \tag{3.3}$$

The gradient ∇T was estimated according to sensor geometry:

- For regular electrode grids or optical pixels, central finite differences or Sobel operators were applied to the activation-time image.
- For irregular electrode layouts, a local plane $T(x, y) = ax + by + c$ was fitted by least squares to each neighbourhood of three or more electrodes, with $\nabla T = [a\ b]^T$.

Global CV measures were summarised as the median and interquartile range of local speeds. If myocardial fibre orientation was known, CV was projected onto longitudinal (fibre-parallel) and transverse (cross-fibre) directions. Outliers (unrealistic CV values or poor local fit error) were excluded from analysis.

Some gradients were detected using the features introduced earlier. These gradients are listed below:

- gradient between the R peak and the S peak:

$$\frac{V}{t_S - t_R}. \tag{3.4}$$

- gradient between the Q point and the R peak:

$$\frac{R_{peak-amplitude}}{t_R - t_Q}. \tag{3.5}$$

- gradient between S peak and EGM offset:

$$\frac{S_{peak-amplitude}}{t_{End} - t_S}. \tag{3.6}$$

.

The baseline of the recordings was not flat due to noise; hence the accuracy of point detection is affected. In order to reduce such an impact, the GUI requires the user to select a time window that contains the point to be detected, which also allows the user to check if the point labelling is accurate. However, this manual selection also introduce subjectivity in some extent.

Normally the data between the R peak and the S peak were continuously decreasing, but sometimes additional peaks were found in some recordings. The number of these peaks was defined as fractionation index (FI) which was considered as a time domain feature.

The extraction of the features related to the T wave were more complex than the previous mentioned features. For MEA recordings, T waves rarely appear due to the small mass of tissue and even if they do appear, they are severely affected by noise or even completely hidden.

Some studies suggests that filters can be helpful in detecting the T wave[115]. However, this method is designed for ECG feature extraction, and the T waves recorded by the MEA system will be significantly distorted after the same filtering. Therefore, the features related to the T wave were not extracted from the MEA data. For Langendorff data, the T wave can be easily obtained even without filters. The amplitude of the T wave was calculated by following the same method as the EGM amplitude. QT interval was detected by calculating the time difference between the Q point and the T wave peak. Field Potential Duration (FPD)[53] was detected by finding the time difference between the S peak and the T wave peak. All the time domain features were list in the Table 3.1

Time domain features		
1. EGM amplitude	2. Average EGM amplitude	3. Variance of EGM amplitude
4. QR interval	5. RS interval	6. S End interval
7. RR interval	8. EGM duration	9. Signal gradient between RS peaks
10. Gradient between Q point and R peak	11. Gradient between S peak and EGM offset	12. RS peak width
13. R width S width ratio	14. R width S width EGM duration ratio	15. Fractionation index
16. QT interval	17. Field potential duration	18. T wave amplitude

Table 3.1: List of time domain features.

3.2.4 Frequency-domain feature extraction

All the frequency domain features were based on Power spectral density (PSD), an analysis method that calculates the probabilistic distributions of the components of the dynamic response frequency by subjecting the signal to a probabilistic harmonic loading spectrum[116]. In order to generate the power spectrum of the recording, the discrete Fourier transfer[116] is the most widely used method. Fast Fourier transform (FFT) was used to perform the discrete Fourier transform. The DFT of data f_j, sampled at equal intervals, can be described as:

$$F_k = \sum_{j=0}^{N-1} f_j e^{2\pi i j k/N} \quad k = 0, ..., N-1, \tag{3.7}$$

where i is $\sqrt{-1}$, N is the total size of the samples in the entire recording.

The Fourier transform of the biased estimate of the autocorrelation sequence, the periodogram, was used to estimate the PSD of the recording. The periodogram was described as:

$$P(f) = \frac{\Delta t}{N} \left| \sum_{n=0}^{N-1} x_n e^{-j2\pi fn} \right|^2, -\frac{1}{2\Delta t} < f < \frac{1}{2\Delta t}, \tag{3.8}$$

where x_n is the signal, f is the sampling rate, Δt is the sampling interval, N is the total number of samples.

An important factor in the calculation of the periodogram estimate is data windowing, which could be described as:

$$W(s) = \frac{1}{N^2} \left[\frac{\sin(\pi s)}{\sin(\frac{\pi s}{N})} \right]^2, \tag{3.9}$$

where s is the frequency offset in the bins. $W(s)$ falls off around $W(s) \approx (\pi s)^{-2}$. This fall off is slow, which leads to huge leakage in the periodogram from one frequency to another frequency. In order to eliminate this problem, Welch's data windowing method is therefore applied[117]. According to the description of the method, the infinite run of sampled data is multiplied by a scaling factor for every N of sampling points. This factor is equal to 1 in the sampling time and equals to 0 outside the window. Based on the convolution theorem, the previous equation can be changed into another form:

$$W(s) = \frac{1}{N^2} \left| \sum_{k=0}^{N-1} e^{2\pi isk/N} \right|^2, \tag{3.10}$$

Due to large values of s, the Welch's window factor changes rapidly between 0 and 1. To address this problem, the input data is multiplied by a window function, which is a Hamming window in this study:

$$w_j = \frac{1}{2}\left[1 - cos\left(\frac{2\pi j}{N}\right)\right]. \tag{3.11}$$

Python provides a validated package to implement the calculation above. Once the FFT is calculated, the features can be extracted using the periodogram. These features include the dominant frequency (DF), which is the frequency with the maximum power in the power spectrum, the mean frequency of PSD estimates, the median frequency of PSD estimates, maximum PSD estimate and the standard deviation of PSD estimates. In addition, the skewness, s, and kurtosis, k, of PSD estimates were calculated using:

$$s = \frac{\frac{1}{n}\Sigma_{i=1}^{n}(x_i - \bar{x})^3}{\left(\sqrt{\frac{1}{n}\Sigma_{i=1}^{n}(x_i - \bar{x})^2}\right)^3}, \tag{3.12}$$

$$k = \frac{\frac{1}{n}\Sigma_{i=1}^{n}(x_i - \bar{x})^4}{\left(\frac{1}{n}\Sigma_{i=1}^{n}(x_i - \bar{x})^2\right)^2}, \tag{3.13}$$

where x_i are the PSD estimate, $\bar{x}$ is the mean, and n is the number of estimates.

The features related to PSD characterise the distribution of signal energy across frequencies in the recorded EGM. The presence of multiple peaks with varying amplitudes and bandwidths indicates that the total signal energy is partitioned over distinct frequency components. This spectral distribution is expected to exhibit specific patterns; however, such patterns are not readily discernible in the raw time-domain EGM, and thus remain insufficiently investigated. Leveraging frequency-domain features in a manner analogous to clinically established time-domain metrics may enhance the precision and reliability of diagnostic assessments.

All frequency domain features are listed in Table 3.2

Frequency domain features	
1. Dominant frequency	2. Mean frequency of PSD
3. Median frequency of PSD	4. Maximum PSD
5. Skewness of PSD	6. Kurtosis of PSD
7. Standard deviation of PSD	

Table 3.2: List of frequency domain features.

3.2.5 Time-frequency feature extraction

The Continuous Wavelet Transform (CWT) of the EGM recordings was used to achieve complex filtering if the features in the recording were localised in time. This allows analysis on both time and frequency aspect and therefore illustrates local, transient, or intermittent components[118, 119]. The CWT used in this study was the following:

$$f(t) = \frac{1}{\sqrt{\pi^6}} e^{2i\pi f_{c^t}} e^{-\frac{t^2}{\beta}}, \tag{3.14}$$

where β is the bandwidth parameter and f_{c^t} is the centre wavelet frequency which can be calculated by (positive solution):

$$f_c = \sigma \frac{1}{1 - e^{-\sigma f_c}}. \tag{3.15}$$

Based on the above equations, the EGM recording was analysed and the features can be defined. First, the CWT of the EGM recording can be given:

$$C(a,b) = \int_{-\infty}^{\infty} f(t) \frac{1}{\alpha} \psi^* \left(\frac{t-b}{b} \right) dt, \tag{3.16}$$

where $a > 0$, $b \in \mathcal{R}$ and ψ, the mother wavelet, is a function of both time and frequency and $\psi^*(t)$ is the complex conjugation.

In order to find the characterising singularities in wavelet space, the maxima of the wavelet modulus that is the point b_0 with the local extremum b=b_0 were defined. When b changes, an equation is obtained:

$$\frac{\partial T(\alpha_0, b_o)}{\partial b} = 0. \tag{3.17}$$

The wavelet scale of the Morlet wavelet was changed to the wavelet frequency by applying:

$$\tilde{f} = \frac{f}{a \cdot \Delta t}. \tag{3.18}$$

where a is the wavelet and $\tilde{f}$ is the pseudo-frequency corresponding to the scale a.

The energy of signal at each scale can be defined by:

$$E_\alpha = \Sigma_{\alpha=1} |(Ca, b)|^2, \tag{3.19}$$

$$\%E = \frac{E_\alpha}{\Sigma_\alpha E_\alpha} \cdot 100. \tag{3.20}$$

The variance of signal energy across all scales was calculated using:

$$\sigma^2 = \frac{\Sigma(E_\alpha - \mu)^2}{N}. \tag{3.21}$$

where μ is the mean energy on all scales and N is the number of scales α in the distribution.

Based on the equations provided above: the scale corresponding to the minimum energy of the signal; scale corresponding to the maximum energy of the signal; pseudo-frequency corresponding to minimum energy and pseudo-frequency corresponding to maximum energy; were calculated. Time-frequency features were obtained after CWT to illustrate the transient information that the signal may contain. In signal processing, a pseudo-frequency refers to a frequency value derived from the scale parameter, often in the context of wavelet analysis. It does not correspond to a true physical frequency but instead provides an approximate representation of the dominant frequency component associated with a given scale. This mapping between scale and pseudo-frequency offers a practical means of interpreting the signal's behaviour across multiple resolutions. This also means that time-frequency features are also hard to be visualised from the original recordings same as frequency features.

All these calculations were carried out using validated packages in Python, all the time frequency

features are listed in Table 3.3.

Time frequency features	
1. Maximum modulus	2. Variance of signal energy
3. Scale corresponding to minimum energy	4. Scale corresponding to maximum energy
5. Pseudo-frequency corresponding to minimum energy	6. Pseudo-frequency corresponding to maximum energy
7. Percent of energy	

Table 3.3: List of time frequency features.

3.2.6 Entropy

Another important feature of the signal is the entropy; it is used to describe the randomness of the signal[120]. Shannon entropy[121] is used in cardiac research to measure the randomness of the ECG. The entropy defines the discrete probability space of the recorded signal. The equation of entropy is given as follows:

$$\mathcal{H}(A) = -\sum_{i=1}^{k} p_i log_2 p_i, \tag{3.22}$$

where A is the signal recording, N is the total number of the element in A and p is the probability of the element. Shannon entropy is the average information content of the signal and can be used to illustrate the degree of uncertainty, the calculation is as follows:

$$\mathcal{H}_{ShanEn}(A) = -\sum_{i=1}^{k} p_i^2 (log_2 p_i)^2, \tag{3.23}$$

Logarithmic energy entropy was calculated as well by applying:

$$\mathcal{H}_{LogEn}(A) = \sum_{i=1}^{k} (log_2 p_i)^2. \tag{3.24}$$

Due to the special data structure of the MEA recording, The calculations of both shannon entropy and logarithmic energy entropy were developed by the author. The features related to

entropy are listed in Table 3.4

Features related to entropy	
1. Shannon Entropy	2. Log Energy Entropy

Table 3.4: List of features related to entropy.

3.2.7 Statistic analysis

Because the tool is developed in-house, it needs to be validated by comparing the features extracted by different users with manually extracted features.

In this study, blinded cell data and slice data were given to three individual users, two of them were asked to extract the features using the tool and the last one was asked to manually extract the features.

Statistical analysis was performed using the GraphPad Prism software. Pared t-tests were implemented to compare the means of two dependent sample populations with normally distributed populations. Unpaired t-tests were implemented to compare the means of two independent sample populations with normally distributed populations. For data sets with at least one group showing non-normal distribution Mann–Whitney test was applied. One-way analysis of variance (ANOVA) was performed on the extracted features to test the reliability and repeatability of the tool. Once the code was validated, the ability of the underlying substrate to influence the features was tested by comparing the features extracted from human donor BMS and human failing BMS. The features extracted from pure NRVM and co-cultured NRVM/SNs were also compared.

3.3 Results

3.3.1 quantification of electrogram features

The frequency domain features, time frequency features and entropy features are calculated automatically without human input, frequency domain features and time frequency features were calculated via validated packages and entropy features were only based on equations.

As for time domain features, the point detection required manual input and all the feature calculations were based on these points. Therefore, the point detections of all the recording were first checked by the user and supervised by another person. The examples of the point detection, features calculation and the GUI are shown in Figure 3.2 and Figure 3.3. Once the time window were selected, the GUI automatically show the results and save all the features in an Excel file.

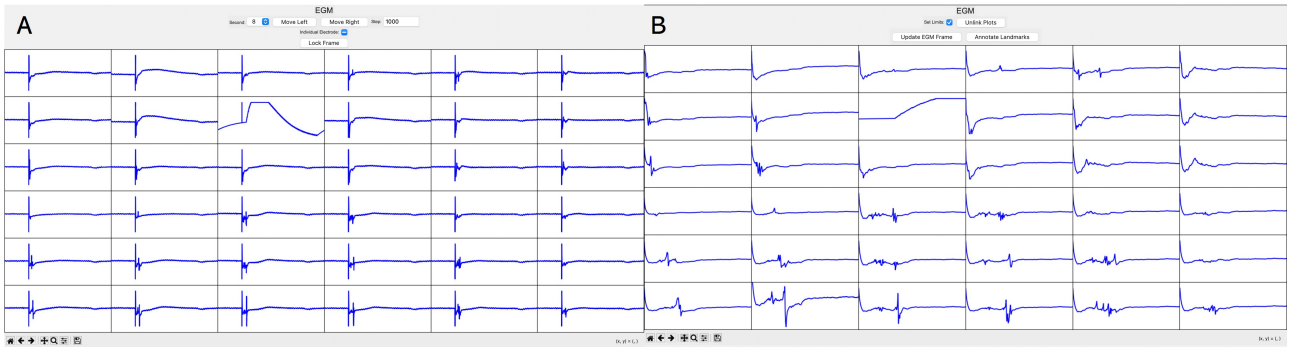


Figure 3.2: Stimulation removal process. (A) Original EGMs. (B) EGMs after stimulation removal process.

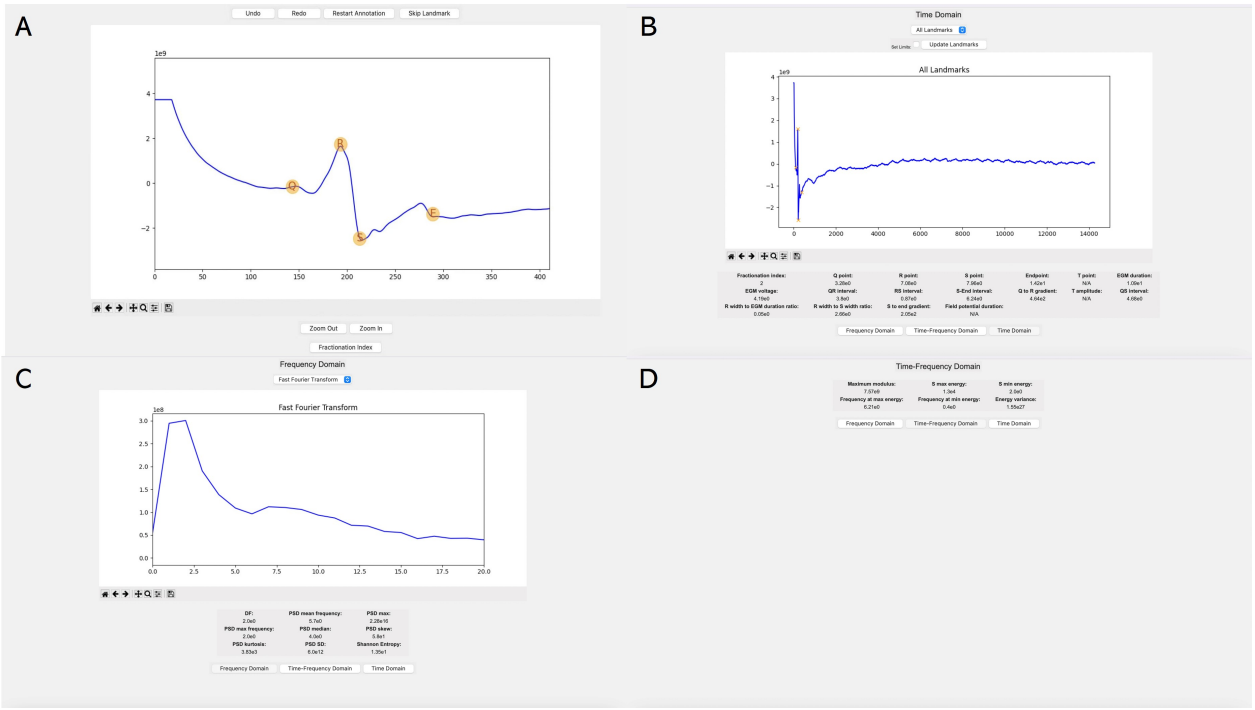


Figure 3.3: Example of the feature extraction of one EGM. (A) The point detection including Q, R, S and end point. (B) Time-domain features of a single EGM. (C) Frequency- domain features of a single EGM. (D) Time-Frequency features of a single EGM.

3.3.2 Validation of the accuracy

Data (1Hz) from one human donor BMS (EGM n number = 36) were used to first compare the features extracted using the tool against the manual calculation. Due to the fact that all time domain features were calculated based on the time point detection, three features (EGM voltage, EGM duration, and FI) were compared as all the time points were used in the calculation of them. The results are shown in Figure 3.4. As for the frequency domain features, time frequency features and entropy features, they cannot be calculated manually. Therefore, no comparison between these features was carried out.

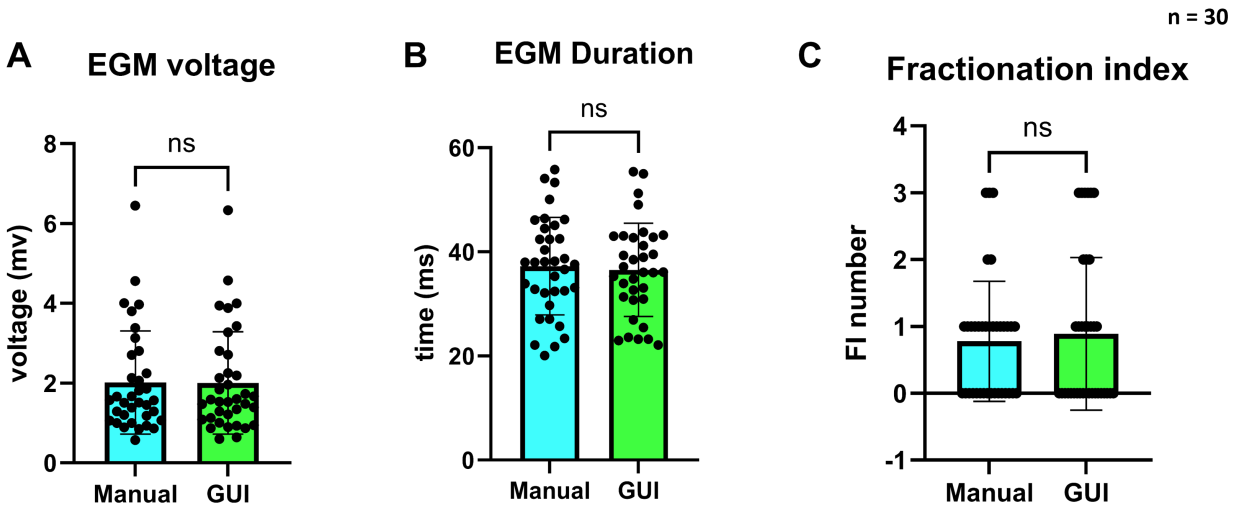


Figure 3.4: Comparison between features (from one human donor BMS) extracted manually and by using GUI. No significant difference were found in the three groups, features were extracted from 30 electrodes. (A) Comparision between manually calculated EGM voltage (mean value = 2.010 mv) and EGM voltage extracted using the tool(mean value = 2.008 mv), p = 0.36. (B) Comparision between manually calculated EGM duration (mean value = 37.25 ms) and EGM duration extracted using the tool(mean value = 38.97 mv), p = 0.10. (C) Comparision between manually counted FI (mean value = 0.78) and FI extracted using the tool(mean value = 0.80), p = 0.62. All bar charts represent mean ± S.D.; ns $0.05 < p \leq 1$ *$p \leq 0.05$, **$p \leq 0.01$, ***$p \leq 0.001$, ****$p \leq 0.0001$.

Data (1Hz) from two BMS (one from human donor heart and one from human failing heart) were given to three students to extract all the features. The extracted features were then compared to check the variability and repeatability between users. In details, the extraction of time domain features requires users to select range for time points, so if different input can cause features with significant difference need to be test. As for frequency domain features and time-frequency features, manual extraction requires a selection of stimulation, no user input are required if using the GUI. In that case, the features extracted by user 2 and user 3 should be exactly same, so the comparison of these features are only used to test the inter-user repeatability. The inter-user comparison between the time domain features of a human failing BMS is shown in Figure 3.5. The inter-user repeatability test of the frequency domain features of a human failing BMS is shown in Figure 3.6. The inter-user repeatability test of the time-frequency features of a human failing BMS is shown in Figure 3.7. No significant differences were found in all the features extracted by different users.

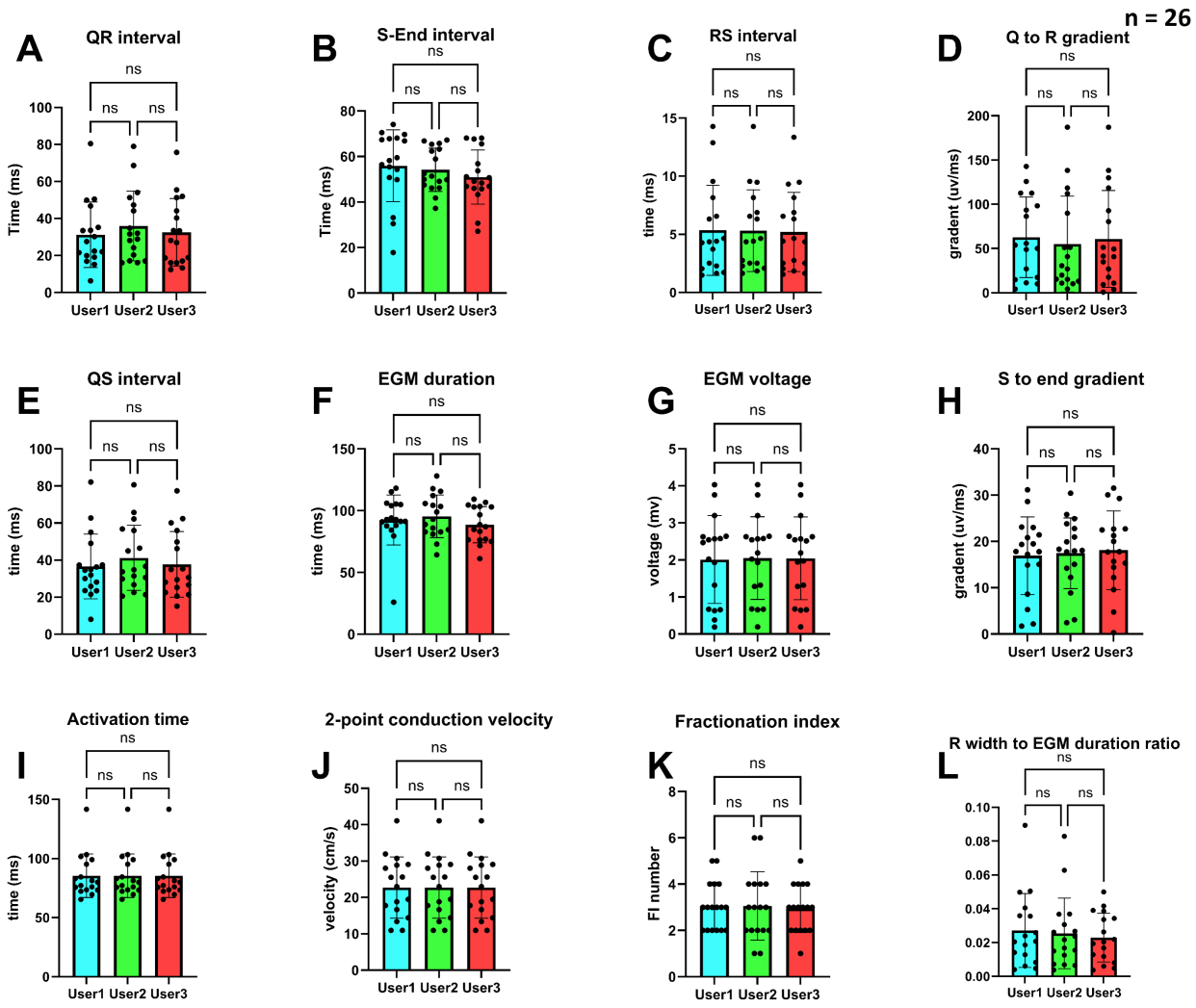


Figure 3.5: Inter-user variability detection using a BMS from human failing heart. The time domain features were included in this figure, features were extracted from 26 electrodes. (A) QR interval. (B) S End interval. (C) RS interval. (D) Q to R gradient. (E) QS interval. (F) EGM duration. (G) EGM voltage. (H) S to end gradient. (I) Activation time. (J) 2-point conduction velocity. (K) Fractionation index. (L) R width to EGM duration ratio. All bar charts represent mean ± S.D.; ns $0.05 < p \leq 1$, *$p \leq 0.05$, **$p \leq 0.01$, ***$p \leq 0.001$, ****$p \leq 0.0001$.

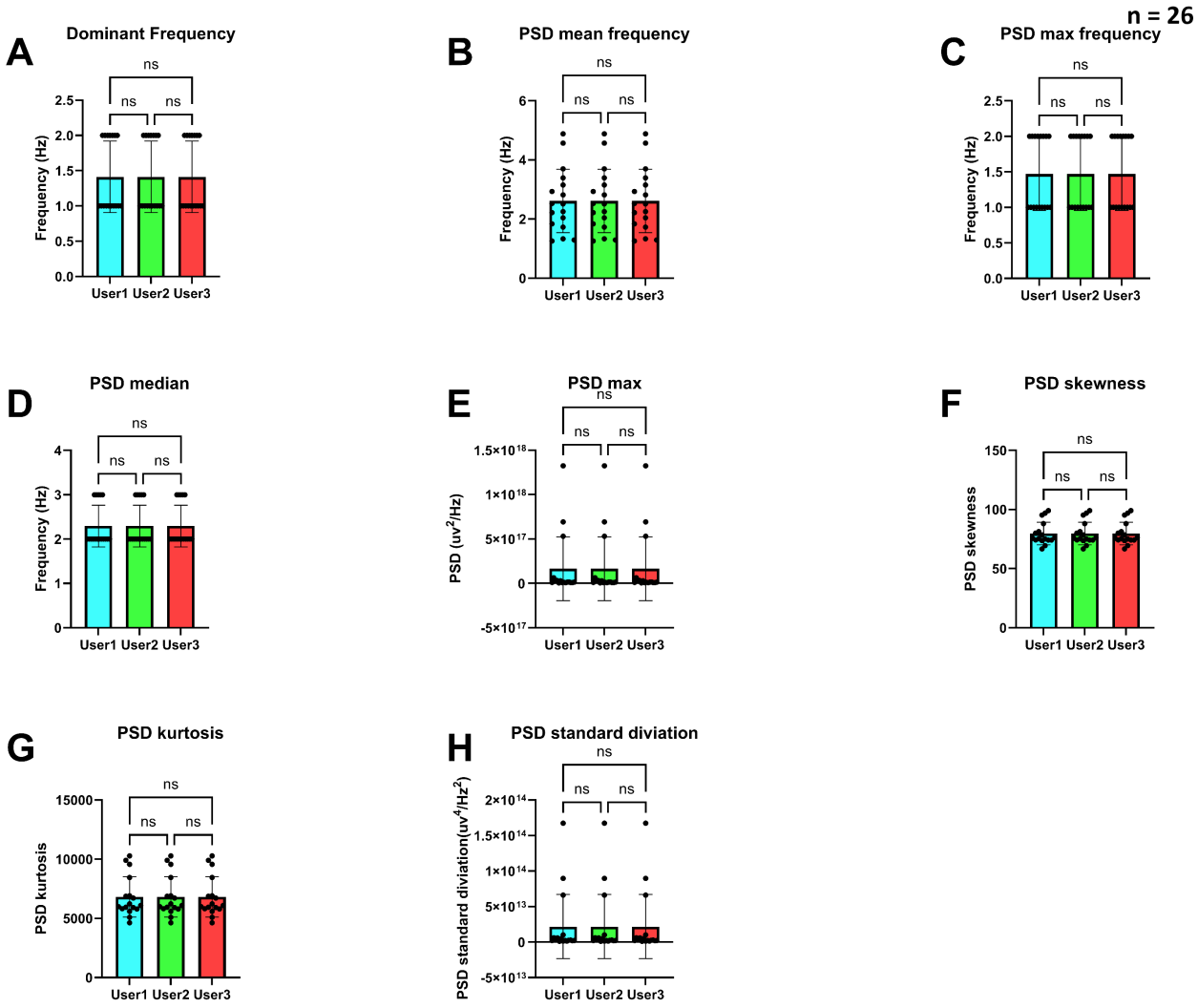


Figure 3.6: inter-user repeatability test using a BMS from human failing heart. The frequency domain features were included in this figure, features were extracted from 26 electrodes. (A) Dominant frequency. (B) PSD mean frequency. (C) PSD max frequency. (D) PSD median. (E) Maximum PSD. (F) PSD skewness. (G) PSD kurtosis. (H) PSD standard diviation. All bar charts represent mean ± S.D.; ns $0.05 < p \leq 1$, *$p \leq 0.05$, **$p \leq 0.01$, ***$p \leq 0.001$, ****$p \leq 0.0001$.

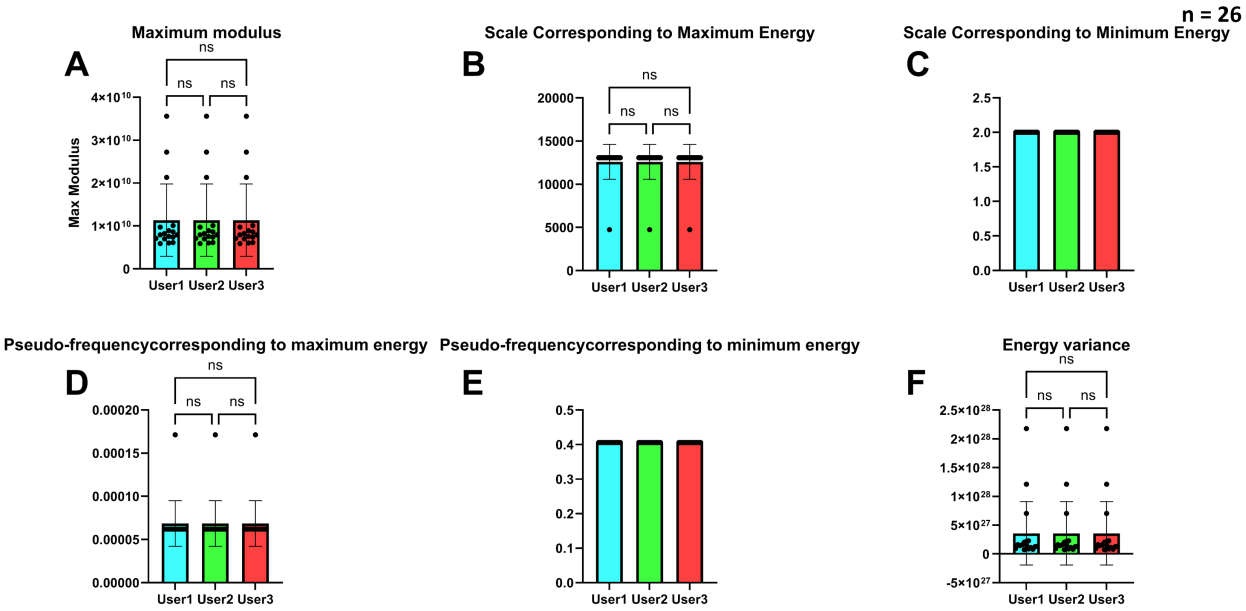


Figure 3.7: inter-user repeatability test using a BMS from human failing heart. The time frequency features were included in this figure, features were extracted from 26 electrodes. (A) Maximum modulus. (B) Scale corresponding to maximum energy. (C) Scale corresponding to minimum energy. (D) Pseudo-frequency corresponding to maximum energy. (E) Pseudo-frequency corresponding to minimum energy. (F) Energy variance. All bar charts represent mean ± S.D.; ns $0.05 < p \leq 1$, *$p \leq 0.05$, **$p \leq 0.01$, ***$p \leq 0.001$, ****$p \leq 0.0001$.

The inter-user variability check using the EGM recording (1Hz) from another human donor heart BMS was shown in Figure 3.8 (time domain), the inter-user repeatability test is shown in Figure 3.9 (frequency domain) and Figure 3.10 (time frequency) respectively. No significant differences were found in all the features extracted by different users.

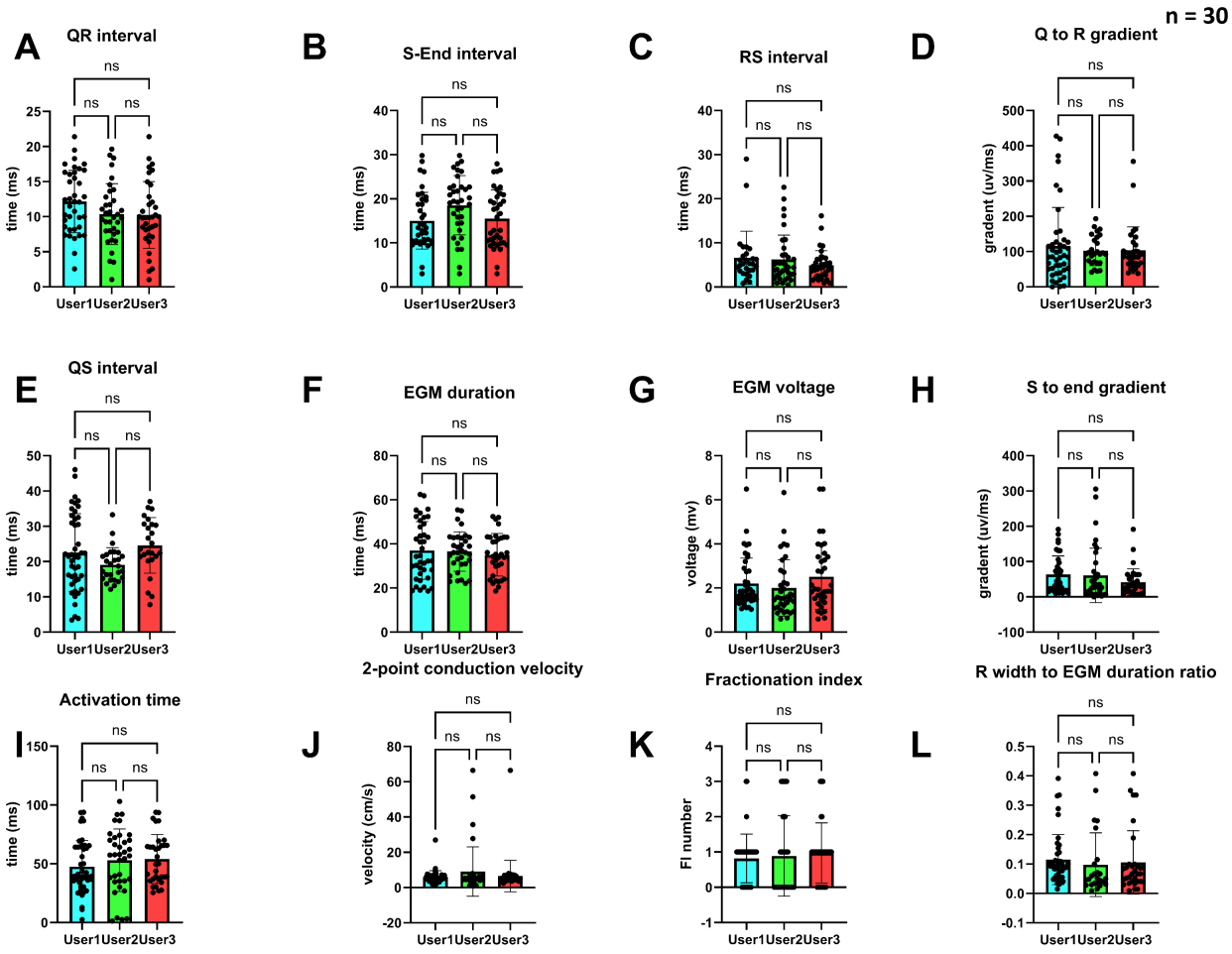


Figure 3.8: Inter-user variability detection using a BMS from human donor heart. The time domain features were included in this figure, features were extracted from 30 electrodes. (A) QR interval. (B) S End interval. (C) RS interval. (D) Q to R gradient. (E) QS interval. (F) EGM duration. (G) EGM voltage. (H) S to end gradient. (I) Activation time. (J) 2-point conduction velocity. (K) Fractionation index. (L) R width to EGM duration ratio. All bar charts represent mean ± S.D.; ns $0.05 < p \leq 1$, *$p \leq 0.05$, **$p \leq 0.01$, ***$p \leq 0.001$, ****$p \leq 0.0001$.

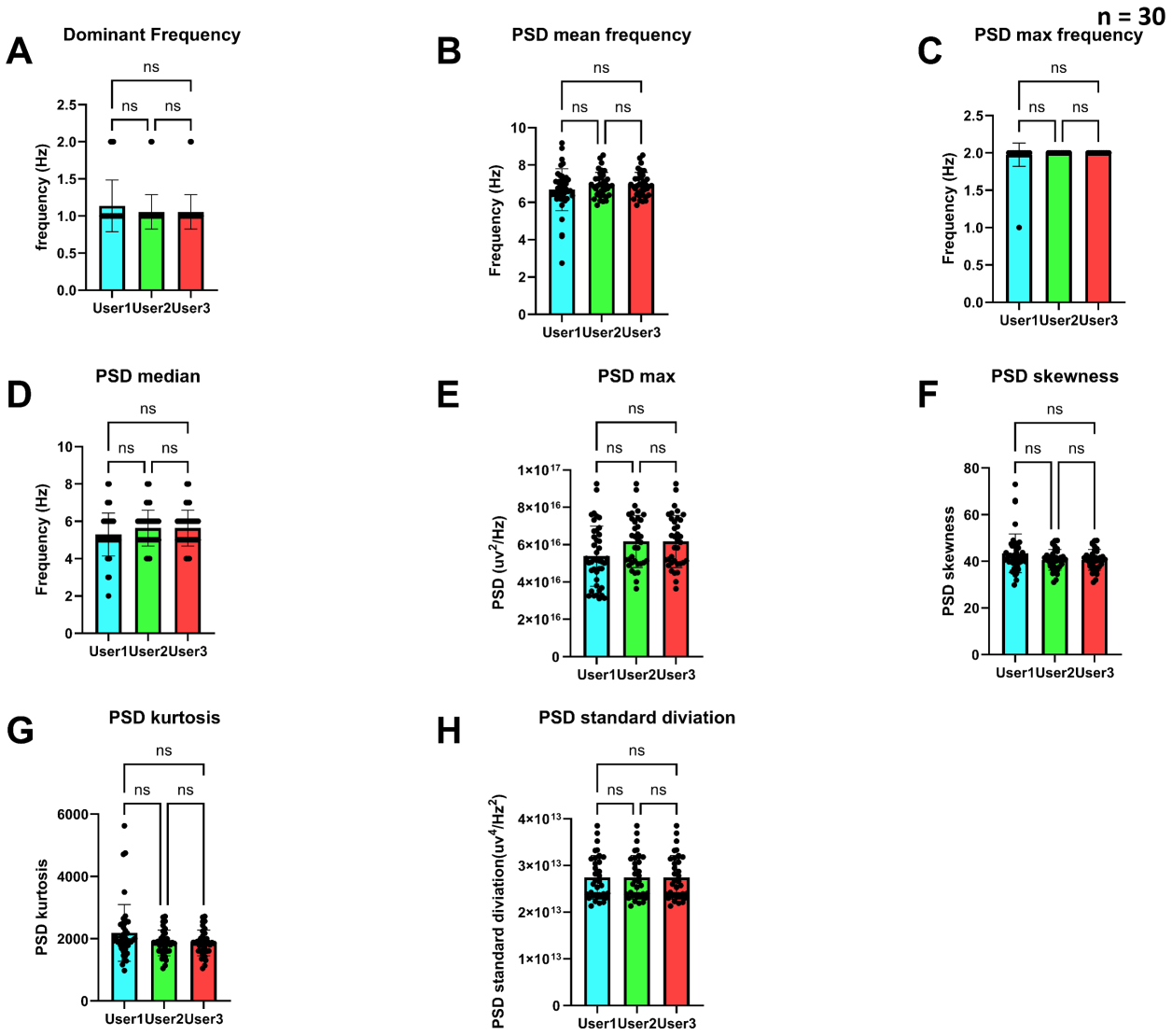


Figure 3.9: inter-user repeatability test using a BMS from human donor heart. The frequency domain features were included in this figure, features were extracted from 30 electrodes. (A) Dominant frequency. (B) PSD mean frequency. (C) PSD max frequency. (D) PSD median. (E) Maximum PSD. (F) PSD skewness. (G) PSD kurtosis. (H) PSD standard diviation. All bar charts represent mean ± S.D.; ns $0.05 < p \leq 1$, *$p \leq 0.05$, **$p \leq 0.01$, ***$p \leq 0.001$, ****$p \leq 0.0001$.

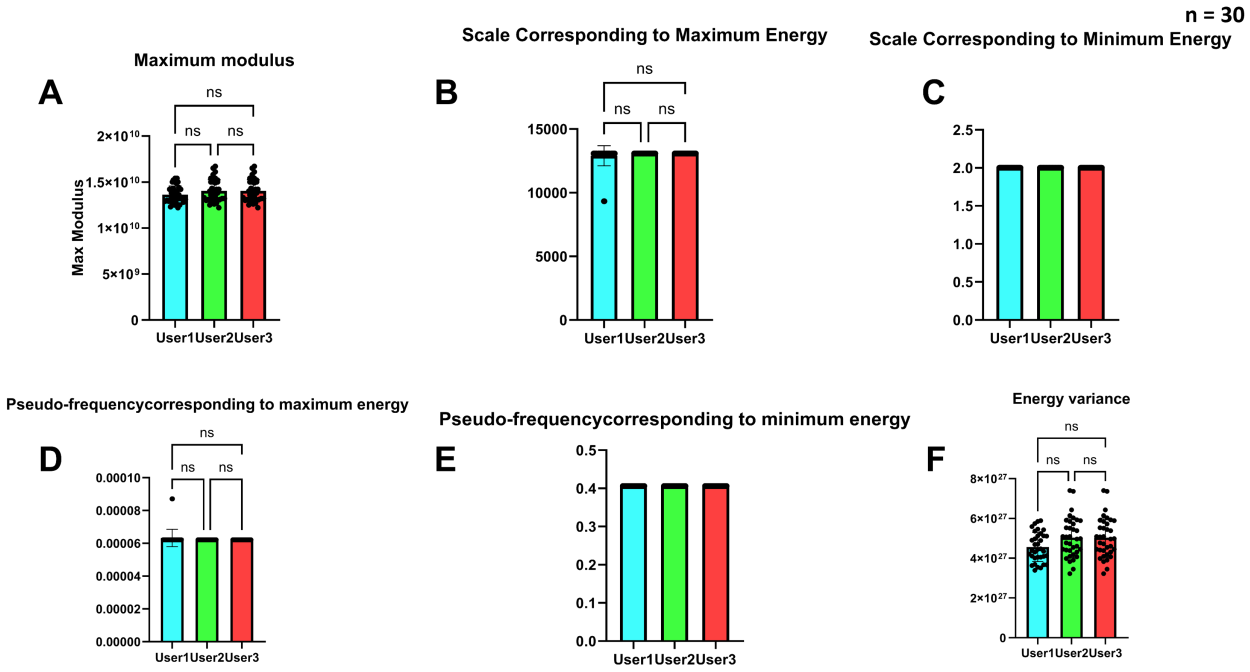


Figure 3.10: inter-user repeatability test using a BMS from human donor heart. The time frequency features were included in this figure, features were extracted from 30 electrodes. (A) Maximum modulus. (B) Scale corresponding to maximum energy. (C) Scale corresponding to minimum energy. (D) Pseudo-frequency corresponding to maximum energy. (E) Pseudo-frequency corresponding to minimum energy. (F) Energy variance. All bar charts represent mean ± S.D.; ns $0.05 < p \leq 1$, *$p \leq 0.05$, **$p \leq 0.01$, ***$p \leq 0.001$, ****$p \leq 0.0001$.

3.3.3 Comparison between different models

The EGM recordings (1Hz) from one human donor (DN) BMS and one human failing (HF) BMS were selected to first compare whether the differences in features caused by different reasons can be extracted. Significant differences were obtained from QR interval (DN: 16.45 ms, HF: 25.59 ms P = 0.0347), S End interval (DN: 16.09 ms, HF: 40.82 ms, P < 0.0001), RS interval (DN: 2.285 ms, HF: 4.133 ms, P = 0.0044), Q to R gradient (DN: 189.6, HF: 85.67, P = 0.0082), QS interval (DN: 18.76 ms, HF: 29.72 ms, P = 0.0160), EGM duration (DN: 37.12 ms, HF: 69.13 ms, P < 0.0001), EGM voltage (DN: 2.092 mv, HF: 1.181 mv, P = 0.0085), S to end gradient (DN: 99.02, HF: 55.29, P = 0.0001), Activation time (DN: 42.73 ms, HF: 87.75 ms, P < 0.0001), 2-point conduction velocity (DN: 41.58 cm/s, HF: 26.36 cm/s, P < 0.0001), Fractionation index (DN: 16.45, HF: P < 0.0001), Dominant frequency (DN: 1.192 Hz, HF: 4.743 Hz, P < 0.0001), PSD mean frequency (DN: 2.955 Hz, HF: 2.360 Hz, P < 0.0001), PSD max

frequency (DN: 1.446 Hz, HF: 1.029 Hz, P < 0.0001), PSD median (DN: 2.0 Hz, HF: 2.3 Hz, P = 0.0001), Maximum PSD (DN: 1.175e+017 uv2/Hz, HF: 4.501e+017 uv2/Hz, P < 0.0001), PSD skewness (DN: 81.05, HF: 75.38, P < 0.0001), PSD kurtosis (DN: 7213, HF: 6187, P < 0.0001), PSD standard diviation (DN: 1.836e+013 uv4/Hz2, HF: 7.669e+013 uv4/Hz2, P < 0.0001), Maximum modulus (DN: 2.183e+010, HF: 3.847e+010, P < 0.0001), Scale corresponding to maximum energy (DN: 12700.4, HF: 10846.2, P = 0.0005), Scale corresponding to minimum energy (DN: 3.523, HF: 3.001, P = 0.0003), Energy variance (DN: 1.214e+028, HF: 3.777e+028, P < 0.0001) and Shannon entropy (DN: 5.758, HF: 5.813, P = 0.0007). And no significant differences were obtained from R width to EGM duration ratio (DN: 0.101, HF: 0.126, P = 0.6765). For pseudo-frequency corresponding to maximum energy (DN: 6.212e-005, HF: 6.212e-005) and pseudo-frequency corresponding to minimum energy (DN: 0.406, HF: 0.406) as the features extracted from all the electrodes were the same, so p value can not be calculated. The results are shown in Figure 3.11 (time domain), Figure 3.12 (frequency domain and Shannon Entropy) and Figure 3.13 (time frequency) respectively.

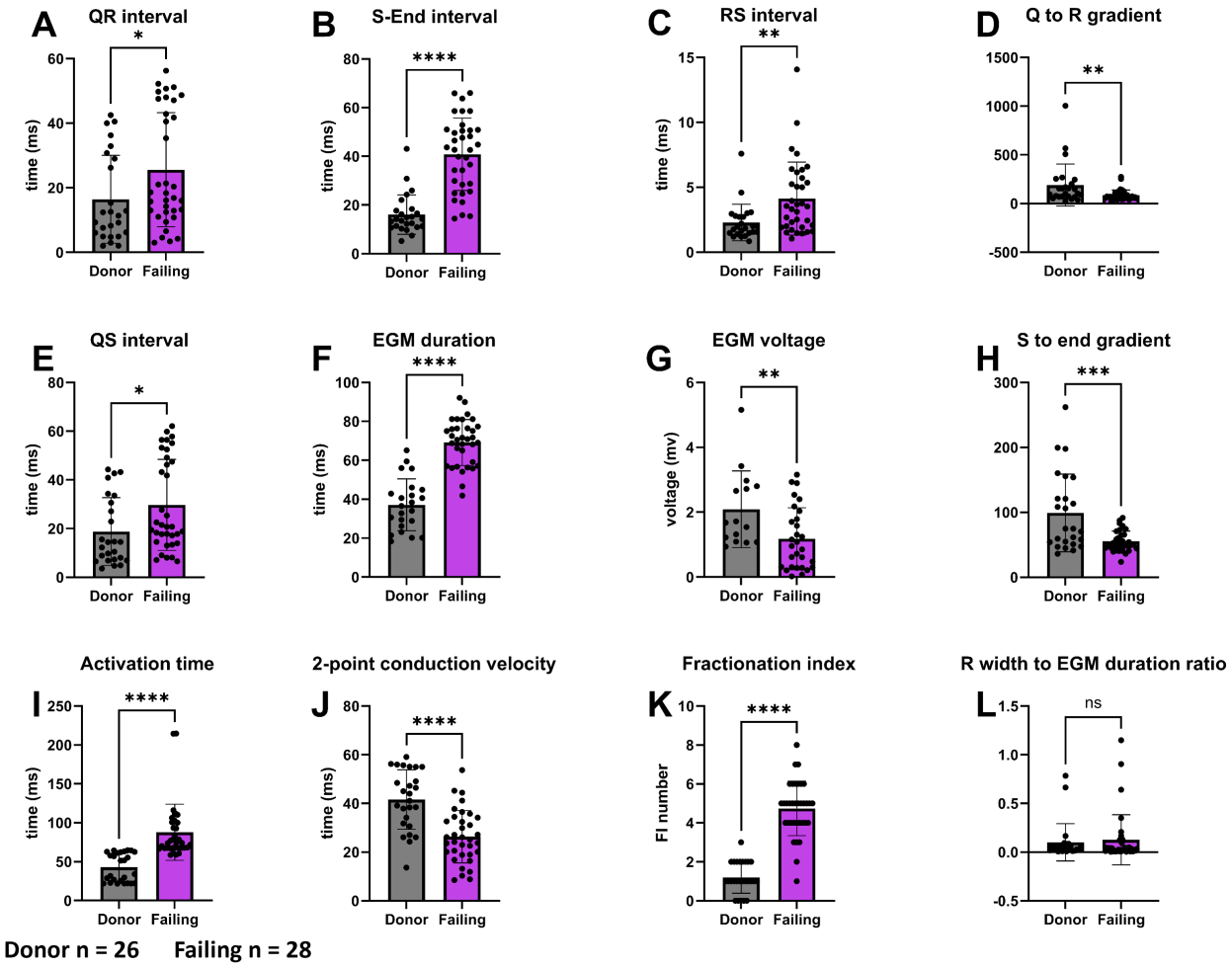


Figure 3.11: Comparison between time domain features extracted from human donor BMS and human failing BMS. For donor BMS, features were extracted from 26 electrodes, for failing BMS, features were extracted from 28 electrodes. (A) QR interval. (B) S End interval. (C) RS interval. (D) Q to R gradient. (E) QS interval. (F) EGM duration. (G) EGM voltage. (H) S to end gradient. (I) Activation time. (J) 2-point conduction velocity. (K) Fractionation index. (L) R width to EGM duration ratio. All bar charts represent mean ± S.D.; ns $0.05 < p \leq 1$, *$p \leq 0.05$, **$p \leq 0.01$, ***$p \leq 0.001$, ****$p \leq 0.0001$.

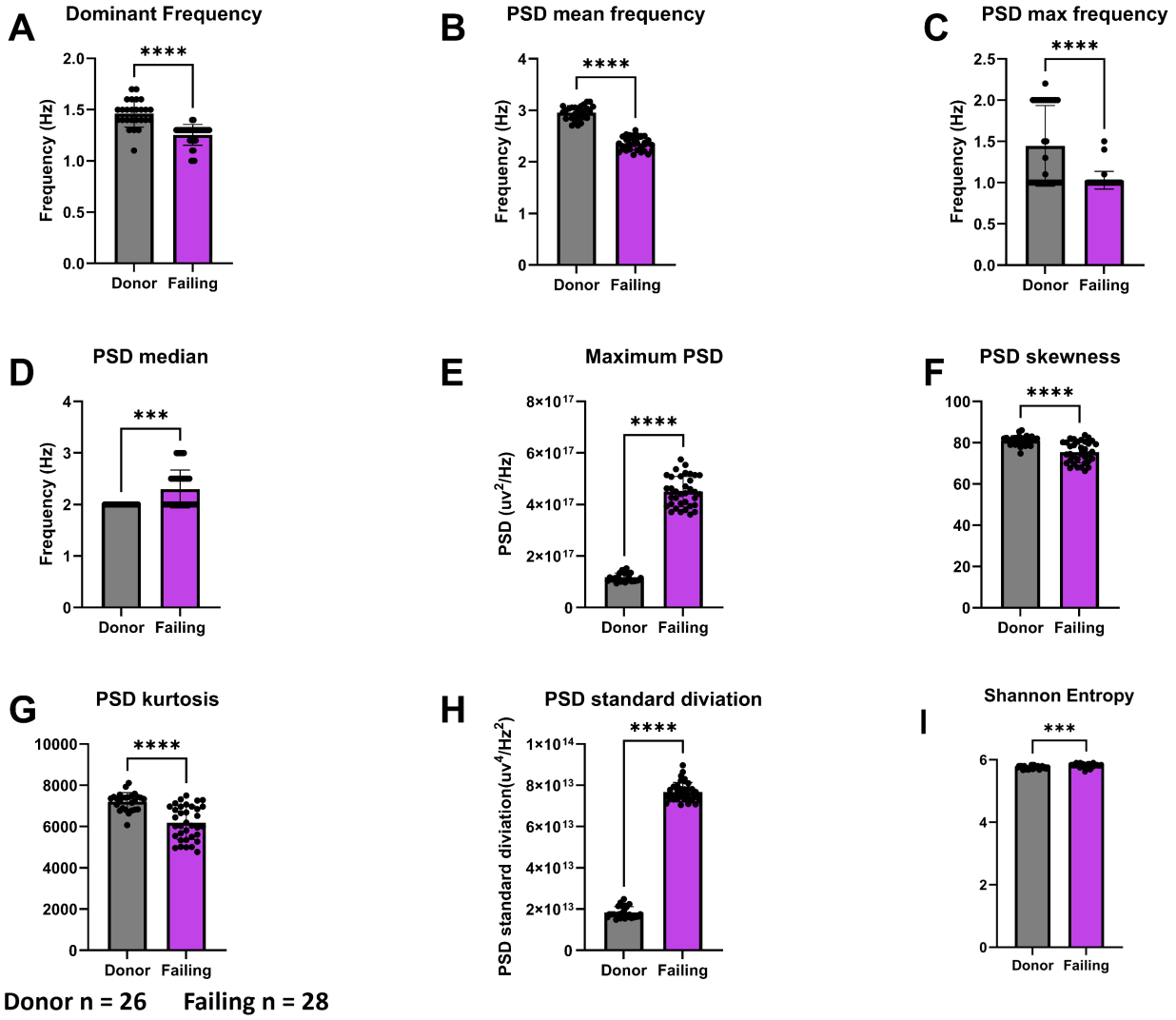


Figure 3.12: Comparison between frequency domain features and Shannon entropy extracted from human donor BMS and human failing BMS. For donor BMS, features were extracted from 26 electrodes, for failing BMS, features were extracted from 28 electrodes. (A) Dominant frequency. (B) PSD mean frequency. (C) PSD max frequency. (D) PSD median. (E) Maximum PSD. (F) PSD skewness. (G) PSD kurtosis. (H) PSD standard diviation. All bar charts represent mean ± S.D.; ns $0.05 < p \leq 1$, *$p \leq 0.05$, **$p \leq 0.01$, ***$p \leq 0.001$, ****$p \leq 0.0001$.

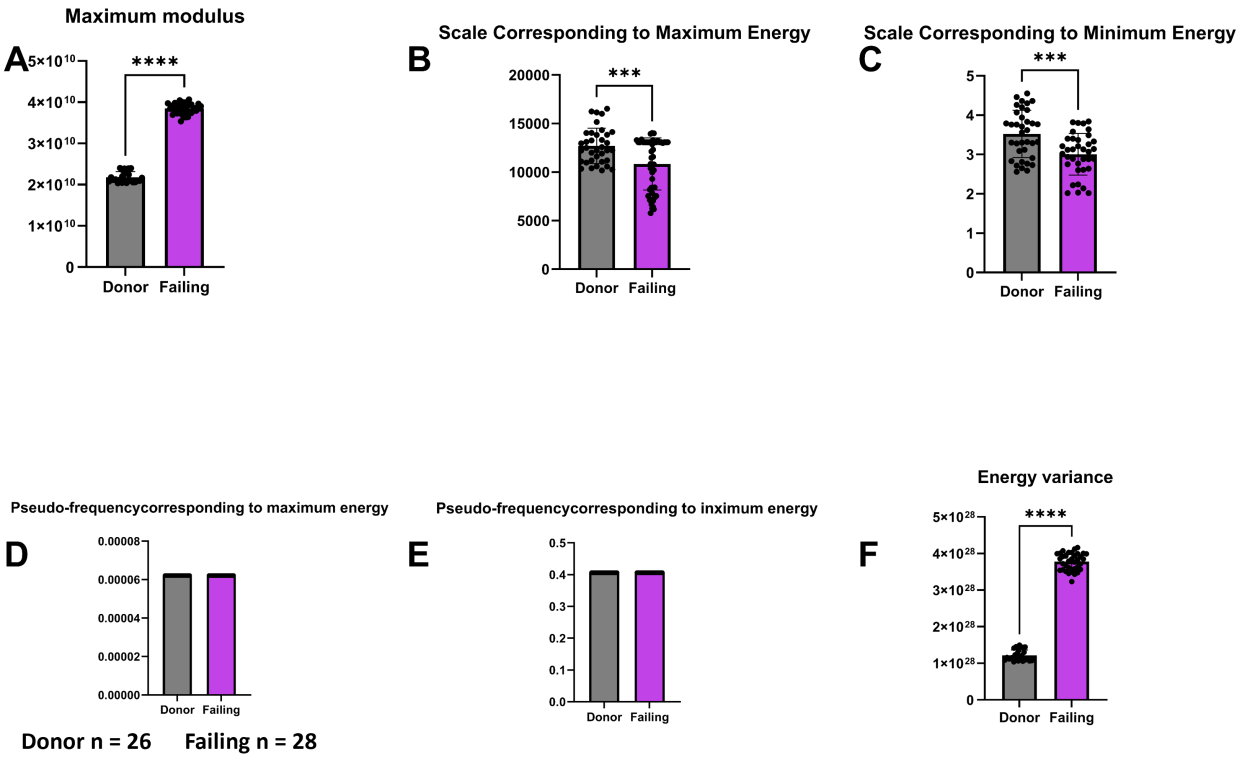


Figure 3.13: Comparison between time frequency features extracted from human donor BMS and human failing BMS. For donor BMS, features were extracted from 26 electrodes, for failing BMS, features were extracted from 28 electrodes. (A) Maximum modulus. (B) Scale corresponding to maximum energy. (C) Scale corresponding to minimum energy. (D) Pseudo-frequency corresponding to maximum energy. (E) Pseudo-frequency corresponding to minimum energy. (F) Energy variance. All bar charts represent mean ± S.D.; ns $0.05 < p \leq 1$, *$p \leq 0.05$, **$p \leq 0.01$, ***$p \leq 0.001$, ****$p \leq 0.0001$.

3.4 Discussion

The development and validation of the tool for feature extraction were presented in this chapter. The tool can be used on the EGM recording from the MEA experiment and the Langendorff experiment. The tool allows the user to extract time domain features, frequency domain features, time frequency features, and entropy features.

The influence of the change of the underlying substrate on the cardiac electrogram morphology needs to be quantified. Conduction velocity and electrical propagation direction were commonly the features used to assess cardiac electrophysiology[122, 123]. However, these characteristics are not sufficient to describe how the EGM was affected by cellular and structural abnormal-

ities. Therefore, there is a huge gap in investigating the relationship between electrogram morphology and structural and functional changes in cardiac tissues. In order to fill this gap, 37 features including unique features of cardiac EGM and general signal features in different domain were selected. Some of these features, such as voltage, dominant frequency, and Shannon entropy, were already already applied in ECG signal analysis for a long time[119]. Some features (fractionation index) were used to quantify complex cardiac signal recordings such as complex fractionated atrial electrogram (CFAE) in recent research[124]. Other features were widely used in general signal processing in other areas[125]. In this study, all features were used to analyse unipolar extracellular EGMs recorded from different biological models.

Simple ECG morphology and contact EGM morphology were considered as reference to arrhythmias[126, 127]. Unlike the quantified ECG morphology that was used for diagnosis, the abnormal EGM morphology was selected by trained physicians during therapy. Such feature selection without quantification was based on experience and has the possibility of misjudgment. In addition, all applications were designed to determine whether arrhythmia occurs or not[128, 129]. The relationship between the mechanism of cardiac arrhythmia and electrophysiology was not well studied. The cardiac remodelling that occurs with heart failure and how it affects the EGM morphology can be research direction to link arrhythmia from its mechanism to abnormal electrical performance, which is the target of this study. The feature extraction tool is necessary in such study.

The development of an automated EGM feature extraction tool represents a significant methodological advance in the field. Traditional electrogram analysis has often relied upon manual annotation, which is inherently subjective, labour-intensive, and prone to inter-observer variability. By introducing a systematic and computationally efficient method, your work enables high-throughput quantification of multiple EGM features, thereby facilitating more rigorous and reproducible analysis. This is particularly important for the study of remodelling, where subtle changes in EGM morphology may provide key insights into underlying pathophysiological processes.

Some commercial software such as Multi Channel Analyser for MEA and Labchart for Powerlab

have the automated point detection methods and therefore provide functions for the user to calculate some time domain features[130]. However, these implimented functions are for general use, not only targeted on EGM analysis, their accuracy are relatively low. They also require a large amount of input related to signal science, which is not friendly to users of other professions.

Also in comparison with earlier approaches, much of the literature has concentrated on qualitative descriptions of EGM features or the application of limited automated techniques. For example, de Bakker et al. and Stevenson et al. demonstrated the diagnostic value of local electrograms in detecting conduction block and arrhythmogenic substrates, but these analyses were largely reliant on manual interpretation[61, 79]. More recent efforts towards automation have focused primarily on clinical ablation guidance systems, which often capture a restricted set of electrogram features[131]. In contrast, this tool broadens the analytical scope, integrating features that are sensitive to both structural and functional changes in the myocardium.

The main algorithms for the frequency domain features, time frequency features and entropy were developed based on validated packages of Python, and the time points detection was original. In that case, the validation of the algorithms was carried out. The accuracy of the feature extraction by the tool was proved because there is no difference between the manually extracted time-domain features and the features extracted by the tool. The time domain feature extraction requires user input, and by comparing the features extracted by different users from the same EGM recording, it was proved that these inputs had no effect on the features. The last comparison carried out in this chapter is the features of the EGM recorded from a DN BMS and a HF BMS, significant differences were obtained from most of the features, which means that the underlying remodelling caused by heart failure has influence on the EGM morphology. However, EGM recorded from two BMS is not sufficient to prove such hypothesis, more data is needed.

The time domain feature extraction is challenging because its time-varying morphology may be caused by physiological variation factors and noise may cause difficulties to the point detection. Although digital filters can be implanted into the tool, they will cause serious distortion of the data in the time domain. Considering all the factors, no filter was applied in time domain

feature extraction. a Chebyshev type I bandpass filter (50Hz-250Hz) and a notch filter were applied to other feature extraction following a previous study.

3.5 Limitations

Noise is the most important limitation in this study. It has multiple sources and almost imposable to be eliminated. The application of digital filters leads to unacceptable detection, so a balance point was found in this study.

Features related to T wave such as FPD and T wave amplitude were important factors that been used to identify arrhythmia in clinical. But T-wave was absence in the cell EGM and only appears in some BMS EGM recordings. But these T-waves were almost hidden in noise due to high signal-to-noise ratio. But the T-wave detection on Langendorff data is stable due to the fact that the contact EGM was recorded from a complete organ and the system used is commercial with a mature noise reduction system. In that case, the T wave detection was not performed on the MEA recordings.

Another limitation is that some features do not show significant difference in all the comparison, this could be due to the fact that these features of noise are more obvious than them of EGM. Therefore, the pseudo-frequency corresponding to maximum energy, pseudo-frequency corresponding to minimum energy and Log Energy Entropy will not be included in the following chapters.

3.6 Conclusion

Our understanding of the relationship between cardiac electrical features that lead to arrhythmias, the underlying cardiac remodelling, and the morphology of EGM remains limited. There is also no universal set of features that can be used to characterise EGMs. Hence, a standard in-silico feature extraction tool is not available for research purposes. The novelty of this chapter

lies in establishing a standardised platform that can be applied consistently across experimental and computational studies. By doing so, this work bridges a methodological gap between pre-clinical research and clinical practice, providing a framework for objective assessment of EGM morphology that can be used to interrogate remodelling processes under controlled conditions. Although there is still room for improvement, the feasibility and reliability of the tool were demonstrated.

Chapter 4

Effects of Structural remodelling on Cardiac Electrogram Morphology

4.1 Introduction

In the introduction chapter, it was mentioned that the cardiac fibrosis is scaring. As scars are not conductive, macroscopic scars within the heart muscle seriously affect electrical signals throughout the chamber, even the whole heart. However, many fibrosis are just microscopic scars in the myocardium. The utility of voltage can be used to detect macroscopic scars in clinical practice, but the microscopic scar cannot be detected by ECG or catheter mapping. It remains unclear how scars at the tissue level influence EGM morphology. The conduction pathways through fibrotic tissue at microscopic level can be entirely different compared to macroscopic level. A greater understanding of how cellular-level scars lead to specific modifications of EGM morphology could be beneficial to find the underlying mechanism of arrhythmias. This chapter aims to illustrate this relationship using rat and human BMS models. Such a relationship can be further imported into in-silico simulations, which can potentially become guidance for clinical therapy. Also as mentioned in the introduction chapter, cardiac scar is formed by different type of cells, only collagen is focused in this study due to the fact that it is the major composition of the scar and its autofluorescence property. The development of the

scar rat model was carried out by Dimitrios Panagopoulos. The collagen registration code was developed by Konstantinos Ntagiantas and improved by the writer.

4.1.1 Development and the rule of scar

It has been proved that fetal and neonatal cardiomyocytes proliferate and then repair damaged tissues[132]. However, the functional myocardium cannot be regenerated in adult mammalian hearts due to inadequate cardiomyocyte renewal. Scars are formed to provide the heart with the necessary mechanical properties to ensure that it can beat normally after a large number of myocardial cells have died. In the normal scar formation process, scars develop from microscopic size to macroscopic size. An Python code developed within the group has the ability to quantify the microscopic size of collagen and collocate the collagen with the distribution of the electrodes.

4.1.2 Structural remodelling affects cardiac electrophysiology

The macroscopic size scars block the electrical propagation in one large region, which may cause cardiac reentry and further lead to VT. However, it remains to be studied how structural remodelling like the development of microscopic-size collagen affects cardiac electrophysiology at the tissue level.

The variability of EGM morphology has not been fully studied, and research on the mechanisms underlying these changes is lacking. Compared to the in vivo model, ex vivo models are easier to establish in the early stages of research, and the remodelling can be directly obtsained.

Therefore, the rat BMS model and the human BMS model were used to investigate the relationship between EGM morphology and structural remodelling at the cellular level. The hypotheses to be addressed were as follows:

1. Structural remodelling occurs more extensively in rat scar models and human failing hearts compare to control rat models and human donor hearts respectively.

2. Structural remodelling leads to slower conduction velocity and abnormal conduction pathways in human and rat BMS models.

3. The EGM morphology is affected by structural remodelling, directly reflected in various EGM features.

For this purpose, the following studies described in this chapter were carried out:

1. Record EGM from different BMS model.

2. Image the collagen distribution on BMS and quantify the collagen level.

3. Correlate the collagen distribution and the locations of the micro-electrode array.

4. Correlate the collagen level and the EGM features.

4.2 Methods

4.2.1 Microelectrode array recording

The BMS of the rat models were prepared as described in Section 2.2.2. The BMS of human models was prepared as described in Section 2.2.3. Due to the fact that some human heart has animal restrictions, BMS preparation, MEA recording, data processing for rat BMS and human BMS were carried out separately. In this study, two groups of rats (myocardial fibrosis model and healthy model) and two human groups (human donor heart and human failing heart) were used.

EGM was recorded from each BMS following the standard protocol described in Section 2.3, and BMS were fixed and saved as described in the same section. Examples of EGMs recorded from rat BMS and human BMS shown in figure 4.1 and figure 4.2.

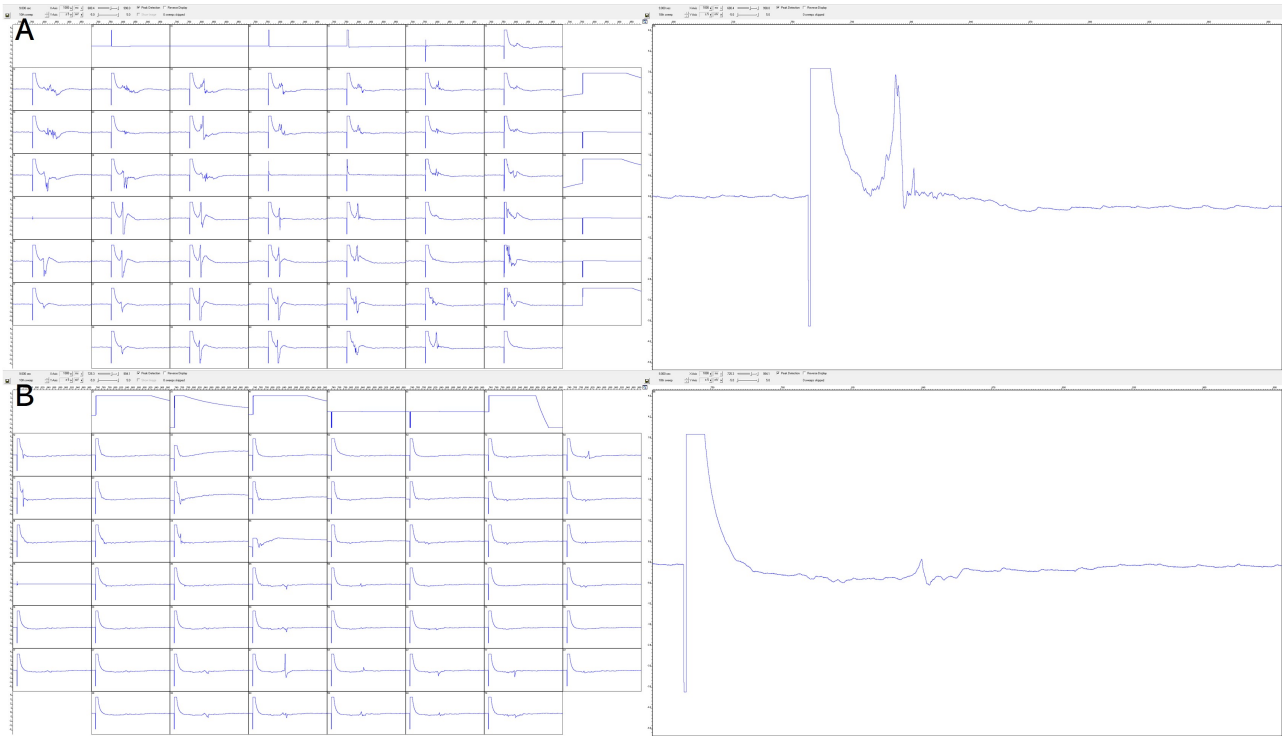


Figure 4.1: Examples of the raw EGMs recorded from rat BMS. (A) control rat. The left image shows the EGMs recorded from all the electrodes, the right images shows the EGM recorded from a single electrode. The stimulation direction is north. (B) Myocardial fibrosis rat. The left image shows the EGMs recorded from all the electrodes, the right images shows the EGM recorded from a single electrode. The stimulation direction is north.

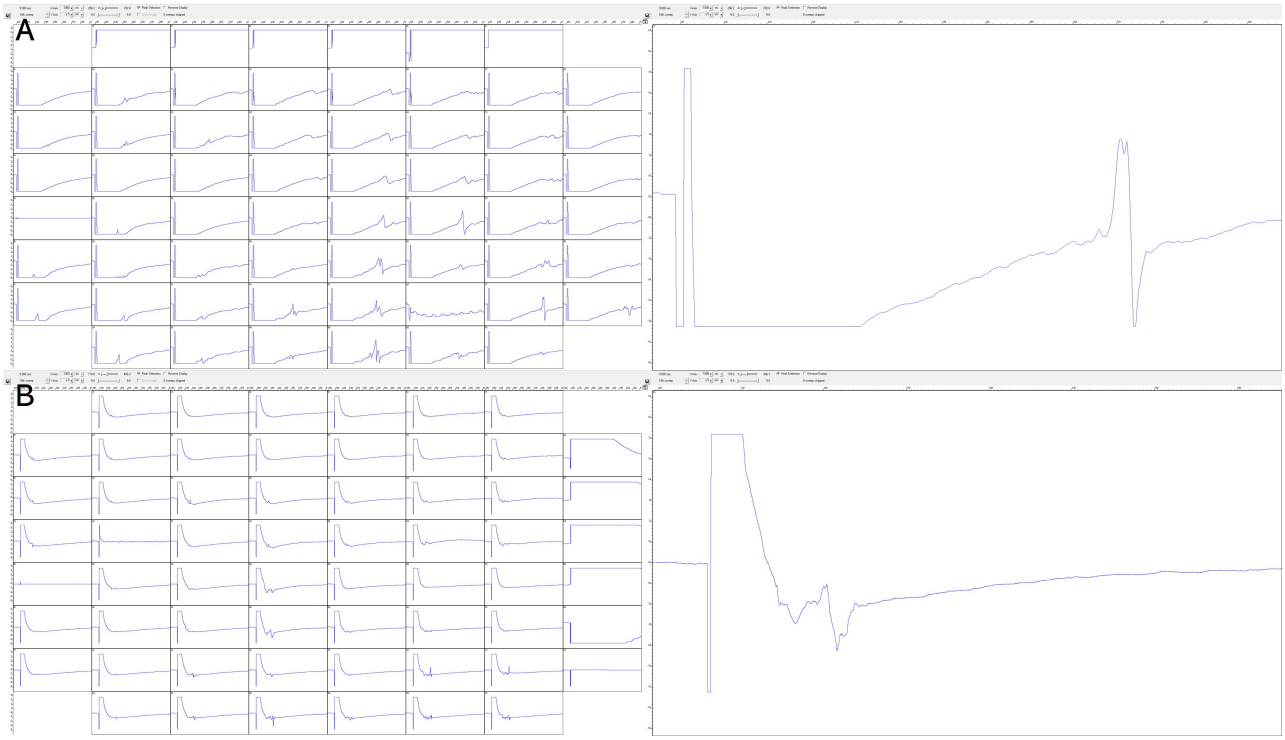


Figure 4.2: Examples of the raw EGMs recorded from rat BMS. (A) Donor heart. The left image shows the EGMs recorded from all the electrodes, the right images shows the EGM recorded from a single electrode. The stimulation direction is north. (B) Failing heart. The left image shows the EGMs recorded from all the electrodes, the right images shows the EGM recorded from a single electrode. The stimulation direction is east.

4.2.2 Microscope and image processing

An image of each BMS and the locations of micro electrodes on the BMS were taken before the BMS was removed from the MEA dish. The image was used for further colocalisation between the collagen and the electrodes.

All BMS were imaged using a Leica SP5 inverted confocal microscope with a multiphoton laser as described in Section 2.6.2.

The image was then post processed using ImageJ software. Custom macro commands were then used to identify the maximum intensity per pixel in each image, adjust the gamma (value = 0.50) and subtract the background (rolling = 5) while removing the outlier pixels based on the change of brightness (radius = 2 threshold = 50). The noise was removed by setting the threshold (3000 - 65535). The six-by-six electrode grid is then overlaid over the microscopy

image using fiducial points from the MEA picture taken earlier for accurate colocalisation. The mean pixel intensity is then calculated per field of view of each electrode (calculated as a circle of 350μm diameter, equal to half the distance between electrodes) and a collagen index (CI) number is generated. The CI can then be correlated with each recorded EGM. The colocalisation and CI calculations were achieved using a validated in-house Python code. The code reads the image of the BMS on the MEA dish and the microscope image of the same BMS to colocalise the electrode positions and collagen on the BMS. Then it quantifies the collagen expression (collagen index) in the area covered by the electrodes.

Examples of the imaging processing and electrode colocalisation are shown in Figure 4.3, Figure 4.4, Figure 4.5 and Figure 4.6 respectively.

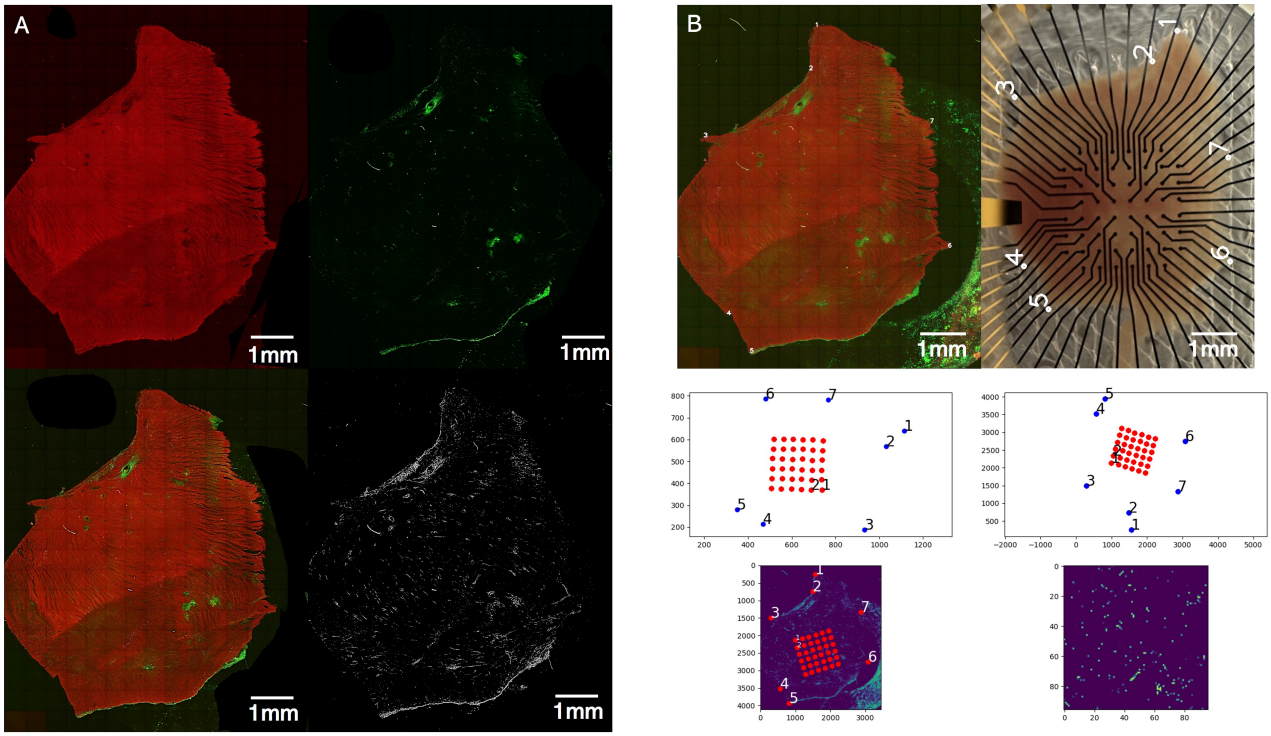


Figure 4.3: Colocalisation and Quantification of collagen in a rat healthy BMS. (A) SHG image of the BMS. Slice channel (top left); Collagen channel (top right); Merged image (bottom left); processed collagen channel (bottom right). (B) Colocalisation of collagen and micro electrodes. Reference points were selected on both SHG image and the picture of the BMS, the locations of the electrodes were selected from the same picture (top); Colocalisarion process and the collagen pixels in electrode area (bottom).

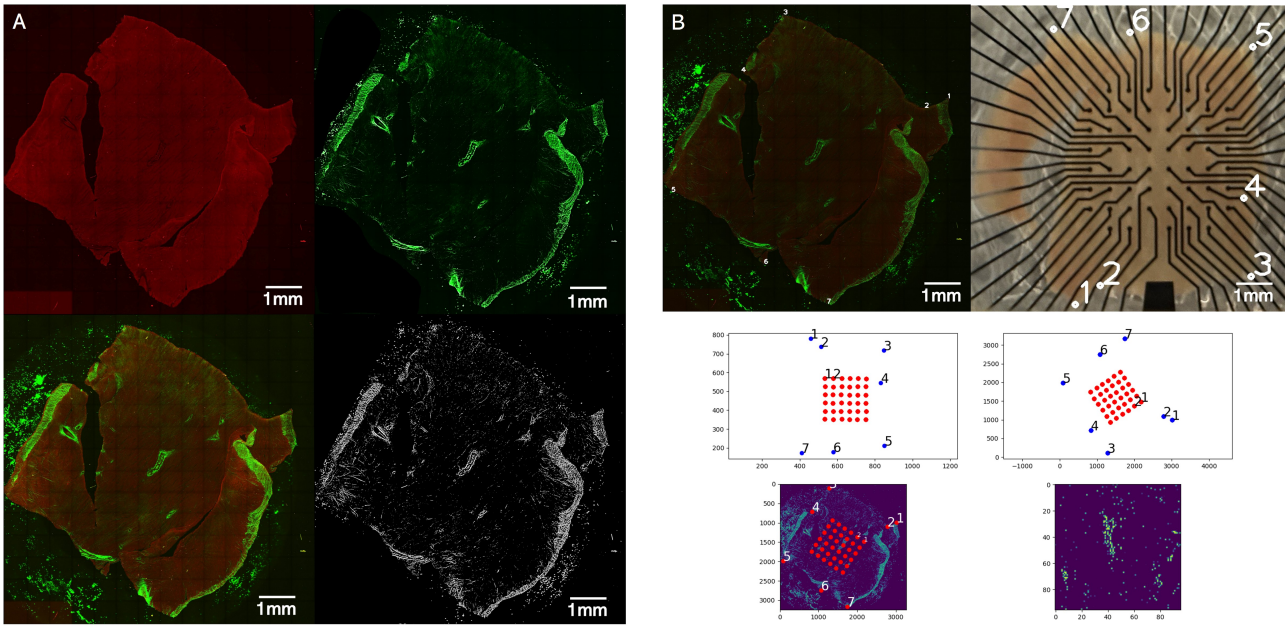


Figure 4.4: Colocalisation and Quantification of collagen in a rat myocardial fibrosis BMS. (A) SHG image of the BMS. Slice channel (top left); Collagen channel (top right); Merged image (bottom left); processed collagen channel (bottom right). (B) Colocalisation of collagen and micro electrodes. Reference points were selected on both SHG image and the picture of the BMS, the locations of the electrodes were selected from the same picture (top); Colocalisarion process and the collagen pixels in electrode area (bottom).

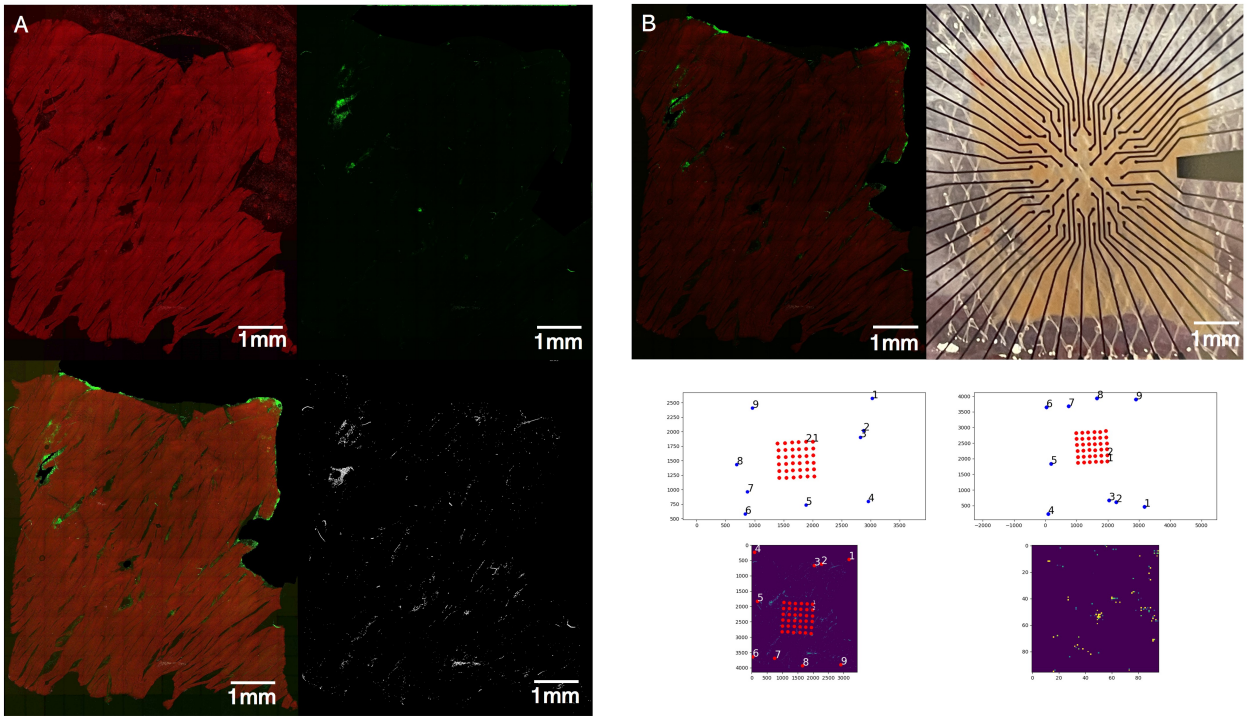


Figure 4.5: Colocalisation and Quantification of collagen in a human donor BMS. (A) SHG image of the BMS. Slice channel (top left); Collagen channel (top right); Merged image (bottom left); processed collagen channel (bottom right). (B) Colocalisation of collagen and micro electrodes. Reference points were selected on both SHG image and the picture of the BMS, the locations of the electrodes were selected from the same picture (top); Colocalisation process and the collagen pixels in electrode area (bottom).

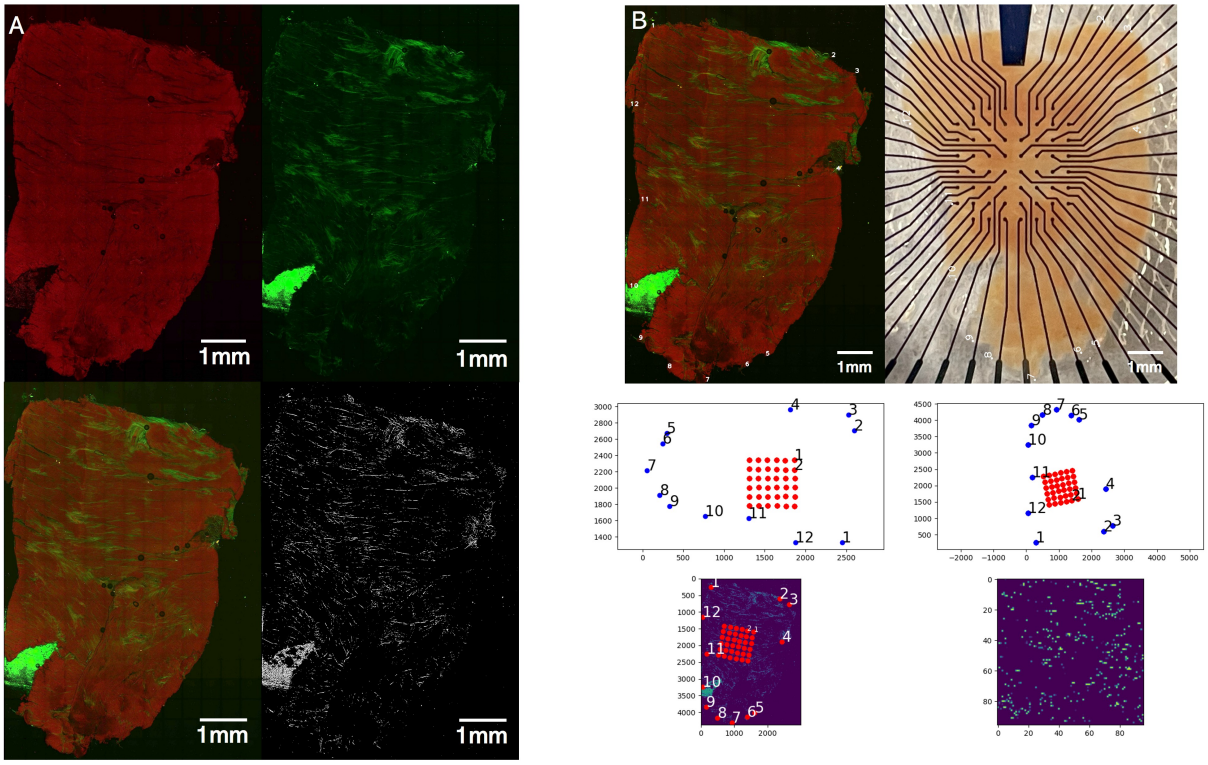


Figure 4.6: Colocalisation and Quantification of collagen in a human failing BMS. (A) SHG image of the BMS. Slice channel (top left); Collagen channel (top right); Merged image (bottom left); processed collagen channel (bottom right). (B) Colocalisation of collagen and micro electrodes. Reference points were selected on both SHG image and the picture of the BMS, the locations of the electrodes were selected from the same picture (top); Colocalisation process and the collagen pixels in electrode area (bottom).

4.2.3 Data analysis

The features of EGMs were extracted using the tool described in chapter 3. Statistical analysis was performed using the GraphPad Prism software.

Unpaired t-tests were implemented to compare the means of two independent sample populations with normally distributed populations. For data sets with at least one group showing non-normal distribution Mann–Whitney test was applied. Statistical analyses of the correlation between CI and EGM features were performed using linear regression.

4.3 Results

4.3.1 Collagen development in rat models

4 healthy rats and 4 myocardial fibrosis rats were used, 18 healthy rat heart BMS (4 + 4 + 4 + 6) 22 myocardial fibrosis heart BMS (4 + 6 + 6 + 6) were cut from these hearts. Higher CI was obtained from myocardial fibrosis heart BMS (myocardial fibrosis heart BMS = 0.1844 $\pm$ 0.1606; healthy heart BMS: 0.0432 $\pm$ 0.0514;p $\leq$ 0.0001). The conduction velocity measured from myocardial fibrosis heart BMS is lower than the conduction velocity measured from healthy heart BMS (myocardial fibrosis heart BMS = 31.15 $\pm$ 7.14 cm/s; healthy heart BMS: 39.05 $\pm$ 4.98 cm/s;p $\leq$ 0.0001). The results and two examples of the activation map, the conduction vorticity map and the conduction direction compass for a healthy heart BMS and a myocardial fibrosis heart BMS are shown in Figure 4.7.

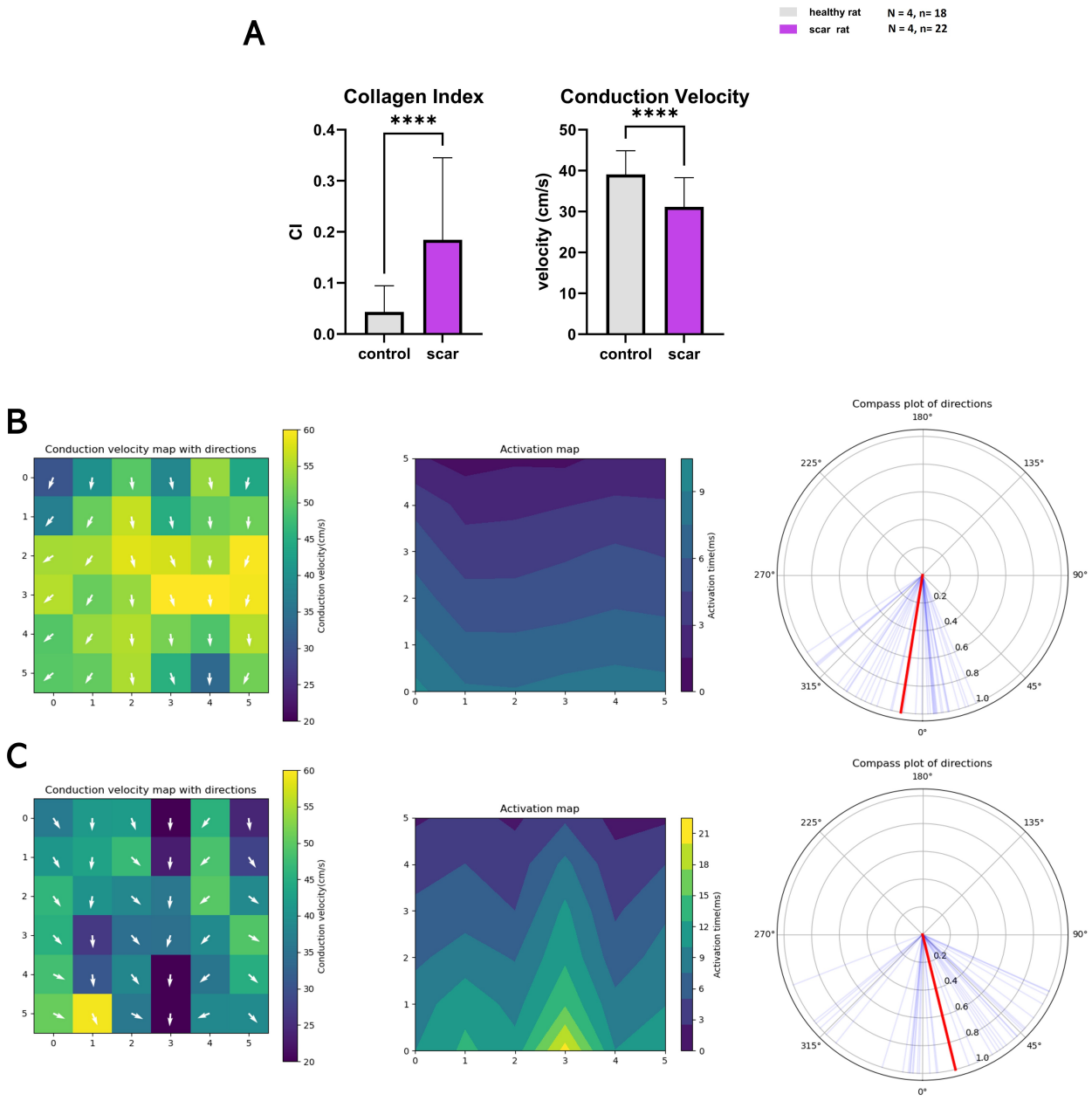


Figure 4.7: Development of collagen in rat models and it's effects on electrical propagation and conduction velocity. Data was collected from 4 healthy rats (18 BMS) and 4 myocardial fibrosis rat (22 BMS). (A) Higher CI was calculated from myocardial fibrosis heart BMS; Conduction velocity measured on myocardial fibrosis heart BMS was lower than that on healthy heart BMS. (B) The conduction velocity map, activation map and compress of conduction directions of a healthy heart BMS. (C) The conduction velocity map, activation map and compress of conduction directions of a myocardial fibrosis heart BMS. Grey error bars represent the standard deviation. All bar charts represent mean ± S.D.; ns $0.05 < p \leq 1$, *$p \leq 0.05$, **$p \leq 0.01$, ***$p \leq 0.001$, ****$p \leq 0.0001$.

4.3.2 Collagen development human donor samples and human failing samples

BMS (number of human donor BMS = 33, bumber of human failing BMS = 47) were prepared from 7 human donor hearts and 11 human failing hearts. In general, EGM can be recorded from 6 slices per donor heart and 4 slices per failing heart because of the quality of the hearts, but this number could vary due to different heart conditions.

The CI of human failing BMS is higher than that of human donor BMS (human donor BMS: mean value = 0.0237 $\pm$ 0.01024; human failing BMS: mean value = 0.0825 $\pm$ 0.04472). The conduction velocity measured from human failing BMS is lower than the conduction velocity measured from human donor BMS. (human donor BMS = 35.63 $\pm$ 3.43 cm/s; human failing BMS: 30.12 $\pm$ 6.88 cm/s;p $\leq$ 0.0001). The results and two examples of the activation map, conduction vorticity map and conduction direction compass for a healthy heart BMS and a myocardial fibrosis heart BMS are shown in Figure 4.8.

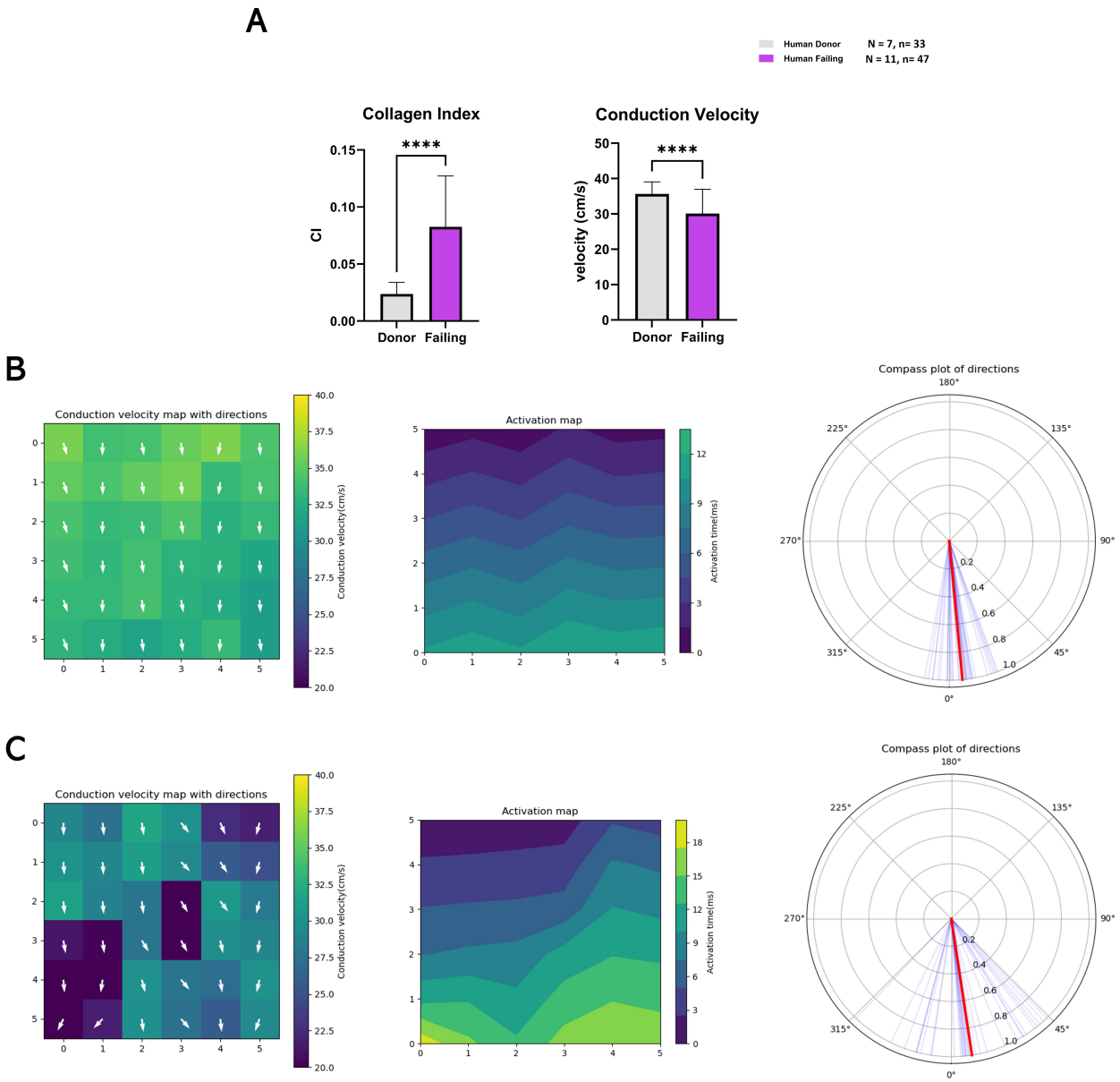


Figure 4.8: Development of collagen in human models and it's effects on electrical propagation and conduction velocity. Data was collected from 7 donor hearts (33 BMS) and 11 failing hearts (47 BMS). (A) Higher CI was calculated from human failing heart BMS; Conduction velocity measured on human failing BMS was lower than that on human donor BMS. (B) The conduction velocity map, activation map and compress of conduction directions of a human donor BMS. (C) The conduction velocity map, activation map and compress of conduction directions of a human failing BMS. Grey error bars represent the standard deviation. All bar charts represent mean ± S.D.; ns $0.05 < p \leq 1$, *$p \leq 0.05$, **$p \leq 0.01$, ***$p \leq 0.001$, ****$p \leq 0.0001$.

4.3.3 Collocation of EGM features and locations of collagen in rat model

The colocalisation code and the feature extraction tool theoretical have the function of relating the EGM features and CI for all electrodes. However, the slices prepared from the same rat heart had similar CIs, and therefore the n number is too low to perform the collocation for every electrode. The collocation was carried out at the heart level. This will be discussed in the Discussion Section.

All features were first compared between the control group and the myocardial fibrosis group. The results are shown in Figure 4.9, Figure 4.10 and Figure 4.11 respectively. Significant differences were obtained from nine time domain, seven frequency domain and four time frequency features. There were four features in the time domain, four features in the frequency domain, and three features in the time frequency that decreased with the development of collagen. These features are as follows: EGM voltage (Control: 2833 ± 636.9 μv, Scar: 1390 ± 666.7 μv, p $\leq$ 0.0001), QR gradient (Control: 142.1 ± 47.86 uv/ms, Scar: 63.81 ± 35.58 uv/ms, p $\leq$ 0.0001), SEnd gradient (Control: 137.6 ± 49.46 uv/ms, Scar: 50.01 ± 35.58 uv/ms, p $\leq$ 0.0001), conduction velocity (Control: 39.05 ± 5.801 cm/s, Scar: 31.15 ± 7.133 cm/s, p $\leq$ 0.0001), dominant frequency (Control: 1.171 ± 0.1392 Hz, Scar: 0.990 ± 0.1189 Hz, p $\leq$ 0.0001), maximum PSD (Control: 2.461e+015 ± 3.657e+014 uv^2/Hz, Scar: 1.454e+015 ± 3.428e+014 uv^2/Hz, p $\leq$ 0.0001), PSD skewness (Control: 65.31 ± 4.298, Scar: 55.09 ± 2.927, p $\leq$ 0.0001), PSD kurtosis (Control: 4435 ± 306.0, Scar: 3640 ± 370.8, p $\leq$ 0.0001), maximum modulus (Control: 1.07e+010 ± 1.96e+09, Scar: 7.06e+09 ± 1.91e+09, p $\leq$ 0.0001). scale corresponding to maximum energy (Control: 0.1116 ± 0.03185, Scar: 0.03084 ± 0.01803, p $\leq$ 0.0001 and scale corresponding to minimum energy (Control: 0.0003039 ± 0.0001171, Scar: 0.0002788 ± 0.0001078, p = 0.3516). Increases were obtained from the remaining features, which are RS interval (Control: 1.928 ± 0.6806 ms, Scar: 3.001 ± 0.7155 ms, p $\leq$ 0.0001), QR interval (Control: 1.928 ± 0.6806 ms, Scar: 3.001 ± 0.7155 ms, p = 0.000158), SEnd interval (Control: 11.03 ± 2.624 ms, Scar: 14.88 ± 3.371 ms, p $\leq$ 0.0001), EGM duration (Control: 23.37 ± 3.646 ms, Scar: 29.46 ± 4.309 ms, p $\leq$ 0.0001), fractionation index (Control: 1.22 ±

1.189, Scar: 2.27 ± 1.476, p ≤ 0.0001), PSD mean frequency (Control: 11.91 ± 2.104 Hz, Scar: 17.60 ± 2.753 Hz, p ≤ 0.0001), PSD median (Control: 2.429 ± 1.351 Hz, Scar: 2.887 ± 2.116 Hz, p = 0.025), PSD standard deviation (Control: 3.553e+011 ± 5.878e+010 uv^2/Hz^2, Scar: 6.547e+011 ± 8.813e+010 uv^2/Hz^2, p ≤ 0.0001) and energy variance (Control: 4.916e+026 ± 1.683e+026, Scar: 1.107e+027 ± 2.257e+026, p ≤ 0.0001).

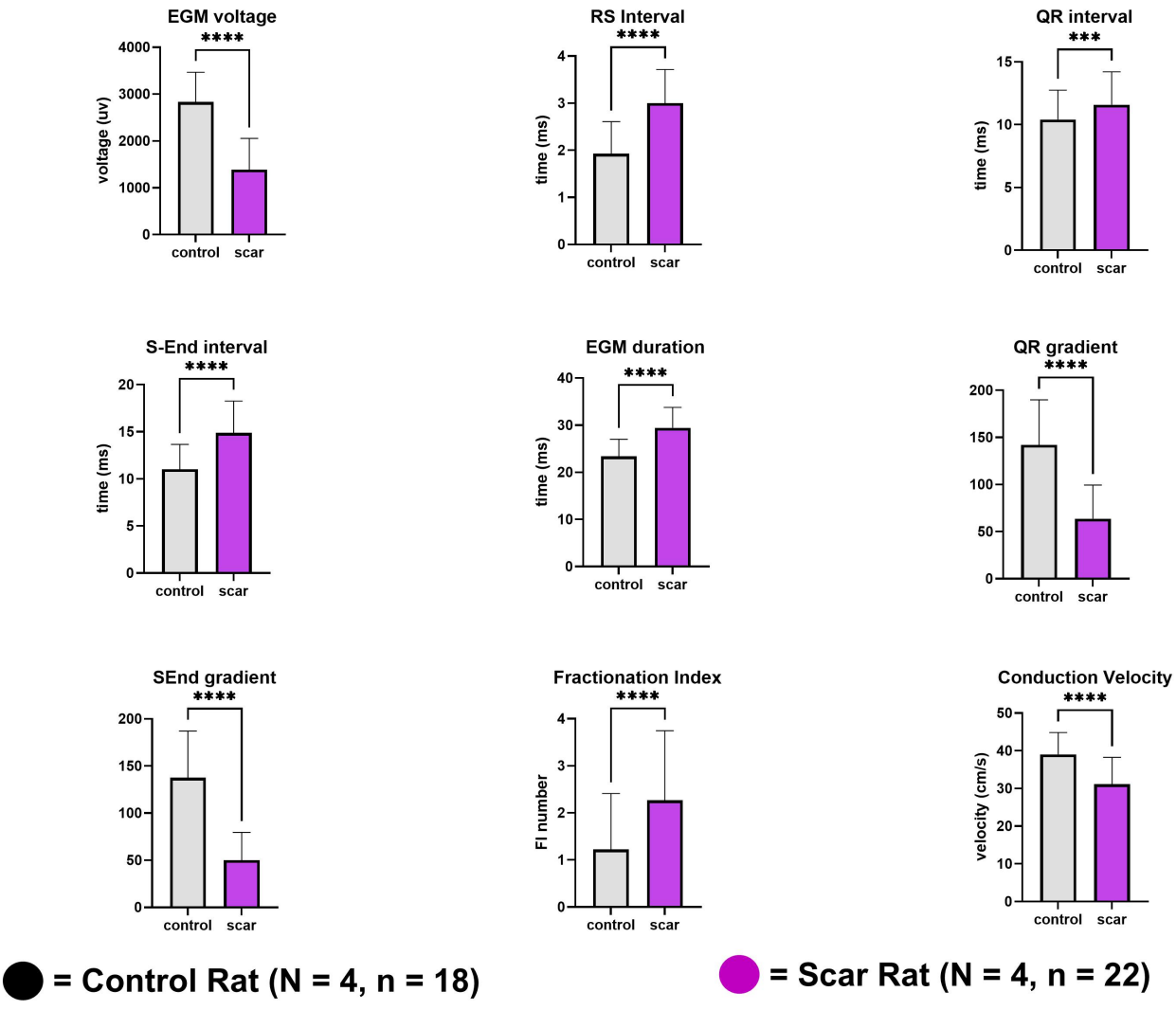


Figure 4.9: Comparison between time domain features of EGM recorded from healthy rat heart BMS and myocardial fibrosis heart BMS. Contains 9 graphs of time-domain features from BMS from scared (N=4, n=18) and control (N=4, n=22) hearts. Grey error bars represent the standard deviation. All bar charts represent mean ± S.D.; ns $0.05 < p \leq 1$, *$p \leq 0.05$, **$p \leq 0.01$, ***$p \leq 0.001$, ****$p \leq 0.0001$.

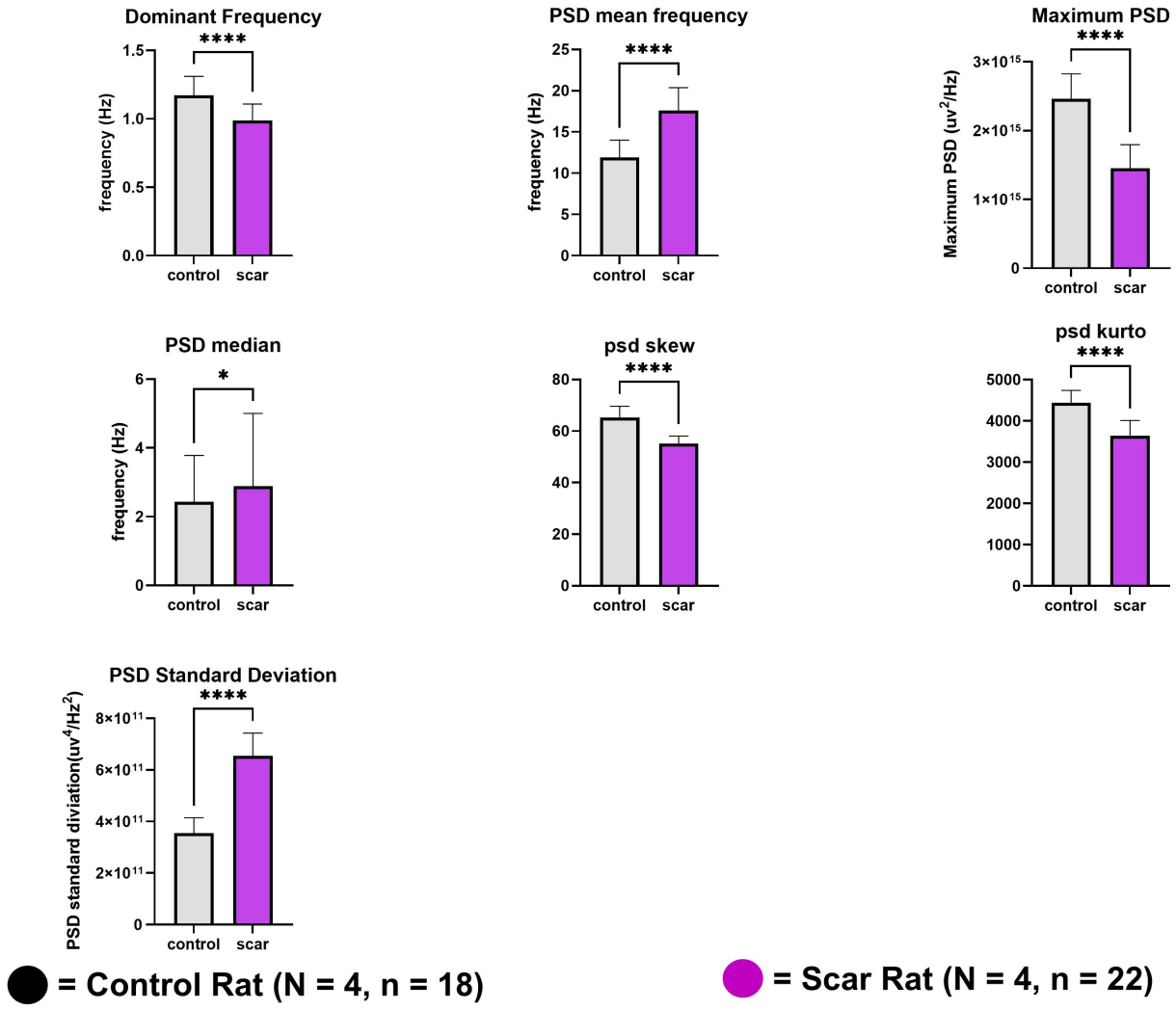


Figure 4.10: Comparison between frequency domain features of EGM recorded from healthy rat heart BMS and myocardial fibrosis heart BMS. Contains 7 graphs of frequency-domain features from BMS from scared (N=4) and control (N=4) hearts. Grey error bars represent the standard deviation. All bar charts represent mean ± S.D.; ns $0.05 < p \leq 1$, *$p \leq 0.05$, **$p \leq 0.01$, ***$p \leq 0.001$, ****$p \leq 0.0001$.

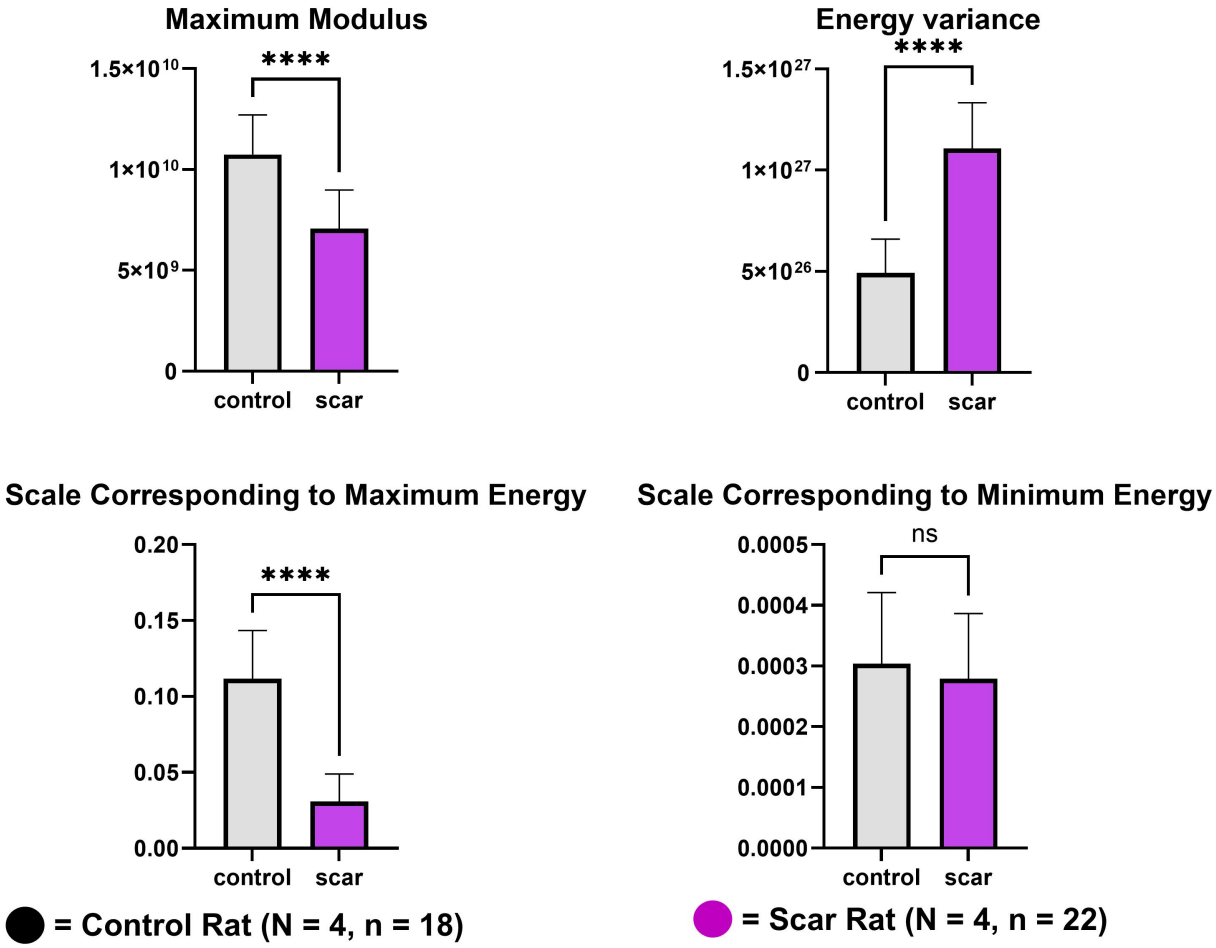


Figure 4.11: Comparison between time frequency features of EGM recorded from healthy rat heart BMS and myocardial fibrosis heart BMS. Contains 4 graphs of time frequency features from BMS from scared (N=4, n=18) and control (N=4, n=22) hearts. Grey error bars represent the standard deviation. All bar charts represent mean ± S.D.; ns $0.05 < p \leq 1$, *$p \leq 0.05$, **$p \leq 0.01$, ***$p \leq 0.001$, ****$p \leq 0.0001$.

The results show a significant linear relationship between the collagen index and 9 time domain features, which is shown in Figure 4.12. In details, Voltage: $R^2 = 0.5510$, $p \leq 0.0001$, QR interval: $R^2 = 0.04850$, $p \leq 0.0001$, RS interval: $R^2 = 0.3585$, $p \leq 0.0001$, Send point interval: $R^2 = 0.2991$, $p \leq 0.0001$, EGM Duration: $R^2 = 0.3674$, $p \leq 0.0001$, QR gradient: $R^2 = 0.4512$ $p \leq 0.0001$, Send gradient: $R^2 = 0.5156$, $p \leq 0.0001$, fractionation index: $R^2 = 0.1389$, ≤ 0.0001, conduction velocity: $R^2 = 0.3921$, ≤ 0.0001.

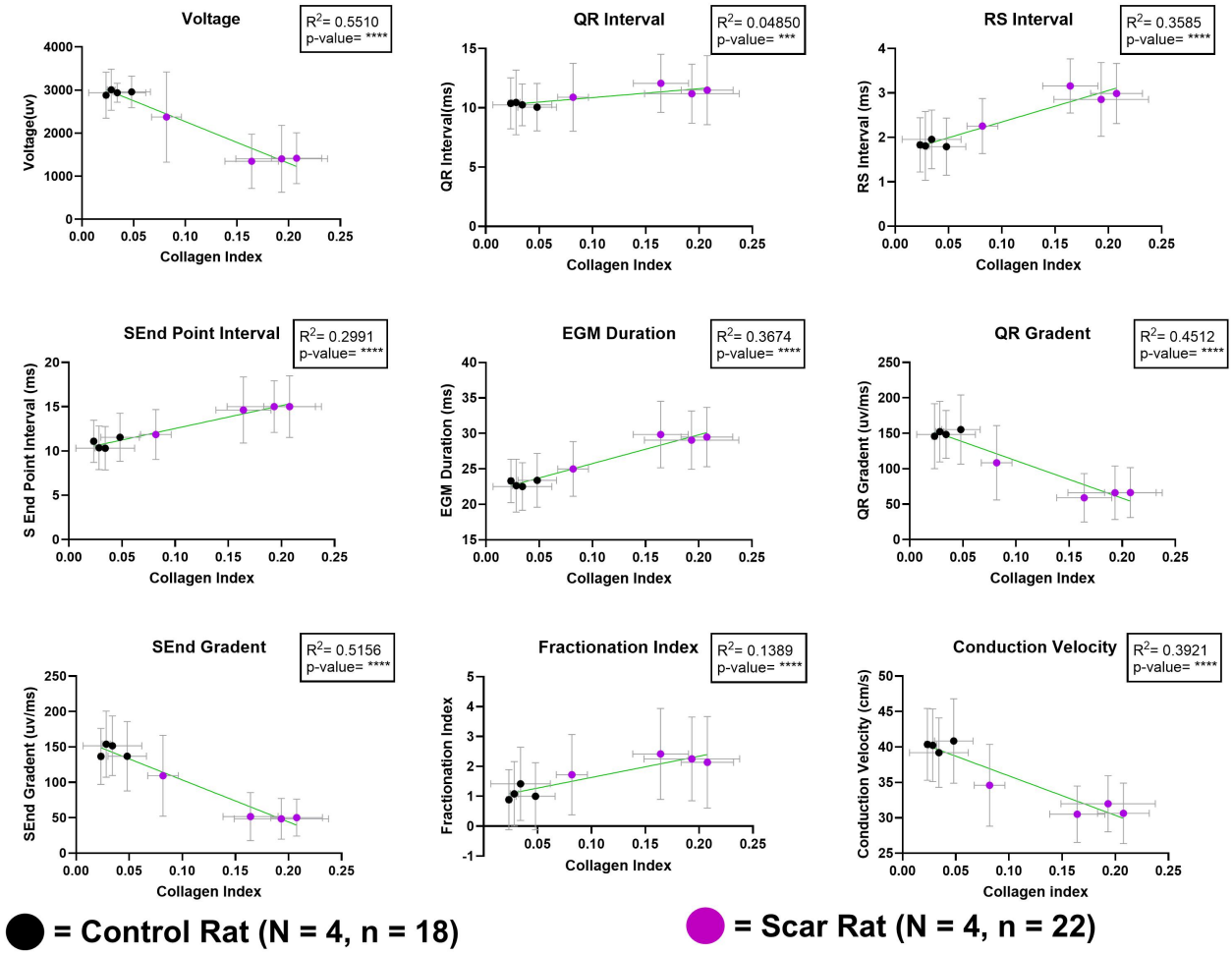


Figure 4.12: Collagen Index with relation to time domain features of the EGMs of rat heart BMS. Contains 9 graphs of time-domain features from BMS from scared (N=4, n=18) and control (N=4, n=22) hearts. The graphs show the time-domain features against the collagen expression. A simple linear regression was used to assess the significance of the correlation between the two features, the theoretical line of best fit is shown in green. Grey error bars represent the standard deviation. All bar charts represent mean ± S.D.; ns $0.05 < p \leq 1$, *p ≤ 0.05, **p ≤ 0.01, ***p ≤ 0.001, ****p ≤ 0.0001.

The frequency domain features were extracted from the same MEA recordings mentioned in the last section to investigate if there is a correlation between the collagen index and the frequency domain features. The results are shown in Figure 4.13. The result shows that all features of the frequency domain were significantly correlated with the collagen index. Domain frequency: $R^2 = 0.3306$, p ≤ 0.0001, PSD median frequency: $R^2 = 0.0213$, p $= 0.0132$, PSD mean frequency: $R^2 = 0.6088$, p ≤ 0.0001, Maximum PSD: $R^2 = 0.7443$, p ≤ 0.0001, PSD skewness: $R^2 = 0.6772$ p ≤ 0.0001, PSD kurtosis: $R^2 = 0.6358$, p ≤ 0.0001, PSD standard deviation: $R^2 = 0.9021$, p

≤ 0.0001. The R^2 value of the PSD median frequency is very low (correlation coefficient, R^2 ¡0.1) suggesting that for the PSD median frequency many data points are very off the best fit line. In addition, the p-value of the same feature is also higher than those of other features.

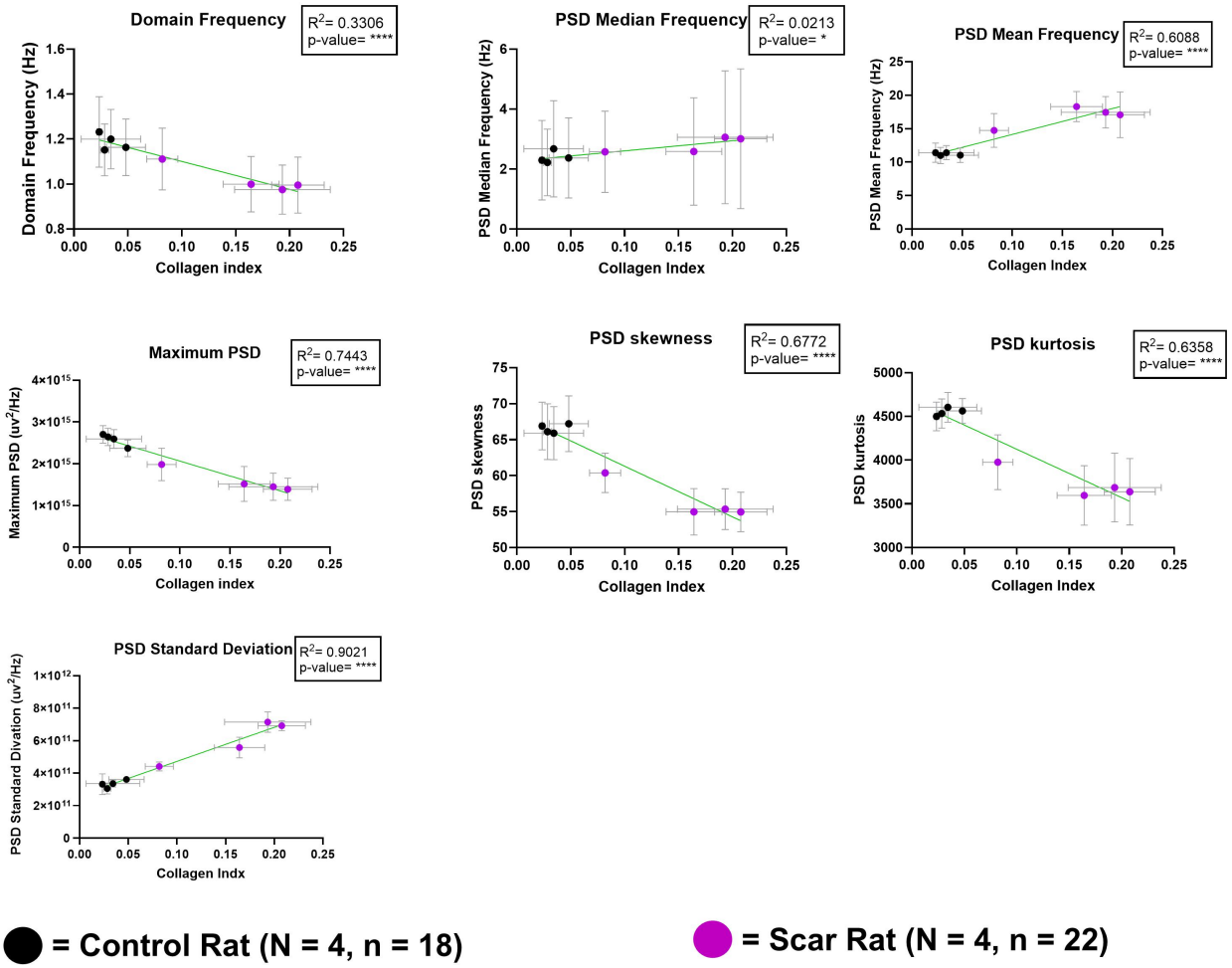


Figure 4.13: Collagen Index with relation to frequency domain features of the EGMs of rat heart BMS. Contains 7 graphs of frequency-domain features from BMS from scared (N=4, n=18) and control (N=4, n=22) hearts. The graphs show the frequency-domain features against the collagen expression. A simple linear regression was used to assess the significance of the correlation between the two features, the theoretical line of best fit is shown in green. Grey error bars represent the standard deviation. All bar charts represent mean ± S.D.; ns $0.05 < p \leq 1$, *$p \leq 0.05$, **$p \leq 0.01$, ***$p \leq 0.001$, ****$p \leq 0.0001$.

The next step was to investigate whether there is a relationship between collagen index and time-frequency features of the EGMs. The features were extracted from the same set of recordings as in the last section. The correlation is shown in Figure 4.14. The results illustrate a significant correlation between the collagen index and the time-frequency features (Maximum

modulus: $R^2 = 0.5586$, p ≤ 0.0001, Variance of signal energy: $R^2 = 0.7596$, p ≤ 0.0001, Scale corresponding to maximum energy: $R^2 = 0.7498$, p ≤ 0.0001, Scale corresponding to minimum energy: $R^2 = 0.01632$, p $= 0.032$.) Among all time-frequency domain features, scale corresponding to minimum energy has a very low R^2 value (correlation coefficient, R^2 ¡ 0.1) and the p value is relatively higher than other features.

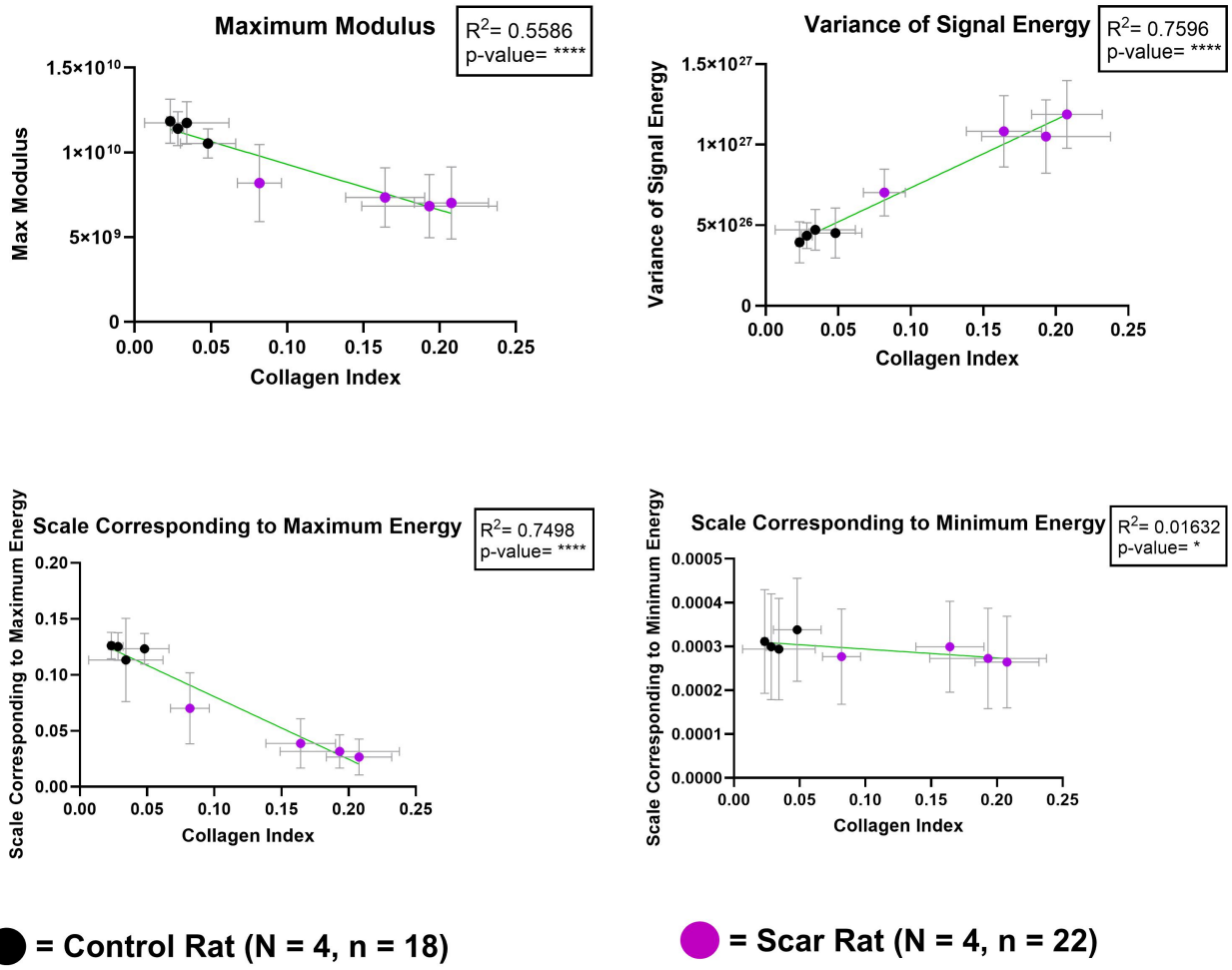


Figure 4.14: Collagen Index with relation to time frequency features features of the EGMs of rat heart BMS. Contains 4 graphs of time frequency features from BMS from scared (N=4, n=18) and control (N=4, n=22) hearts. The graphs show the time-domain features against the collagen expression. A simple linear regression was used to assess the significance of the correlation between the two features, the theoretical line of best fit is shown in green. Grey error bars represent the standard deviation. All bar charts represent mean ± S.D.; ns $0.05 <$ p ≤ 1, *p ≤ 0.05, **p ≤ 0.01, ***p ≤ 0.001, ****p ≤ 0.0001.

4.3.4 Collocation of EGM features and locations of collagen in human model

To further investigate whether the same correlation can be obtained from human hearts, the same MEA experiment, confocal imaging, and image process were carried out on slices from human failing hearts and donor hearts. Unlike rat models, patients and donors have a more complex disease history, so the number of the BMS from a LV block of one heart is not controllable and the collagen index of different BMS from the same heart could have a huge difference in numbers. Therefore, the collocation was performed at the slice level.

All features were first compared between the control group and the myocardial fibrosis group. The results are shown in Figure 4.15, Figure 4.16 and Figure 4.17 respectively. Significant differences were obtained from nine time domain, seven frequency domain and four time frequency features. There were four features in the time domain, three features in the frequency domain, and three features in the time frequency that decreased in human failing BMS. These features are as follows: EGM voltage (Donor: 3572 ± 811.3 μv, Failing: 2549 ± 859.6 μv, p $\leq$ 0.0001), QR gradient (Donor: 108.5 ± 30.53 uv/ms, Failing: 67.92 ± 28.34 uv/ms, p $\leq$ 0.0001), SEnd gradient (Donor: 82.83 ± 19.95 uv/ms, Failing: 51.71 ± 19.62 uv/ms, p $\leq$ 0.0001), conduction velocity (Donor: 32.34 ± 2.428 cm/s, Failing: 29.26 ± 3.506 cm/s, p $\leq$ 0.0001), dominant frequency (Donor: 1.483 ± 0.1602 Hz, Failing: 1.243 ± 0.1994 Hz, p $\leq$ 0.0001), maximum PSD (Donor: 6.987e+016 ± 5.639e+015 uv^2/Hz, Failing: 4.020e+016 ± 1.226e+016 uv^2/Hz, p $\leq$ 0.0001), PSD skewness (Donor: 70.45 ± 4.967, Failing: 58.75 ± 10.77, p $\leq$ 0.0001), PSD kurtosis (Donor: 5260 ± 210.3, Failing: 4691 ± 414.7, p $\leq$ 0.0001), maximum modulus (Donor: 2.07e+010 ± 2.67e+09, Failing: 1.36e+010 ± 4.99e+09, p $\leq$ 0.0001) and scale corresponding to maximum energy (Donor: 3819 ± 635.4, Failing: 2540 ± 1258, p $\leq$ 0.0001). Increases were obtained from the remaining features, which are RS interval (Donor: 4.024 ± 0.6744 ms, Failing: 4.373 ± 0.6506 ms, p $\leq$ 0.0001), QR interval (Donor: 16.91 ± 2.616 ms, Failing: 19.31 ± 2.295 ms, p $\leq$ 0.0001), SEnd interval (Donor: 21.71 ± 1.832 ms, Failing: 23.99 ± 2.807 ms, p $\leq$ 0.0001), EGM duration (Donor: 42.65 ± 3.408 ms, Failing: 47.67 ± 4.034 ms, p $\leq$ 0.0001), fractionation index (Donor: 1.028 ± 1.174, Failing: 2.083 ± 1.377, p $\leq$ 0.0001), PSD mean

frequency (Donor: 15.31 ± 2.494 Hz, Failing: 19.30 ± 4.965 Hz, p ≤ 0.0001), PSD median (Donor: 1.711 ± 0.0755 Hz, Failing: 1.765 ± 0.0883 Hz, p ≤ 0.0001), PSD standard deviation (Donor: 1.53e+013 ± 5.644e+012 uv^2/Hz^2, Failing: 5.583e+012 ± 2.102e+012 uv^2/Hz^2, p ≤ 0.0001), Shannon entropy (Donor: 5.758 ± 0.05534, Failing: 5.813 ± 0.06333, p ≤ 0.00027), energy variance (Donor: 2.901e+027 ± 5.519e+026, Failing: 5.192e+027 ± 1.660e+027, p ≤ 0.0001) and scale corresponding to minimum energy (Donor: 2.863 ± 0.8033, Failing: 3.129 ± 0.7485, p = 0.00064).

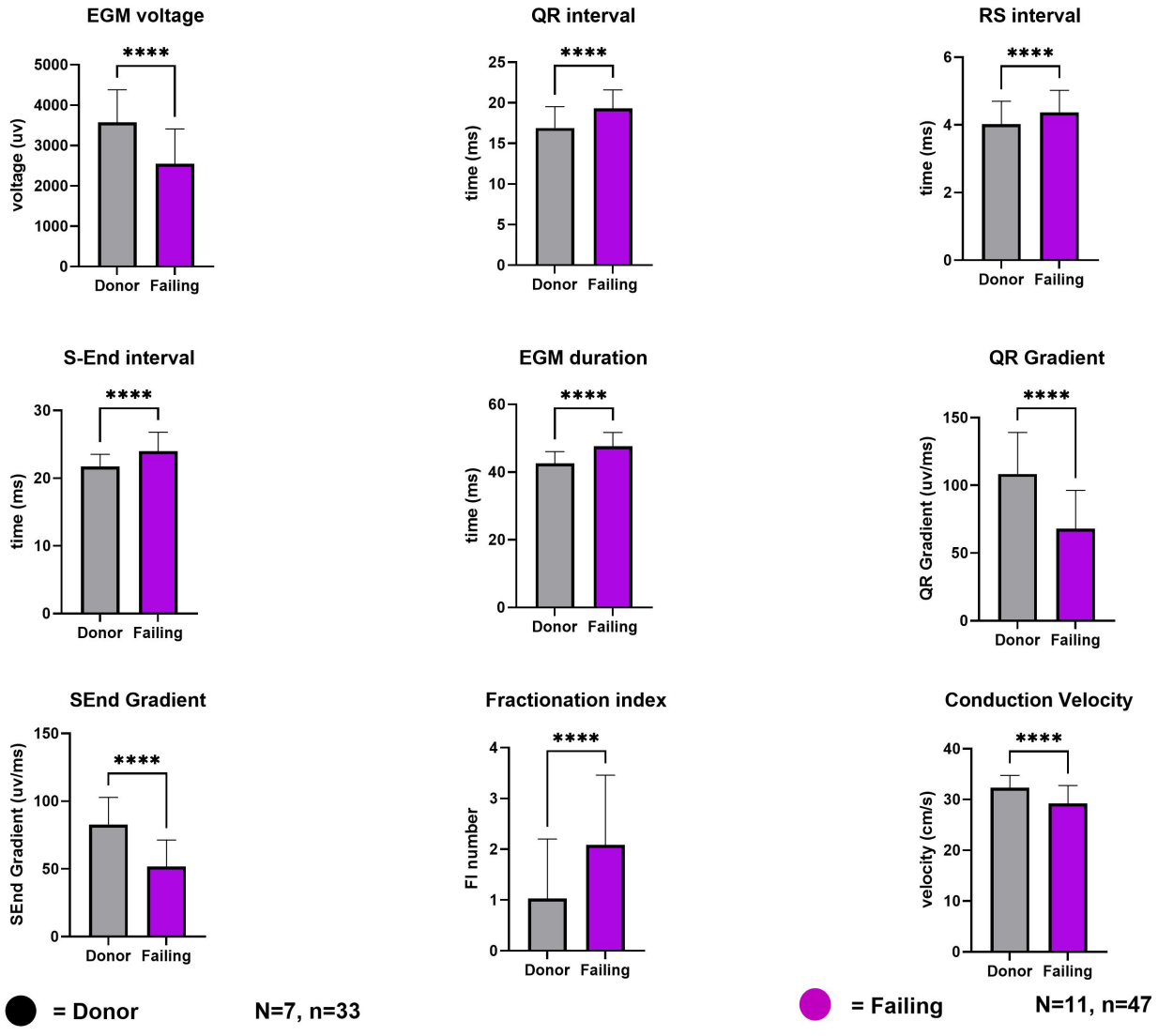


Figure 4.15: Comparison between time domain features of EGM recorded from human donor BMS and human failing BMS. Contains 9 graphs of time-domain features from BMS (33+47) from human donor (N=9) and human failing (N=11) hearts. Grey error bars represent the standard deviation. All bar charts represent mean ± S.D.; ns $0.05 < p \leq 1$, *$p \leq 0.05$, **$p \leq 0.01$, ***$p \leq 0.001$, ****$p \leq 0.0001$.

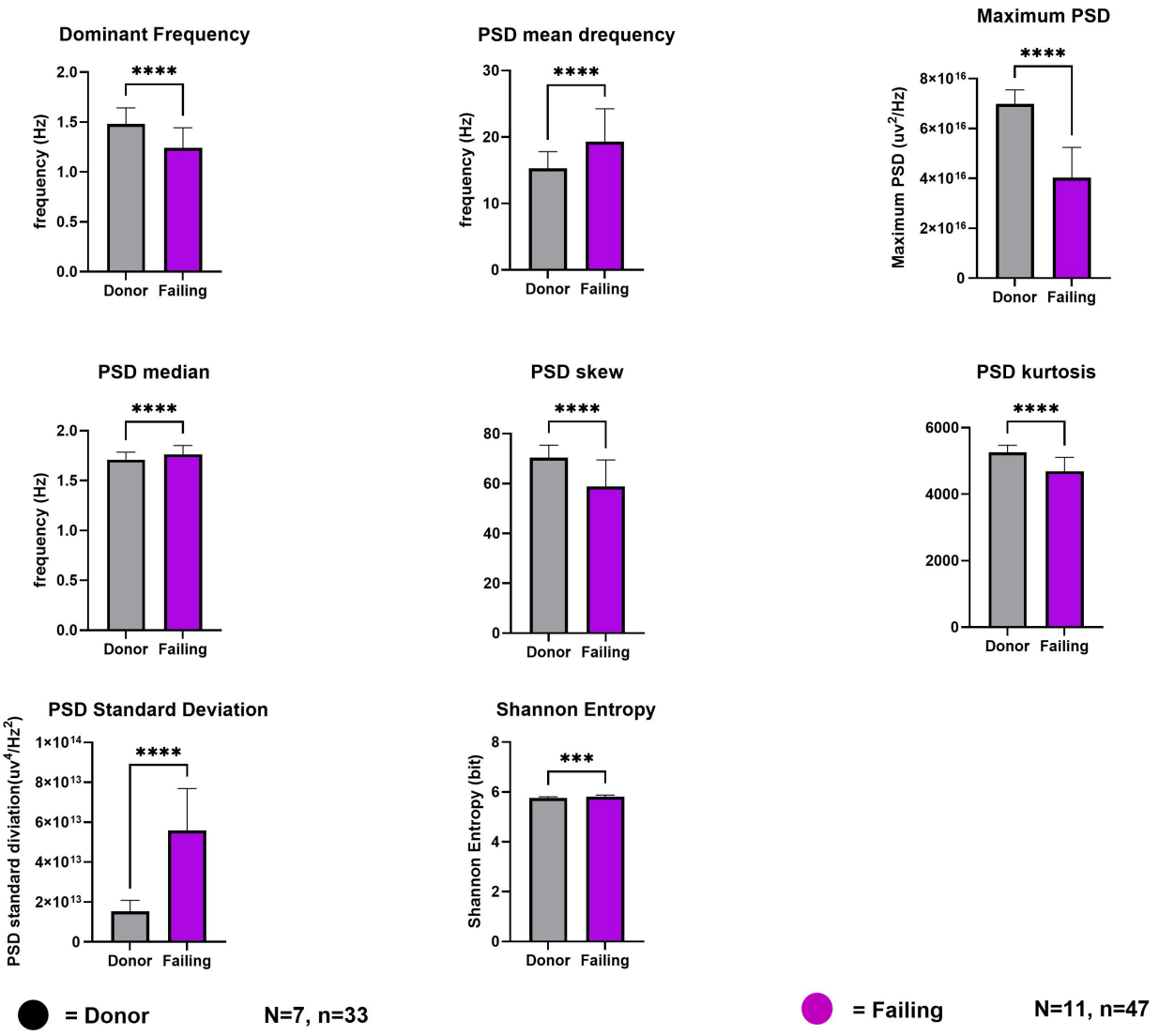


Figure 4.16: Comparison between frequency domain features and Shannon entropy of EGM recorded from human donor BMS and human failing BMS. Contains 7 graphs of frequency-domain features and 1 graph of Shannon entropy from BMS (33+47) from human donor (N=9) and human failing (N=11) hearts. Grey error bars represent the standard deviation. All bar charts represent mean ± S.D.; ns $0.05 < p \leq 1$, *$p \leq 0.05$, **$p \leq 0.01$, ***$p \leq 0.001$, ****$p \leq 0.0001$.

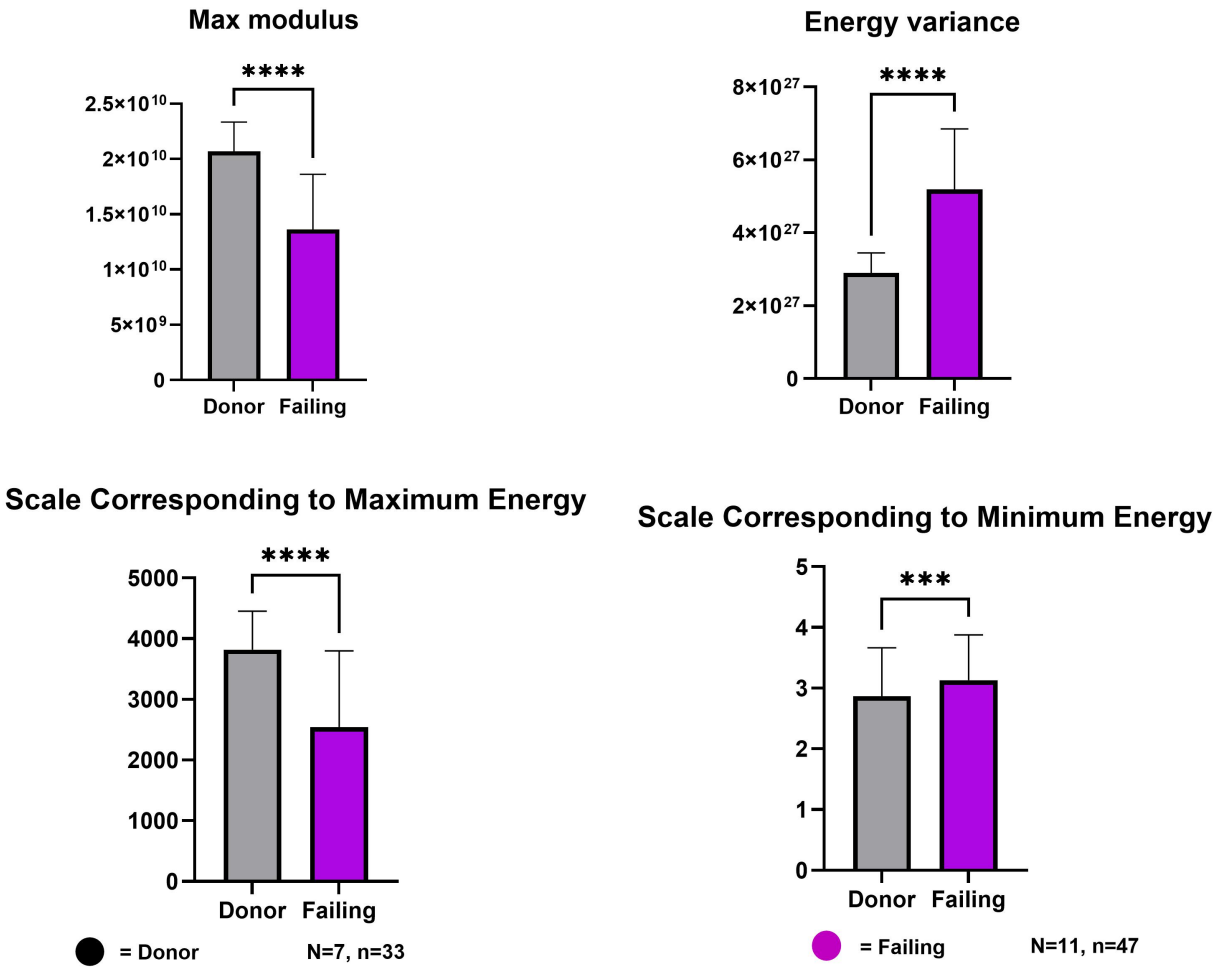


Figure 4.17: Comparison between time frequency features of EGM recorded from human donor BMS and human failing BMS. Contains 4 graphs of time frequency features from BMS (33+47) from human donor (N=9) and human failing (N=11) hearts. Grey error bars represent the standard deviation. All bar charts represent mean ± S.D.; ns $0.05 < p \leq 1$, *$p \leq 0.05$, **$p \leq 0.01$, ***$p \leq 0.001$, ****$p \leq 0.0001$.

The correlations are shown in Figure 4.18, Figure 4.19 and Figure 4.20 respectively. The results show a significant linear relationship between the collagen index and 21 features extracted from the EGM. Voltage: $R^2 = 0.06998$, $p \leq 0.0001$, QR interval: $R^2 = 0.1135$, $p \leq 0.0001$, RS interval: $R^2 = 0.003989$, $p = 0.002$, QS interval: $R^2 = 0.09597$, $p \leq 0.0001$, Send point interval: $R^2 = 0.04481$, $p \leq 0.0001$, EGM Duration: $R^2 = 0.08344$, $p \leq 0.0001$, QR gradient: $R^2 = 0.1371$ $p \leq 0.0001$, Send gradient:$R^2 = 0.09691$ $p \leq 0.0001$, fractionation index: $R^2 = 0.08990$, ≤ 0.0001, conduction velocity: $R^2 = 0.04974$, ≤ 0.0001, Domain frequency: $R^2 = 0.3306$, $p \leq 0.0001$, PSD median frequency: $R^2 = 0.08379$, $p \leq 0.0001$, PSD mean frequency: $R^2 = 0.05282$, $p \leq 0.0001$, Maximum PSD: $R^2 = 0.1761$, $p \leq 0.0001$, PSD skewness: $R^2 =$

0.02198 p $\leq$ 0.0001, PSD kurtosis: $R^2 = 0.04978$, p $\leq$ 0.0001, PSD standard deviation: $R^2 = 0.1415$, p $\leq$ 0.0001, Shannon entropy: $R^2 = 0.03677$, p = 0.00038, Maximum modulus: $R^2 = 0.1487$, p $\leq$ 0.0001, Variance of signal energy: $R^2 = 0.06458$, p $\leq$ 0.0001, Scale corresponding to maximum energy: $R^2 = 0.01317$, p $\leq$ 0.0001. There are two features that have no significant linear relationship with CIs, R width to EGM duration ratio: $R^2 = 0.0007709$, p = 0.1739, Scale corresponding to minimum energy: $R^2 = 0.0007248$, p = 0.1874. All the R^2 values of the linear regression for all features were lower than those of the corresponding rat models.

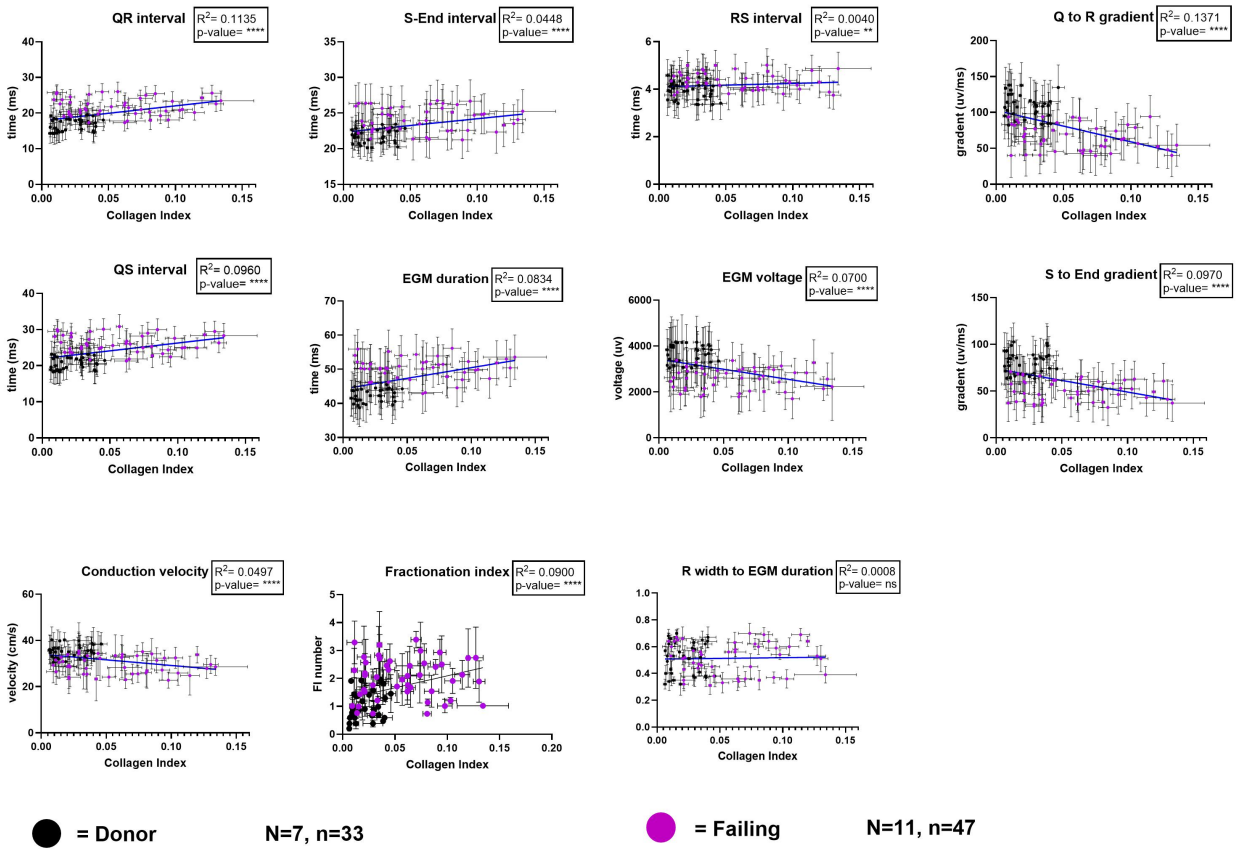


Figure 4.18: Collagen Index with relation to time domain features of the EGMs of human BMS. Contains 12 graphs of time-domain features from left ventricle slices from human donor BMS (N=7, n=33) and human failing BMS (N=11, n=47). The graphs show the time-domain features against the collagen expression. A simple linear regression was used to assess the significance of the correlation between the two features, the theoretical line of best fit is shown in blue. Grey error bars represent the standard deviation. All bar charts represent mean $\pm$ S.D.; ns 0.05 < p $\leq$ 1, *p $\leq$ 0.05, **p $\leq$ 0.01, ***p $\leq$ 0.001, ****p $\leq$ 0.0001.

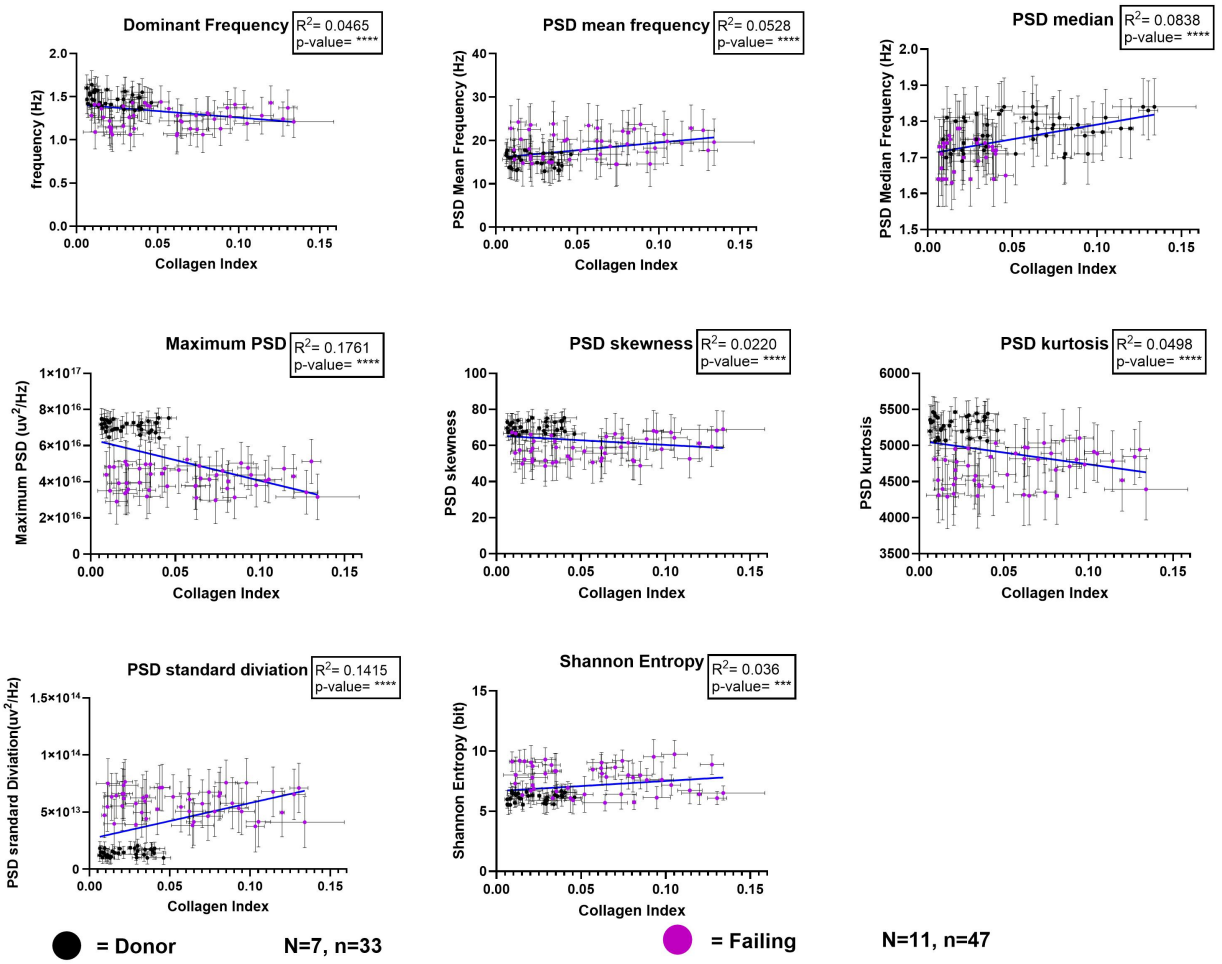


Figure 4.19: Collagen Index with relation to frequency domain features and Shannon entropy of the EGMs of human heart BMS. Contains 7 graphs of frequency-domain features and 1 graph of Shannon entropy from human donor BMS (N=7, n=33) and human failing BMS (N=11, n=47). The graphs show the frequency-domain features and Shannon entropy against the collagen expression. A simple linear regression was used to assess the significance of the correlation between the two features, the theoretical line of best fit is shown in blue. Grey error bars represent the standard deviation. All bar charts represent mean ± S.D.; ns $0.05 < p \leq 1$, *$p \leq 0.05$, **$p \leq 0.01$, ***$p \leq 0.001$, ****$p \leq 0.0001$.

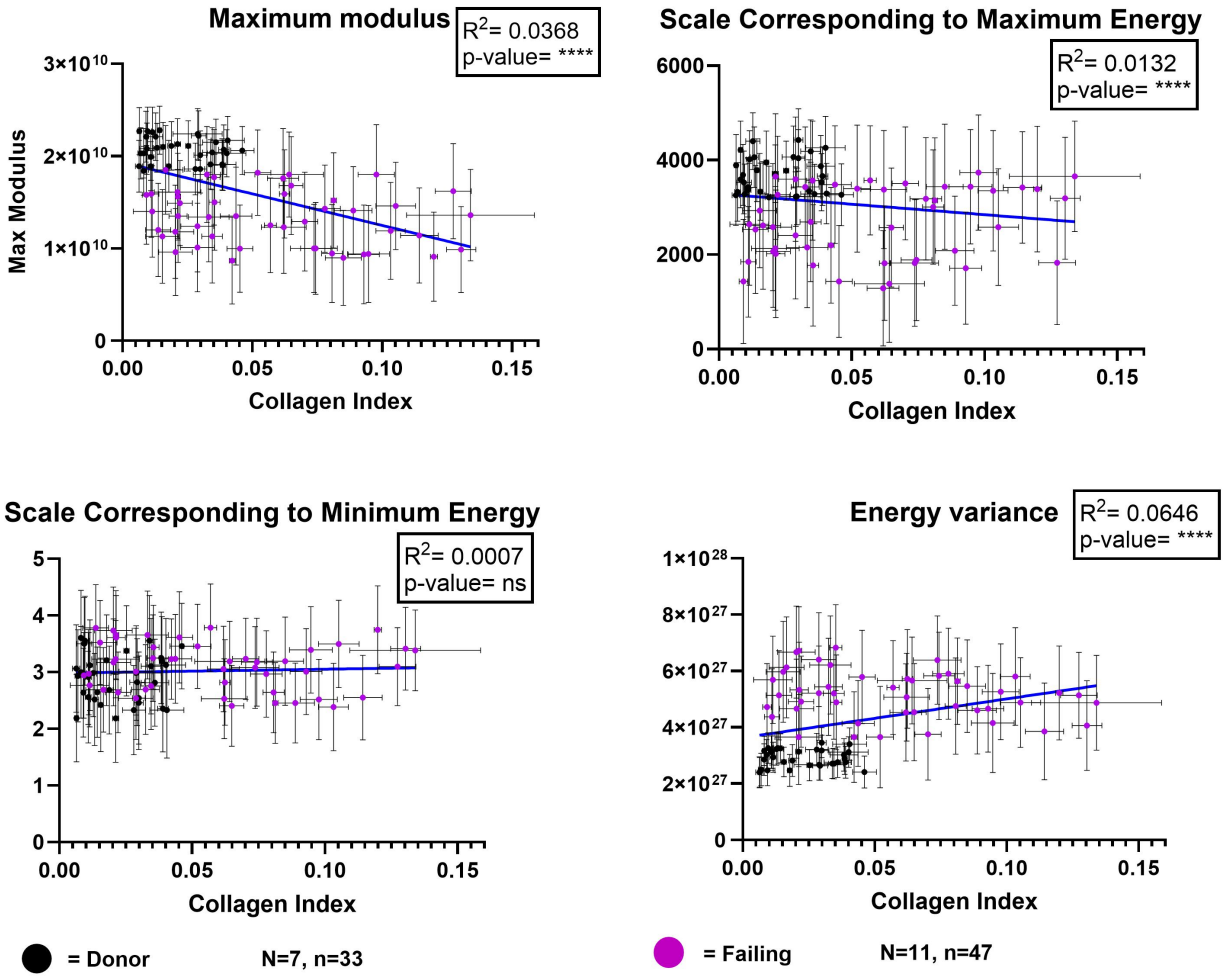


Figure 4.20: Collagen Index with relation to time frequency features of the EGMs of human heart BMS. Contains 4 graphs of time frequency features from human donor BMS (N=7, n=33) and human failing BMS (N=11, n=47). The graphs show the time frequency features against the collagen expression. A simple linear regression was used to assess the significance of the correlation between the two features, the theoretical line of best fit is shown in blue. Grey error bars represent the standard deviation. All bar charts represent mean ± S.D.; ns $0.05 < p \leq 1$, *$p \leq 0.05$, **$p \leq 0.01$, ***$p \leq 0.001$, ****$p \leq 0.0001$.

The type of heart was found to exert a significant influence on specific features, including frequency domain features (maximum PSD, PSD skewness, PSD kurtosis, and PSD standard deviation) as well as time–frequency features (maximum modulus and energy variance). Such influences adversely affected the correlations between the collagen index and these features. To mitigate this confounding effect, donor hearts and failing hearts were analysed separately. The results are shown in figure 4.21, figure 4.22, figure 4.23 and figure 4.24 respectively. The results show that significant linear relationship was obtained from several features (donor:

PSD skewness: $R^2 = 0.004$ p = 0.0407, PSD standard diviation: $R^2 = 0.008$ p = 0.0031 and maximum modulus: $R^2 = 0.0003$ p = 0.0217; failing: PSD skewness: $R^2 = 0.026$ p ≤ 0.0001, PSD kurtosis: $R^2 = 0.024$ p ≤ 0.0001, maximum modulus: $R^2 = 0.012$ p ≤ 0.0001, Energy variance: $R^2 = 0.024$ p ≤ 0.0001.).

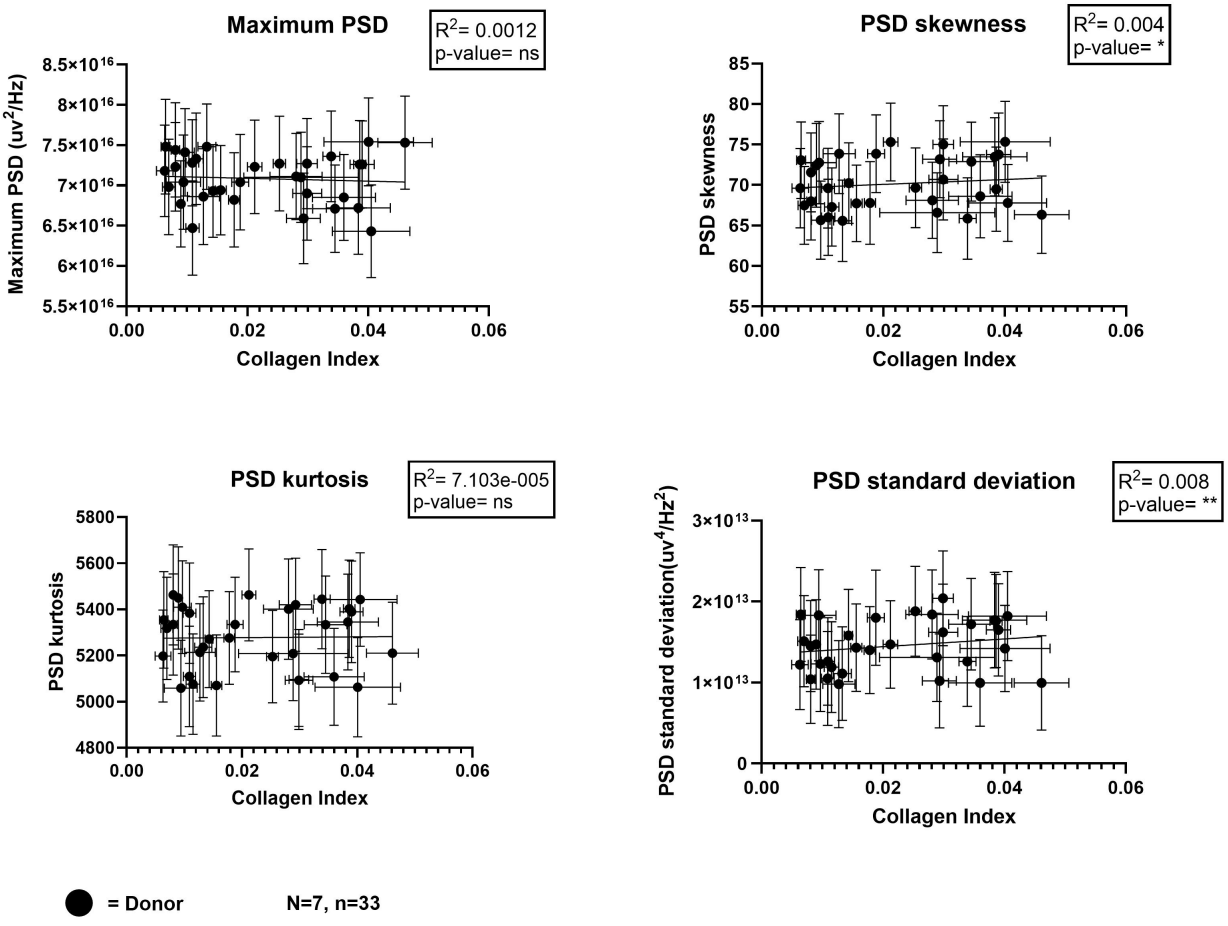


Figure 4.21: Collagen Index with relation to frequency domain features of the EGMs of human donor heart BMS. Contains 4 graphs of frequency domain features from left ventricle slices from human donor BMS (N=7, n=33). The graphs show thefrequency domain features against the collagen expression. A simple linear regression was used to assess the significance of the correlation between the two features, the theoretical line of best fit is shown in blue. Grey error bars represent the standard deviation. All bar charts represent mean ± S.D.; ns $0.05 <$ p ≤ 1, *p ≤ 0.05, **p ≤ 0.01, ***p ≤ 0.001, ****p ≤ 0.0001.

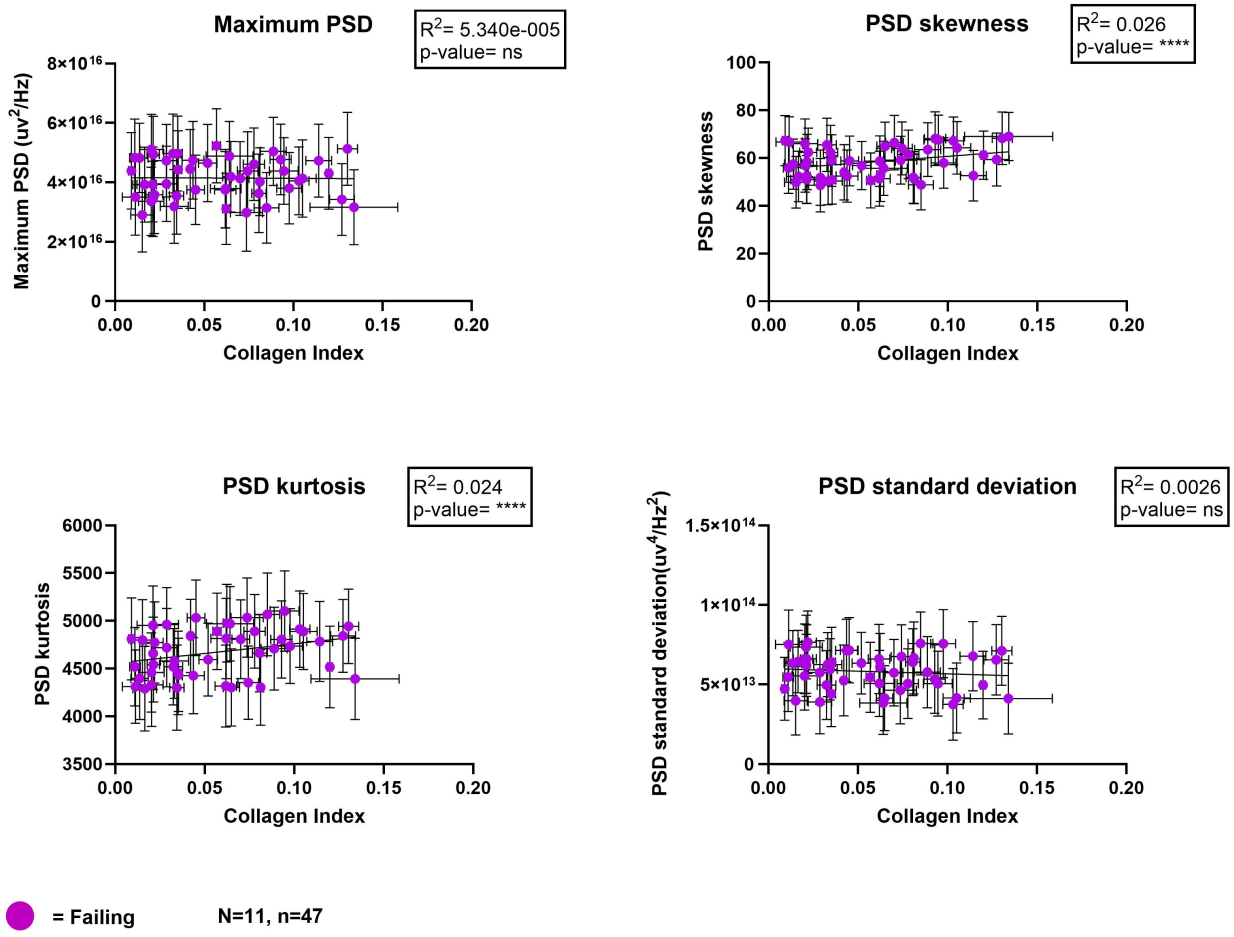


Figure 4.22: Collagen Index with relation to frequency domain features of the EGMs of human failing heart BMS. Contains 4 graphs of frequency-domain features from human failing BMS (N=11, n=47). The graphs show the frequency domain features against the collagen expression. A simple linear regression was used to assess the significance of the correlation between the two features, the theoretical line of best fit is shown in blue. Grey error bars represent the standard deviation. All bar charts represent mean ± S.D.; ns $0.05 < p \leq 1$, *$p \leq 0.05$, **$p \leq 0.01$, ***$p \leq 0.001$, ****$p \leq 0.0001$.

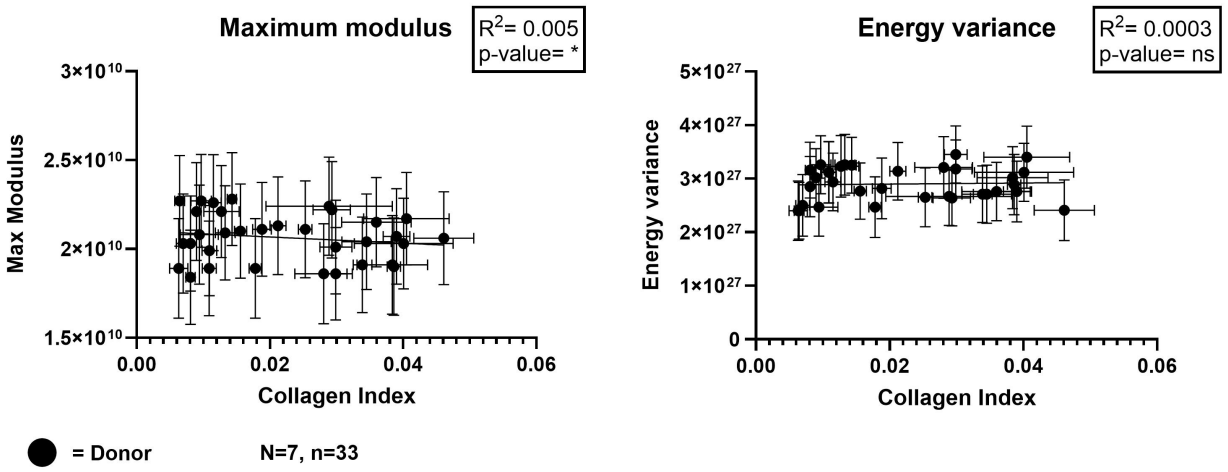


Figure 4.23: Collagen Index with relation to time frequency features of the EGMs of human donor heart BMS. Contains 2 graphs of time frequency features from human donor BMS (N=7, n=33). The graphs show the time frequency features against the collagen expression. A simple linear regression was used to assess the significance of the correlation between the two features, the theoretical line of best fit is shown in blue. Grey error bars represent the standard deviation. All bar charts represent mean ± S.D.; ns $0.05 < p \leq 1$, *$p \leq 0.05$, **$p \leq 0.01$, ***$p \leq 0.001$, ****$p \leq 0.0001$.

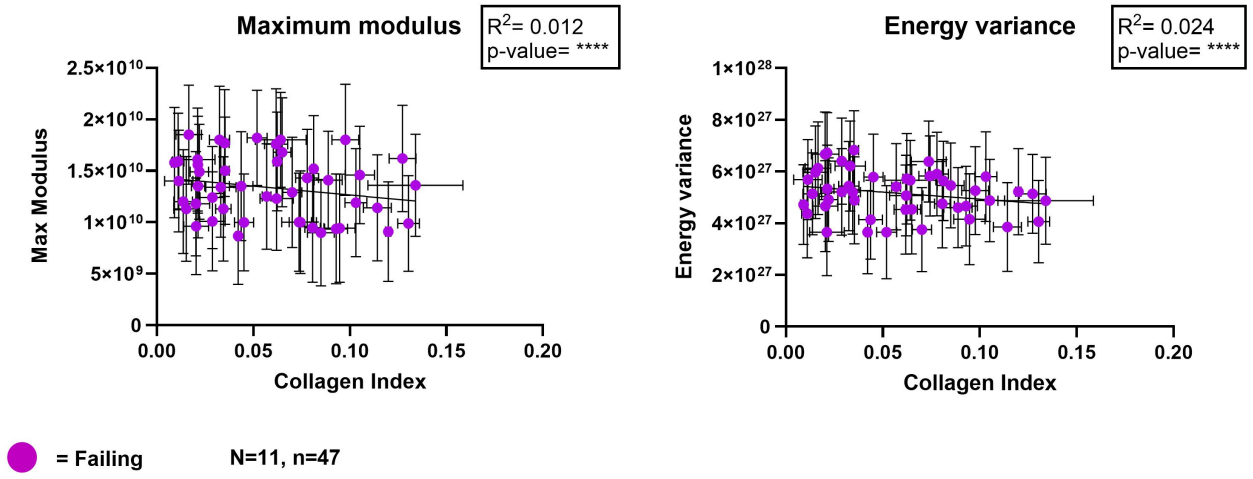


Figure 4.24: Collagen Index with relation to time frequency features of the EGMs of human failing heart BMS. Contains 2 graphs of time frequency features from human failing BMS (N=11, n=47). The graphs show the time frequency features against the collagen expression. A simple linear regression was used to assess the significance of the correlation between the two features, the theoretical line of best fit is shown in blue. Grey error bars represent the standard deviation. All bar charts represent mean ± S.D.; ns $0.05 < p \leq 1$, *$p \leq 0.05$, **$p \leq 0.01$, ***$p \leq 0.001$, ****$p \leq 0.0001$.

More EGMs were recorded from human models than from rat models, and the collagen distribution of the BMS prepared from the same human heart was different, which provides a

sufficient number of EGM and CI to achieve collocation at the electrode level.

Electrode-level collocations were performed on two features: EGM voltage and EGM duration. The results are shown in Figure 4.25. The R^2 value increases when change the collocation level from slices to electrodes.

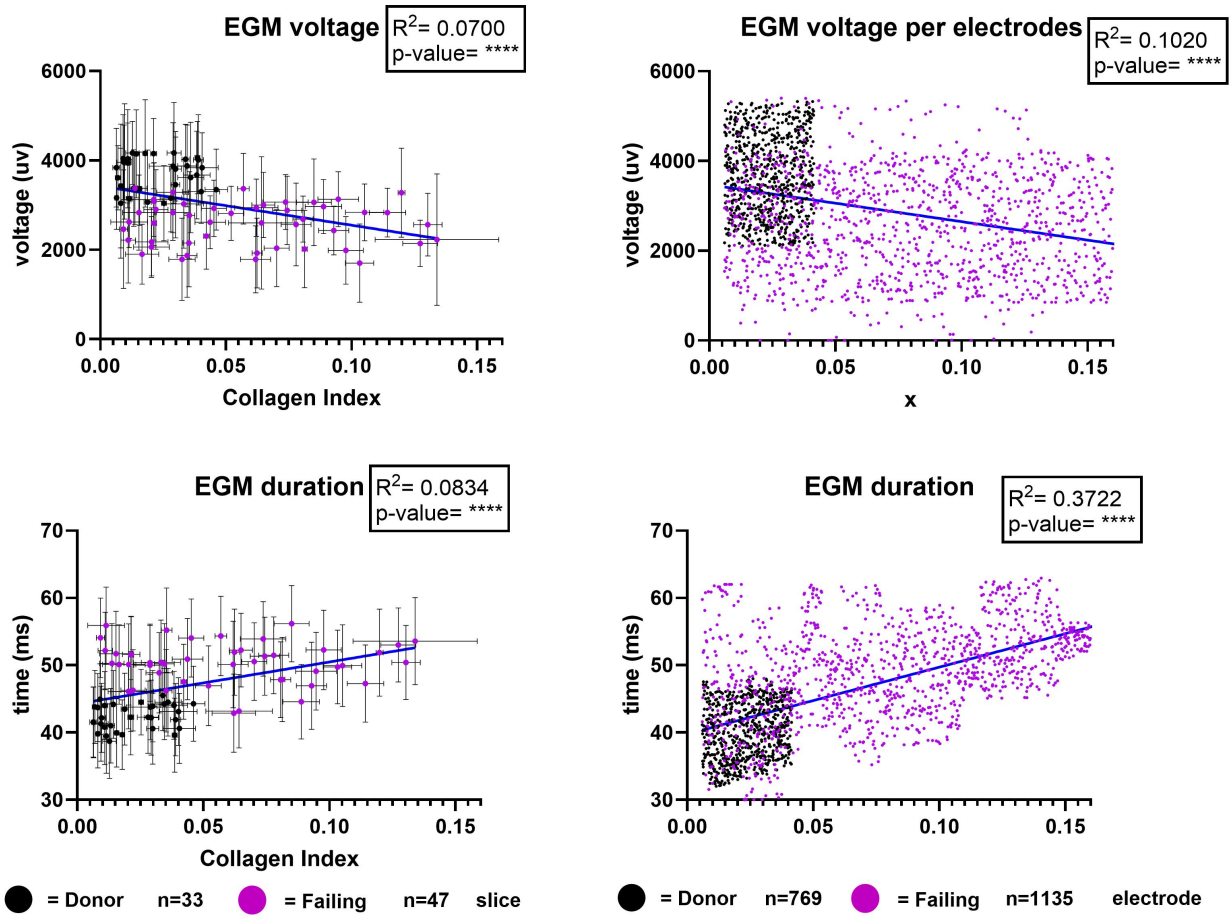


Figure 4.25: Comparison between electrode level and slice level collocations, 33 BMS and 769 electrodes were selected from human donor hearts; 47 BMS and 1135 electrodes were selected from human failing hearts. A simple linear regression was used to assess the significance of the correlation between the two features, the theoretical line of best fit is shown in blue.Grey error bars represent the standard deviation. All bar charts represent mean ± S.D.; ns $0.05 < p \leq 1$, *$p \leq 0.05$, **$p \leq 0.01$, ***$p \leq 0.001$, ****$p \leq 0.0001$.

4.4 Discussion

4.4.1 Collagen index

In this study a novel analysis method to quantify the amount of collagen in the extracellular matrix using a combination of second harmonic generation microscopy and image analysis is described. Using an established microscopy technique[133] that allows the presence of extracellular collagen to be detected, the collagen was then accurately quantified and also colocalised with the recording electrodes.

There was a statistically significant difference in the amount of collagen detected by this method between both the healthy and myocardial fibrosis models, as well as between the human donor and the failing hearts. The CI increased in concordance with the amount of expected fibrosis in the slices.

Although other methods for imaging collagen are available[134], SHG microscopy is the only modality that can accurately image clusters of collagen I, while also allowing adequate tissue section thickness for a meaningful analysis of the electrophysiological properties of the tissue on MEA plates. This is crucial for drawing direct correlations with clinical electrophysiological findings from the results. Tissue staining would require further sectioning into thinner slices, which would alter the overall shape of the slice and make it impossible for fiducial points to be used for accurate electrode/tissue colocalisation. Mueller matrix polarimetric imaging has been shown to accurately quantify and score fibrillar collagen[135]. However, the slice thickness in the experiments of this study would be likely to introduce increased light scattering and depolarisation artefacts which, in combination with the size of the micro electrodes, would not allow for accurate collagen quantification[136].

4.4.2 BDM limitations

2,3-Butanedione monoxime (BDM) has historically been used in cardiac electrophysiology experiments as a means of reducing motion artefacts by suppressing myocardial contraction. Its

application has been particularly common in optical mapping and whole-heart preparations where contractile activity interferes with stable recordings. While effective as a mechanical uncoupler, BDM possesses a number of significant limitations that arise from its non-specific pharmacological actions.

Although BDM inhibits actomyosin cross-bridge cycling, it also directly alters electrophysiological processes by modulating ionic currents. It has been reported to depress the fast sodium current (INa), thereby reducing action potential amplitude and upstroke velocity[137]. In addition, BDM suppresses the L-type calcium current (ICa,L) and outward potassium currents, leading to concentration-dependent changes in action potential duration[138, 139]. Such effects make it difficult to distinguish between experimental findings that reflect native physiology and those attributable to BDM-induced current inhibition.

BDM also interferes with intracellular calcium handling. In addition to reducing myofilament activation, it decreases calcium transient amplitude, impairs sarcoplasmic reticulum calcium release, and alters reuptake kinetics[138]. These disturbances confound studies of excitation–contraction coupling and arrhythmogenesis, since both contraction and electrophysiological outcomes are affected simultaneously.

Furthermore, BDM can modify arrhythmia mechanisms in unpredictable ways. Its suppression of INa slows conduction and may mimic pathological conduction slowing, while its inhibition of calcium entry reduces the likelihood of calcium-dependent afterdepolarisations[140]. This dual action means that arrhythmia initiation or suppression observed under BDM cannot reliably be extrapolated to physiological conditions. The variability of its effects across concentrations and preparations further limits reproducibility and complicates comparisons between studies.

For these reasons, BDM has increasingly been replaced by more selective electromechanical uncouplers, most notably blebbistatin, which inhibits myosin II ATPase without significantly affecting ionic currents or action potential morphology[141]. While BDM remains effective at preventing motion artefacts, its broad off-target effects render it a suboptimal tool for experiments designed to study native cardiac electrophysiological properties.

4.4.3 The effects of collagen on EGM features

MEA experiment and further data processing were carried out to study whether there are relationships between some other features of EGMs and collagen expression. The pertinent and the most important new finding of this study is that 9 time domain features, 7 frequency domain features, shannon entropy and 4 time-frequency features of the EGMs of the BMS have high correlation with their collagen expressions. The same correlations have been observed from most of the features of the EGMs recorded from BMS from both the rat models and human hearts.

The results of this chapter demonstrate the profound influence of structural remodelling on EGM morphology. Alterations such as fibre disarray, tissue discontinuities, and microstructural heterogeneities were shown to produce characteristic changes, including fractionation, broadening of EGM complexes, and slowed conduction signatures. These findings are significant because they provide direct mechanistic evidence linking microstructural changes to surface-recorded EGM abnormalities, thereby supporting the use of EGM analysis as a non-invasive marker of structural disease.

These observations are in close agreement with classical work by Spach, who showed that anisotropic conduction and tissue discontinuities are major determinants of conduction slowing and fractionated EGM[142, 143]. However, much of the existing literature has focused either on histological correlations or on in vivo patient EGM, where numerous confounding factors complicate interpretation. By utilising a controlled model, this work isolates the effects of structure per se on EGM morphology, providing a clearer causal relationship than has previously been reported.

In details, the EGM peak to peak amplitude, QR gradient, SEnd gradient, and the conduction velocity decrease with the increase of the CI. On the other hand, the QR interval, RS interval, SEnd point interval, EGM duration and fractionation index increase with the increase of the CI. Such correlations show that collagen makes the BMS less active on the time scale and the entire EGM process is elongated on the slice scale. More fractionated EGMs are obtained from

the BMS with more collagen on them.

As for the frequency domain features, dominant frequency, maximum PSD, PSD skewness and PSD Kurtosis decrease rapidly with the increase of the collagen index. PSD median frequency, PSD mean frequency slightly increase with the increase of the CI and PSD standard deviation significantly increase with the increase of the increase of the collagen index. These relationships illustrate that the frequency with maximum energy density is low, and also the energy density is distributed in a larger frequency range. In frequency domain, the degree of dispersion of energy density is high if the CI is high.

It was also found that maximum modulus, scale corresponding to maximum energy decrease with the increase of the CI, variance of signal energy increase with the increase of the CI. These trends match the frequency domain features that EGMs contain less energy if the slices contain more collagen, and the degree of energy dispersion is high. The Shannon entropy increases slightly with the increase of CI, which means that the average rate at which information is produced increases. Unlike the Shannon entropy of the ECG, the Shannon entropy of the EGM recorded from the BMS does not have a significant change, which could be due to the fact that the EGM is caused by the stimulation.

As for scale corresponding to minimum energy, different trends are obtained from rat models and human models. Scale corresponding to minimum energy of the EGMs recorded from rat models slightly decreases with the increase of the CI and for the EGMs recorded from human BMS, it slightly increases with the increase of the CI. Such difference could mean that the CI do not have strong relationship with scale corresponding to minimum energy, this feature may not be able to be used to verify the collagen expression and the development of cardiac disease.

Although there is statistical significance for each individual feature, a single feature value represents a wide range of collagen index. In that case, the collagen index can not be accurately predicted with only few features. Therefore, increasing the number of features of the EGMs that need to be analysed and combining them together could be a method to accurately predict the microscopic collagen in clinical practice.

4.4.4 Differences between rat models and human models

It was noticed that the R^2 values of the correlations between EGM features from rat BMS is higher that them from human heart BMS. This could be due to the fact that unlike the rat models, donors and patients have more complex cardiac disease histories and there are differences in gender and age etc. These uncontrollable variables may influence the functions of the heart and further influence the EGM features. In addition, there was no significant change in the collagen index in the BMS taken from the same rat left ventricles, but the collagen index could change a lot even if the BMS are from the same block from human left ventricle, bringing more uncontrollable factors in research with human left ventricle. Furthermore, some functional changes such as gap junction remodelling, ion channel remodelling may also have impact on the EGM features. How these changes are in relation to the collagen and their alignment with the EGM features will be studied in the next chapter.

In addition, the CI was calculated for each electrode, allowing the user to analyse the relationship between the EGM features and the CI at the electrode level. But such analysis requires a large amount of data and analysis time, a more detailed method is also needed.

4.5 Limitations

Even the CI detection code was validated, the manual labelling step in the image processing caused errors to the image registration. In addition, there were some differences between the microscopic image of the BMS and the picture of the BMS on the MEA dish, although the BMS was fixed immediately after the MEA experiment. These errors resulted in the electrode positioning not being 100% accurate. These inaccuracies were eventually reflected in the error of the CI.

For now, the collagen across the whole thickness of the BMS was imaged and the effects of the collagen at different layers on the EGM features were considered to be same. This influencing factor can become one of the future research directions.

Another limitation is the unstable contact between the BMS and the electrodes. This could be due to the flow caused by perfusion during the recording and the BMS were not well placed on the MEA dish.

In addition, although a significant linear regression was obtained, based on the images, there may be a more complex relationship between EGM features and collagen, and proper fitting of the data can better demonstrate this relationship. Such fitting process requires more and more accurate data.

4.6 Conclusion

In this chapter, the collagen expression in rat models and human models was quantified and higher CIs were calculated from rat myocardial fibrosis model and human failing BMS. Collagen expression was shown to reduce conduction velocity ex vivo and lead to dramatic changes in the morphology of EGM. Since how micro level collagen can influence the EGM morphology had been poorly studied, it was interestingly shown that the changes were not only occurring in time domain features but also in frequency domain features, time frequency features and Shannon entropy. Compared to human models, rat models more directly demonstrate the relationship between scarring and EGM morphology. Human models involve more functional changes, the relationships between these changes and collagen expression and how they influence the EGM morphology will be studied in later chapters of this thesis.

The novelty of this chapter lies in combining quantitative EGM feature extraction with well-defined structural perturbations in an experimental setting. This approach allowed you to map specific structural alterations to measurable EGM outcomes, establishing a translational link between microstructural pathology and clinically observable EGM markers.

Chapter 5

Effects of Functional remodelling on Cardiac Electrogram Morphology

5.1 Introduction

In the last chapter, collagen development and its relationship with the EGM features in rat and human models were studied and discussed. Linear regression was obtained from most of the features but all the R^2 values were low. Such low R^2 values could be due to other factors that could also affect the morphology of EGM. In this chapter, the gap junction remodelling, $Na_v1.5$ sodium channel remodelling in human heart models, and how these functional changes influence the EGM morphology of human BMS were investigated. The symphatetic neurons (SNs) was also considered as a functional change and investigated. Some immunofluorescence, imaging experiments and image processing were carried out by the project students supervised by the author: Fasai Wutthiphakdee, Vivienne Ting and Yuan Zhang.

5.1.1 Neuronal cells affect cardiac electropgyology

The development of the heart (cardiogenesis) and the nervous system are closely interconnected, with neurons playing key roles in regulating heart formation, function, and maturation.

Neural crest cells (NCCs) are a transient, multipotent population originating from the neural tube that play essential roles in cardiac development. These specialised cells migrate into the developing heart and contribute to three critical processes: (1) outflow tract septation (separating the aorta and pulmonary artery), (2) formation of the aorticopulmonary septum, and (3) patterning of the great arteries[144].

The autonomic nervous system (ANS) provides crucial innervation to the developing and mature heart. Parasympathetic (vagal) neurons originating in the hindbrain release acetylcholine to slow heart rate, while sympathetic neurons (derived from neural crest cells) enhance heart rate and contractility through norepinephrine signaling. Proper ANS innervation is vital for postnatal cardiac function, enabling appropriate responses to physiological stress and maintaining cardiovascular homeostasis[145]. The mechanism of ANS in the development of arrhythmias has been studied over the past decade. It is now believed that cardiac autonomic nerves significantly influence the development of AF[146]. Avazzadeh S et al. demonstrated that these GP sites overlap with sites of abnormal contact electrograms in the atria[147]. Adding GP ablation to PVI can improve success rates and reduce recurrence by addressing both the electrical triggers from the pulmonary veins and the autonomic influences that sustain AF [148, 149]. However, the long-term efficacy of PVI combined with GP ablation to suppress paroxysmal atrial fibrillation (PAF) remains unclear. A recent clinical study in Japan compared PVI alone with PVI plus GP ablation in patients with PAF over a more than four-year follow-up period. The study showed that GP ablation combined with PVI provided better long-term inhibition of PAF than PVI alone. This finding suggests that GP ablation is a promising treatment for AF[150]. However, identifying these GP sites is challenging due to the lack of control in vitro models, leading to a limited understanding of the role of ANS in the heart and its effect on the EGM. Therefore, establishing an in-vitro co-culture model of cardiomyocytes and neuronal cells will help to better understand the effect of neuronal cells on EGM and improve treatment, thus refining therapeutic strategies for AF.

5.1.2 Gap junctional remodelling

In pathological conditions, such as heart failure, gap junctional remodelling can occur. This can manifest in multiple ways, for example, a reduction in CX43 expression or a redistribution of CX43 to lateral cell borders[151]. The change in expression alone does not mean a change in protein function thus looking at the effect on electrophysiology is important. A reduction in CX43 expression has been shown to cause conduction slowing via cell-to-cell uncoupling, this can cause arrhythmias due to dispersed impulse conduction[38]. In Peters et al. paper, marked disturbed gap-junctional distribution has been shown to increase around healed infarcts in canines, this can lead to non-uniformity of conduction and lead to reentry, which are characteristics of arrhythmias. Additionally, the marked disruption of connexin spanned the full thickness of canines with VT but only spanned partially in canines without VT, suggesting a spatial relationship between connexin remodelling and damages within the heart[152]. However, this was limited to post myocardial infarction only and has not yet been fully extended to humans.

From past research and the study included in the last chapter, it is known that scaring plays a role in changing the electrophysiology of the heart in pathological conditions[55]. It is also known that the gap junctional remodelling occurs due to pathological conditions and shows a possible spatial relationship with damage within the heart such as infarctions[152]. However, research on the spatial relationship between scar and gap junctional remodelling and its effects on electrophysiology is limited. The hypothesis explored in this chapter is that gap junctional remodelling increases around the scar compared to remote tissue in the failing myocardium in the human left ventricle. The mechanisms of gap junctional remodelling under investigation are lateralisation, reduced expression and homogeneity. A clearer understanding of gap junctional remodelling and its spatial relationship with scar can provide new insight into the electrical properties behind heart failure.

5.1.3 Fast sodium ion channel remodelling

Cardiac voltage-gated sodium channels are proteins embedded in the membranes of cardiomyocytes, crucial for initiating action potentials throughout the myocardium. $Na_v1.5$ channels are typically distributed homogeneously in the t-tubules and external sarcolemma[153]. Their significance is underscored by the potentially lethal arrhythmias that can arise from both inherited and acquired sodium channel disorders[154]. Remodelling of these sodium channels can lead to arrhythmias by exacerbating slow conduction, primarily through prolonging action potential duration (APD)[155, 156]. This increases the dispersion of the refractory period, heightening the risk of unidirectional conduction block and facilitating reentry[155]. Changes in sodium channel density have been observed in animal models of heart failure[157], and human sodium channel disorders, such as SCN5A mutations, exhibit reduced sodium channel expression with an altered electrophysiological phenotype[156].

Although the importance of scar structure in the influence of pump function and remodelling is well-established , developing therapies that effectively enhance cardiac function or mitigate remodelling through the modification of the scar structure presents substantial challenges. A comprehensive understanding of the properties affecting left ventricular function, remodelling, and electrical conduction is essential to advance therapeutic strategies[158]. Hence, this study aims to explore the colocalisation of scar tissue and sodium channel remodelling concerning the electrophysiology of cardiomyocytes in human heart failure samples.

The hypotheses to be addressed were as follows:

1. Co-culture with SNs accelerates the growth of cardiomyocytes and increases Connexin 43 expression, thus modifying certain EGM features.

2. Gap junction remodelling increases in human failing hearts comparing to human donor hearts.

3. Gap junction remodelling increases around scar compared to remote tissue in both donor and failing human left ventricle and has influence on EGM features.

4. Nav1.5 fast sodium channel remodelling increases in human failing hearts comparing to human donor hearts.

3. Nav1.5 fast sodium channel remodelling increases around scar compared to remote tissue in both donor and failing human left ventricle and has influence on EGM features.

For this purpose, the following studies described in this chapter were carried out:

1. Record EGM from cell model and human BMS.

2. Image Cx43 and cell morphology from cell model and quantify them.

3. Image Cx43 and Nav1.5 sodium channel from human heart LV slides and quantify their remodelling.

4. Correlate the concentration of SNs and the EGM features.

5. Correlate the gap junction remodelling/ ion channel remodelling and the EGM features.

5.2 Methods

5.2.1 Cell culture

Pure NRVMs and NRVMs/SNs co culture were prepared as described in Section 2.2.1. The cells were checked with a microscope on a daily basis to ensure there was no contamination and the NRVMs were contracting. The culture time were controlled to 4 days.

Pure NRVMs, NRVMs and 5% SNs co culture and 10% SNs co culture were prepared to test the effect of different concentrations of SNs on conduction velocity and EGM morphology.

5.2.2 Microelectrode array recording

MEA experiment was carried out on cells cultured in MEA dishes and human heart BMS. The BMS of human models was prepared as described in Section 2.2.3. Due to the fact that some

human heart has animal restrictions, BMS preparation, MEA recording, data processing for cells and human heart BMS were carried out separately.

EGM was recorded from each BMS following the standard protocol described in Section 2.3. For cells EGM recording, no perfusion was applied, the rest of the protocol remained the same. Only 4 time domain features (EGM duration, EGM voltage, RS interval and conduction velocity) were extracted from the EGM of cells because the EGM morphology of cells are simpler than BMS EGM features. Examples of EGMs recorded from NRVMs and NRVMs/SNs is shown in figure 5.1. The examples of EGM recorded from human BMS are included in the Method part of previous chapter.

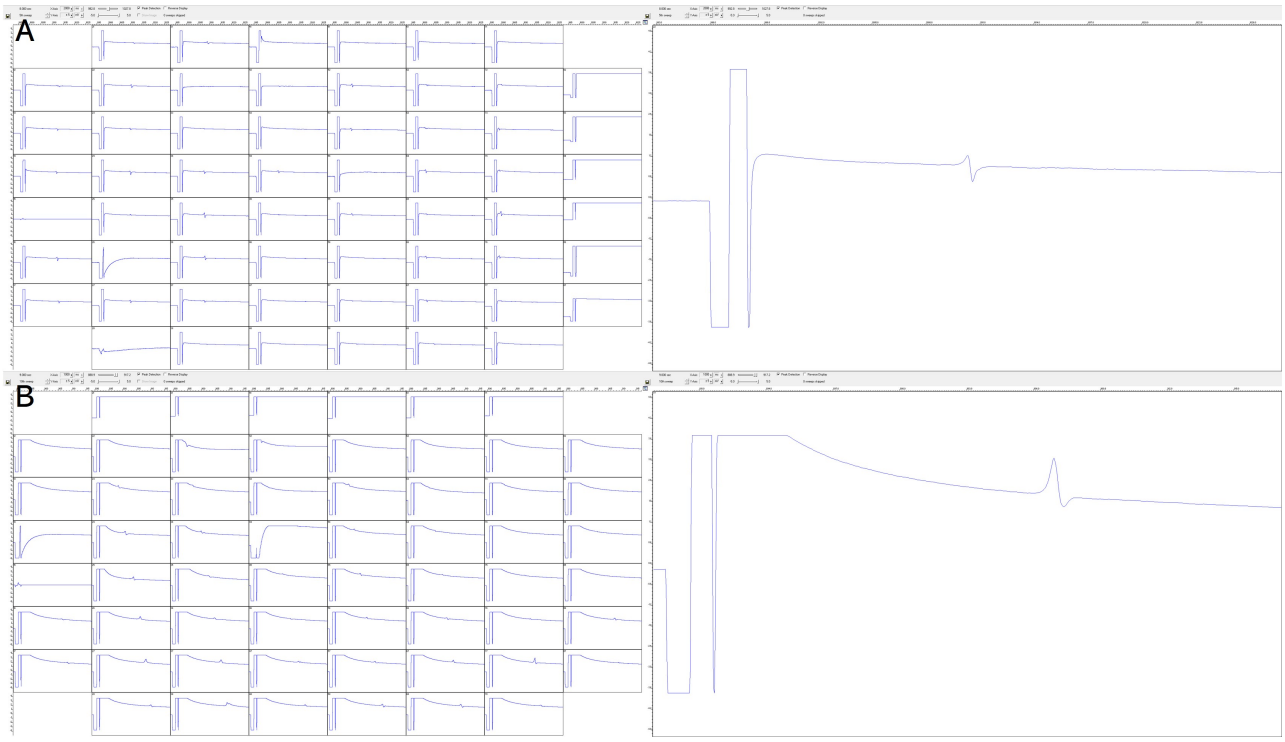


Figure 5.1: Examples of the raw EGMs recorded from cells. (A) Pure NRVMs. The left image shows the EGMs recorded from all the electrodes, the right images shows the EGM recorded from a single electrode. The stimulation direction is east. (B) NRVMs/SNs. The left image shows the EGMs recorded from all the electrodes, the right images shows the EGM recorded from a single electrode. The stimulation direction is north.

The EGM features of human heart BMS will be further colocate with the immunofluorence data, but the slides were prepared from the adjacent block not the BMS, so the collocation can only be carried out at heart level. Due to the fact that the slides were prepared using

myocardium near the endocardium, so for each heart a BMS near the endocardium was used to represent the whole heart.

The cells were fixed with 100% methanol (-20°C , VWR Chemicals) for 10 minutes at room temperature after recording the EGM.

5.2.3 Immunofluoresence

Cell dishes and human LV slides were prepared and immunolabeled following the protocols described in Section 2.2.3 and 2.5.2.

Cx 43, SNs and WGA was immunolabeled on cell models to measure the influence of SNs on the cell growth and Cx43 expression.

Cx 43, $Na_v1.5$ ion channel were immunolabeled on human LV slides to study the effects of scars on their remodelling and the effects of remodelling on conduction velocity and EGM morphology.

5.2.4 Microscope and imaging processing

The stained cell samples and human LV samples were imaged 3 days after the staining to ensure that fading will not influence the imaging results.

For cell models, widefield microscopy was used to image Cx43 expressions and confocal microscopy was used to examine the morphological changes in the NRVMs.

For human LV slides, widefield microscopy was used to image Cx43 remodelling and scars, confocal microscopy was used to image $Na_v1.5$ ion channel remodelling and scars.

All imaging followed the protocols described in Section 2.6.2. All image processing and analysis were completed under blind conditions. Images from microscope were taken into FIJI (Version 2.9.0).

For Cx43 expression in cells, the image brightness and contrast were adjusted making sure all images had the same values (Cy3/Cx43 channel: Minimum - 3500 Maximum - 12000). Then the image thresholds were adjusted (Cy3/Cx43 channel: Minimum - 5500 Maximum - 65535). After thresholding, images were binarised, turning them black and white, allowing FIJI only to count the white pixels in pixel counting. The measurement represents the average relative intensity of the pixels in the region. Example images are shown in Figure 5.10.

Moreover, the diameter of cardiomyocytes was measured using the "straight line" tool. A random blind selection was performed on each slide, and a line was drawn through the longest axis of the selected cardiomyocyte to represent its diameter. The results of the measurements were recorded from "Analyse" > "Measure". In the quantitative analysis of the images, in order to eliminate possible interference from background noise, the threshold of each channel was established by using an area without any visual features as a negative control. The example images are shown in Figure 5.11.

For Cx43 imaging of human LV slides, the image brightness and contrast were adjusted making sure all images had the same values (Cy3/Cx43 channel: Minimum- 334- Maximum-11400, 488/Scar channel: Minimum-6500 Maximum-19650). Then the image thresholds were adjusted (Cy3/Cx43 channel: Minimum- 5550 Maximum-65535, 488/Scar channel: Minimum-11960 Maximum-65535). After thresholding, images were binarised, turning them black and white, allowing FIJI only to count the white pixels in pixel counting. All squares used in pixel counting covered an area of 200,0002 microns. Example images are shown in Figure 5.2.

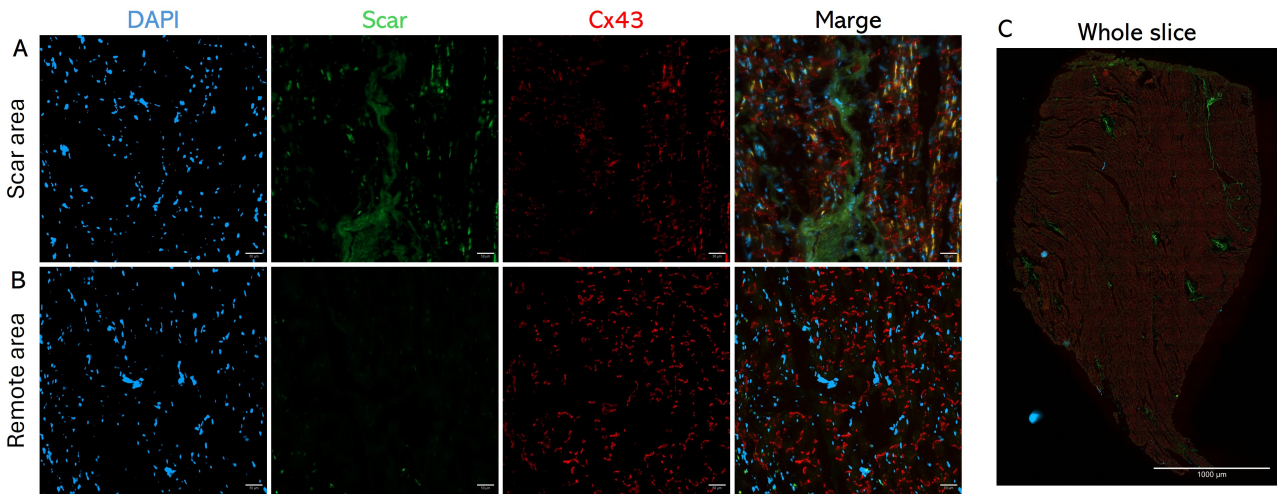


Figure 5.2: Example images of Cx 43 staining. (A) Zoomed in scar area from a donor heart sample. (B) Zoomed in remote area from a donor heart sample. (C) The whole image of a donor heart sample.

In this thesis, scar refers to areas next to fibrosis. Remote areas refer to areas far from fibrosis. The areas in relation to the scar were chosen by looking at the 488 channel and choosing an area with high intensity (near scar) and an area far from this (remote). The areas (remote and near scar) were kept consistent for all types of gap junctional remodelling analyses per heart. In details, the area within 250 μm from the scar is considered as near scar area.

A main form of Cx43 remodelling is a reduction in the expression of Cx43. The reduction can be used as a marker for the extent of remodelling. Cx43 expression was assessed quantitatively via pixel counting of en face gap junctions. Examples of image processing and pixel counting of en-face gap junctions are shown in Figure 5.3. Pixel counting was completed on 5 random en-face gap junctions across the heart slice and the mean was taken to represent the whole slice. For each area (remote and near scar), 5 en face gap junctions were chosen, and a mean was taken. Another form of Cx43 remodelling in disease is a heterogeneous distribution of Cx43 which can suggest the extent of remodelling. This manner of remodelling was assessed via the quantitative method of pixel counting where standard deviation across different areas was taken to assess homogeneity. Pixel counting was completed on 5 random squares across the entire sample, and the standard deviation across these squares was taken. For each area (remote and near scar), pixel counting for 4 squares was completed and a standard deviation

across these squares was taken.

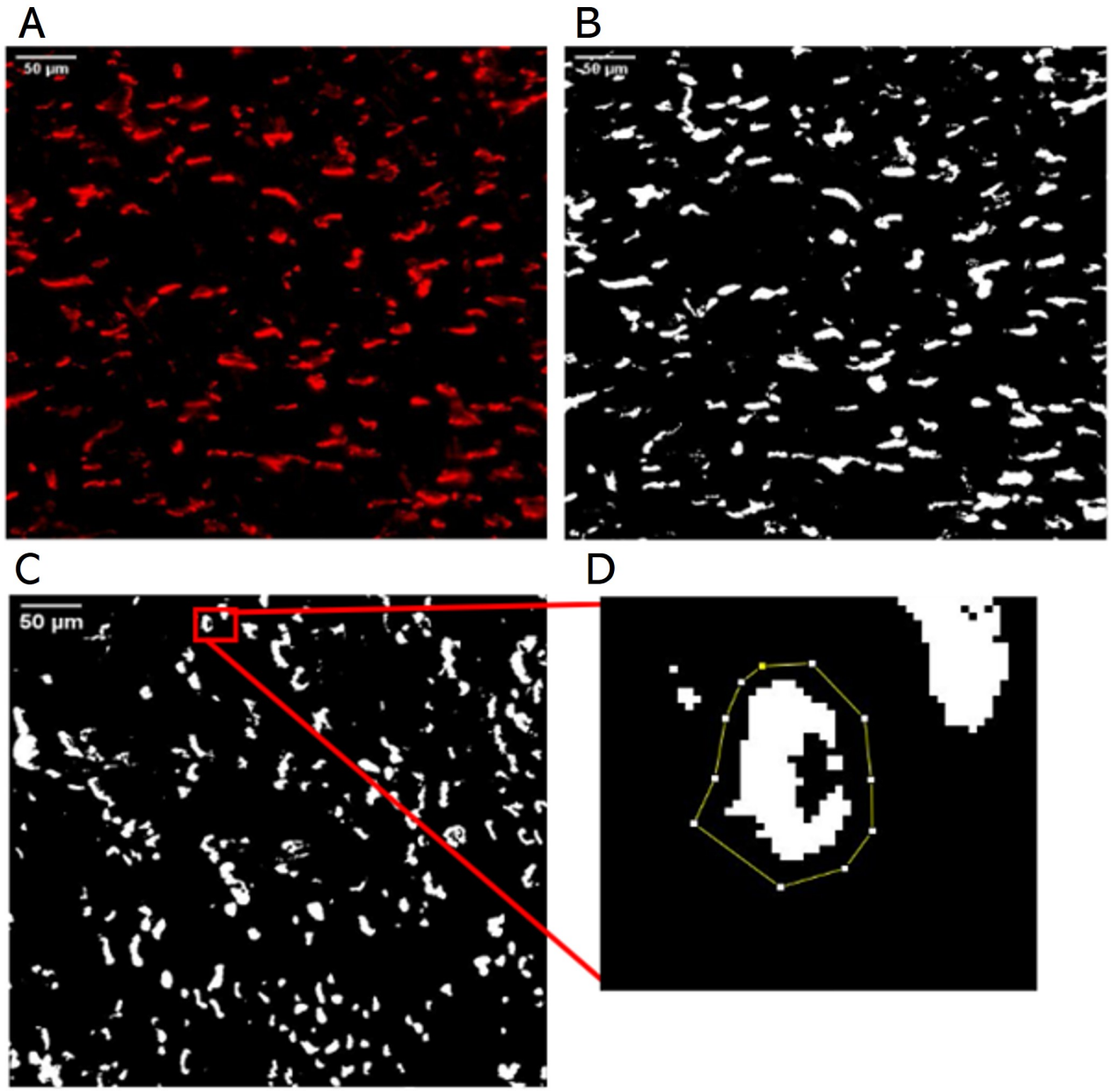


Figure 5.3: Example images of the Cy3 channel from a Cx43 immunolabelled human left ventricle after adjusting brightness (A) Thresholding and binarising (B) Pixel counting is shown on the bottom row. (C) The process of locating an en-face gap junction. (D) The marking of an area of Cx43 labelling at the en-face gap junction for pixel counting (yellow outline).

The amount of Cx43 lateralisation can represent the extent of remodelling; this concept is utilised in a semi-quantitative scoring system used to measure the percentage of cells showing lateralisation. The scores for different levels of lateralisation is shown in Table 5.1. Images were scored by 3 trained researchers, where a score of 1 was given for images with normally

distributed Cx43 (less than 10% of cells showing lateralisation) and a score of 5 was given if a high extent of lateralisation was seen (more than 40% of cells showing lateralisation). The score was recorded if at least two researchers gave the same score. An example of scoring is shown in Figure 5.4.

Score	Amount of cells showing lateralisation (%)
1	<10
2	10-20
3	20-30
4	30-40
5	>40

Table 5.1: A semi-quantitative scoring system is used for assessing the connexin43 distribution.

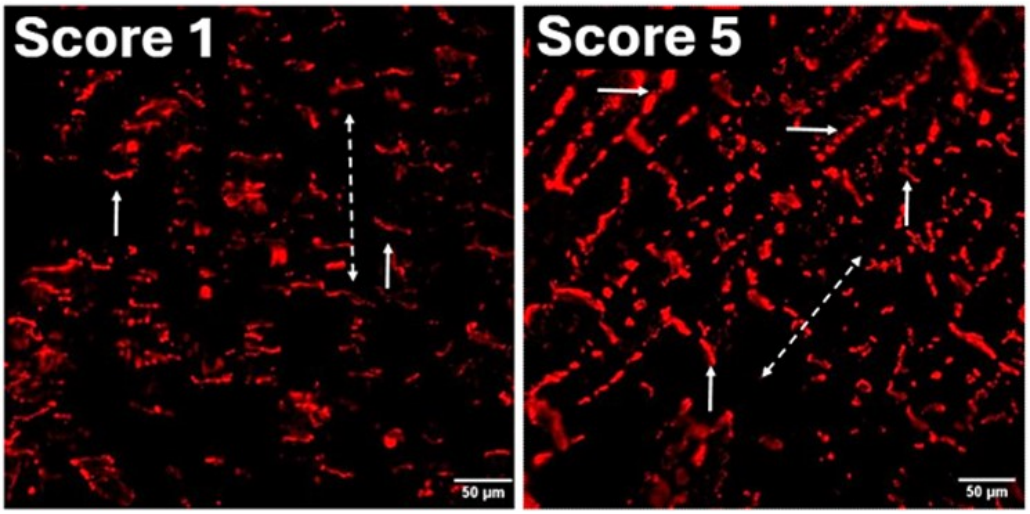


Figure 5.4: Example images showing the scoring system and Cx43 distribution. The dashed double-ended arrows indicate the longitudinal fibre orientation.
Vertical arrows show examples of Cx43 at intercalated discs, whilst horizontal arrows show examples of lateralised Cx43. In Score 1, most of the Cx43 immunolabels are at the intercalated disc. In Score 5, it is found at the lateral cell borders.

For $Na_v1.5$ ion channel imaging, slides imagery was performed using both Widefield (Zeiss Axio Observer) and confocal (Leica Stellaris 8 inverted) microscopes. Collagen exhibited autofluorescence when excited at 488 nm, while Alexa Fluor 680 was used for $Na_v1.5$ detection. DAPI was employed to stain nuclei. For large-area visualisation, widefield tiling and stitching were conducted using a 63x oil objective, with settings configured for a minimum overlap of 5% and a maximum shift of 10% in the dimension of 20x20. The confocal microscope was calibrated with the following parameters: Smart gain at 66.0%, Smart intensity at 5.9%, Smart

wavelength at 498.0 nm, a pinhole size of 1.00, and a zoom factor of 1.00. The images were captured in a resolution of 2048 x 2048 pixels at a speed of 400. Z-stack imaging was conducted using both microscopy techniques; however, the widefield microscope was unable to effectively scan through the layers of the tissue sample. Therefore, the confocal microscope was employed to evaluate $Na_v1.5$ expression. And the Widefield microscope was used to locate scars, which provides the reference for confocal imaging. Example images are shown in Figure 5.5 and Figure 5.6. Areas in relation to the scar were selected by analysing the 488 channels, identifying a region with high intensity (near scar) and another area positioned farther away (remote). Both remote and near-scar areas were selected following the same standard used for Cx43 remodelling analysis. For each heart sample, five remote and five near-scar areas were selected.

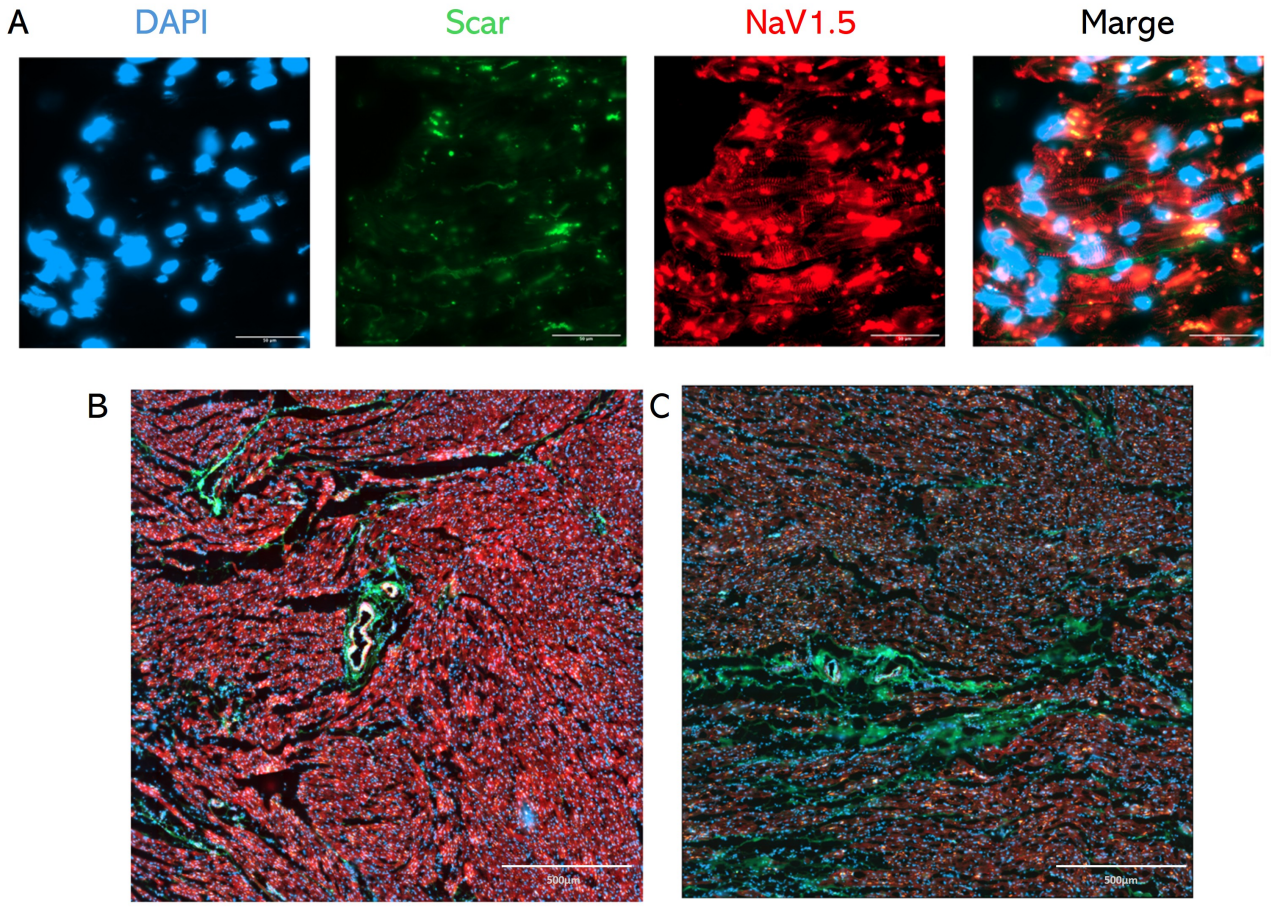


Figure 5.5: Example Widefield microscope images of $Na_v1.5$ ion channel. (A) Separated channels of a image of a small area (250 μm*250 μm). (B) Merged images of a large area (2 mm*2 mm) from a donor heart. (C) Merged images of a large area (2 mm*2 mm) from a failing heart. Both B and C include scar.

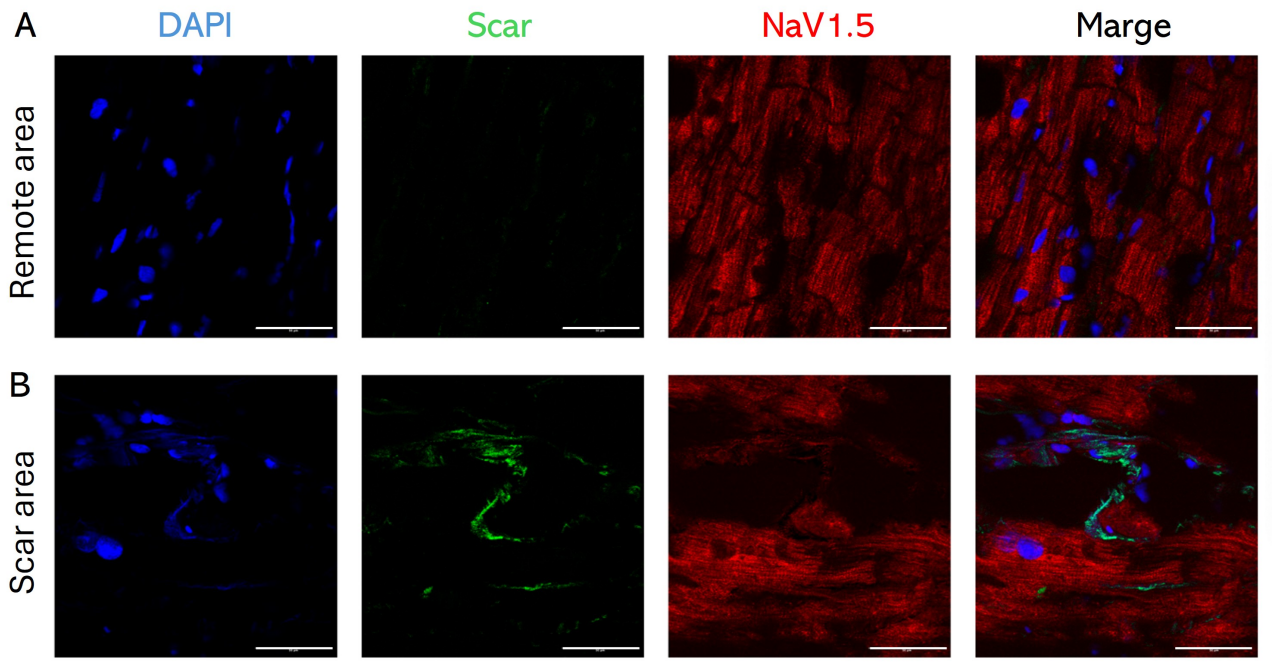


Figure 5.6: Example Confocal microscope images of $Na_v1.5$ ion channel. (A) Image acquired using Widefield microscopy, including an example depicting t-tubules. (B) Tailed large area images (3842.6μm*3842.6μm) from a donor heart. (C) Tailed large area images (3842.6μm*3842.6μm) from a failing heart.

To address the issue of autofluorescence (lipofuscin) present in both the 488/Scar (green channel) and Alexa Fluor 680 (red channel) channels24,25, the channels were separated after z-stack compression, and signal subtraction was performed. For $Na_v1.5$ expression, pixel values from the 488 channel were subtracted from those in the 680 channel, and vice versa for collagen expression. This process effectively reduced autofluorescence, improving signal detection. A fixed threshold was applied across all processed images, with minimum values set at 3011 for $Na_v1.5$ and 468 for collagen expression; the maximum value was 65535 for both. After thresholding, the images were binarised into black and white, enabling FIJI to quantify only the white pixels. Pixel counting was performed over an area of 184.61 x 184.61 microns, and the area of white pixels was calculated to represent the expression levels of the targets of interest. The image processing is shown in Figure 5.7.

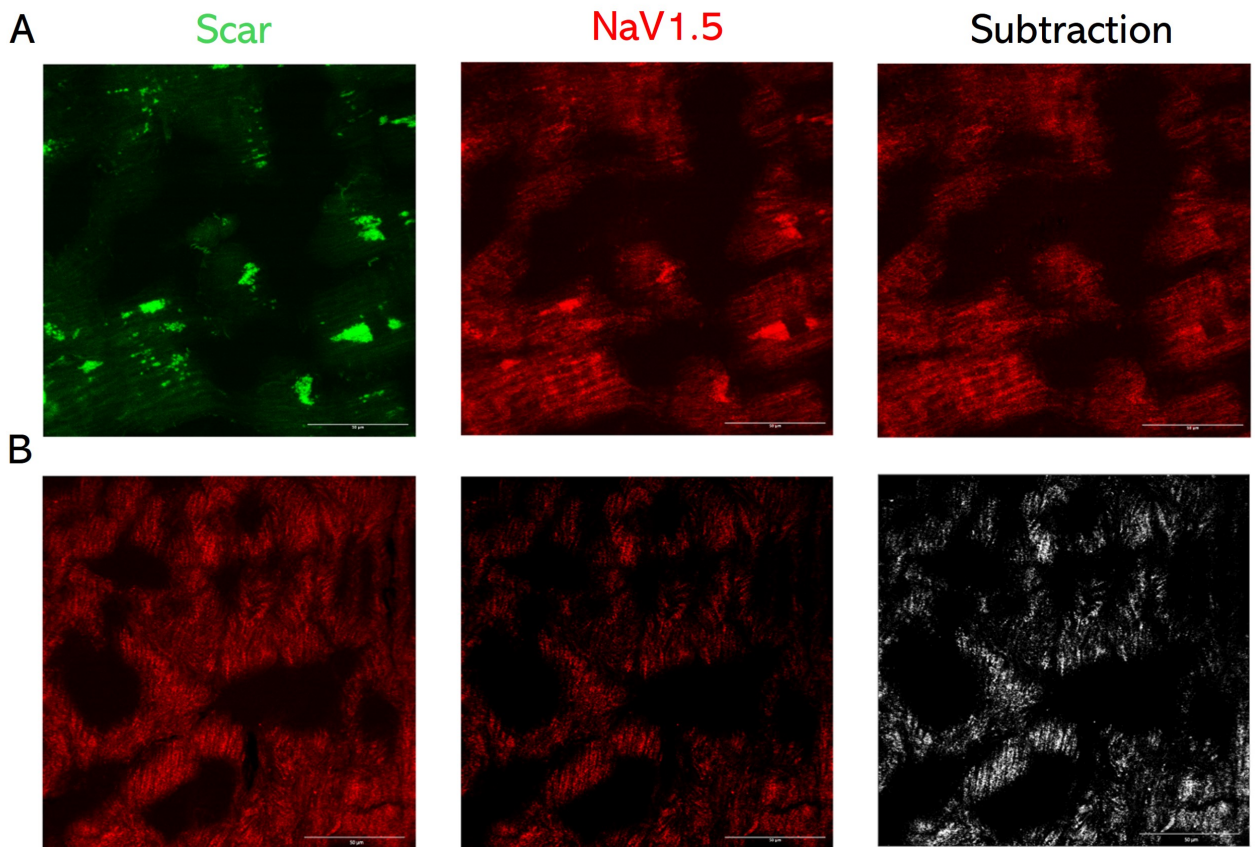


Figure 5.7: Example images illustrating the image processing steps for measuring $Na_v1.5$ ion channel expression levels. (A) Representative image of a heart sample slice under the 488/Scar (green channel) and the Alexa Fluor 680 (red channel), along with the resultant image after autofluorescence signal subtraction. (B) Representative images demonstrating the effect of applying a fixed threshold to the processed images for pixel counting.

For $Na_v1.5$ ion channel expression levels comparison donor hearts and failing hearts, five random areas were selected from each heart sample, and pixel counting was conducted as outlined in the previous paragraphs to assess overall $Na_v1.5$ expression. The mean $Na_v1.5$ expression levels were calculated for the remote, scar, and random areas of each sample. Standard deviations were hence determined for both the donor heart and heart failure groups to evaluate homogeneity.

5.2.5 Data analysis

The features of EGMs were extracted using the tool described in chapter 3. Statistical analysis was performed using the GraphPad Prism software.

Unpaired t-tests were implemented to compare the means of two independent sample populations with normally distributed populations. For data sets with at least one group showingnon-normal distribution Mann–Whitney test was applied. One-way analysis of variance (ANOVA) for unpaired data was applied to compare means of three or more groups.

Statistical analyses of the correlation between functional characteristics and electrophysiology were conducted using simple linear regression. The correlation between $Na_v1.5$ channel remodelling and electrophysiology was also assessed using simple linear regression.

5.3 Results

5.3.1 The effects of SNs on EGM features of NRVMs

4 time domain features of EGMs recorded form cells cultured in different conditions were calculated. The results are shown in Figure 5.8 and Figure 5.9. The results show that the conduction velocity of NRVMs + 10% SNs (n = 7) was significantly increased compared with NRVMs only control (n = 7) ($p \leq 0.0001$) and NRVMs + 5% SNs (n = 6) ($p \leq 0.0001$) (NRVMs-only: 26.42 ± 1.04 cm/s, NRVMs + 5% SNs: 25.8 ± 0.9 cm/s, NRVMs + 10% SNs: 35.461 ± 1.348 cm/s). This suggests that the involvement of 10% SNs improves the electrical conductivity of cardiomyocytes. However, there was no statistical difference between NRVMs-only control groupsand NRVMs + 5% SNs (p = 0.65), indicating that this density of SNs may not be sufficient to produce a significant effect. Additionally, the activation time of NRVMs + 10% SNs was significantly shorter, with higher velocities in some areas and the distribution was anisotropic. These findings suggest that SNs play an important role in cardiac conduction and are related to their density.

Both the EGM duration (NRVMs-only: 1.77 ± 0.03 ms, NRVMs + 10% SNs: 1.581 ± 0.06 ms, p = 0.0561, p = 0.0485, p = 0.79) and R-S interval of the NRVMs + 10% SNs groups were significantly shortened (NRVMs-only: 0.459 ± 0.021 ms, NRVMs + 10% SNs: 0.42 ± 0.033 ms, p = 0.1330, p = 0.0476, p = 0.55). However, the NRVMs + 5% SNs groups did not

show statistical changes (NRVMs + 5% SNs: 1.576 ± 0.02 ms, NRVMs + 5% SNs: 0.411 ± 0.052 ms). These results are consistent with the observation of conduction velocity, indicating similar effects on EGM time domain features. Additionally, the voltage amplitude ($p = 0.3368$, $p \leq 0.0001$, $p \leq 0.0001$) was significantly higher in NRVMs + 10% SNs (0.819 ± 0.045 mV) compared to NRVMs-only (0.471 ± 0.025 mV) and NRVMs + 5% SNs (0.406 ± 0.02 mV). This suggests that the presence of 10% SNs enhanced the electrophysiological properties of cardiomyocytes. Therefore, it was chosen to focus on 10% SNs co-cultures in comparison with culturing NRVMs alone in subsequent studies. These findings provide valuable insights into the dose-dependent regulation of multiple EGM features by SNs.

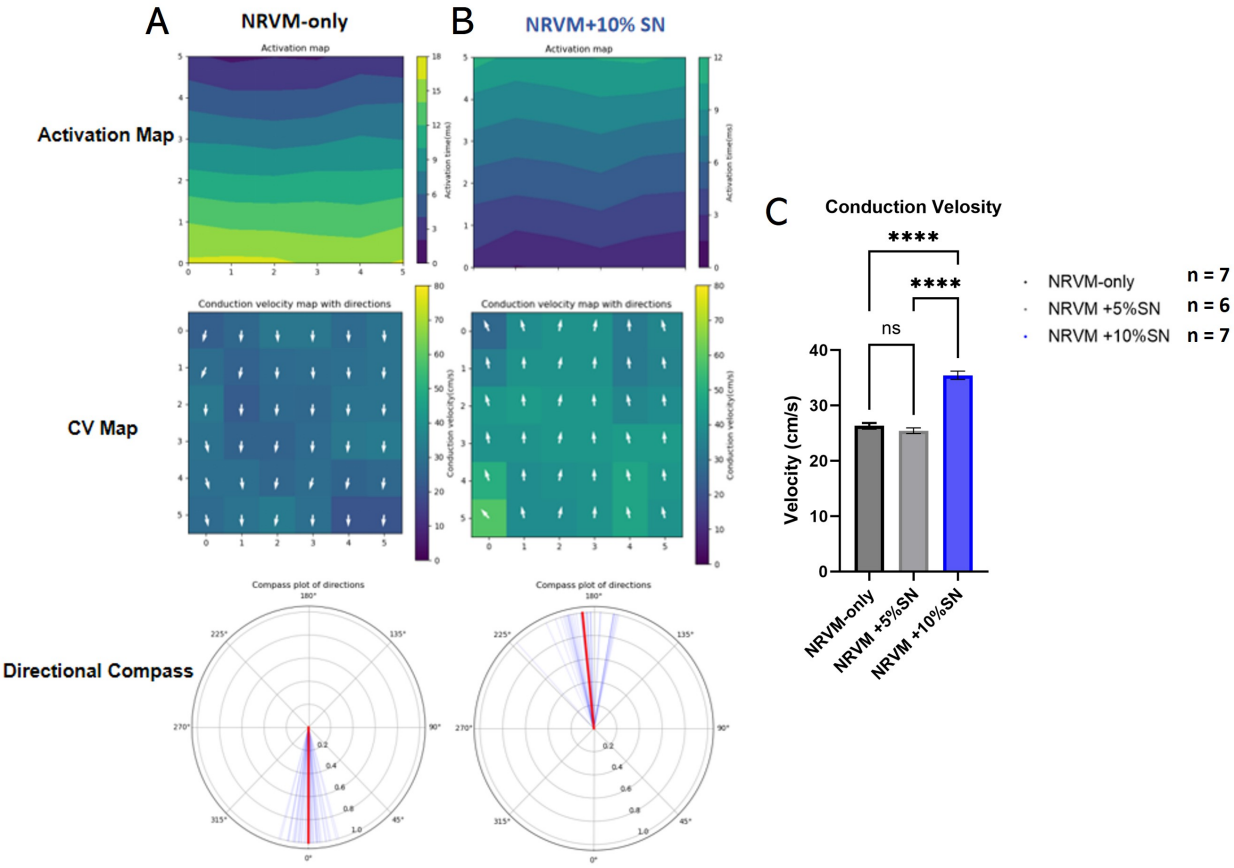


Figure 5.8: Conductance of NRVMs under all culture conditions. NRVMs only control: n = 7; NRVMs + 5% SNs: n = 6; NRVMs + 10% SNs: n = 7. (A) Representative conduction maps of NRVMs-only. (B) Representative conduction maps of NRVMs + 10% SNs. (C) Conduction velocity. All bar charts represent mean ± S.D.; ns $0.05 < p \leq 1$ *$p \leq 0.05$, **$p \leq 0.01$, ***$p \leq 0.001$, ****$p \leq 0.0001$.

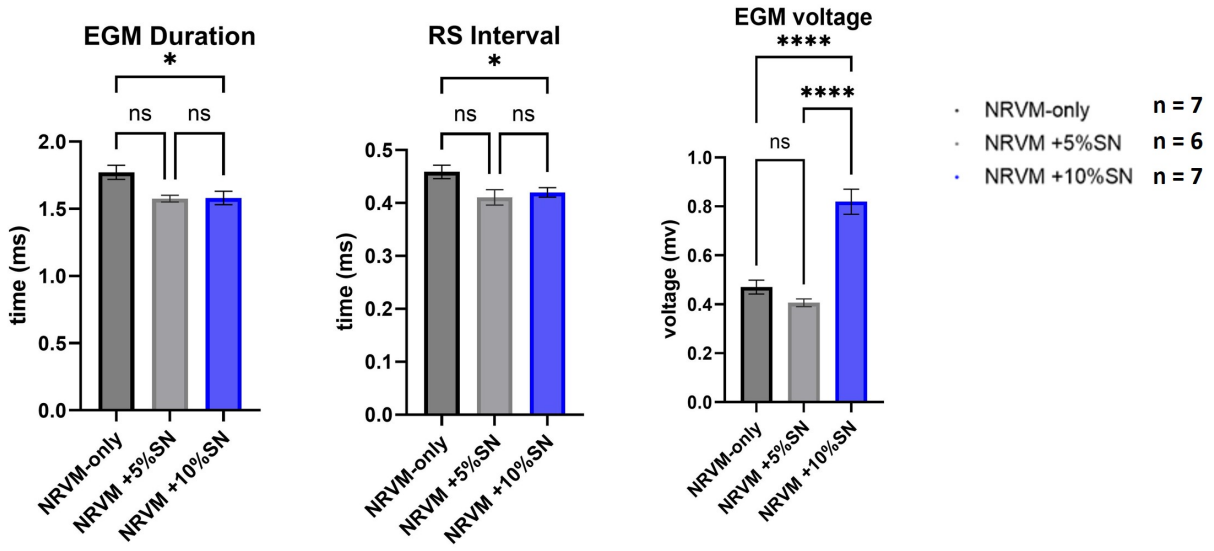


Figure 5.9: Co-culture with SNs alters time domain EGM Features of NRVMs. NRVMs only control: n = 7; NRVMs + 5% SNs: n = 6; NRVMs + 10% SNs: n = 7. Histograms and dot plots compare (A) EGM duration (B) R-S interval (C) Voltage amplitude between NRVMs-only controls and co-cultured NRVMs. All bar charts represent mean ± S.D.; ns $0.05 < p \leq 1$ *$p \leq 0.05$, **$p \leq 0.01$, ***$p \leq 0.001$, ****$p \leq 0.0001$.

Due to the fact that no significant differences were obtained between the EGM features extracted from pure NRVMs and NRVMs + 10% SNs, only pure NRVMs and NRVMs + 10% SNs were focused. To investigate the effect of SNs on cardiomyocyte conductance, the changes in the expression levels of Cx43 in isolated NRVMs under both culture conditions were examined. The result is shown in Figure 5.10, significant difference ($p \leq 0.0001$) was obtained form the Cx43 expression level between pure NRVMs (n=15) and NRVMs co cultured with SNs (n=16). Cx43 expression in NRVMs + 10% SNs was significantly higher than that in NRVMs-only controls (NRVMs-only: 23.912 ± 0.812, NRVMs ± 10% SNs: 39.144 ± 0.8505). This finding indicates that co-culturing NRVMs with 10% SNs enhances Cx43 expression, suggesting a regulatory interaction between SNs and cardiomyocytes that may influence cardiac electrophysiological processes.

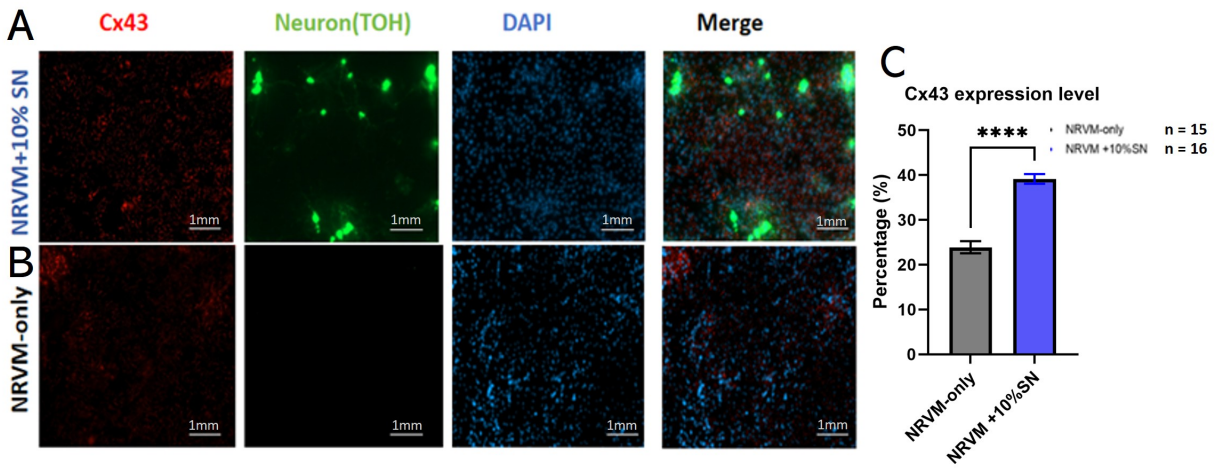


Figure 5.10: Cx43 expression of NRVMs under all culture condition. NRVMs only control: n=15; NRVMs + 10% SNs: n=16. (A)Double immunofluorescence staining of Cx43 and SNs in NRVMs + 10% SNs condition. (B) Double immunofluorescence staining of Cx43 and SNs in NRVMs-only condition. (C) Expression of Cx43. All bar charts represent mean ± S.D.; ns $0.05 < p \leq 1$ *$p \leq 0.05$, **$p \leq 0.01$, ***$p \leq 0.001$, ****$p \leq 0.0001$.

To further investigate the effect of SNs on the growth of cardiomyocytes, the changes in the growth rate of cardiomyocytes under two different culture conditions were analysed: pure NRVMs culture (N = 7) and co-culture with 10% SNs (N = 7). The cellular response was observed after 4 days of culture, co-culture and fixation. Result demonstrates there are clear differences in the morphology of these cardiomyocytes. The presence of SNs significantly accelerated the cell growth of cardiomyocytes. The result is shown in Figure 5.11, significant difference ($p \leq 0.0001$) was obtained form the cell diameters between pure NRVMs and NRVMs co cultured with SNs. The diameter of cells in NRVMs + 10% SNs was significantly longer, indicating a faster growth rate (NRVMs-only: 29.54 ± 1.146um, NRVMs + 10% SN: 41.53 ± 1.32um).

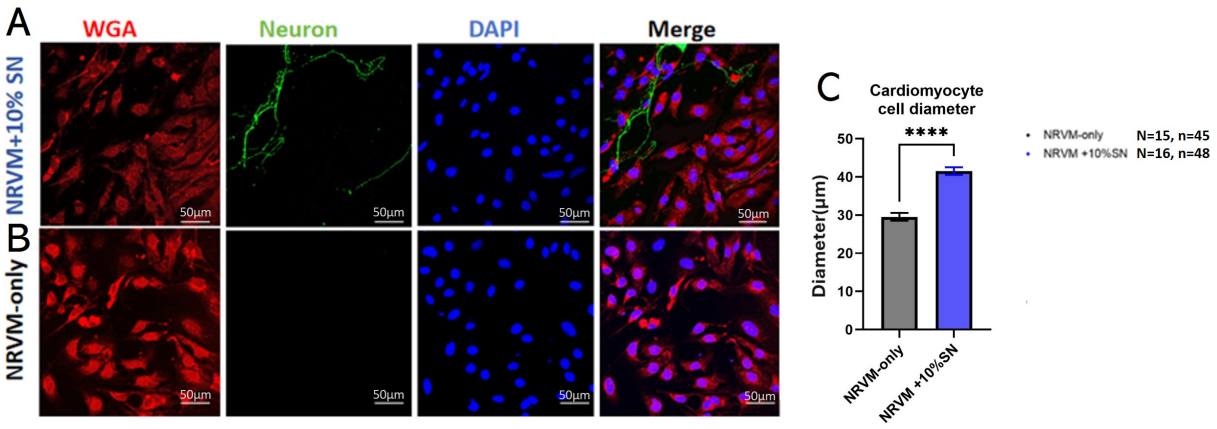


Figure 5.11: Cell morphology of NRVMs under both culture conditions. NRVMs only control: N=15, n=45; NRVMs + 10% SNs: N=16, n=48. (A) Double immunofluorescence staining of WGA and SNs in NRVMs + 10%SN condition. (B) Double immunofluorescence staining of WGA and TOH in NRVMs-only condition. (C) Cell diameters. All bar charts represent mean ± S.D.; ns $0.05 < p \leq 1$ *$p \leq 0.05$, **$p \leq 0.01$, ***$p \leq 0.001$, ****$p \leq 0.0001$.

5.3.2 Gap junctional remodelling and its relationship between scar in human donor and human failing samples

To investigate the structural characteristics of gap junctional remodelling (Cx43 expression, homogeneity, and lateralisation), donor hearts (N=7, n=21) and failing hearts (N=9, n=27) were immunolabelled for Cx43 visualisation. The statistical analysis shows that all structural characteristics' changes are significant. The results are shown in Figure 5.12. There was a decrease in Cx43 expression in failing compared to donor hearts which aligned with the expected trend (Donor: 618.7 ± 132.3 pixels, Failing: 344.5 ± 143.3 pixels, $p = 0.0021$). Further analysis was completed on homogeneity which assessed the distribution of Cx43 expression in different areas of the heart. Since a higher standard deviation suggests a more heterogeneous distribution of Cx43, a higher standard deviation thus a decrease in homogeneity of Cx43 was obtained in failing hearts compared to donor hearts (Donor: 74.75 ± 18.36, Failing: 103.6 ± 14.50 pixels, $p = 0.0033$). The last feature of GJ remodelling explored was the lateralisation of Cx43, where an increase in lateralisation was expected in failing compared to donor hearts. Results show that there was an increase of about 66.5% in scores for Cx43 lateralisation in failing hearts compared to donor hearts (Donor: 1.929 ± 0.4045, Failing: 3.211 ± 0.6849, $p = 0.0041$).

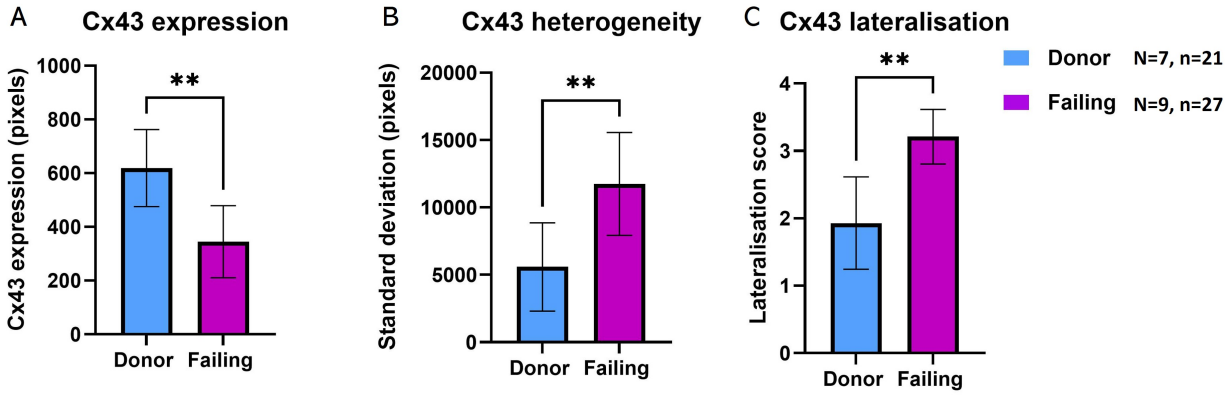


Figure 5.12: Gap junction remodelling characteristics with relation to heart types. For donor hearts: N=7, n=21; for failing hearts: N=9, n=27. (A) Cx43 expression. (B) Cx43 heterogeneity. (C) Cx43 lateralisation. All bar charts represent mean ± S.D.; ns $0.05 < p \leq 1$ *$p \leq 0.05$, **$p \leq 0.01$, ***$p \leq 0.001$, ****$p \leq 0.0001$.

The next step was to investigate if there is a relationship between scar location and gap junctional remodelling in failing and donor hearts. To explore this relationship the left ventricle myocardium samples were immunolabelled for Cx43, and autofluorescence of collagen was visualised to identify scar location. The results are shown in Figure 5.13. A decrease in Cx43 expression in areas near scar compared to remote areas was obtained, due to higher gap junctional remodelling near scar (Donor remote: 820.2 ± 52.42 pixels, Donor scar: 426.2 ± 160.5 pixels, $p \leq 0.0001$; Failing remote: 466.3 ± 143.4 pixels, Failing scar: 212.7 ± 62.78 pixels, $p = 0.0004$). Furthermore, the expected trend was a higher standard deviation thus a decrease in homogeneity in areas near scar compared to remote areas. Results aligned with this expected trend, as a visual decrease was seen in the homogeneity of Cx43 expression in areas near scar compared to remote areas (Donor remote: 63.22 ± 10.18 pixels, Donor scar: 85.17 ± 10.04 pixels,$p \leq 0.0001$; Failing remote: 87.45 ± 5.624 pixels, Failing scar: 99.26 ± 3.689 pixels, $p = 0.0125$). In addition, an increase in lateralisation scores was expected in areas near the scar compared to remote areas. This trend was obtained from donor hearts (Donor remote: 1.500 ± 0.5774, Donor scar: 2.357 ± 0.6901, $p = 0.0389$). However, even the lateralisation score in the scar areas of human failing hearts is higher than that of the remote area of human failing hearts, but no significant differences were obtained from the statistic analysis (Failing remote: 2.778 ± 0.4410, Failing scar: 3.078 ± 0.5585, $p = 0.6755$).

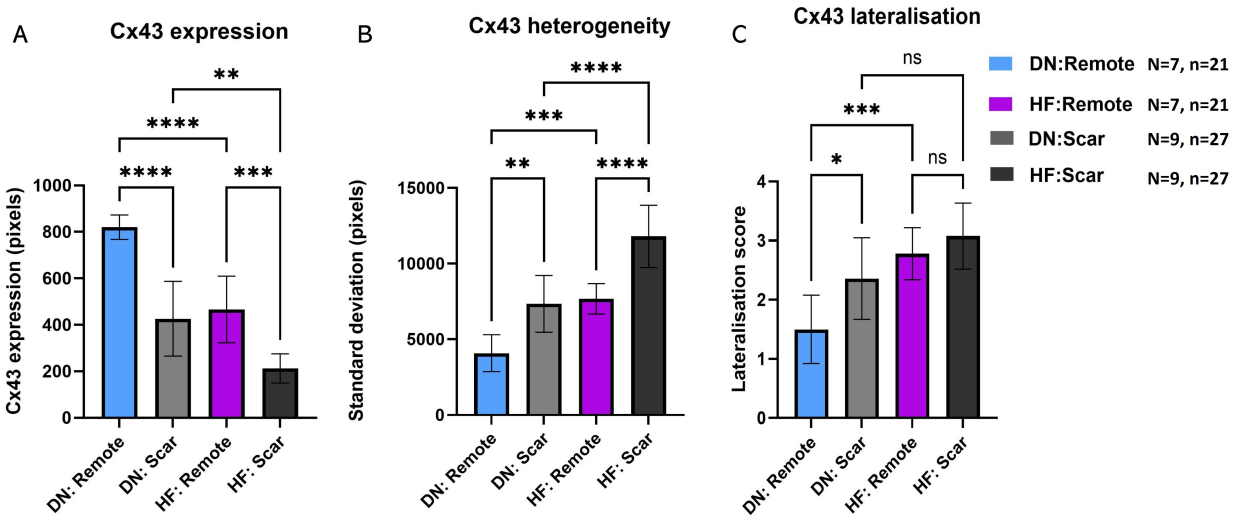


Figure 5.13: Gap junction remodelling characteristics with relation to scar. For donor hearts: N=7, n=21; for failing hearts: N=9, n=27. (A) Cx43 expression. (B) Cx43 heterogeneity. (C) Cx43 lateralisation. All bar charts represent mean ± S.D.; ns $0.05 < p \leq 1$ *$p \leq 0.05$, **$p \leq 0.01$, ***$p \leq 0.001$, ****$p \leq 0.0001$.

5.3.3 Characterisation of EGM feature modifications correlating to gap junctional remodelling

To explore the correlation between gap junctional remodelling and EGM features within the hearts, MEA experiments and Cx43 immunohistochemistry were carried out on failing (N=9, n=27) and donor (N=7, n=21) human left ventricle myocardium samples. The correlation between Cx43 expression and EGM features are shown in Figure 5.14, Figure 5.15 and Figure 5.16. Results show a significant linear relationship between Cx43 expression and nine time domain features (QR interval: $R^2 = 0.1583$, $p \leq 0.0001$, S End interval: $R^2 = 0.2221$, $p \leq 0.0001$, RS interval: $R^2 = 0.03669$, $p \leq 0.0001$, Q to R gradient: $R^2 = 0.2487$, $p \leq 0.0001$, EGM duration: $R^2 = 0.1285$, $p \leq 0.0001$, EGM voltage: $R^2 = 0.1628$, $p \leq 0.0001$, S to End gradient: $R^2 = 0.2358$, $p \leq 0.0001$, Conduction velocity: $R^2 = 0.1796$, $p \leq 0.0001$, Fractionation index: $R^2 = 0.1446$, $p \leq 0.0001$). For all time domains, the R^2 values are higher than the R^2 values of the linear relationship between collagen and EGM features.

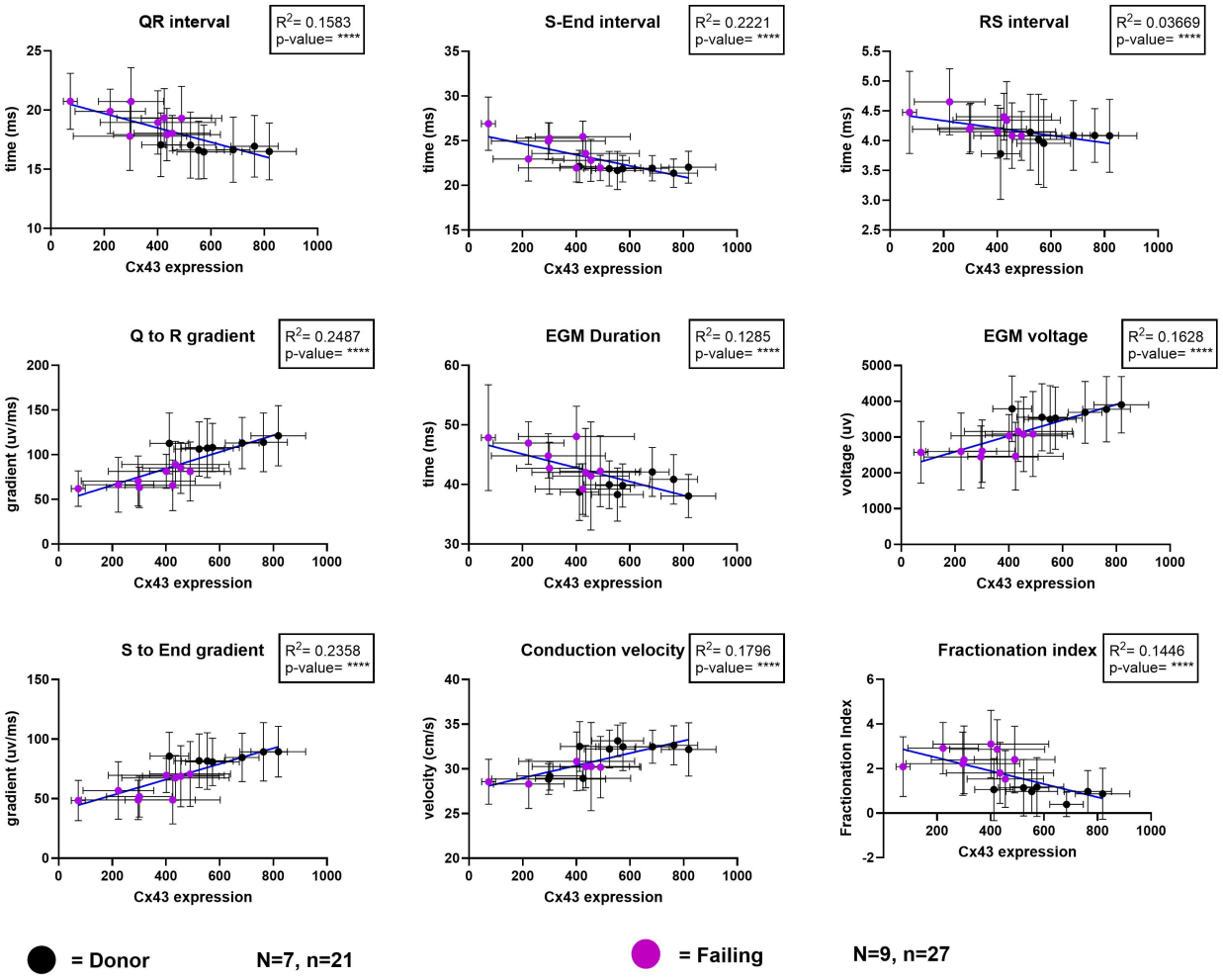


Figure 5.14: Cx43 expression with relation to time domain features of the EGMs of human hearts. For donor hearts: N=7, n=21; for failing hearts: N=9, n=27. Contains 9 graphs of time-domain features from human donor hearts and human failing hearts. The graphs show the time-domain features against the Cx43 expression. A simple linear regression was used to assess the significance of the correlation between the two features, the theoretical line of best fit is shown in blue. Grey error bars represent the standard deviation. All bar charts represent mean ± S.D.; ns $0.05 < p \leq 1$, *$p \leq 0.05$, **$p \leq 0.01$, ***$p \leq 0.001$, ****$p \leq 0.0001$.

The results also showed that all frequency domain features and Shannon entropy were significantly correlated to Cx43 expression (Dominant frequency: $R^2 = 0.1902$, $p \leq 0.0001$, PSD mean frequency: $R^2 = 0.1302$, $p \leq 0.0001$, Maximum PSD: $R^2 = 0.5174$, $p \leq 0.0001$, PSD median: $R^2 = 0.07185$, $p \leq 0.0001$, PSD skewness: $R^2 = 0.2096$, $p \leq 0.0001$, PSD kurtosis: $R^2 = 0.2824$, $p \leq 0.0001$, PSD standard deviation: $R^2 = 0.4301$, $p \leq 0.0001$, Shannon entropy: $R^2 = 0.1675$, $p \leq 0.0001$).

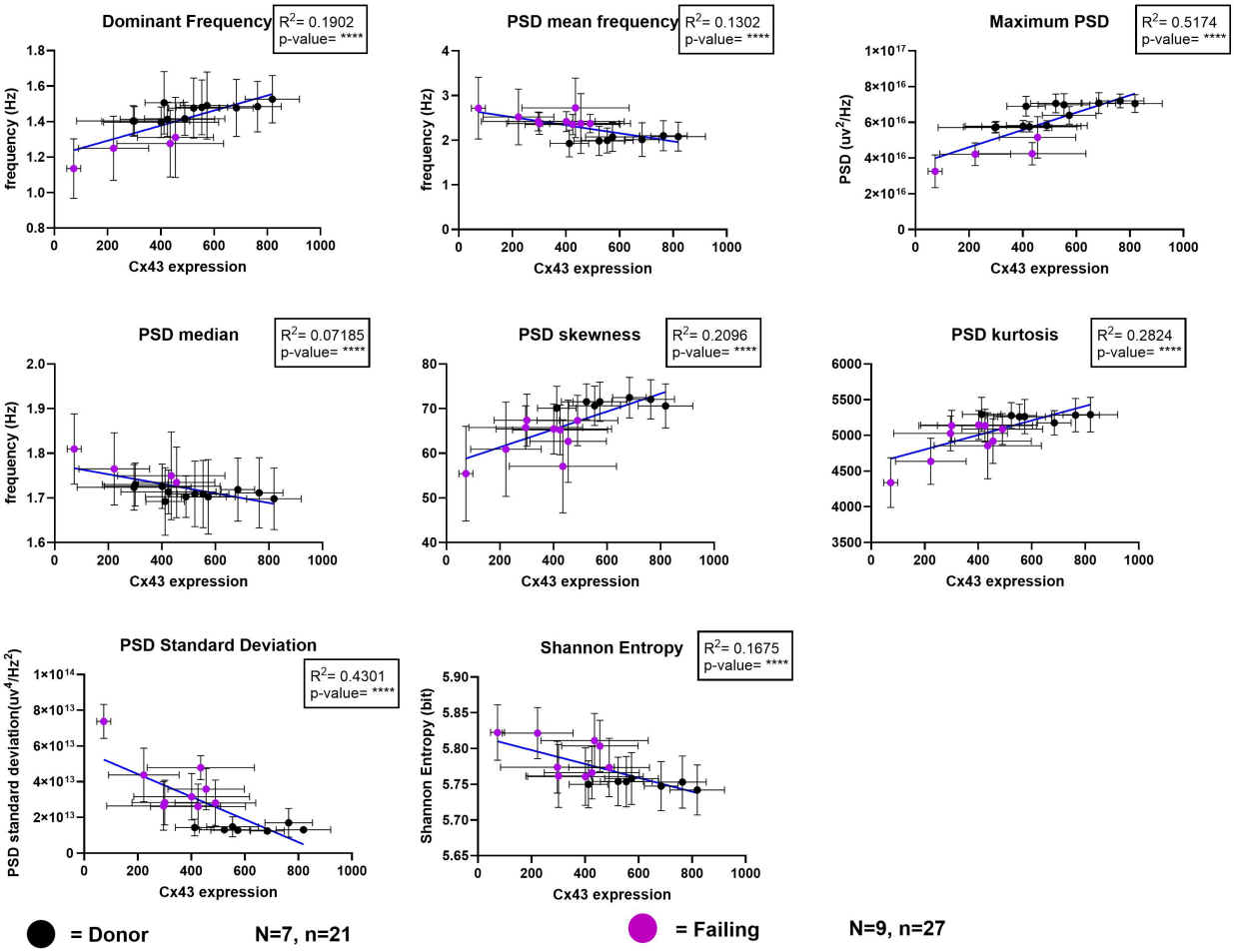


Figure 5.15: Cx43 expression with relation to frequency domain features and Shannon entropy of the EGMs of human hearts. For donor hearts: N=7, n=21; for failing hearts: N=9, n=27. Contains 7 graphs of frequency domain features and 1 graph of Shannon entropy from human donor hearts and human failing hearts. The graphs show the frequency domain features and Shannon entropy against the Cx43 expression. A simple linear regression was used to assess the significance of the correlation between the two features, the theoretical line of best fit is shown in blue. Grey error bars represent the standard deviation. All bar charts represent mean ± S.D.; ns $0.05 < p \leq 1$, *$p \leq 0.05$, **$p \leq 0.01$, ***$p \leq 0.001$, ****$p \leq 0.0001$.

Further results showed a significant correlation between Cx43 expression and all time frequency features (Max modulus: $R^2 = 0.3694$, $p \leq 0.0001$, Energy variance: $R^2 = 0.5155$, $p \leq 0.0001$, Scale corresponding to max energy: $R^2 = 0.1701$, $p \leq 0.0001$, Scale corresponding to min energy: $R^2 = 0.01671$, $p = 0.0041$). Therefore, there are significant correlations between Cx43 expression remodelling and electrophysiology within the hearts. For all the features apart from Scale corresponding to min energy, the R^2 values are higher than the R^2 values of the linear relationship between collagen and EGM features.

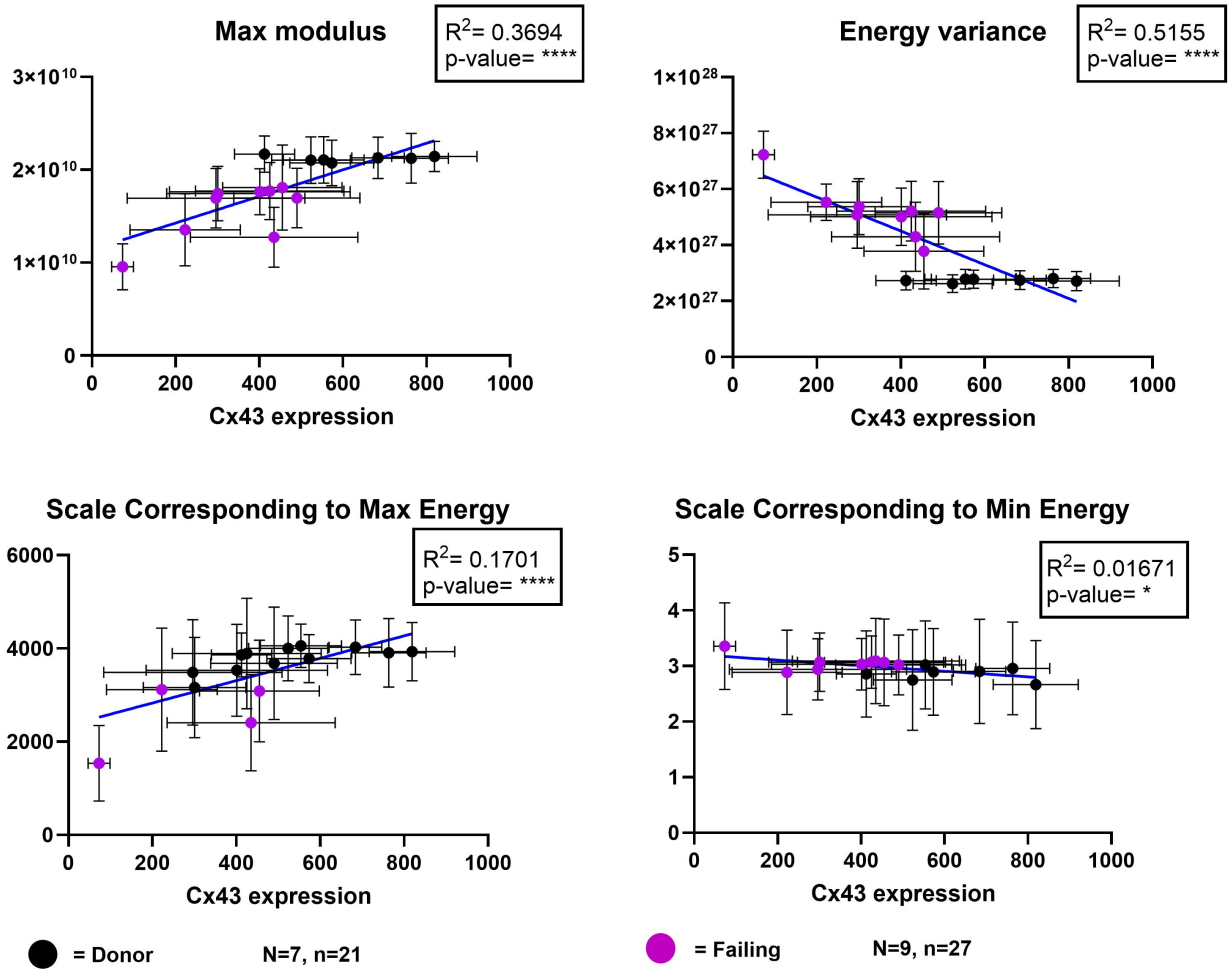


Figure 5.16: Cx43 expression with relation to time frequency features of the EGMs of human hearts. For donor hearts: N=7, n=21; for failing hearts: N=9, n=27. Contains 4 graphs of time frequency features from human donor hearts and human failing hearts. The graphs show the time frequency features against the Cx43 expression. A simple linear regression was used to assess the significance of the correlation between the two features, the theoretical line of best fit is shown in blue. Grey error bars represent the standard deviation. All bar charts represent mean ± S.D.; ns $0.05 < p \leq 1$, *$p \leq 0.05$, **$p \leq 0.01$, ***$p \leq 0.001$, ****$p \leq 0.0001$.

The correlation between homogeneity of Cx43 expression and EGM features are shown in Figure 5.17, Figure 5.18 and Figure 5.19. The results show a significant linear relationship between homogeneity of Cx43 expression and all the features (QR interval: $R^2 = 0.1337$, $p \leq 0.0001$, S End interval: $R^2 = 0.1715$, $p \leq 0.0001$, RS interval: $R^2 = 0.04054$, $p \leq 0.0001$, Q to R gradient: $R^2 = 0.2227$, $p \leq 0.0001$, EGM duration: $R^2 = 0.1397$, $p \leq 0.0001$, EGM voltage: $R^2 = 0.1514$, $p \leq 0.0001$, S to End gradient: $R^2 = 0.2131$, $p \leq 0.0001$, Conduction velocity: $R^2 = 0.1727$, $p \leq 0.0001$, Fractionation index: $R^2 = 0.1632$, $p \leq 0.0001$, Dominant frequency:

$R^2 = 0.1422$, p ≤ 0.0001, PSD mean frequency: $R^2 = 0.1035$, p ≤ 0.0001, Maximum PSD: $R^2 = 0.4049$, p ≤ 0.0001, PSD median: $R^2 = 0.05657$, p ≤ 0.0001, PSD skewness: $R^2 = 0.1641$, p ≤ 0.0001, PSD kurtosis: $R^2 = 0.2204$, p ≤ 0.0001, PSD standard deviation: $R^2 = 0.3103$, p ≤ 0.0001, Shannon entropy: $R^2 = 0.1287$, p ≤ 0.0001, Max modulus: $R^2 = 0.2878$, p ≤ 0.0001, Energy variance: $R^2 = 0.4393$, p ≤ 0.0001, Scale corresponding to max energy: $R^2 = 0.1081$, p ≤ 0.0001, Scale corresponding to min energy: $R^2 = 0.007926$, p $= 0.0487$).

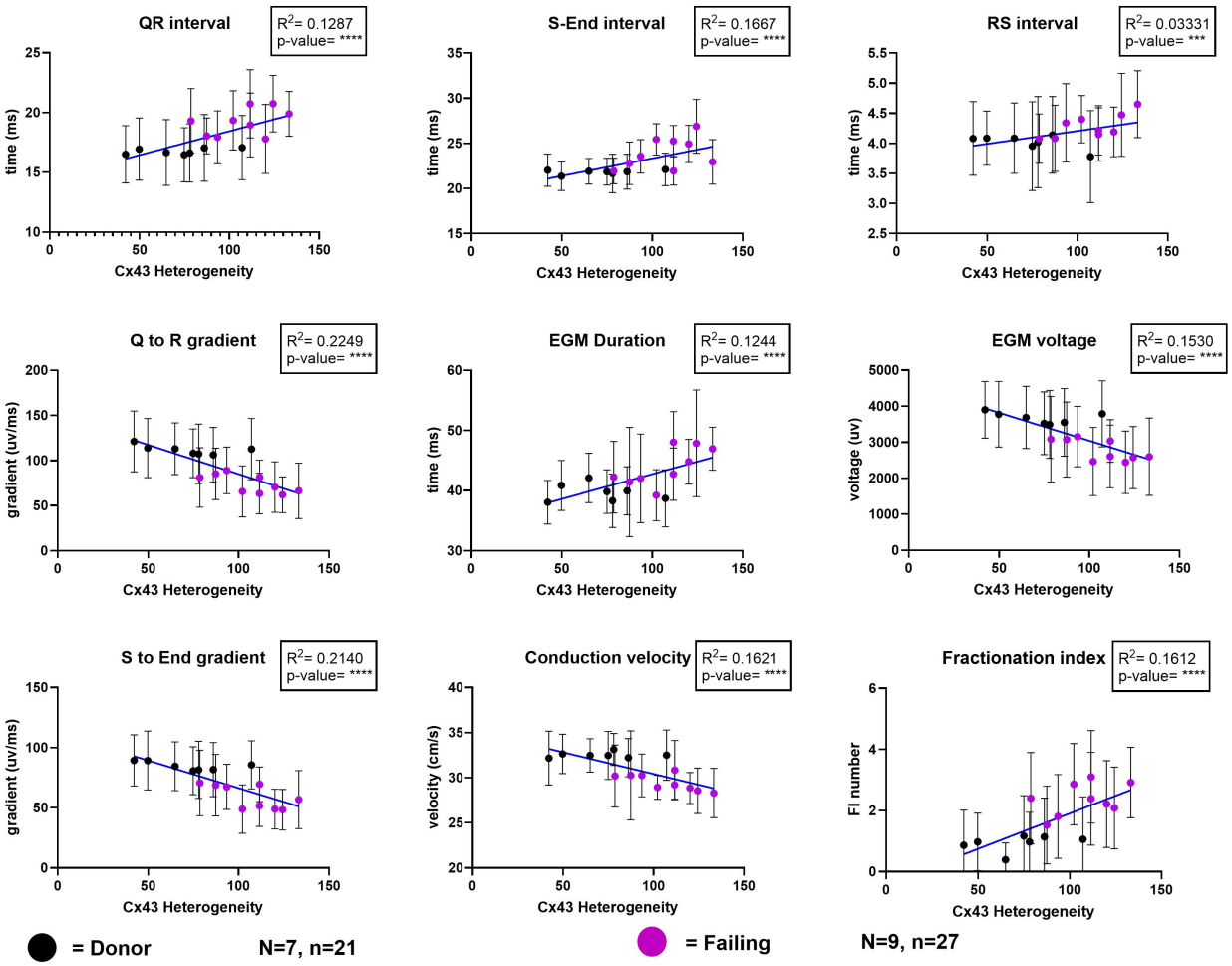


Figure 5.17: Homogeneity of Cx43 with relation to time domain features of the EGMs of human hearts. For donor hearts: N=7, n=21; for failing hearts: N=9, n=27. Contains 9 graphs of time-domain features from human donor hearts and human failing hearts. The graphs show the time-domain features against the homogeneity of Cx43. A simple linear regression was used to assess the significance of the correlation between the two features, the theoretical line of best fit is shown in blue. Grey error bars represent the standard deviation. All bar charts represent mean ± S.D.; ns $0.05 <$ p ≤ 1, *p ≤ 0.05, **p ≤ 0.01, ***p ≤ 0.001, ****p ≤ 0.0001.

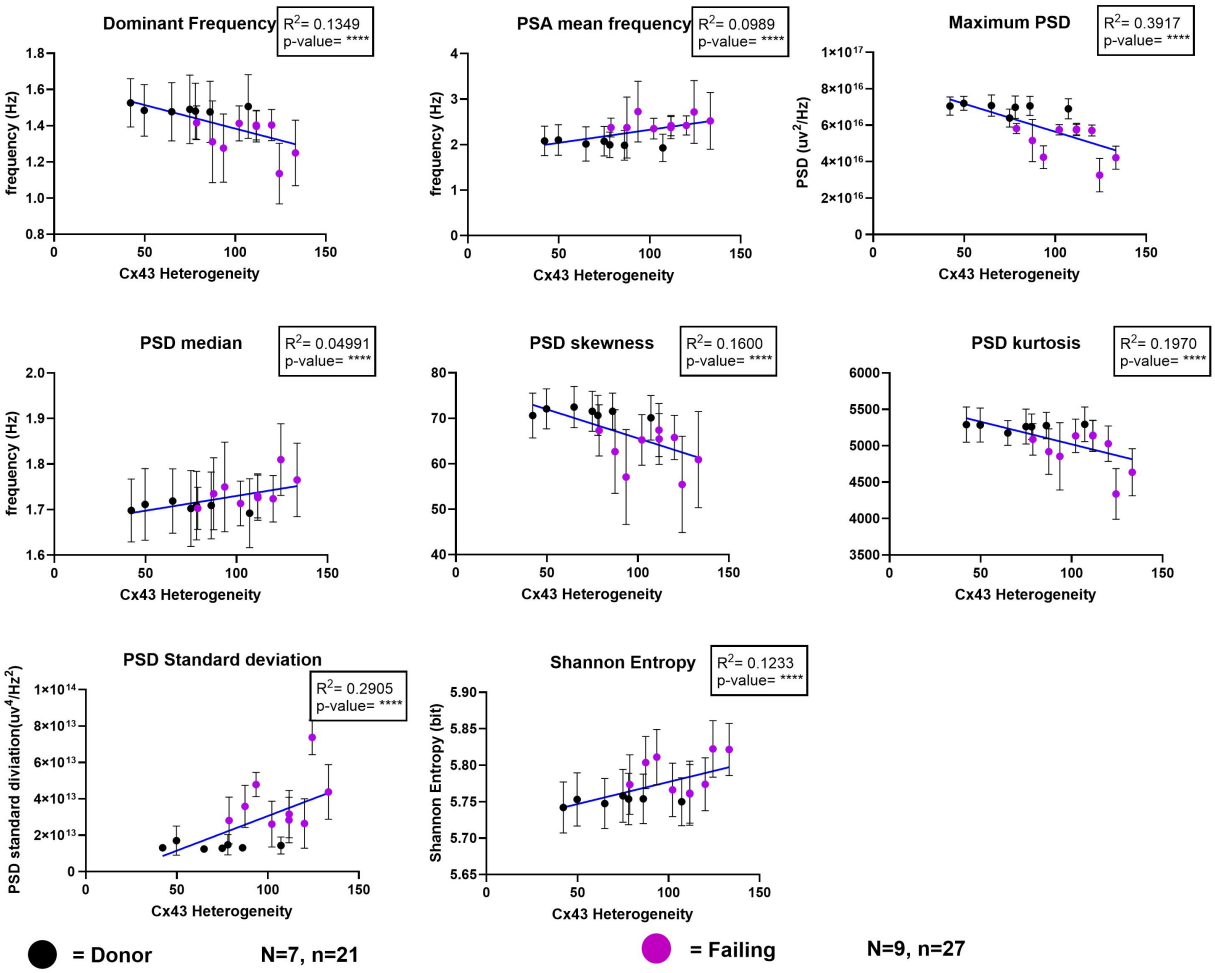


Figure 5.18: Homogeneity of Cx43 with relation to frequency domain features and Shannon entropy of the EGMs of human hearts. For donor hearts: N=7, n=21; for failing hearts: N=9, n=27. Contains 7 graphs of frequency domain features and 1 graph of Shannon entropy from human donor hearts and human failing hearts. The graphs show the frequency domain features and Shannon entropy against the homogeneity of Cx43. A simple linear regression was used to assess the significance of the correlation between the two features, the theoretical line of best fit is shown in blue. Grey error bars represent the standard deviation. All bar charts represent mean ± S.D.; ns $0.05 < p \leq 1$, *$p \leq 0.05$, **$p \leq 0.01$, ***$p \leq 0.001$, ****$p \leq 0.0001$.

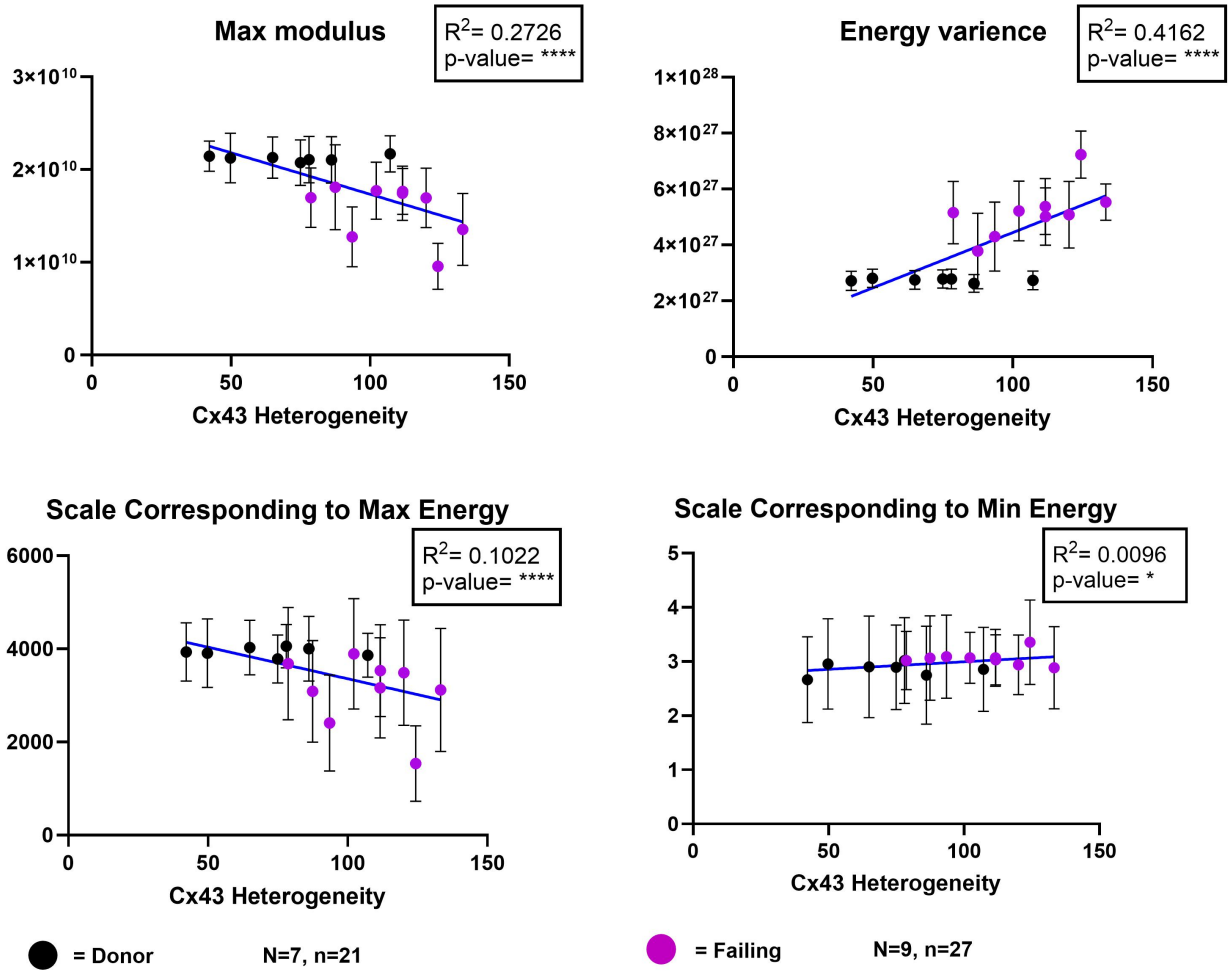


Figure 5.19: Homogeneity of Cx43 with relation to time frequency features of the EGMs of human hearts. For donor hearts: N=7, n=21; for failing hearts: N=9, n=27. Contains 4 graphs of time frequency features from human donor hearts and human failing hearts. The graphs show the time frequency features against the homogeneity of Cx43. A simple linear regression was used to assess the significance of the correlation between the two features, the theoretical line of best fit is shown in blue. Grey error bars represent the standard deviation. All bar charts represent mean ± S.D.; ns $0.05 < p \leq 1$, *$p \leq 0.05$, **$p \leq 0.01$, ***$p \leq 0.001$, ****$p \leq 0.0001$.

Further results show a significant correlation between the lateralisation of Cx43 and all the features (QR interval: $R^2 = 0.1287$, $p \leq 0.0001$, S End interval: $R^2 = 0.1667$, $p \leq 0.0001$, RS interval: $R^2 = 0.03331$, $p \leq 0.0001$, Q to R gradient: $R^2 = 0.2249$, $p \leq 0.0001$, EGM duration: $R^2 = 0.1244$, $p \leq 0.0001$, EGM voltage: $R^2 = 0.1530$, $p \leq 0.0001$, S to End gradient: $R^2 = 0.2140$, $p \leq 0.0001$, Conduction velocity: $R^2 = 0.1621$, $p \leq 0.0001$, Fractionation index: $R^2 = 0.1612$, $p \leq 0.0001$, Dominant frequency: $R^2 = 0.1349$, $p \leq 0.0001$, PSD mean frequency: $R^2 = 0.0989$, $p \leq 0.0001$, Maximum PSD: $R^2 = 0.3917$, $p \leq 0.0001$, PSD median: $R^2 =$

0.04991, p = 0.0018, PSD skewness: $R^2 = 0.1600$, p $\leq$ 0.0001, PSD kurtosis: $R^2 = 0.1970$, p $\leq$ 0.0001, PSD standard deviation: $R^2 = 0.2905$, p $\leq$ 0.0001, Shannon entropy: $R^2 = 0.1233$, p $\leq$ 0.0001, Max modulus: $R^2 = 0.2726$, p $\leq$ 0.0001, Energy variance: $R^2 = 0.4162$, p $\leq$ 0.0001, Scale corresponding to max energy: $R^2 = 0.1022$, p $\leq$ 0.0001, Scale corresponding to min energy: $R^2 = 0.009603$, p = 0.0299). The results are shown in Figure 5.20, Figure 5.21 and Figure 5.22.However, for Cx43 lateralisation, there were very low R2 values comparing to Cx43 expression and homogeneity of Cx43, which suggests that many data points vary off the line of best fit.

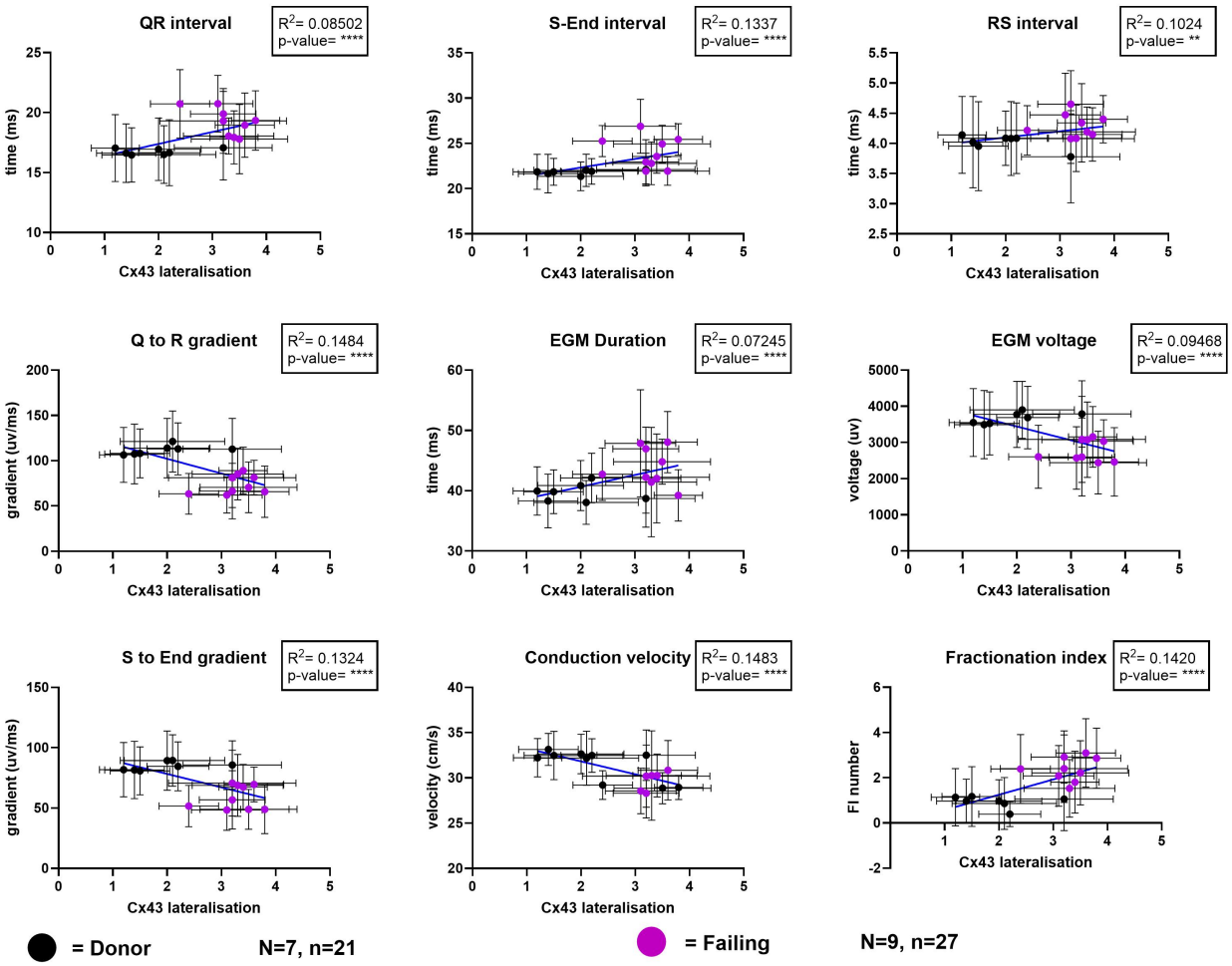


Figure 5.20: Lateralisation of Cx43 with relation to time domain features of the EGMs of human hearts. For donor hearts: N=7, n=21; for failing hearts: N=9, n=27. Contains 9 graphs of time-domain features from human donor hearts and human failing hearts. The graphs show the time-domain features against the lateralisation of Cx43. A simple linear regression was used to assess the significance of the correlation between the two features, the theoretical line of best fit is shown in blue. Grey error bars represent the standard deviation. All bar charts represent mean $\pm$ S.D.; ns 0.05 < p $\leq$ 1, *p $\leq$ 0.05, **p $\leq$ 0.01, ***p $\leq$ 0.001, ****p $\leq$ 0.0001.

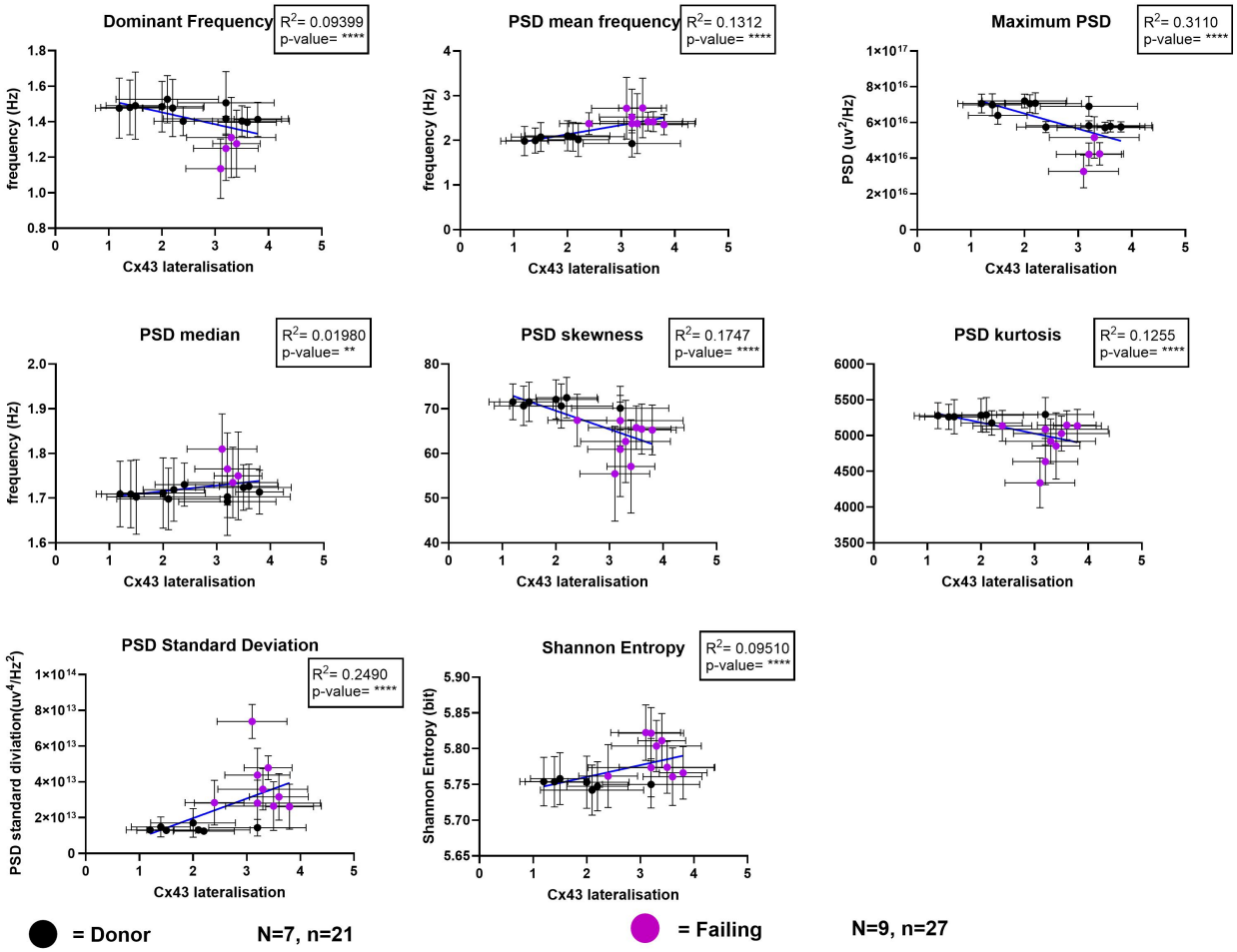


Figure 5.21: Lateralisation of Cx43 with relation to frequency domain features and Shannon entropy of the EGMs of human hearts. For donor hearts: N=7, n=21; for failing hearts: N=9, n=27. Contains 7 graphs of frequency domain features and 1 graph of Shannon entropy from human donor hearts and human failing hearts. The graphs show the frequency domain features and Shannon entropy against the lateralisation of Cx43. A simple linear regression was used to assess the significance of the correlation between the two features, the theoretical line of best fit is shown in blue. Grey error bars represent the standard deviation. All bar charts represent mean ± S.D.; ns $0.05 < p \leq 1$, *$p \leq 0.05$, **$p \leq 0.01$, ***$p \leq 0.001$, ****$p \leq 0.0001$.

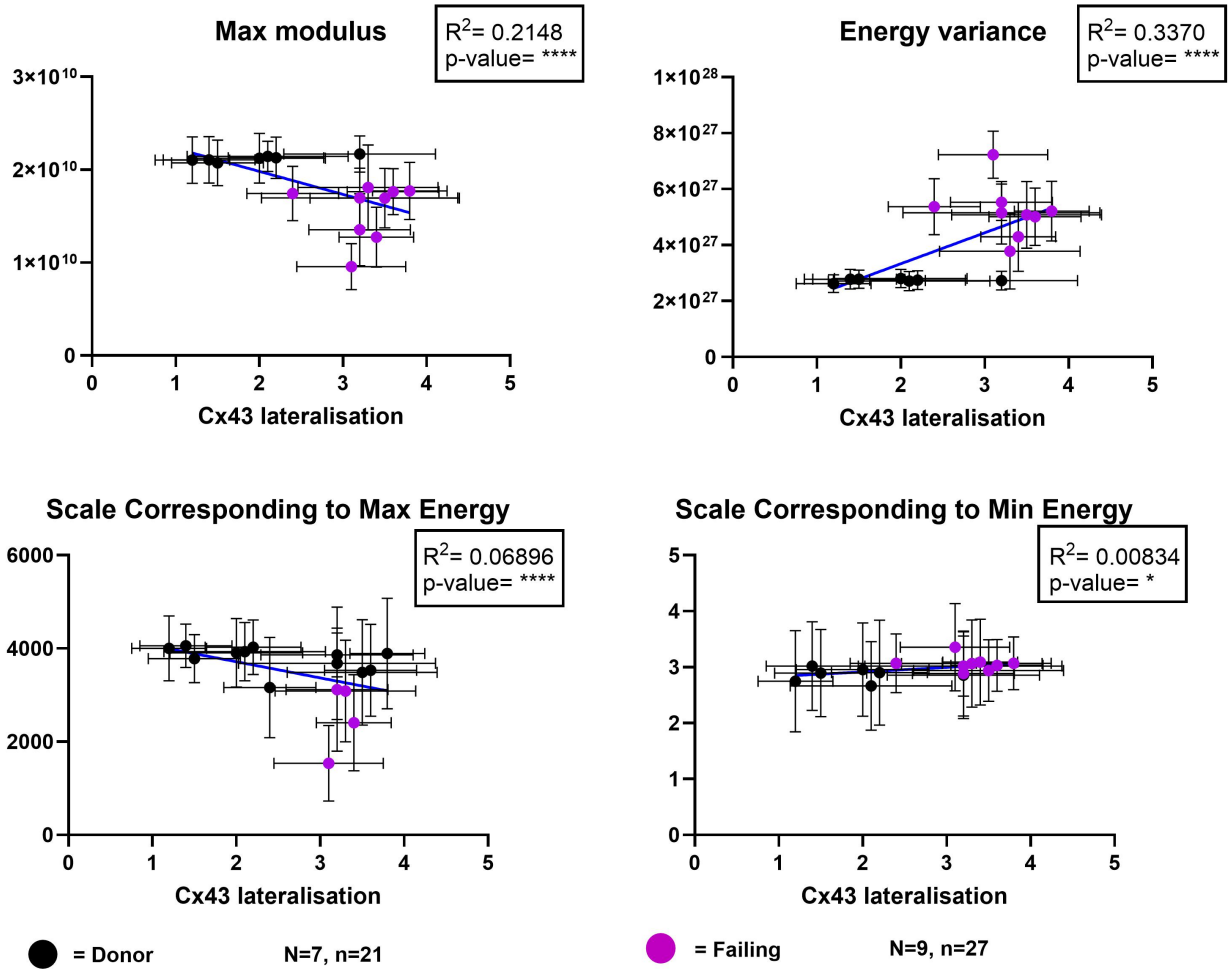


Figure 5.22: Lateralisation of Cx43 with relation to time frequency features of the EGMs of human hearts. For donor hearts: N=7, n=21; for failing hearts: N=9, n=27. Contains 4 graphs of time frequency features from human donor hearts and human failing hearts. The graphs show the time frequency features against the lateralisation of Cx43. A simple linear regression was used to assess the significance of the correlation between the two features, the theoretical line of best fit is shown in blue. Grey error bars represent the standard deviation. All bar charts represent mean ± S.D.; ns $0.05 < p \leq 1$, *$p \leq 0.05$, **$p \leq 0.01$, ***$p \leq 0.001$, ****$p \leq 0.0001$.

Similar to the correlations observed between the collagen index and certain features, heart type also exerted negative influences on the correlations between Cx43 remodelling and these features. Accordingly, these correlations were stratified into two groups—donor hearts and failing hearts—to account for this effect. The correlations between Cx43 expression and these features are shown in figure 5.23, figure 5.24, figure 5.25 and figure 5.26. The results show that significant linear relationship was obtained from several features (donor: Maximum PSD: $R^2 = 0.0315$ $p = 0.0076$; failing: Maximum PSD: $R^2 = 0.2870$, $p \leq 0.0001$, PSD skewness: R^2

= 0.049, p = 0.0003, PSD kurtosis: R^2 = 0.2474, p ≤ 0.0001, PSD standard deviation: R^2 = 0.2678, p ≤ 0.0001, maximum modulus: R^2 = 0.1981, p ≤ 0.0001, Energy variance: R^2 = 0.2788, p ≤ 0.0001.).

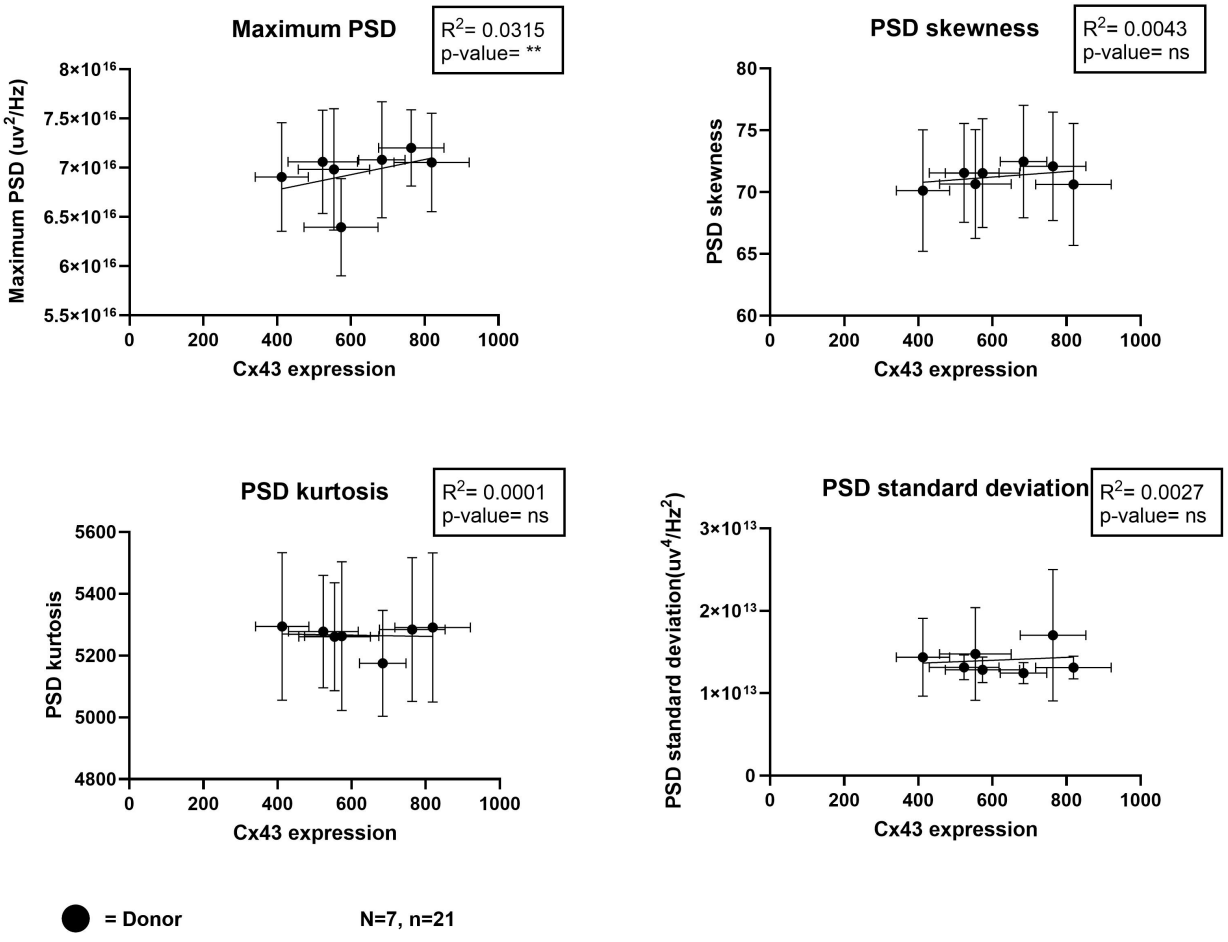


Figure 5.23: Cx43 expression with relation to frequency domain features of the EGMs of human donor hearts (N=7, n=21). Contains 4 graphs of frequency domain features from human donor hearts. The graphs show the frequency domain features and Shannon entropy against the Cx43 expression. A simple linear regression was used to assess the significance of the correlation between the two features, the theoretical line of best fit is shown in blue. Grey error bars represent the standard deviation. All bar charts represent mean ± S.D.; ns 0.05 < p ≤ 1, *p ≤ 0.05, **p ≤ 0.01, ***p ≤ 0.001, ****p ≤ 0.0001.

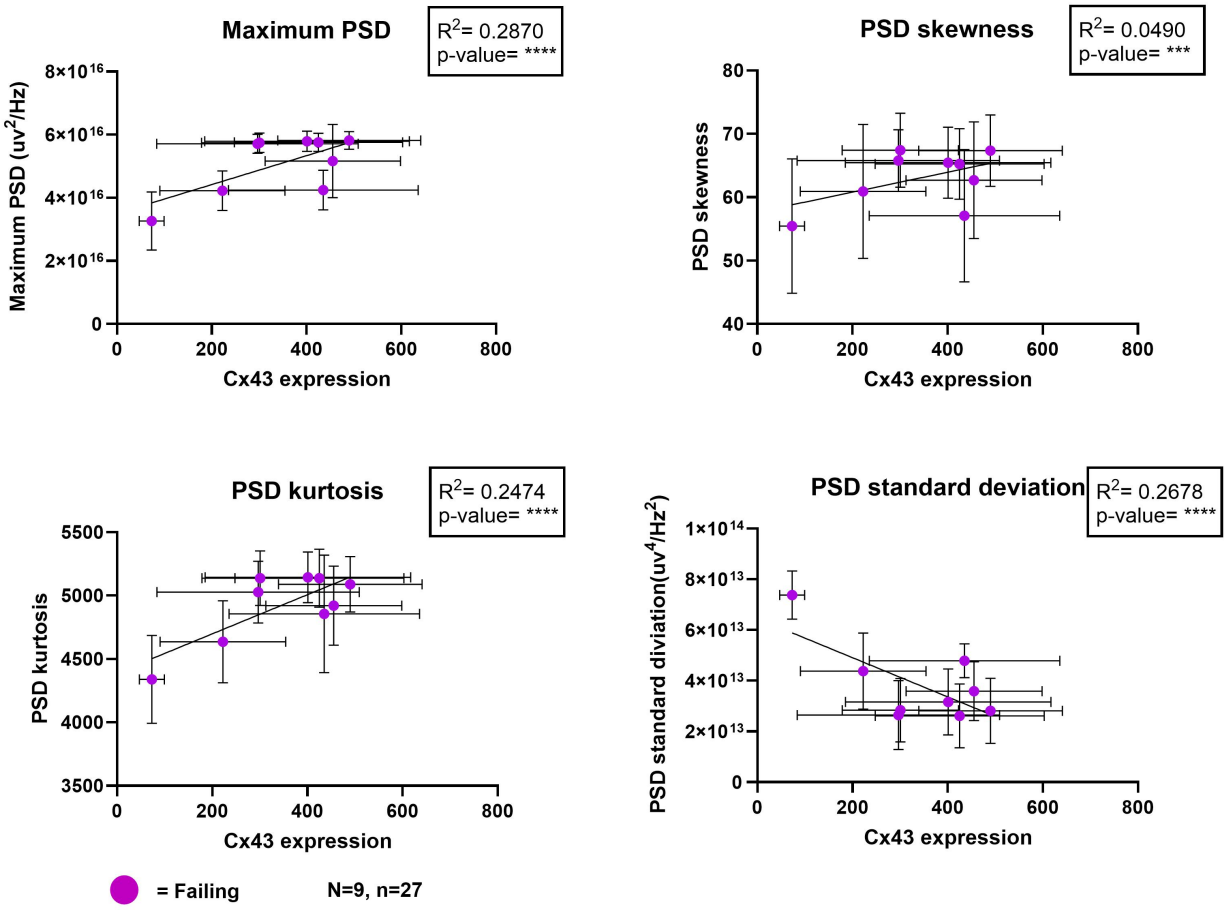


Figure 5.24: Cx43 expression with relation to frequency domain features of the EGMs of human failing hearts (N=9, n=27). Contains 4 graphs of frequency domain features from human failing hearts. The graphs show the frequency domain features against the Cx43 expression. A simple linear regression was used to assess the significance of the correlation between the two features, the theoretical line of best fit is shown in blue. Grey error bars represent the standard deviation. All bar charts represent mean ± S.D.; ns $0.05 < p \leq 1$, *$p \leq 0.05$, **$p \leq 0.01$, ***$p \leq 0.001$, ****$p \leq 0.0001$.

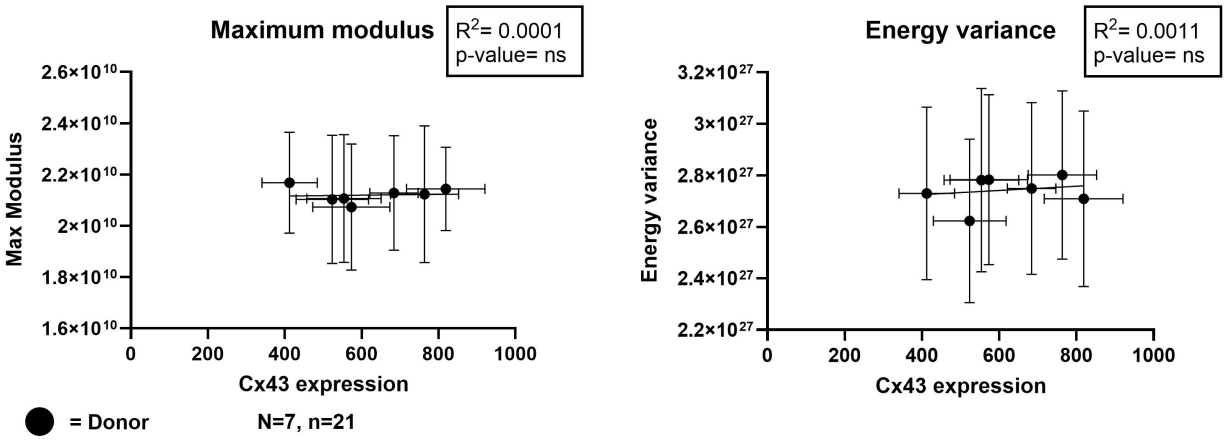


Figure 5.25: Cx43 expression with relation to time frequency features of the EGMs of human donor hearts (N=7, n=21). Contains 2 graphs of time frequency features from human donor hearts. The graphs show the time frequency features against the Cx43 expression. A simple linear regression was used to assess the significance of the correlation between the two features, the theoretical line of best fit is shown in blue. Grey error bars represent the standard deviation. All bar charts represent mean ± S.D.; ns $0.05 < p \leq 1$, *$p \leq 0.05$, **$p \leq 0.01$, ***$p \leq 0.001$, ****$p \leq 0.0001$.

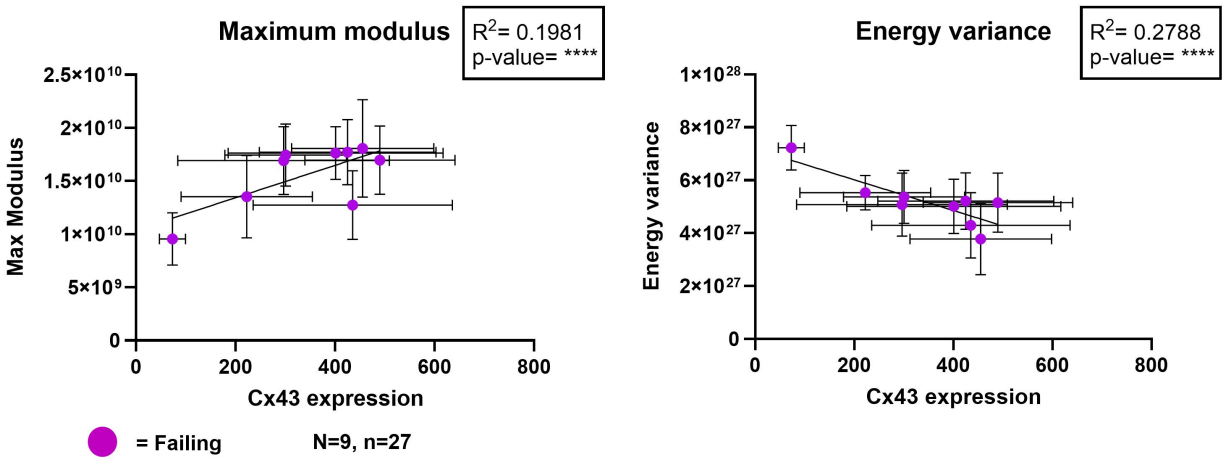


Figure 5.26: Cx43 expression with relation to time frequency features of the EGMs of human failing hearts (N=9, n=27). Contains 2 graphs of time frequency features from human failing hearts. The graphs show the time frequency features against the Cx43 expression. A simple linear regression was used to assess the significance of the correlation between the two features, the theoretical line of best fit is shown in blue. Grey error bars represent the standard deviation. All bar charts represent mean ± S.D.; ns $0.05 < p \leq 1$, *$p \leq 0.05$, **$p \leq 0.01$, ***$p \leq 0.001$, ****$p \leq 0.0001$.

The correlations between homogeneity of Cx43 expression and these features are shown in figure 5.27, figure 5.28, figure 5.29 and figure 5.30. The results show that significant correlations

were obtained from some features (donor: Maximum PSD: $R^2 = 0.0216$, p = 0.0274; failing: Maximum PSD: $R^2 = 0.1040$, p $\leq$ 0.0001, PSD kurtosis: $R^2 = 0.0986$, p $\leq$ 0.0001, PSD standard deviation: $R^2 = 0.0701$, p $\leq$ 0.0001, maximum modulus: $R^2 = 0.0736$, p $\leq$ 0.0001, Energy variance: $R^2 = 0.1515$, p $\leq$ 0.0001.).

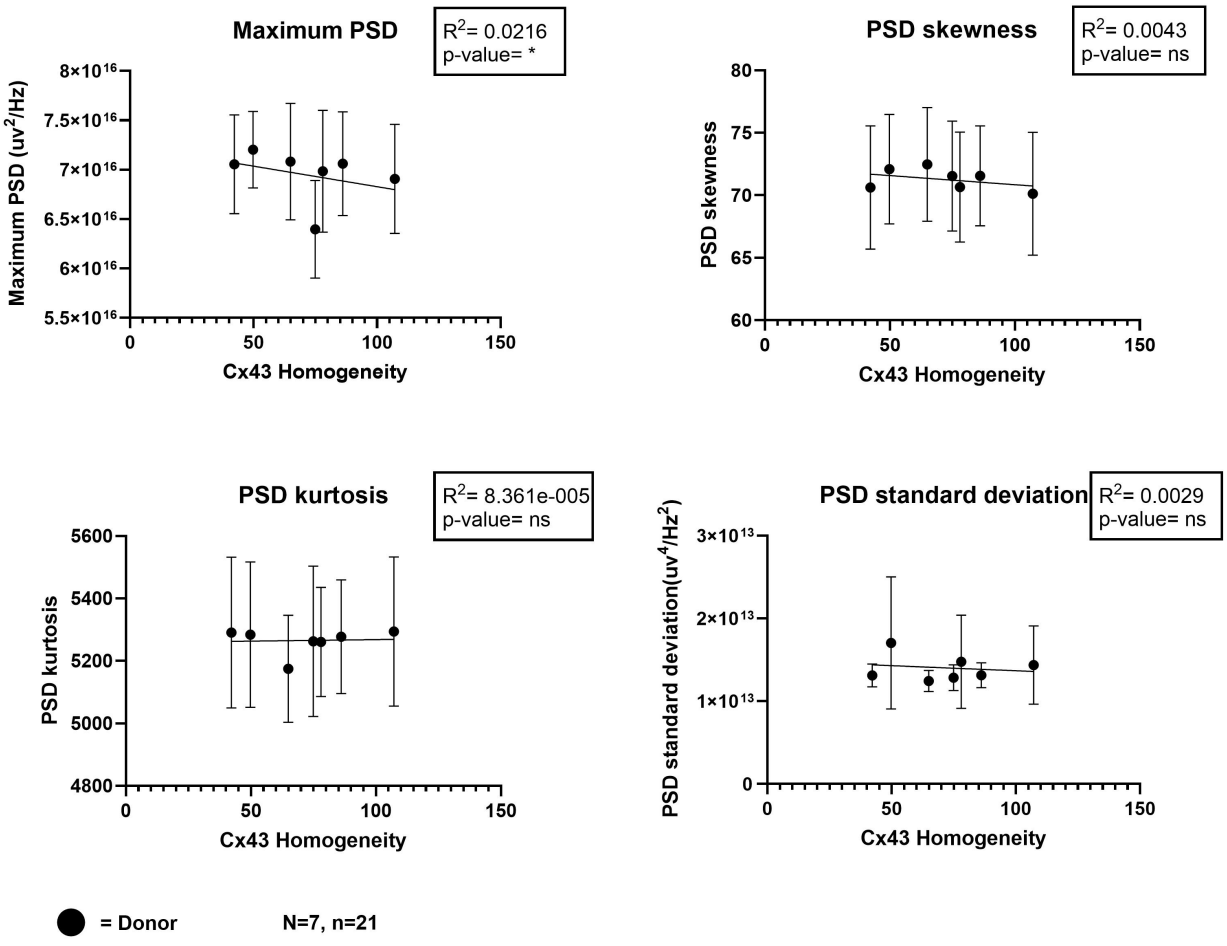


Figure 5.27: Homogeneity of Cx43 with relation to frequency domain features of the EGMs of human donor hearts (N=7, n=21). Contains 4 graphs of frequency domain features from human donor hearts. The graphs show the frequency domain features against the homogeneity of Cx43. A simple linear regression was used to assess the significance of the correlation between the two features, the theoretical line of best fit is shown in blue. Grey error bars represent the standard deviation. All bar charts represent mean ± S.D.; ns $0.05 <$ p ≤ 1, *p ≤ 0.05, **p $\leq$ 0.01, ***p ≤ 0.001, ****p ≤ 0.0001.

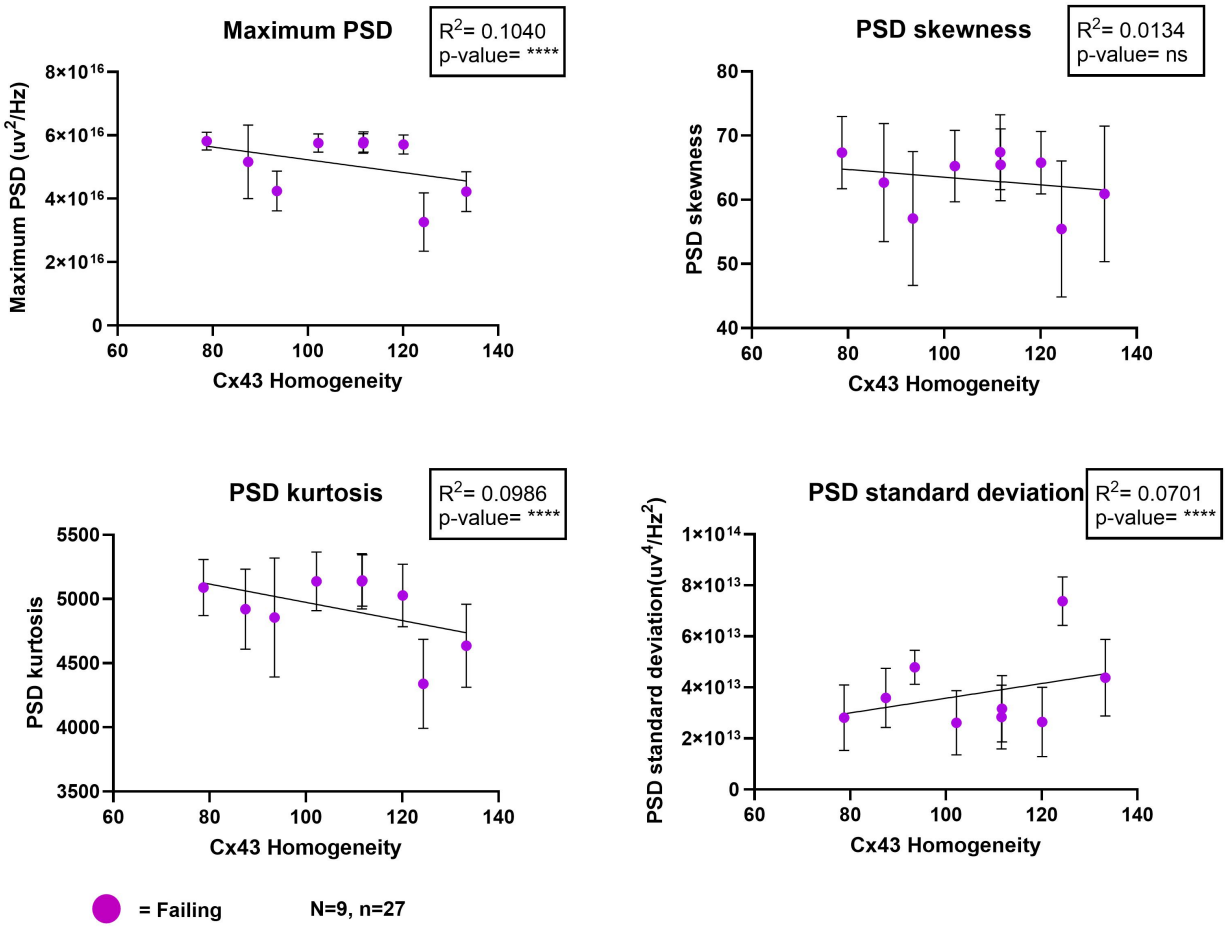


Figure 5.28: Homogeneity of Cx43 with relation to frequency domain features of the EGMs of human failing hearts (N=9, n=27). Contains 4 graphs of frequency domain features from human failing hearts. The graphs show the frequency domain features against the homogeneity of Cx43. A simple linear regression was used to assess the significance of the correlation between the two features, the theoretical line of best fit is shown in blue. Grey error bars represent the standard deviation. All bar charts represent mean ± S.D.; ns $0.05 < p \leq 1$, *$p \leq 0.05$, **$p \leq 0.01$, ***$p \leq 0.001$, ****$p \leq 0.0001$.

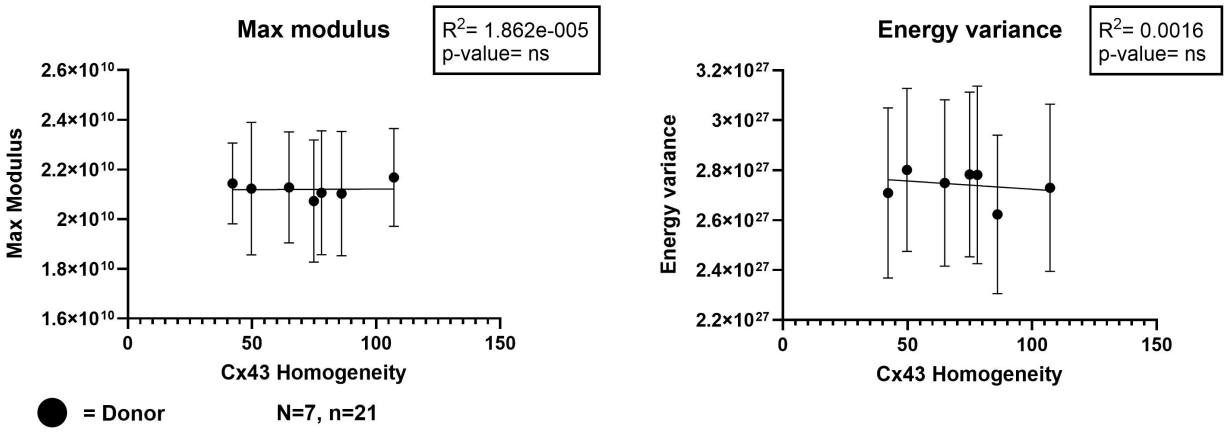


Figure 5.29: Homogeneity of Cx43 with relation to time frequency features of the EGMs of human donor hearts (N=7, n=21). Contains 2 graphs of time frequency features from human donor hearts. The graphs show the time frequency features against the homogeneity of Cx43. A simple linear regression was used to assess the significance of the correlation between the two features, the theoretical line of best fit is shown in blue. Grey error bars represent the standard deviation. All bar charts represent mean ± S.D.; ns $0.05 < p \leq 1$, *$p \leq 0.05$, **$p \leq 0.01$, ***$p \leq 0.001$, ****$p \leq 0.0001$.

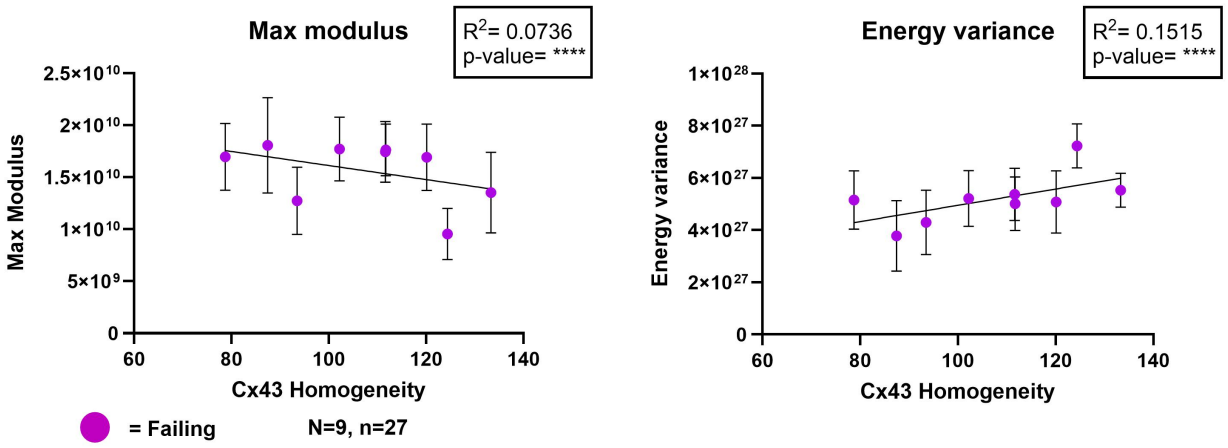


Figure 5.30: Homogeneity of Cx43 with relation to time frequency features of the EGMs of human failing hearts (N=9, n=27). Contains 2 graphs of time frequency features from human failing hearts. The graphs show the time frequency features against the homogeneity of Cx43. A simple linear regression was used to assess the significance of the correlation between the two features, the theoretical line of best fit is shown in blue. Grey error bars represent the standard deviation. All bar charts represent mean ± S.D.; ns $0.05 < p \leq 1$, *$p \leq 0.05$, **$p \leq 0.01$, ***$p \leq 0.001$, ****$p \leq 0.0001$.

The correlations between the lateralisation of Cx43 and these features are shown in figure 5.27, figure 5.28, figure 5.29 and figure 5.30. The results show that most of the features do not have

significant correlation after the hearts are separated into two groups, significant correlation was only obtained from Energy variance of failing group ($R^2 = 0.0250$, p = 0.0098).

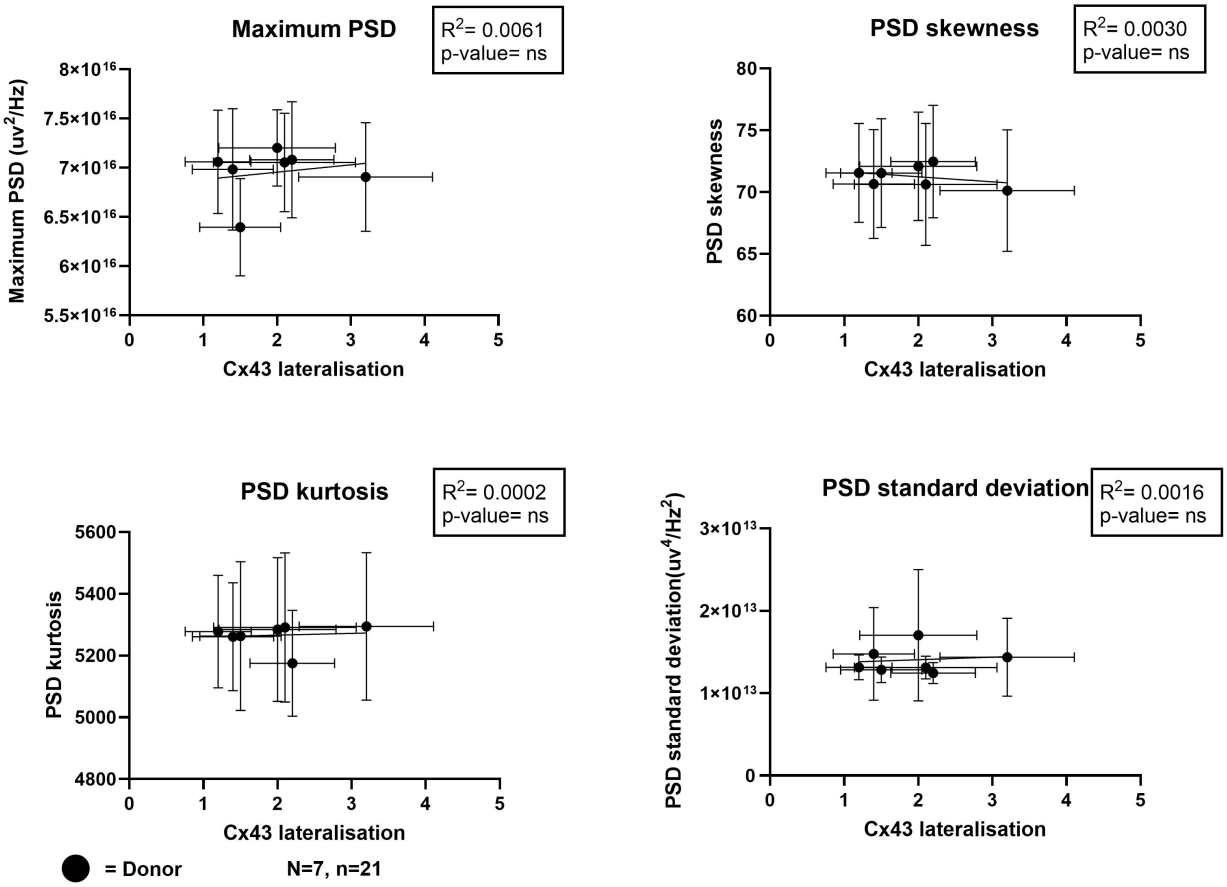


Figure 5.31: Lateralisation of Cx43 with relation to frequency domain features of the EGMs of human donor hearts (N=7, n=21). Contains 4 graphs of frequency domain features from human donor hearts. The graphs show the frequency domain features against the lateralisation of Cx43. A simple linear regression was used to assess the significance of the correlation between the two features, the theoretical line of best fit is shown in blue. Grey error bars represent the standard deviation. All bar charts represent mean ± S.D.; ns $0.05 < p \leq 1$, *$p \leq 0.05$, **$p \leq 0.01$, ***$p \leq 0.001$, ****$p \leq 0.0001$.

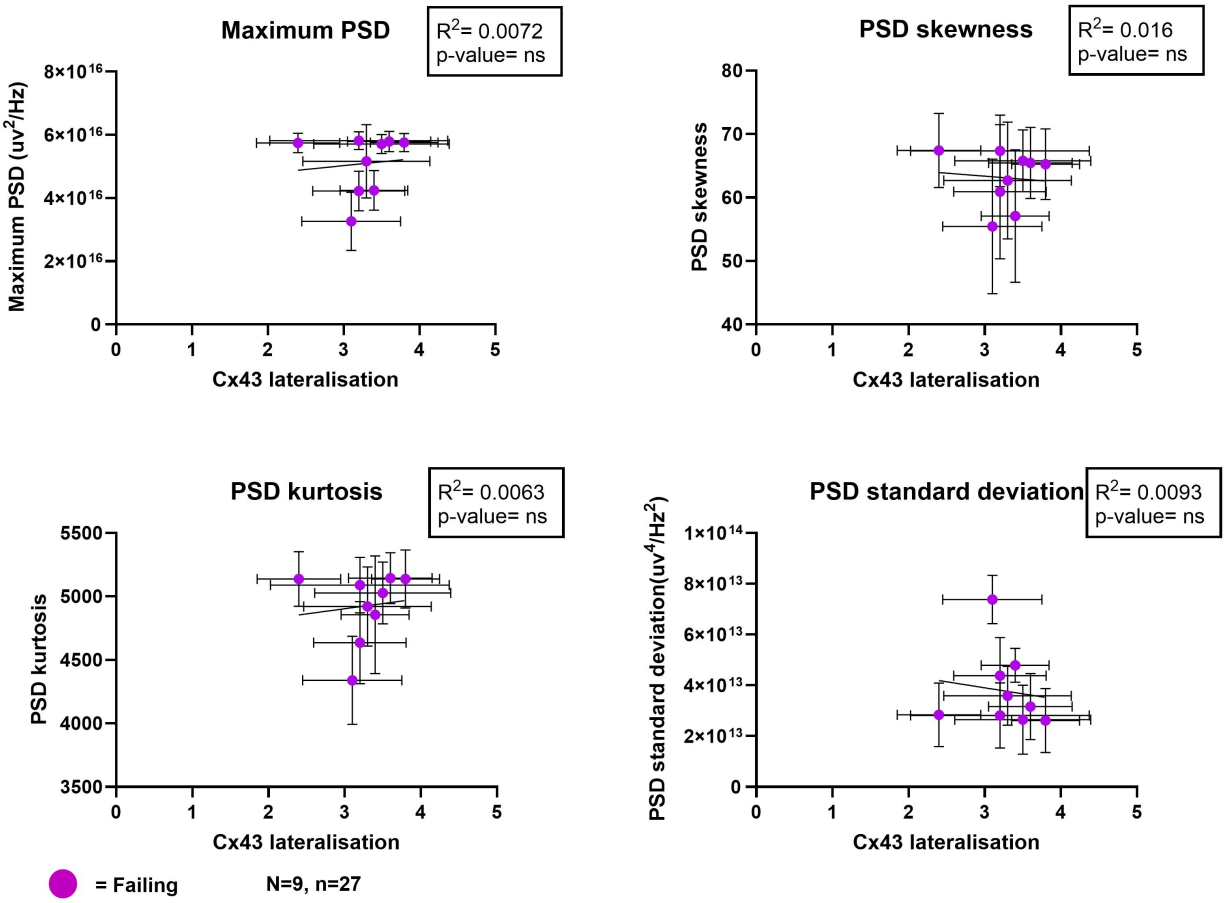


Figure 5.32: Lateralisation of Cx43 with relation to frequency domain features of the EGMs of human failing hearts (N=9, n=27). Contains 4 graphs of frequency domain features from human failing hearts. The graphs show the frequency domain features against the lateralisation of Cx43. A simple linear regression was used to assess the significance of the correlation between the two features, the theoretical line of best fit is shown in blue. Grey error bars represent the standard deviation. All bar charts represent mean ± S.D.; ns $0.05 < p \leq 1$, *$p \leq 0.05$, **$p \leq 0.01$, ***$p \leq 0.001$, ****$p \leq 0.0001$.

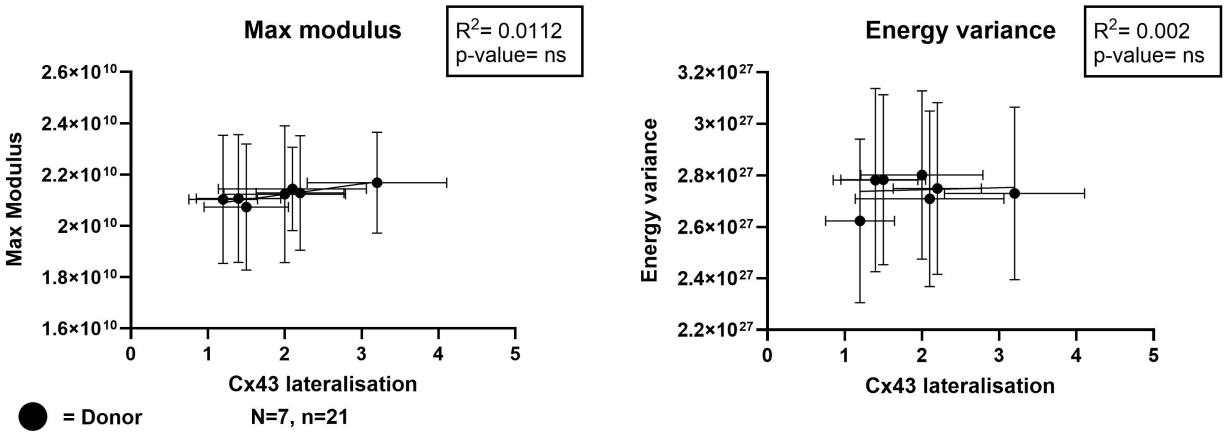


Figure 5.33: Lateralisation of Cx43 with relation to time frequency features of the EGMs of human donor hearts (N=7, n=21). Contains 2 graphs of time frequency features from human donor hearts. The graphs show the time frequency features against the lateralisation of Cx43. A simple linear regression was used to assess the significance of the correlation between the two features, the theoretical line of best fit is shown in blue. Grey error bars represent the standard deviation. All bar charts represent mean ± S.D.; ns $0.05 < p \leq 1$, *$p \leq 0.05$, **$p \leq 0.01$, ***$p \leq 0.001$, ****$p \leq 0.0001$.

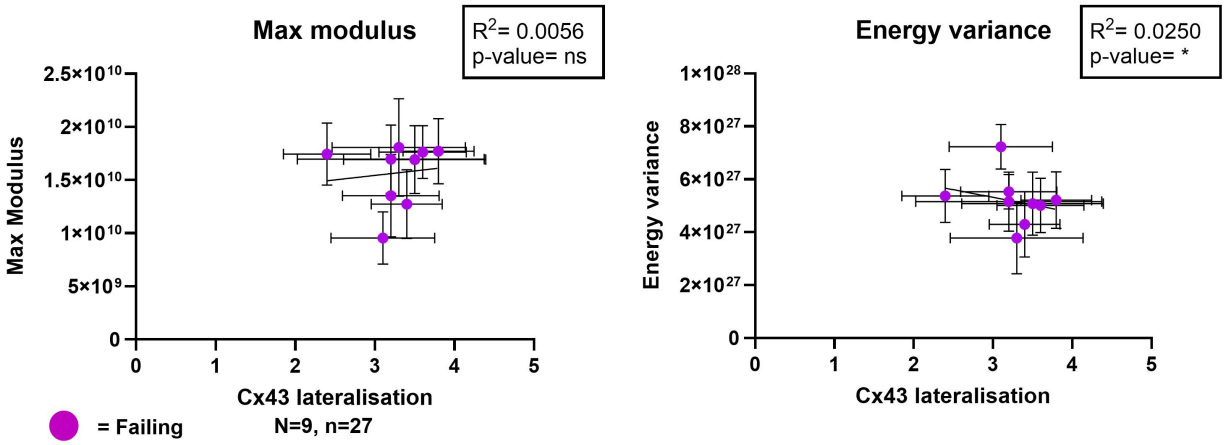


Figure 5.34: Lateralisation of Cx43 with relation to time frequency features of the EGMs of human failing hearts (N=9, n=27). Contains 2 graphs of time frequency features from human failing hearts. The graphs show the time frequency features against the lateralisation of Cx43. A simple linear regression was used to assess the significance of the correlation between the two features, the theoretical line of best fit is shown in blue. Grey error bars represent the standard deviation. All bar charts represent mean ± S.D.; ns $0.05 < p \leq 1$, *$p \leq 0.05$, **$p \leq 0.01$, ***$p \leq 0.001$, ****$p \leq 0.0001$.

5.3.4 $Na_v1.5$ ion channel remodelling and its relationship between scar in human donor and human failing samples

To investigate the structural characteristics of $Na_v1.5$ ion channel remodelling ($Na_v1.5$ ion channel expression, homogeneity), donor hearts (N=7, n=21) and failing hearts (N=9, n=27) were immunolabelled for $Na_v1.5$ ion channel visualisation. The statistical analysis shows that all structural characteristics' changes are significant. The results are shown in Figure 5.35. A significant decrease in $Na_v1.5$ ion channel expression (Donor: 4370 ± 1348 pixels, Failing: 2249 ± 1592 pixels, p = 0.0082) and an increase in $Na_v1.5$ ion channel heterogeneity (Donor: 607.6 ± 214.2 pixels, Failing: 1092 ± 554.5 pixels, p = 0.0356) were obtained from human failing hearts compared to human donor hearts.

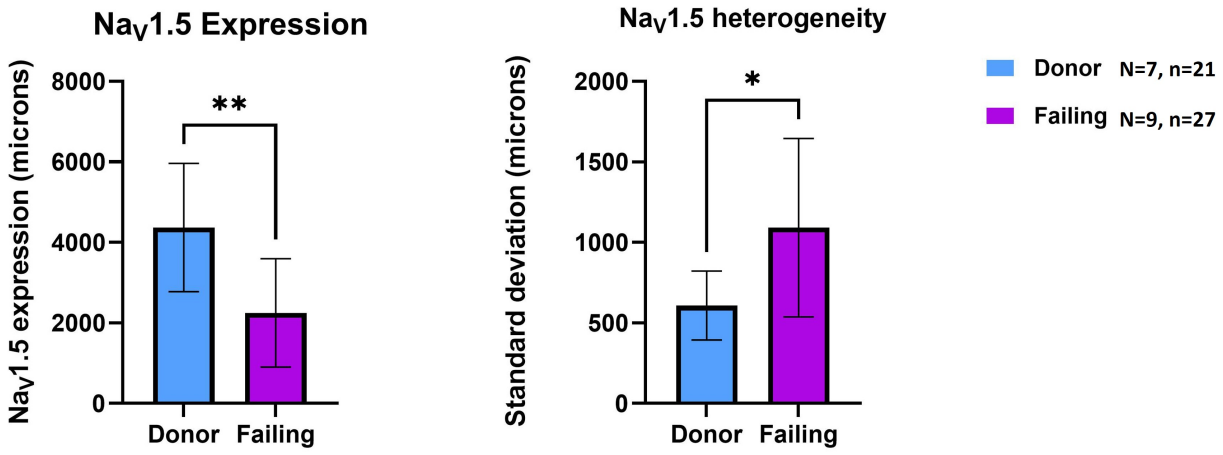


Figure 5.35: $Na_v1.5$ ion channel remodelling characteristics with relation to heart types. For donor hearts: N=7, n=21; for failing hearts: N=9, n=27. (A) $Na_v1.5$ ion channel expression. (B) $Na_v1.5$ ion channel heterogeneity. All bar charts represent mean ± S.D.; ns $0.05 < p \leq 1$ *$p \leq 0.05$, **$p \leq 0.01$, ***$p \leq 0.001$, ****$p \leq 0.0001$.

The next step was to investigate if there is a relationship between scar location and $Na_v1.5$ ion channel remodelling in failing and donor hearts same as gap junctional remodelling. To explore this relationship the left ventricle myocardium samples were immunolabelled for $Na_v1.5$ ion channel, and autofluorescence of collagen was visualised to identify the locations of the scars. The results are shown in Figure 5.36. A decrease in $Na_v1.5$ ion channel expression in areas near scar compared to remote areas was obtained, due to higher $Na_v1.5$ ion channel remodelling

near scar (Donor remote: 5242 ± 1857 pixels, Donor scar: 3238 ± 1163 pixels, p = 0.0372; Failing remote: 3165 ± 1335 pixels, Failing scar: 1469 ± 790.5 pixels, p = 0.0484). However, statistical analysis shows that the changes in the heterogeneity of the Na_v 1.5 ion channel are not significant when p = 0.05, some visual patterns were observed. There was an increase in Na_v 1.5 ion channel heterogeneity in scar areas of donor heart compared to remote areas of donor hearts (Donor remote: 1237 ± 589.5 pixels, Donor scar: 1392 ± 899.5 pixels, p = 0.9737), but such pattern was not obtained from the failing hearts (Failing remote: 945.3 ± 543.1 pixels, Failing scar: 861.4 ± 683.3 pixelss, p = 0.9936).

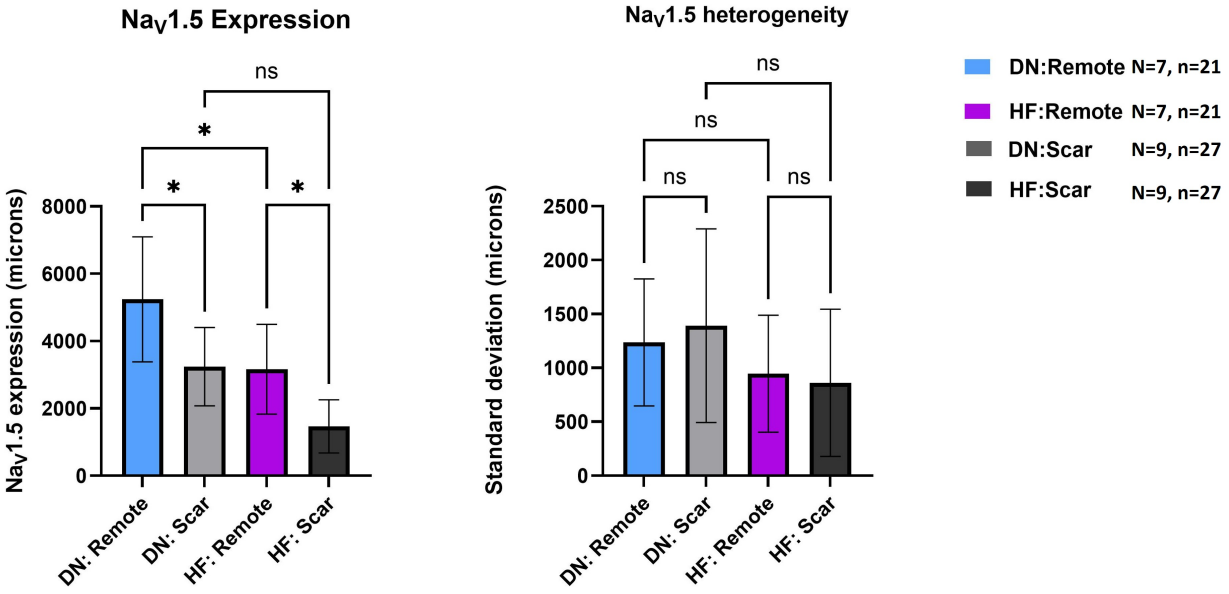


Figure 5.36: Na_v1.5 ion channel remodelling characteristics with relation to scar. For donor hearts: N=7, n=21; for failing hearts: N=9, n=27. (A) Na_v1.5 ion channel expression. (B) Na_v1.5 ion channel heterogeneity. All bar charts represent mean ± S.D.; ns $0.05 < p \leq 1$ *p ≤ 0.05, **p ≤ 0.01, ***p ≤ 0.001, ****p ≤ 0.0001.

5.3.5 Characterisation of EGM feature modifications correlating to Na_v1.5 ion channel remodelling

To explore the correlation between Na_v1.5 ion channel remodelling and EGM features within the hearts, MEA experiments and Na_v1.5 ion channel immunohistochemistry were carried out on failing and donor human left ventricle myocardium samples. The correlation between Na_v1.5

ion channel expression and EGM features are shown in Figure 5.37, Figure 5.38 and Figure 5.39. Results show a significant linear relationship between Cx43 expression and all the features (QR interval: $R^2 = 0.1314$, $p \leq 0.0001$, S End interval: $R^2 = 0.1670$, $p \leq 0.0001$, RS interval: $R^2 = 0.02831$, $p = 0.0002$, Q to R gradient: $R^2 = 0.2162$, $p \leq 0.0001$, EGM duration: $R^2 = 0.09129$, $p \leq 0.0001$, EGM voltage: $R^2 = 0.1502$, $p \leq 0.0001$, S to End gradient: $R^2 = 0.2043$, $p \leq 0.0001$, Conduction velocity: $R^2 = 0.1361$, $p \leq 0.0001$, Fractionation index: $R^2 = 0.1166$, $p \leq 0.0001$, Dominant frequency: $R^2 = 0.09294$, $p \leq 0.0001$, PSD mean frequency: $R^2 = 0.06404$, $p \leq 0.0001$, Maximum PSD: $R^2 = 0.2393$, $p \leq 0.0001$, PSD median: $R^2 = 0.03382$, $p \leq 0.0001$, PSD skewness: $R^2 = 0.07899$, $p \leq 0.0001$, PSD kurtosis: $R^2 = 0.1457$, $p \leq 0.0001$, PSD standard deviation: $R^2 = 0.1912$, $p \leq 0.0001$, Shannon entropy: $R^2 = 0.06552$, $p \leq 0.0001$, Max modulus: $R^2 = 0.1971$, $p \leq 0.0001$, Energy variance: $R^2 = 0.4268$, $p \leq 0.0001$, Scale corresponding to max energy: $R^2 = 0.04667$, $p \leq 0.0001$, Scale corresponding to min energy: $R^2 = 0.01630$, $p = 0.0046$). For all the features, the R^2 values are lower than the R^2 values of the linear relationship between Cx43 expression and EGM features.

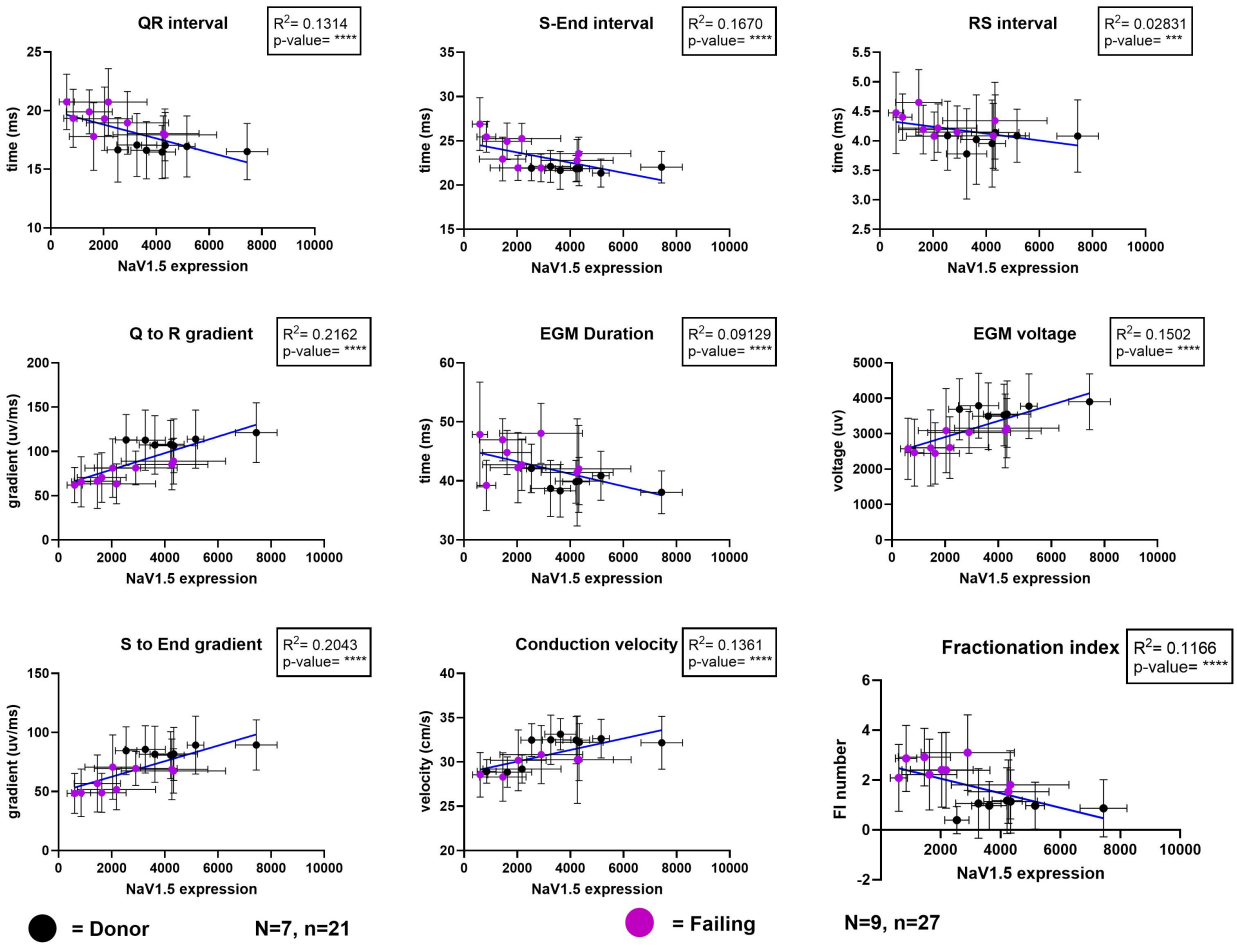


Figure 5.37: $Na_v1.5$ ion channel expression with relation to time domain features of the EGMs of human hearts. For donor hearts: N=7, n=21; for failing hearts: N=9, n=27. Contains 9 graphs of time-domain features from human donor hearts and human failing hearts. The graphs show the time-domain features against $Na_v1.5$ ion channel expression. A simple linear regression was used to assess the significance of the correlation between the two features, the theoretical line of best fit is shown in blue. Grey error bars represent the standard deviation. All bar charts represent mean ± S.D.; ns $0.05 < p \leq 1$, *$p \leq 0.05$, **$p \leq 0.01$, ***$p \leq 0.001$, ****$p \leq 0.0001$.

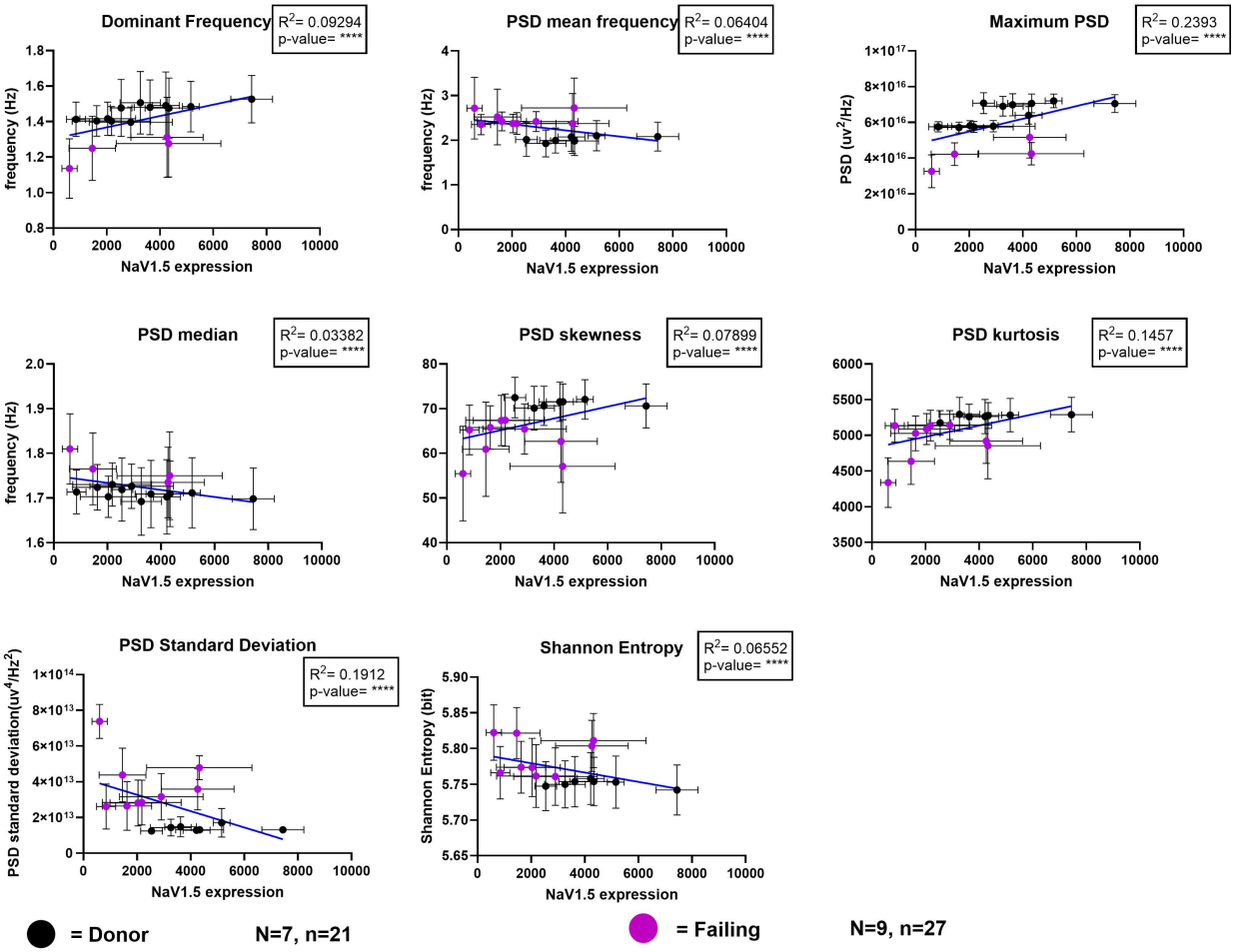


Figure 5.38: $Na_v1.5$ ion channel expression with relation to frequency domain features and Shannon entropy of the EGMs of human hearts. For donor hearts: N=7, n=21; for failing hearts: N=9, n=27. Contains 7 graphs of frequency domain features and 1 graph of Shannon entropy from human donor hearts and human failing hearts. The graphs show the frequency domain features and Shannon entropy against $Na_v1.5$ ion channel expression. A simple linear regression was used to assess the significance of the correlation between the two features, the theoretical line of best fit is shown in blue. Grey error bars represent the standard deviation. All bar charts represent mean ± S.D.; ns $0.05 < p \leq 1$, *$p \leq 0.05$, **$p \leq 0.01$, ***$p \leq 0.001$, ****$p \leq 0.0001$.

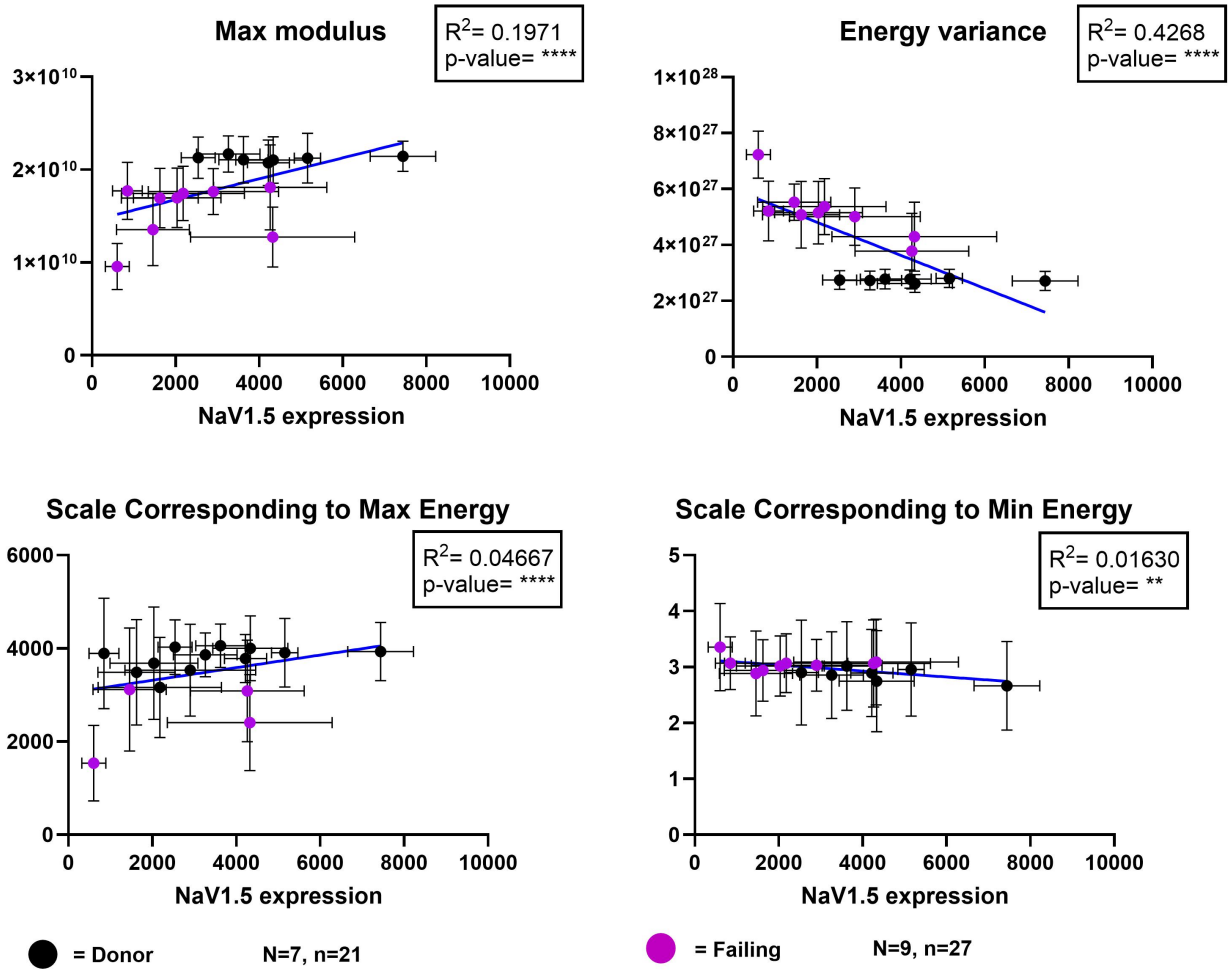


Figure 5.39: $Na_v1.5$ ion channel expression with relation to time frequency features of the EGMs of human hearts. For donor hearts: N=7, n=21; for failing hearts: N=9, n=27. Contains 4 graphs of time frequency features from human donor hearts and human failing hearts. The graphs show the time frequency features against $Na_v1.5$ ion channel expression. A simple linear regression was used to assess the significance of the correlation between the two features, the theoretical line of best fit is shown in blue. Grey error bars represent the standard deviation. All bar charts represent mean ± S.D.; ns $0.05 < p \leq 1$, *$p \leq 0.05$, **$p \leq 0.01$, ***$p \leq 0.001$, ****$p \leq 0.0001$.

The correlation between homogeneity of $Na_v1.5$ ion channel expression and EGM features are shown in Figure 5.17, Figure 5.18 and Figure 5.19. The results show a significant linear relationship between the homogeneity of the Na_v 1.5 ion channel expression and 16 features, no significant linear relationship was obtained from the rest 5 features. In addition, the R^2 values for most the linear regressions are extremely low (lower than 0.05) (QR interval: $R^2 = 0.01860$, $p = 0.0024$, S End interval: $R^2 = 0.0005897$, $p = 0.5914$, RS interval: $R^2 = 0.001052$, $p = 0.4733$, Q to R gradient: $R^2 = 0.02843$, $p = 0.0002$, EGM duration: $R^2 = 0.01818$, p

= 0.0028, EGM voltage: R^2 = 0.01254, p = 0.0130, S to End gradient: R^2 = 0.01586, p = 0.0054, Conduction velocity: R^2 = 0.02254, p = 0.0008, Fractionation index: R^2 = 0.03988, p $\leq$ 0.0001, Dominant frequency: R^2 = 0.02345, p = 0.0006, PSD mean frequency: R^2 =0.06048, p $\leq$ 0.0001, Maximum PSD: R^2 = 0.09385, p $\leq$ 0.0001, PSD median: R^2 = 0.001941, p = 0.3300, PSD skewness: R^2 = 0.06358, p $\leq$ 0.0001, PSD kurtosis: R^2 = 0.007041, p = 0.0632, PSD standard deviation: R^2 = 0.05167, p $\leq$ 0.0001, Shannon entropy: R^2 = 0.03047, p $\leq$ 0.0001, Max modulus: R^2 = 0.05792, p $\leq$ 0.0001, Energy variance: R^2 = 0.03120, p $\leq$ 0.0001, Scale corresponding to max energy: R^2 = 0.03404, p $\leq$ 0.0001, Scale corresponding to min energy: R^2 = 0.0005008, p = 0.6208). Such results illustrate that heterogeneity of $Na_v1.5$ ion channel has no effect on EGM features.

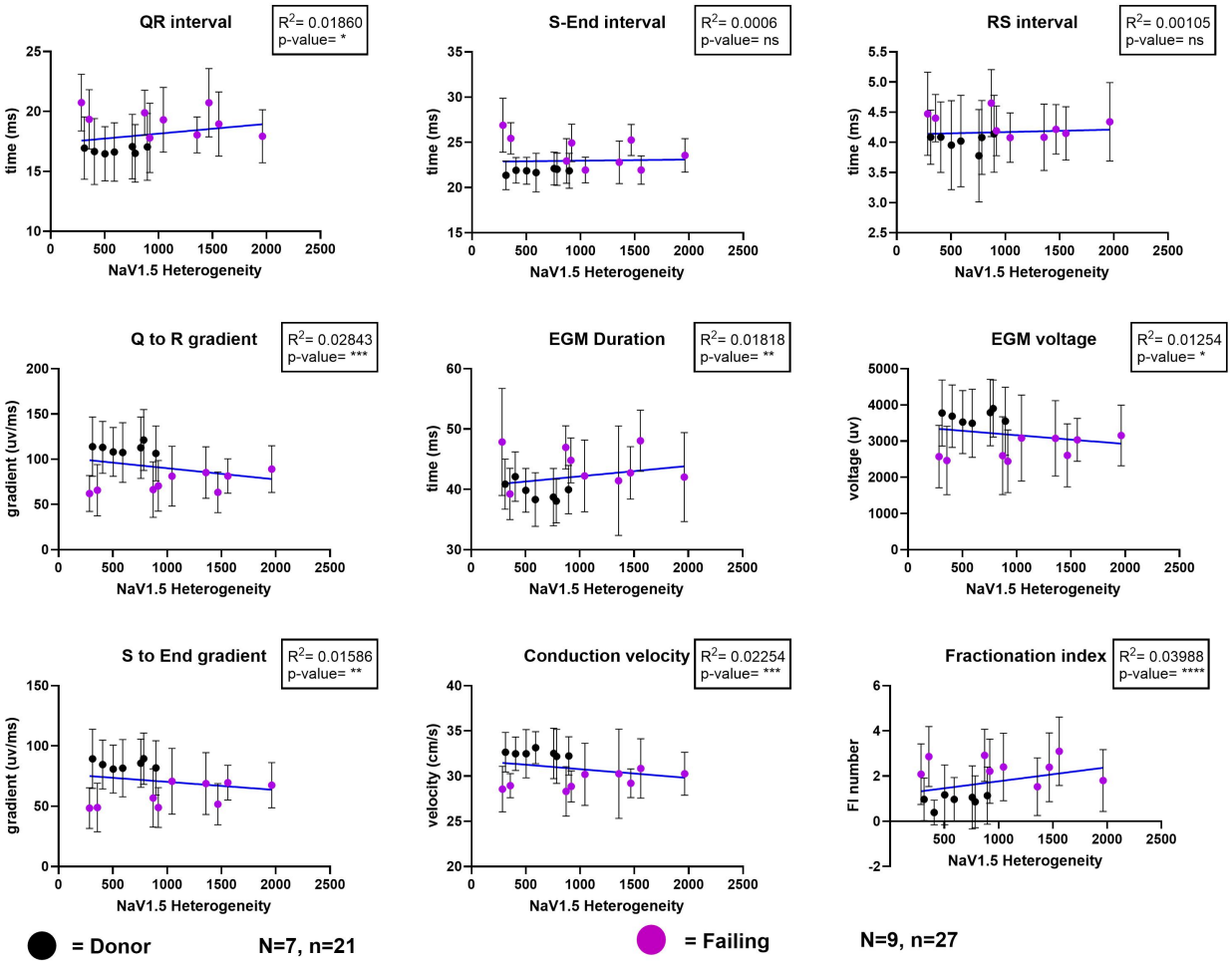


Figure 5.40: Homogeneity of $Na_v1.5$ ion channel with relation to time domain features of the EGMs of human hearts. For donor hearts: N=7, n=21; for failing hearts: N=9, n=27. Contains 9 graphs of time-domain features from human donor hearts and human failing hearts. The graphs show the time-domain features against the homogeneity of $Na_v1.5$ ion channel. A simple linear regression was used to assess the significance of the correlation between the two features, the theoretical line of best fit is shown in blue. Grey error bars represent the standard deviation. All bar charts represent mean ± S.D.; ns $0.05 < p \leq 1$, *$p \leq 0.05$, **$p \leq 0.01$, ***$p \leq 0.001$, ****$p \leq 0.0001$.

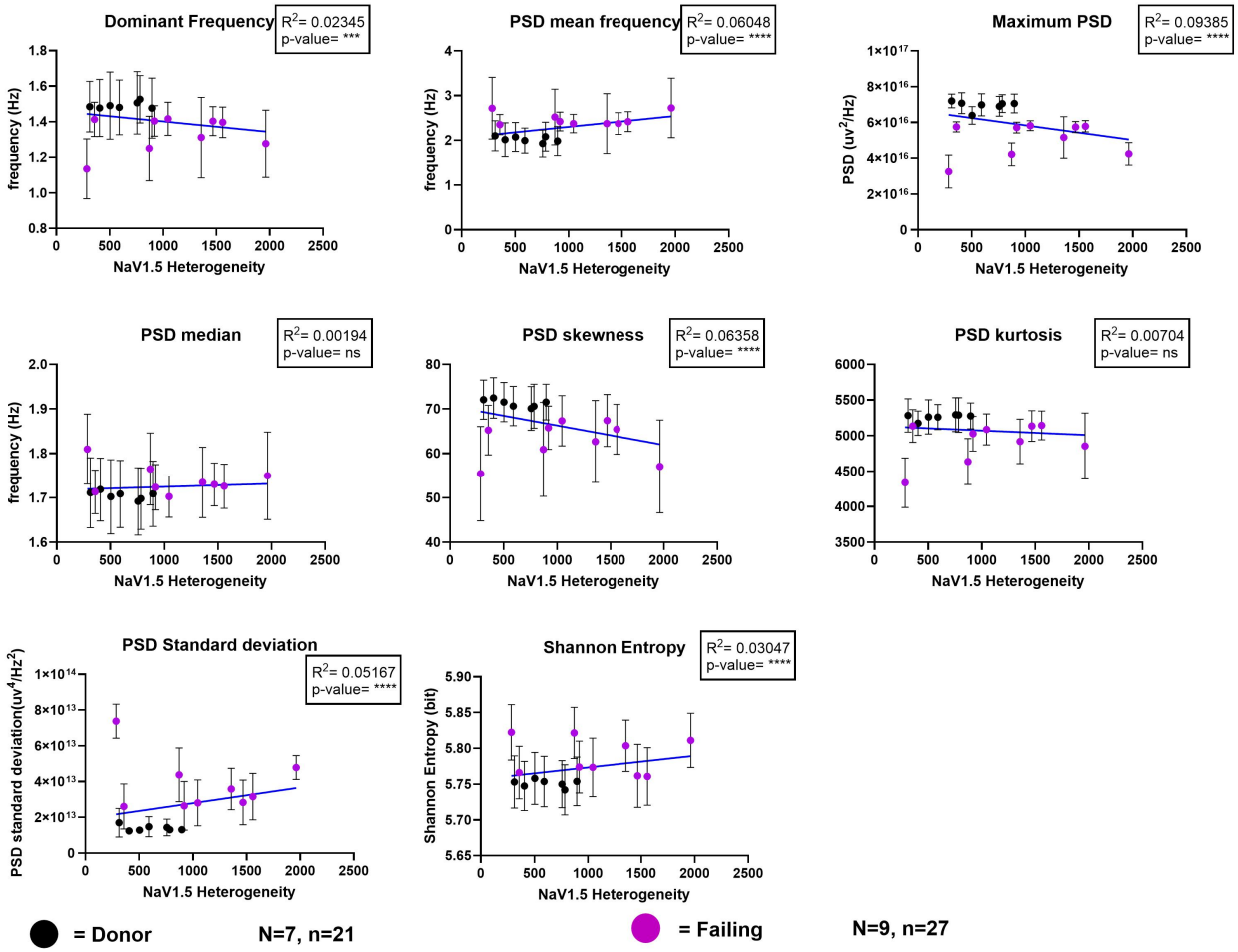


Figure 5.41: Homogeneity of $Na_v1.5$ ion channel with relation to frequency domain features and Shannon entropy of the EGMs of human hearts. For donor hearts: N=7, n=21; for failing hearts: N=9, n=27. Contains 7 graphs of frequency domain features and 1 graph of Shannon entropy from human donor hearts and human failing hearts. The graphs show the frequency domain features and Shannon entropy against the homogeneity of $Na_v1.5$ ion channel. A simple linear regression was used to assess the significance of the correlation between the two features, the theoretical line of best fit is shown in blue. Grey error bars represent the standard deviation. All bar charts represent mean ± S.D.; ns $0.05 < p \leq 1$, *$p \leq 0.05$, **$p \leq 0.01$, ***$p \leq 0.001$, ****$p \leq 0.0001$.

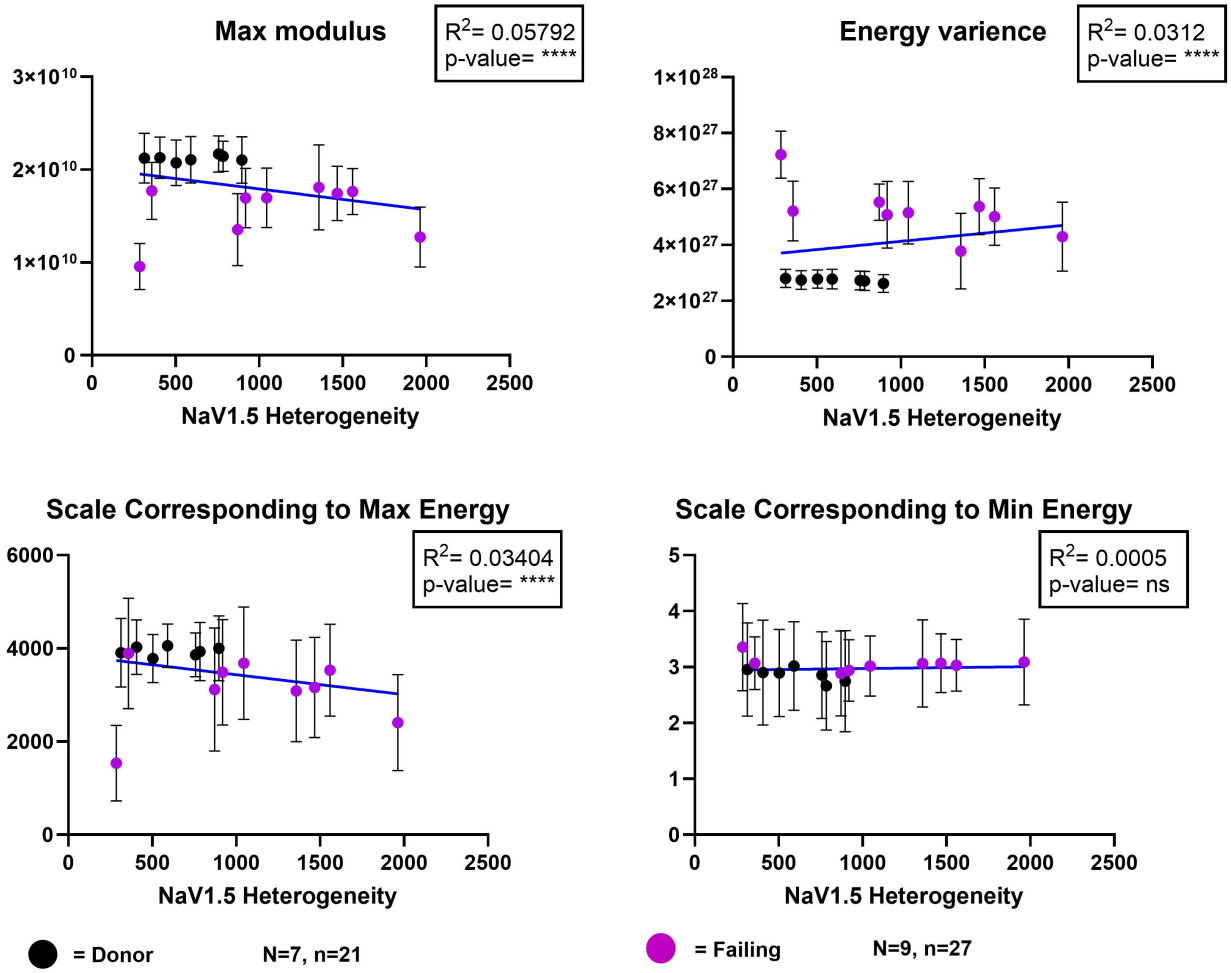


Figure 5.42: Homogeneity of $Na_v1.5$ ion channel with relation to time frequency features of the EGMs of human hearts. For donor hearts: N=7, n=21; for failing hearts: N=9, n=27. Contains 4 graphs of time frequency features from human donor hearts and human failing hearts. The graphs show the time frequency features against the homogeneity of $Na_v1.5$ ion channel. A simple linear regression was used to assess the significance of the correlation between the two features, the theoretical line of best fit is shown in blue. Grey error bars represent the standard deviation. All bar charts represent mean ± S.D.; ns $0.05 < p \leq 1$, *$p \leq 0.05$, **$p \leq 0.01$, ***$p \leq 0.001$, ****$p \leq 0.0001$.

It is noticed that, unlike collagen index and Cx43 remodelling, the negative influences of heart type on $Na_v1.5$ ion channel remodelling can only be obtained from less features (Maximum PSD, PSD standard deviation and energy variance.). The correlations between these three features and $Na_v1.5$ ion channel remodelling in different heart type are shown in figure 5.43, figure 5.44, figure 5.45 and figure 5.46. For $Na_v1.5$ ion channel expression, significant difference was only obtained from energy variance in the failing group ($R^2 = 0.2771$, $p \leq 0.0001$). For Homogeneity of $Na_v1.5$ ion channel, significant correlations were obtained from most of the

features (donor: PSD standard deviation: $R^2 = 0.0234$, p = 0.0218, Energy variance: $R^2 = 0.0194$, p = 0.0370; failing: Maximum PSD: $R^2 = 0.0255$, p = 0.0091, PSD standard deviation: $R^2 = 0.0316$, p = 0.0036, Energy variance: $R^2 = 0.1871$, p $\leq$ 0.0001.).

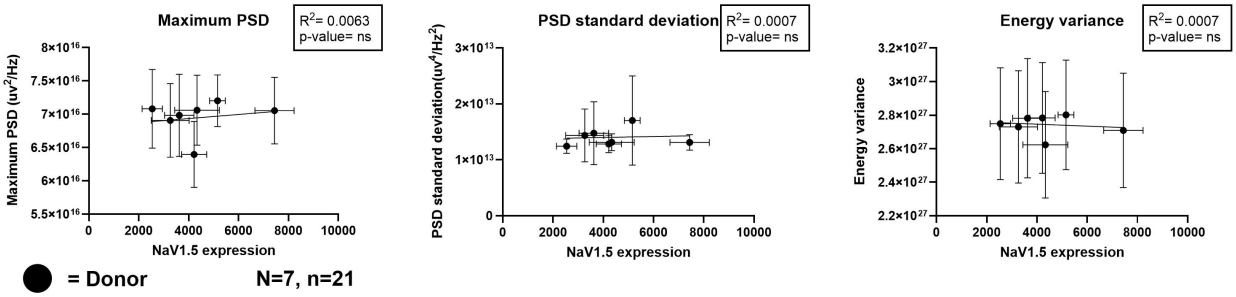


Figure 5.43: $Na_v1.5$ ion channel expression with relation to time frequency features of the EGMs of human donor hearts (N=7, n=21). Contains 2 graphs of frequency domain features and 1 time-frequency feature from human donor hearts. The graphs show the time frequency features against $Na_v1.5$ ion channel expression. A simple linear regression was used to assess the significance of the correlation between the two features, the theoretical line of best fit is shown in blue. Grey error bars represent the standard deviation. All bar charts represent mean ± S.D.; ns 0.05 < p $\leq$ 1, *p $\leq$ 0.05, **p $\leq$ 0.01, ***p $\leq$ 0.001, ****p $\leq$ 0.0001.

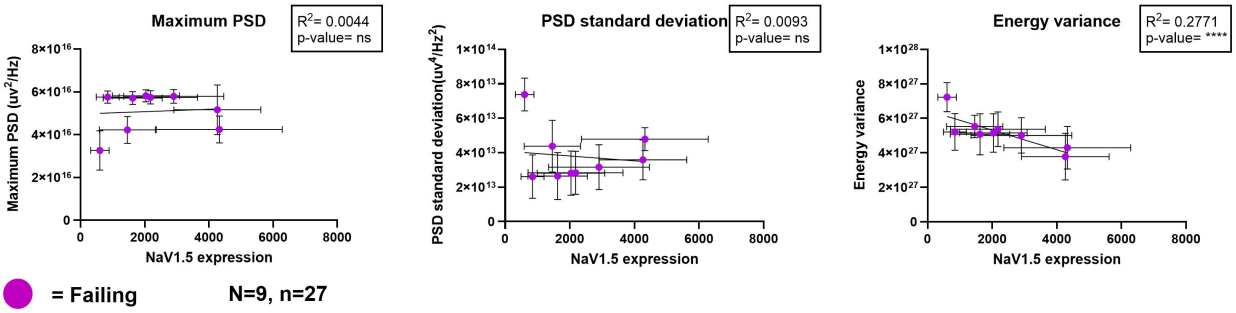


Figure 5.44: $Na_v1.5$ ion channel expression with relation to time frequency features of the EGMs of human failing hearts (N=9, n=27). Contains 2 graphs of frequency domain features and 1 time-frequency feature from human failing hearts. The graphs show the time frequency features against $Na_v1.5$ ion channel expression. A simple linear regression was used to assess the significance of the correlation between the two features, the theoretical line of best fit is shown in blue. Grey error bars represent the standard deviation. All bar charts represent mean ± S.D.; ns 0.05 < p $\leq$ 1, *p $\leq$ 0.05, **p $\leq$ 0.01, ***p $\leq$ 0.001, ****p $\leq$ 0.0001.

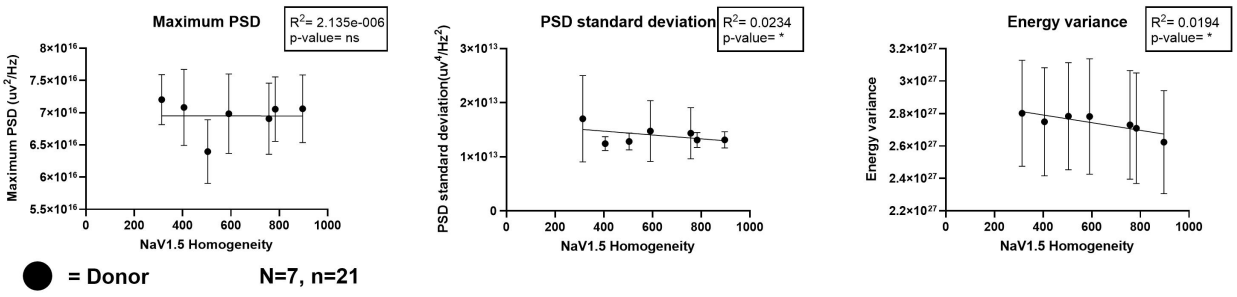


Figure 5.45: Homogeneity of $Na_v1.5$ ion channel with relation to time frequency features of the EGMs of human donor hearts (N=7, n=21). Contains 2 graphs of frequency domain features and 1 time-frequency feature from human donor hearts. The graphs show the time frequency features against the homogeneity of $Na_v1.5$ ion channel. A simple linear regression was used to assess the significance of the correlation between the two features, the theoretical line of best fit is shown in blue. Grey error bars represent the standard deviation. All bar charts represent mean ± S.D.; ns $0.05 < p \leq 1$, *$p \leq 0.05$, **$p \leq 0.01$, ***$p \leq 0.001$, ****$p \leq 0.0001$.

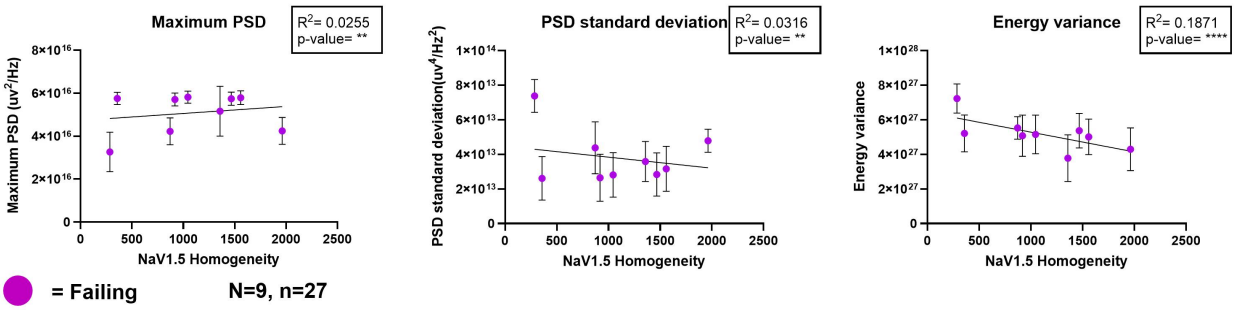


Figure 5.46: Homogeneity of $Na_v1.5$ ion channel with relation to time frequency features of the EGMs of human failing hearts (N=9, n=27). Contains 2 graphs of frequency domain features and 1 time-frequency feature from human failing hearts. The graphs show the time frequency features against the homogeneity of $Na_v1.5$ ion channel. A simple linear regression was used to assess the significance of the correlation between the two features, the theoretical line of best fit is shown in blue. Grey error bars represent the standard deviation. All bar charts represent mean ± S.D.; ns $0.05 < p \leq 1$, *$p \leq 0.05$, **$p \leq 0.01$, ***$p \leq 0.001$, ****$p \leq 0.0001$.

5.4 Discussion

5.4.1 The effects of SNs on NRVMs and its EGM features

Changes in cellular metabolism and microenvironment caused by co-culture with SNs may significantly affect cardiomyocyte growth rates[159]. Previous studies have demonstrated the

positive effects of SNs on cardiomyocyte maturation[160, 159]. This study observed that the diameter of NRVMs co-cultured with 10% SNs was larger than that of cells cultured alone. This growth enhancement may be due to the fact that sympathetic neurotransmitters, such as norepinephrine (NE) and epinephrine (Epi), can significantly influence cardiomyocyte growth rates, primarily through β-adrenergic receptor ($\beta - AR$) signaling[161, 162]. In details, The binding of NE or Epi to β_1- and β_2-adrenergic receptors ($\beta - AR$s) activates G_s proteins, leading to increased cAMP production and subsequent protein kinase A (PKA) activation. PKA then phosphorylates key targets including L-type calcium channels, phospholamban, and ryanodine receptors, resulting in elevated intracellular Ca^{2+} levels. Under sustained β-AR stimulation, this cascade further activates Ca^{2+}/calmodulin-dependent kinase II (CaMKII) and calcineurin/NFAT signaling pathways, ultimately promoting the expression of hypertrophic genes such as ANP, BNP, and β-MHC[161, 162, 163]. Also recent research showed that sympathetic neurotransmitters locally stimulate cardiomyocyte autophagy and ubiquitin-proteasome systems, controlling cell size via protein turnover[164].

The mechanism by which SNs regulate the Cx43 expression in neonatal cardiomyocytes remains unclear. This study investigated the expression of Cx43 of NRVMs under different culture conditions. When co-cultured with 10% SNs, the density of Cx43 in cardiomyocytes was approximately twofold higher than in NRVMs cultured alone. This increase could be due to enhanced translation or other post-transcriptional events affected by SNs[160, 165]. In addition, it has been shown that Cx43 expression is upregualted by stimulating BAR [166], which may explain the reason how SNs are increaseing Cx43 density. These findings highlight the influence of SNs on signalling between cardiomyocytes, suggesting a potential role in regulating their electrophysiological properties.

The results showed that the participation of 10% SN significantly increased the conduction velocity of cardiomyocytes. This enhancement could be due to the promotion of Cx43 expression by SNs, which results in better electrical connections and faster conduction velocities[160, 167]. Boer, T.P. et al. also observed that β-adrenergic (β-AR) stimulation substantially enhanced CV in neonatal cardiomyocytes[168]. In addition, co-culture with 10% SNs shortened the EGM duration and R-S interval, reflecting improved electrical coupling and faster action potential

propagation. Activation of the β-AR pathway generates a positive chronotropic response, including the opening of L-type calcium channels and an increase in Ca^{2+} influx, which accelerates cardiac depolarisation[163]. A study by Kowalski, W.J. et al. compared calcium transients during contraction in cardiomyocytes and cardiomyocytes co-cultured with SNs (CM+SNs). The researchers observed a higher amplitude of calcium transients in CMs + SNs, suggesting that co-culture with SNs improves intracellular calcium handling[160]. In summary, the upregulation of ion channels and enhanced calcium handling contribute to faster depolarisation and repolarisation phases, thereby shortening EGM duration and R-S interval. Our results also showed significantly increased voltage amplitude in 10% SNs co-culture, which was also due to stronger action potentials caused by increased Ca^{2+} influx. Notably, 5% of SNs co-cultures did not significantly differ from NRVMs-only cultures in any of the measured EGM features. This may be due to insufficient nerve-cardiac interactions at lower neuronal densities. Eisenhofer, G.et al. also demonstrated that reduced density of SNs endings is associated with down-regulation of cardiac function[169]. Therefore, we focused on 10% SNs co-culture as the primary control. This study developed an in vitro model suitable for studying innervated cardiomyocytes and SNs, highlighting the critical role of the autonomic nervous system in cardiac electrophysiology and the importance of neuronal density in co-culture systems for cardiac research and therapeutic development.

5.4.2 The effects of gap junctional remodelling on EGM features in human donor and human failing samples

The study shows that heart failure leads to the remodelling of Cx43. There was a decrease in Cx43 expression in human failing hearts compared to donor hearts, which aligns with previous studies[170, 171]. The decrease in Cx43 expression can be explained by the fact that HF leads to cell death, such as necrosis and apoptosis[172, 173]. The heart combats this increase in cell death by replacing lost myocytes with scar tissue, as the heart has limited regenerative properties[152]. It was found that Cx43 expression in the remote region in failing hearts is also lower then it in the remote region in donor hearts. Such funding can be explained by

that in failing hearts, these areas also experience some degree of cell death, but extensive scar tissue has not yet formed. Therefore, it makes sense that there is a decrease in Cx43 in HF as macro and micro scar tissues do not contribute to Cx43 expression. Furthermore, there was a decrease in Cx43 expression in areas near scar compared to remote areas in both donor and failing hearts. Since there is scar buildup in the location of cell death, this explains why Cx43 expression was lower in these areas compared to remote areas. Thus, reinforcing the theory of cell death causing a decrease in Cx43 expression.

An increase in lateralisation of Cx43 was seen in HF compared to donor hearts which aligns with previous findings in the field[171, 174]. Though the mechanism of why this occurs is still unknown there have been theories on the process of Cx43's migration to lateral cell borders. It is thought that Cx43 is docked to the intercalated discs via the scaffolding protein ZO-1[30]. In ischemic and hypoxic conditions Src kinase binds to both Cx43 and ZO-1. Src kinase causes Cx43 to unbind from ZO-1 which allows Cx43 to move away from the intercalated discs, allowing Cx43 to migrate to the lateral cell borders[175]. This mechanism could explain why increased lateralisation occurs during HF, as patients with HF are prone to being under hypoxic conditions[176].

It was also found that decrease in Cx43 expression and heterogeneity of Cx43 expression more are likely to occur in scar areas in both donor hearts and failing hearts. In donor hearts, lateralisation of Cx43 also follow the same trend. However, there seemed to be no change in lateralisation of Cx43 between areas near scar compared to remote areas in failing hearts. This finding contradicts research in the field[170, 25] where there was an increase in lateralisation in areas near infarct border zones compared to remote tissue in post-infarct models. The contradicting results in this study could be explained by the inclusion of a variety of aetiology of HF, as this study included a higher number of dilated cardiomyopathy (DCM) relative to ischemic cardiomyopathy (ICM) patients, whereas previous studies showing a change in lateralisation with distance[170, 25] only included post-infarct models. This suggests that the extent of lateralisation could vary depending on the aetiology of HF, which coincides with the suggested mechanism of lateralisation under ischemic conditions[30, 175].

Future studies should consider using equal numbers of both DCM and ICM or have separate studies focusing on each aetiology. Results from this could suggest that different HF aetiologies require targeted surgical therapeutics instead of general treatment such as catheter ablation. This idea reinforces the findings from a previous study where catheter ablation performance decreased in DCM in comparison to ICM in resolving VT[176].

Further experiments in this study showed a significant correlation between gap junctional remodelling and electrophysiology, as all the gap junctional remodelling features tested showed a significant correlation with all the EGM features. The R^2 values of the gap junctional remodelling are significantly higher than those of collagen, suggesting that the gap junction plays a more important role in the formation of the EGM. It was also noticed that the R^2 values of the linear regression between gap junctional remodelling and the frequency domain and time frequency EGM features are lower than them of time domain features, which suggests that they cold be mainly controlled by other factors or they are following other more complex relationship.

Published work has consistently demonstrated that Cx43 remodelling reduces conduction velocity and promotes arrhythmogenesis (Peters et al.,; Severs.)[177, 178]. While these studies focus primarily on conduction parameters, fewer have investigated how these changes are reflected in EGM morphology. The findings of this study complement and extend the literature by demonstrating that EGM features such as amplitude reduction and signal broadening can serve as indirect markers of impaired gap junctional coupling. This represents an important step in linking molecular-level remodelling to macroscopic EGM readouts.

Recent experimental studies state that an increase in lateralisation is thought to increase EGM duration and decrease CV, which is also obtained from this study[179, 180, 181, 182]. However, other gap junctional remodelling also happened in the human failing hearts, therefore, the relationship between Cx43 lateralisation and the conduction velocity in human hearts needs to be further studied[183].

Furthermore, there were a larger number of highly significant correlations with subtle electrogram features for the structural characteristics of Cx43 expression and homogeneity compared to lateralisation. These data suggest that Cx43 expression and homogeneity have a greater

impact on electrophysiology compared to lateralisation. Furthermore, Cx43 expression has a higher impact on electrophysiology than other structural characteristics.

5.4.3 The effects of Na_v1.5 channel remodelling on EGM features in human donor and human failing samples

The immunohistochemistry analysis revealed a general reduction in Na_v1.5 expression accompanied by an upregulation of collagen in failing heart samples. This finding aligns with previous studies that report increased collagen levels in left ventricular heart failure and a reduction in sodium current in the infarct border zone (IBZ)[184, 185]. The observed changes can be attributed to the replacement of necrotic myocytes with collagenous scar tissue[158]. Given that fibrotic tissue is a poor conductor of electrical signals and lacks sodium channel expression, this contributes to the overall decrease in Na_v1.5 expressions[185]. Furthermore, the reduction in Na_v1.5 expression near scar regions, as compared to remote areas in both donor and failing hearts, can be similarly explained by scar tissue deposition. The heterogeneity of Na_v1.5 expression observed in heart failure samples may stem from significant variability across different sites, with very low Na_v1.5 expression in areas of scar deposition. In contrast, the more consistent Na_v1.5 expression in donor hearts likely reflects less variability in collagen expression. Notably, no enhancement of the reduction effect was observed in failing heart samples, suggesting that the mechanisms underlying Na_v1.5 reduction are consistent across both sample groups[185]. This indicates that the pathological condition does not further exacerbate Na_v 1.5 expression.

The correlation analysis between Na_v 1.5 expression and electrophysiology revealed a significant linear relationship with various extracted EGM features. Heart failure samples exhibited prolonged QR, RS, and S-End intervals, alongside increased EGM duration and reduced conduction velocity. Additionally, there were decreases in the Q to R and S to End gradients, all of which exhibited statistically significant correlations with Na_v 1.5 expression. These findings align with previous studies suggesting that a reduction in the peak I_{Na}, likely due to post-transcriptional decreases in Na_v 1.5 protein, can lead to I_{Na} inactivation. Since I_{Na} is critical

for conduction velocity, these abnormalities can result in APD prolongation, a phenomenon well-documented in heart failure[186]. Moreover, the fractionation index increased, and voltage decreased in heart failure samples, both of which were statistically significant in relation to Na_v 1.5 expression. Previous research indicates that altered ion channel activity and decreased cellular connectivity result in fractionated, low-amplitude extracellular EGMs[158]. Na_v 1.5 expression also significantly correlates with some frequency-domain features, with DF being the primary characteristic. DF is defined as the frequency with the maximum power in the power spectrum, while PSD represents the distribution of power across frequencies, in which they are interlinked[101]. Although Martins et al. highlighted that reduced I_{Na} can influence DF in ventricular fibrillation, they emphasised that the most important contributors to changes in DF are I_{CaL} and I_K1[187]. This may help explain the relatively weak correlation between Na_v 1.5 expression, DF, and PSD-related properties. Additionally, the assessment of time-frequency domain features offers a nuanced perspective on the electrophysiological characteristics of the signals. Time-frequency analysis enables the simultaneous interpretation of signals both in time and frequency, allowing for the identification of local, transient, or intermittent components that may not be evident in traditional analyses[101]. In this study, the four time-frequency features evaluated provide valuable insights into the dynamic behaviour of the signals. The significant relationships between these features and Na_v 1.5 expression warrant further investigation, as they could elucidate the complex interplay between ion channel remodelling and electrophysiological properties in heart failure. Moreover, Shannon entropy was employed to characterise the uncertainty and variability present in EGMs, reflecting alterations in ion channel function and cellular connectivity. Although our results showed no significant correlation with Na_v 1.5 expression, future research should include a broader range of heart failure types, focusing on distinct etiologies, since most samples in this study were from patients with DCM, also the EGM was responding to the stimulation, its hard to capture arrhythmias under pacing. Broadening the scope could help uncover potential pathological mechanisms associated with different heart failure states. Overall, certain features, particularly those from the time-domain analysis, appear to be stronger predictors of EGM abnormalities.

The correlation analysis between Na_v 1.5 heterogeneity and electrophysiology showed no signif-

icant relationship. This implies that Na_v 1.5 heterogeneity alone does not significantly influence alterations in electrophysiology. Previous studies have demonstrated a functional transmural gradient in cardiac sodium channel distribution within the left ventricle of the murine heart, utilising Na_v 1.5 immunohistochemistry and SCN5A mRNA expression analyses[188]. Additionally, reduced SCN5A mRNA expression has been observed in epicardial compared to endocardial tissue in non-diseased human hearts[189]. In light of these findings, a notable limitation in the present study arises from the methodological approach, which will be introduced later in the limitation section. The methodological constraint may have limited the evaluation of Na_v 1.5 heterogeneity and its correlation with electrophysiological measurements, as variations across different regions of the left ventricle may not have been adequately captured. Addressing these limitations in future studies will be essential to enhance the robustness of the findings and provide a more comprehensive understanding of the relationship between Na_v 1.5 distribution and cardiac electrophysiology. Additionally, figures illustrate that data points representing donor hearts are more tightly clustered, while those from failing hearts are more dispersed. For instance, the energy variance graph shows a tight spread of donor heart data compared to the loose spread observed in heart failure samples. This characteristic may be useful in identifying EGM abnormalities.

Overall, the findings support the hypothesis linking scar tissue, sodium channel remodelling, and cardiac electrophysiology. Notably, the moderate linear correlation between Na_v 1.5 expression and electrophysiological features reinforces past studies indicating that peak I_{Na} is reduced in heart failure[186, 190, 191, 192, 193], which can lead to conduction slowing or ventricular arrhythmias through stimulus reentry[194]. This observation may result from post-translational modification of Na_v 1.5 by $CaMK_{II}$ phosphorylation, as evidenced by the significant increase in I_{NaL} associated with $CaMK_{II}\delta C$ over expression in HF-induced mice[195, 196]. Furthermore, elevated I_{NaL} has been observed in both HF-induced canine and human HF ventricular myocytes[191, 192, 197, 198]. Such changes could disrupt sodium and calcium homeostasis, delay repolarisation, prolong ventricular APD, and heighten the risk of ventricular arrhythmias[194]. Recent advances have led to novel therapeutic approaches aimed at reducing arrhythmia incidence by modifying scar structure. Strategies include enhancing impulse

propagation through sodium channel over expression and improving intercellular coupling, potentially using connexin-expressing cell engraftment[199]. A particularly exciting development is the 'homogenisation' of ventricular scar tissue via bio-enzymatic ablation methods, such as topical application of collagenases, to selectively remove arrhythmogenic tissue[200]. This approach not only aims to restore more uniform conduction pathways but also has implications for understanding Na_v 1.5 heterogeneity within the left ventricle. While prior research has predominantly focused on differences between the right and left ventricles, atrial versus ventricular tissues, and transmural heterogeneity, this study paves the way for exploring how changes in scar structure may impact sodium channel distribution and function[153, 188].

5.5 Limitations

Due to the fact that its hard to obtain neurons from BMS, NRVMs were used to study how SNs influence the EGM. However, the morphology of cell EGM is much simpler than the EGM of the BMS, in that case only some time-domain features were compared.

Another limitation is that the EGM recording and immunolabeling were carried out on the different samples due to the fact that the BMS were saved for collagen imaging. Therefore, the correlation between the EGM and functional changes is not direct as its correlation with the structural change even the samples are from the same area of the same heart.

In addition, gap junctional remodelling and ion channel remodelling were quantified via image processing (pixel counting) of microscopy images. This method is less accurate than Western blot (WB) in quantifying expression. However, it is impossible to study how the remodelling correlates with scar using WB and WB also can not illustrate remodelling other than expression reduction such as heterogeneity and lateralisation.

Also, most of the R^2 values are low, so it is necessary to include more ion channels and find out the proportion of the effects of different ion channel remodelling and structural changes on EGM. Once enough functional changes and structural changes were studied, quantification of EGM morphological changes can be performed more accurately.

5.6 Conclusion

In this chapter, the effects of SNs on the growth of NRVMs and its effects on the cell EGM morphology, the relationships between scar and gap junctional remodelling and ion channel remodelling, and the effects of these remodelling on the EGM morphology of BMS were studied. The results show that SNs enhance the growth of the NRVMs and increase the expression of Cx43. Gap junctional remodelling and ion channel remodelling happen more around scar areas and in human failing hearts comparing to farfield area and human donor hearts. All the functional changes were shown to reduce conduction velocity and lead to dramatic changes in the morphology of EGM. The result highlights the importance of functional remodelling, particularly changes in gap junction expression and ion channel function, in shaping EGM morphology. The findings show that modifications in Cx43 and $Na_v1.5$ lead to conduction slowing and characteristic alterations in EGM morphology, distinct from those caused by structural remodelling. These results are significant as they demonstrate that functional remodelling alone can produce identifiable EGM signatures, thereby extending the diagnostic potential of EGM analysis beyond purely structural changes. All the studies in this chapter were carried out on cells and BMS, in order to prove the potential clinical applications of this study, the effects of functional changes on the EGM of ex-vivo hearts will be studied in the next chapter.

The novelty of this chapter lies in providing one of the first direct demonstrations of how functional remodelling, independent of structural alterations, modifies EGM morphology in a controlled experimental system. By using the feature extraction tool, you offer a quantifiable means of detecting functional remodelling through EGM analysis, suggesting potential applications in early detection of arrhythmogenic substrates.

Chapter 6

Analysis of EGM morphology of the ex-vivo porcine hearts with pharmacological modifications

6.1 Introduction

The previous two chapters examined how structural and functional changes affect EGM morphology in cultured-cells and BMS models. These models have significantly advanced our understanding of electrophysiological mechanisms at the cellular and tissue levels. However, both systems have critical limitations that must be addressed to bridge the gap between basic research and clinical application.

Cultured cells were enzymatically dissociated, although they are useful for isolated ion channel studies and simplified control of the extracellular environment, the cells lose their native structural and functional context. The enzymatic digestion process disrupts the cell-cell coupling and the extracellular matrix, resulting in the loss of native electromechanical interactions. In such settings, cells are not subjected to physiological loads, which are essential for maintaining normal cardiac function and for accurately replicating in vivo mechanical conditions[201]. In

addition, cultured-cells do not experience the same level of strong synchronous contraction or conduction as in a whole heart, which limits their utility in the study of complex arrhythmias or mechanical dyssynchrony.

Similarly, BMS models offer a step closer to physiological realism by incorporating multicellular structures and mechanical constraints. However, they still lack several critical components of the intact cardiovascular system. These include complete hemodynamic regulation, realistic chamber pressures, valve functionality, coronary perfusion gradients, and autonomic regulation. In addition, the process of cutting and mounting myocardial tissue for BMS experiments can injure cells and disrupt native tissue architecture, potentially altering their electrophysiological properties, conduction patterns, and contractility. As a result, findings derived from these models may not accurately predict in vivo cardiac behaviour, especially under pathological conditions such as fibrosis or ischemia.

To overcome these limitations and improve translational relevance, it is imperative to examine whether similar structural and functional effects observed in cells and BMS can be reproduced in an intact heart model. The intact heart retains essential features such as native myocardial architecture, conduction pathways, chamber synchrony, and pressure-volume dynamics. These features are crucial for understanding arrhythmogenesis, mechanical dyssynchrony, and the interplay between electrical and mechanical dysfunctions. In particular, the use of the ex vivo Langendorff-perfused porcine heart model provides a controlled yet physiologically relevant platform for such investigations[202, 203]. This model allows for real-time assessment of electrical activity, contractility, and pharmacological responsiveness while preserving the structural and functional integrity of the heart.

Despite its advantages, the Langendorff model also presents practical challenges. Developing a robust porcine model of myocardial fibrosis remains difficult, especially when attempting to image fibrotic scars and ganglionated plexi (GPs) with high spatial precision[204, 205]. Additionally, recording EGMs from defined pathological regions during perfusion experiments is technically demanding due to the heart's dynamic nature and anatomical complexity. Given these constraints, this chapter focuses on functional modifications rather than structural re-

modelling. Pharmacological interventions were employed to mimic ion channel dysfunction and altered autonomic tone, providing an alternative approach to investigating electrophysiological alterations without requiring extensive structural remodelling. While this approach does not fully replicate the chronic remodelling seen in disease states such as heart failure or atrial fibrillation, it allows for controlled manipulation of key functional parameters relevant to arrhythmogenesis and conduction abnormalities.

The data collected from the atria are also not included because the BMS were all from the ventricles. Some of the data were collected by Dr. Joseph Brook.

The hypotheses to be addressed were as follows:

1. Gap junction blockade influences EGM features in porcine ex vivo heart model, similar to what was observed in the BMS model.

2. Sodium ion channel blockage influences EGM features in porcine ex vivo heart model, similar to what was observed in the BMS model.

3. Potassium ion channel enhancement influences EGM features in porcine ex vivo heart model, similar to what was observed in the BMS model.

For this purpose, the following studies described in this chapter were carried out:

1. Record EGM from ex vivo porcine hearts before and after pharmacological modifications.

2. Extract the features from the recorded EGMs.

6.2 Methods

The preparation and collection of porcine hearts was introduced in Section 2.2.4

The Langendorff technique was introduced in Section 2.4.

The pharmacological modulators used in the Langendorff experiments were introduced in Section 2.2.5. The dose responses were carried out by Dr. Joseph Brook[206], so it was not

performed in this thesis.

In detail, the Tyrode's solution in the tank was reduced to 2 L circulating volume after recording the baseline EGM. The determined dosage of drug was dissolved in 3 L Tyrode's solution and added to the Langendorff system through the reservoir at a rate of 50 ml/min for 30mins, the total circulating volume of Tyrode's solution was maintained at 5 L during the recording. For Carbenoxolone, a total of 1 mM (corresponding to maximal dose of 30.735 mg) is administered. For Lidocaine, a total of 0.32 mM (corresponding to half-maximal dose of 200 mg) is administered. For Pinacidil, a total of 0.05 mM (corresponding to a half-maximum dose of 13.1 mg) is administered[206]. Only one pharmacological modulator was applied to each heart to ensure that it is the only variable. The baseline EGMs were recorded after the hearts were stabilised and the pharmacological modulated EGMs were recorded 5 minutes after drug infusions.

EGM recordings were performed at 2-5A steady pacing with cycle lengths of 250, 333, 500, and 1000 ms (1 minutes per cycle length). EGMs were recorded from multiple points mentioned in Chapter 2 using a clinical HD grid mapping catheters (Abbot Medical). The catheter was connected to an Powerlab recording system (AD Instruments) with the Labchart software (AD Instruments), which has a bandwidth filter of 0.3–500 Hz and a 1-KHz sampling rate.

The recorded data was exported after the experiment and analysed using the tool developed in Chapter 3. The example EGMs are shown in Figure 6.1. Although EGMs with different cycle lengths were recorded, the influence of pacing frequency on the EGM features is not the focus of this study, therefore, the features of the EGMs obtained under pacing frequency of 1 Hz (cycle length: 1000ms) were extracted and compared. In addition, all BMS were prepared from the apex of human donor hearts and human failing hearts, only the EGMs recorded at locations 4,8 and 12 were analysed.

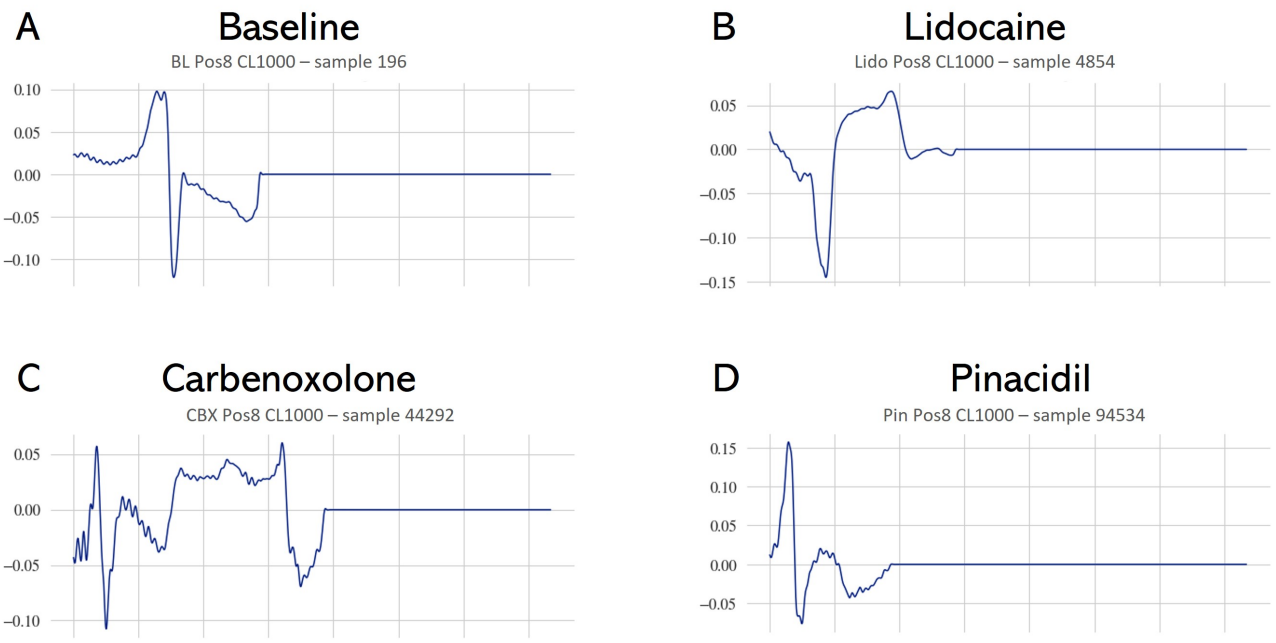


Figure 6.1: Example EGMs with pacing cycle length of 600 ms. (A) Baseline. (B) After administering Lidocaine. (C) After administering Carbenoxolone . (D) After administering Pinacidil.

One-way analysis of variance (ANOVA) for paired data was applied to compare means of the four groups.

6.3 Results

EGMs collected from 10 porcine hearts (10 baselines, 4 CBX, 4 Lido, 2 Pin) were used in this study. Carbenoxolone was used to reduce gap junction coupling, Lidocaine was used to block voltage-gated Na+ channels (SCN10A, SCN9A, SCN5A) and Pinacidil was applied to enhance I_{KATP} channel activity. The results are shown in Figure 6.2, Figure 6.3 and Figure 6.4, the mean values and the standard deviations of all the features (baseline and after pharmacological modifications) are shown in Table 6.2, the P values are shown in Table 6.1 and Table 6.3. Significant differences were obtained from most of the features and the trends were same to the trends obtained in the previous chapter. However, non significant difference were obtained from QR interval (BL and Lido), SEnd interval (BL and Lido), S to End gradient (CBX and Lido), fractionation index (CBX and Lido), dominant frequency (BL and Pin, Lido and Pin), PSD

mean (BL and Lido), maximum PSD (BL and CBX), PSD median (BL and Lido, CBX and Lido), PSD kurtosis (BL and Lido, BL and Pin, Lido and Pin), PSD standard divination (BL and CBX, Bl and Lido, CBX and Lido), shannon entropy (Lido and Pin), scale corresponding to maximum energy (BL and CBX, CBX and Lido) and scale corresponding to minimum energy (all the comparisons).

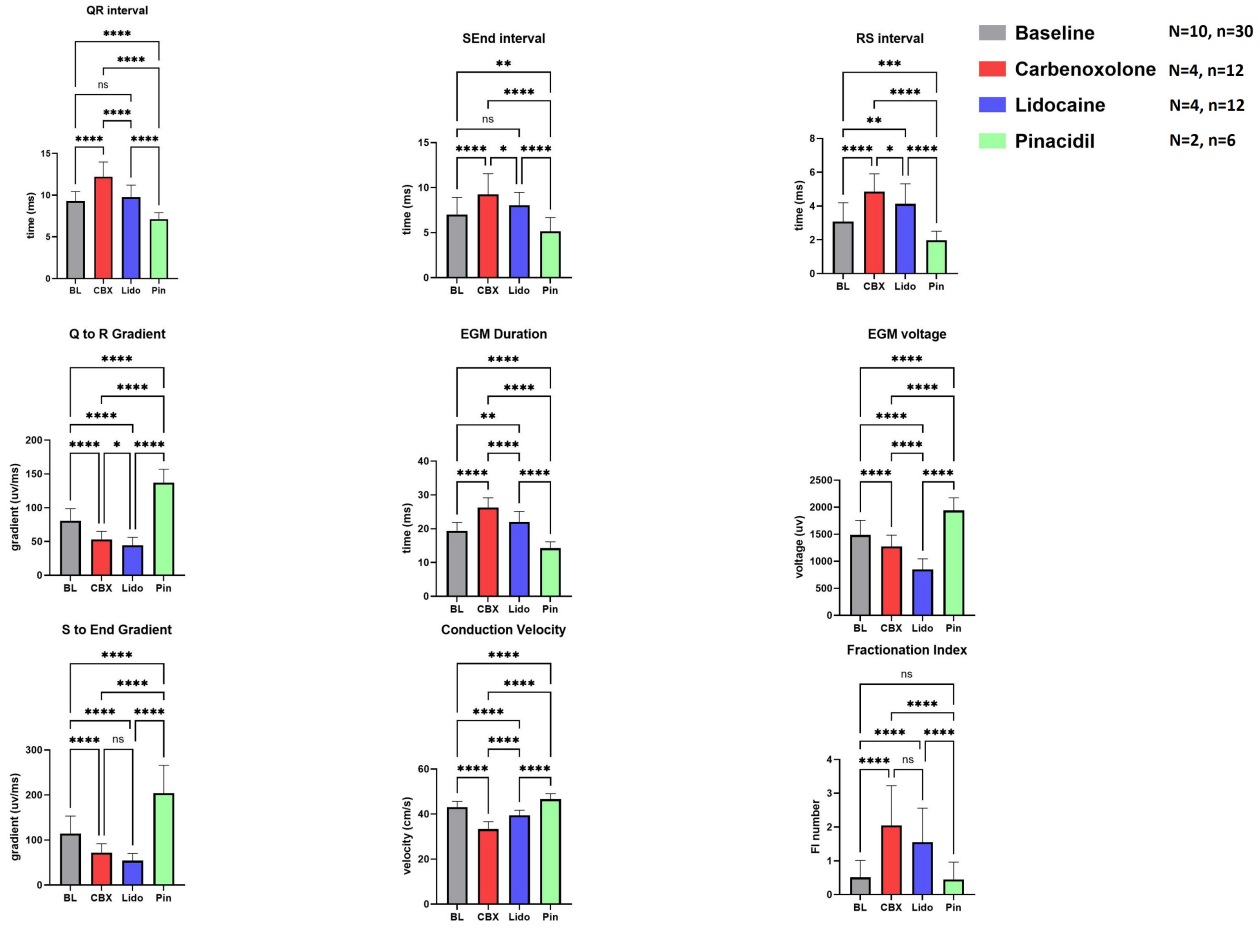


Figure 6.2: Comparison between time domain features of EGM recorded from Langendorff porcine hearts at baseline and after pharmacological modifications. Baseline: N=10, n=30; Carbenoxolone: N=4, n=12; Lidocaine: N=4, n=12; Pinacidil: N=2, n=6. Contains 9 graphs of time-domain features from 10 hearts (10 baselines, 4 CBX, 4 Lido, 2 Pin). Grey error bars represent the standard deviation. All bar charts represent mean ± S.D.; ns $0.05 < p \leq 1$, *p ≤ 0.05, **p ≤ 0.01, ***p ≤ 0.001, ****p ≤ 0.0001.

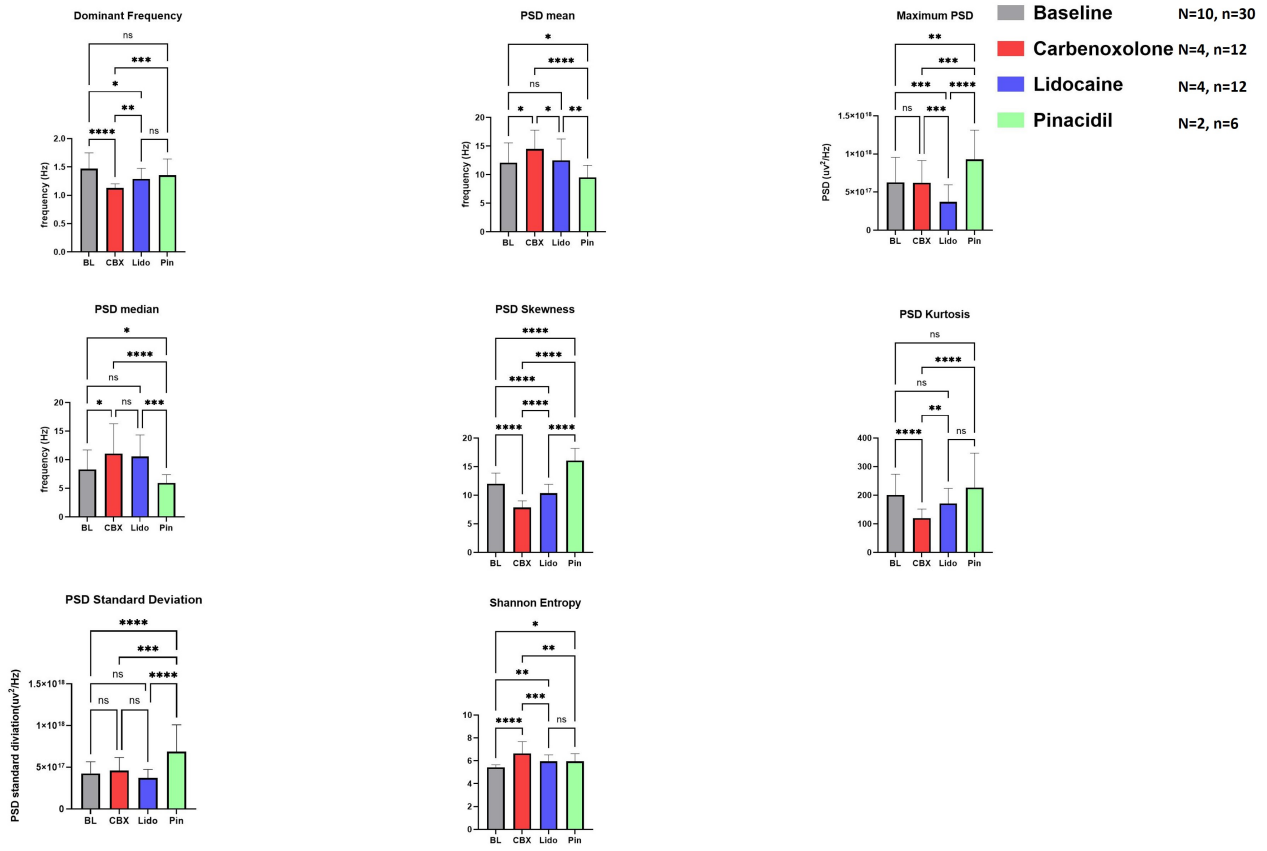


Figure 6.3: Comparison between frequency domain features and Shannon Entropy of EGM recorded from Langendorff porcine hearts at baseline and after pharmacological modifications. Baseline: N=10, n=30; Carbenoxolone: N=4, n=12; Lidocaine: N=4, n=12; Pinacidil: N=2, n=6. Contains 8 graphs of frequency-domain features and Shannon Entropy from 10 hearts (10 baselines, 4 CBX, 4 Lido, 2 Pin). Grey error bars represent the standard deviation. All bar charts represent mean ± S.D.; ns $0.05 < p \leq 1$, *$p \leq 0.05$, **$p \leq 0.01$, ***$p \leq 0.001$, ****$p \leq 0.0001$.

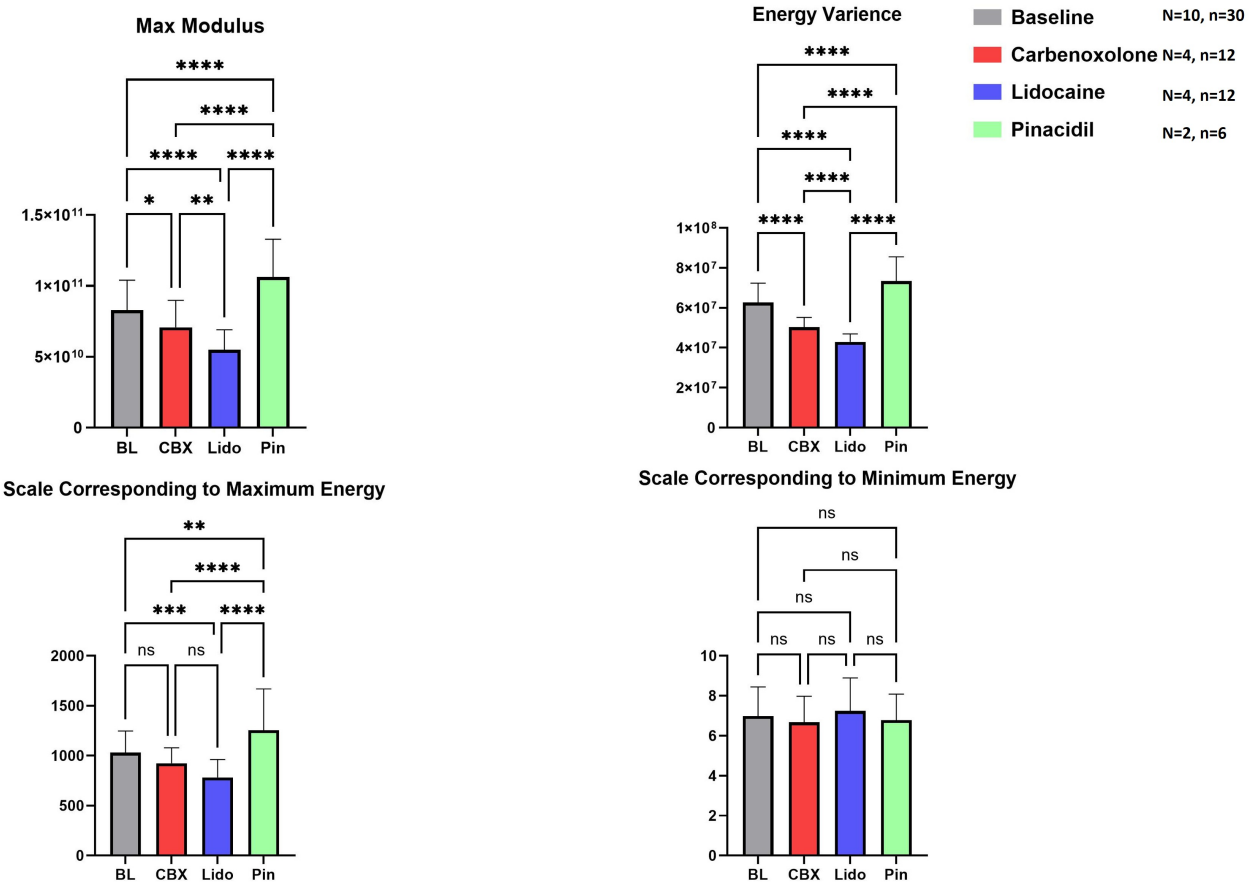


Figure 6.4: Comparison between time frequency features of EGM recorded from Langendorff porcine hearts at baseline and after pharmacological modifications. Baseline: N=10, n=30; Carbenoxolone: N=4, n=12; Lidocaine: N=4, n=12; Pinacidil: N=2, n=6. Contains 4 graphs of time frequency features from 10 hearts (10 baselines, 4 CBX, 4 Lido, 2 Pin). Grey error bars represent the standard deviation. All bar charts represent mean ± S.D.; ns $0.05 < p \leq 1$, *$p \leq 0.05$, **$p \leq 0.01$, ***$p \leq 0.001$, ****$p \leq 0.0001$.

	Baseline	Carbenoxolone	Lidocaine	Pinacidil
QR interval	9.30 ± 1.13	12.22 ± 1.76	9.79 ± 1.42	7.13 ± 0.77
SEnd interval	7.02 ± 1.90	9.25 ± 2.29	8.06 ± 1.42	5.14 ± 1.54
RS interval	3.08 ± 1.12	4.86 ± 1.05	4.13 ± 1.18	1.97 ± 0.54
Q to R Gradient	80.97 ± 17.60	53.18 ± 11.93	44.36 ± 12.94	137.3 ± 19.72
EGM Duration	19.40 ± 2.46	26.33 ± 2.84	21.97 ± 3.13	14.24 ± 1.87
EGM Voltage	1486 ± 271.2	1272 ± 212.8	850.5 ± 195	1941 ± 232
S to End Gradient	114.2 ± 39.17	72.38 ± 19.55	54.45 ± 15.81	204.4 ± 61.66
Conduction Velocity	43.13 ± 2.54	33.34 ± 3.29	39.50 ± 2.24	46.62 ± 2.45
FI	0.51 ± 0.5	2.05 ± 1.18	1.55 ± 1.01	0.45 ± 0.51
DF	1.47 ± 0.28	1.13 ± 0.07	1.29 ± 0.19	1.36 ± 0.29
PSD mean	12.13 ± 3.45	14.51 ± 3.29	12.52 ± 3.74	9.54 ± 2.12
Max PSD	$6.29\times10^{17} \pm 3.26\times10^{17}$	$6.23\times10^{17} \pm 2.91\times10^{17}$	$3.72\times10^{17} \pm 2.23\times10^{17}$	$9.30\times10^{17} \pm 3.82\times10^{17}$
PSD median	8.29 ± 3.41	11.07 ± 5.22	10.56 ± 3.76	5.94 ± 1.45
PSD Skewness	12.01 ± 1.88	7.88 ± 1.14	10.38 ± 1.54	16.08 ± 2.13
PSD Kurtosis	200.9 ± 72.64	119.8 ± 31.97	171.4 ± 52.29	226.6 ± 120.5
PSD SD	$4.26\times10^{17} \pm 1.41\times10^{17}$	$4.61\times10^{17} \pm 1.56\times10^{17}$	$3.71\times10^{17} \pm 1.03\times10^{17}$	$6.89\times10^{17} \pm 3.20\times10^{17}$
Shannon Entropy	5.42 ± 0.23	6.64 ± 1.03	5.95 ± 0.57	5.95 ± 0.66
Max Modulus	$8.30\times10^{10} \pm 2.11\times10^{10}$	$7.09\times10^{10} \pm 1.90\times10^{10}$	$5.50\times10^{10} \pm 1.40\times10^{10}$	$10.64\times10^{10} \pm 3.66\times10^{10}$
Energy Variance	$6.26\times10^{7} \pm 9.80\times10^{6}$	$5.03\times10^{7} \pm 4.88\times10^{6}$	$4.29\times10^{7} \pm 4.01\times10^{6}$	$7.34\times10^{7} \pm 12.11\times10^{7}$
Scale Max Energy	1030 ± 217.8	924.8 ± 154.8	782.7 ± 179.7	1255 ± 413.3
Scale Min Energy	6.99 ± 1.46	6.68 ± 1.30	7.25 ± 1.65	6.79 ± 1.32

Table 6.2: EGM Features for all the porcine hearts at baseline and after pharmacological modulations.

	BL vs CBX	BL vs Lido	BL vs Pin
QR interval	<0.0001	0.2846	<0.0001
SEnd interval	<0.0001	0.1332	0.0061
RS interval	<0.0001	0.0013	0.0002
Q to R Gradient	<0.0001	<0.0001	<0.0001
EGM Duration	<0.0001	0.0016	<0.0001
EGM Voltage	<0.0001	<0.0001	<0.0001
S to End Gradient	<0.0001	<0.0001	<0.0001
Conduction Velocity	<0.0001	<0.0001	<0.0001
FI	<0.0001	<0.0001	0.9335
DF	<0.0001	0.0214	0.7860
PSD mean	0.0109	0.9488	0.0300
Max PSD	0.9751	0.0002	0.0021
PSD median	0.0248	0.1083	0.0421
PSD Skewness	<0.0001	<0.0001	<0.0001
PSD Kurtosis	<0.0001	0.2879	0.6861
PSD SD	0.7478	0.5625	<0.0001
Shannon Entropy	<0.0001	0.0046	0.0281
Max Modulus	0.0354	<0.0001	<0.0001
Energy Variance	<0.0001	<0.0001	<0.0001
Scale Max Energy	0.3006	0.0002	0.0024
Scale Min Energy	>0.9999	0.3090	0.9691

Table 6.1: P values of the comparisons between all the features of baseline EGMs and pharmacological modulated EGMs.

	CBX vs Lido	CBX vs Pin	BL vs Pin
QR interval	<0.0001	<0.0001	<0.0001
SEnd interval	0.0303	<0.0001	<0.0001
RS interval	0.0173	<0.0001	<0.0001
Q to R Gradient	0.0485	<0.0001	<0.0001
EGM Duration	<0.0001	<0.0001	<0.0001
EGM Voltage	<0.0001	<0.0001	<0.0001
S to End Gradient	0.1391	<0.0001	<0.0001
Conduction Velocity	<0.0001	<0.0001	<0.0001
FI	0.0574	<0.0001	<0.0001
DF	0.0027	0.0004	0.5421
PSD mean	0.0483	<0.0001	0.0090
Max PSD	0.0008	0.0007	<0.0001
PSD median	0.9338	<0.0001	0.0001
PSD Skewness	<0.0001	<0.0001	<0.0001
PSD Kurtosis	0.0073	<0.0001	0.0682
PSD SD	0.1034	0.0002	<0.0001
Shannon Entropy	0.0001	0.0069	0.9984
Max Modulus	0.0032	<0.0001	<0.0001
Energy Variance	<0.0001	<0.0001	<0.0001
Scale Max Energy	0.0514	<0.0001	<0.0001
Scale Min Energy	0.3193	0.9721	0.8070

Table 6.3: P values of the comparisons between all the features of different pharmacological modulated EGMs.

6.4 Discussion

Comparing to the baseline EGMs, the pharmacologically modified EGMs recorded from Langendorff porcine hearts showed changes similar to the trends obtained from EGMs of human BMS with functional changes. In detail, the application of CBX/Lido in Langendorff hearts and functional remodelling in BMS prolonged the duration of EGMs, reduced EGM voltage, and delayed the conduction of electrical signals in the time domain. For frequency domain features, reduced dominant frequency and flatter spectral density distribution were obtained from both models. In addition, the time-frequency domain changes of both the Langendorff model and the BMS model showed a reduction in EGM energy. As for the application of Pin, it's effects on EGM features were opposite to those of CBX/Lido and the functional remodelling of BMS, which show that the enhancement of K^+ channel (the activation of I_{KATP}) also has

effects on the EGM features.

Given the well-characterised mechanisms of action of pharmacological agents such as Carbenoxolone, Lidocaine, and Pinacidil, the results of this study support the use of these modulators to replicate functional changes in the whole-heart model[207, 208, 209]. The data demonstrate that pharmacological interventions can, to some extent, substitute for direct structural or electrophysiological alterations in studies of EGM morphology at the organ level. Moreover, the observed changes in EGM morphology induced by functional modulation in BMS (biomechanical simulation) models can also be reproduced in the intact heart when similar physiological changes are introduced. This finding suggests that the effects of functional alterations on EGM are not confined to cells or simplified tissue preparations, but also manifest at the whole-organ level. These results therefore lend further support to the clinical translational potential of findings derived from BMS and cultured-cells, provided they are appropriately validated in integrative models.

However, the results also highlight important differences between simplified and whole-organ models. In the previous chapter, findings suggested that remodelling of Cx43 exerts a more substantial effect on EGM features than modifications in $Na_v1.5$ sodium channel expression. By contrast, the Langendorff-perfused heart experiments presented here showed that Lidocaine, which primarily blocks sodium channels, had a greater impact on several EGM features than Carbenoxolone, which targets gap junction-mediated conduction. This apparent discrepancy may be attributed to the non-specific effects of these drugs, as well as the inherent complexity of the whole-heart environment, including three-dimensional conduction, regional heterogeneity, and the involvement of the Purkinje network.

The intact heart exhibits sophisticated spatial and temporal patterns of activation that are not recapitulated in isolated tissue or cell models. As a result, the effects of pharmacological agents can be influenced by additional factors such as transmural conduction gradients, autonomic inputs, and mechano-electric feedback[69]. Furthermore, both Lidocaine and Carbenoxolone are known to exert off-target effects, which may influence electrophysiological behaviour in ways not directly related to their primary targets[207, 210].

Overall, while pharmacological manipulation provides a useful strategy for inducing functional changes in the intact heart, these results emphasise the need for cautious interpretation when comparing simplified models to whole-organ preparations. Nevertheless, the consistency observed in several key EGM features between BMS and the Langendorff heart supports the broader relevance of functional changes studied in vitro and reinforces the potential of BMS to inform clinically relevant research when properly validated.

6.5 Limitations

Even the usages of pharmaceutical modulators can achieve similar EGM morphology changes obtained from BMS with functional changes, but it is not guaranteed that the trends and degree of whole heart EGM changes are the same as what was obtained from the BMS. In order to establish whether functional changes have the same impacts on the whole heart EGM, Langendorff should be carried out on heart failures induced and healthy animal models following staining of the samples collected from where the EGMs are recorded to confirm the structural and functional changes.

In addition, the EGMs recorded from the Langendorff experiment have a higher noise compared to the EGMs recorded from the MEA experiment. This is because the BMS were directly placed on the electrodes; however, the electrodes on the HD Grid catheter were manually attached to the epicardium. This noise has a negative impact on the accuracy of frequency domain and time-frequency features. For example, non significant difference was obtained from scale corresponding to minimum energy because the minimum energy was generated by noise. The noise also affects the PSD of the recording, which causes different degrees of distortion in the frequency domain features[211].

Due to the low number of human heart (n = 1), the results of the human heart are not included in this thesis. Although several studies illustrate that the EGM obtained from porcine heart Ludendorff shares similar features as human heart[206, 212], but it remains unclear that the pharmacological modulations has the same effects on human heart EGM and can be used to

represent functional changes.

6.6 Conclusion

The application of the EGM analysis framework to ex vivo porcine hearts demonstrates the translational relevance of this work. This chapter shows that pharmacological interventions—targeting conduction, ion channels, or coupling—produce measurable alterations in EGM morphology in a large-animal model that closely resembles human cardiac physiology. The significance of these results lies in their demonstration that EGM features can serve as sensitive biomarkers of pharmacological modulation, providing a bridge between experimental models and potential clinical application.

The novelty of this work lies in combining the automated EGM analysis tool with a translationally relevant large-animal model to assess functional remodelling achieved by pharmacological effects. This represents a methodological advance by providing a reproducible and objective means of quantifying drug-induced changes in cardiac conduction through electrogram morphology, with implications for both pre-clinical testing and safety pharmacology.

Chapter 7

Development of Numerical Simulation of Cardiac Electrophysiology with remodelling

7.1 Introduction

Numerical simulations of cardiac electrical and mechanical activity are becoming a popular research topic because of their important guiding role in clinical practice. If an accurate in-silico simulation model of the patient's heart can be built before the treatment, the efficiency and success rate of the treatment may be greatly improved. However, current models are not yet sufficient for clinical use. First, the accuracy of the simulations are sacrificed due to simplifications. Second, only scar has been considered in most 2D and 3D large-scale models, and ion channel remodelling was only been included in some small-scale 1D simulations. This chapter includes simulations using both a continuum propagation model and a discrete cell model with gap junctional remodelling at BMS level, which provides guidance for the development of the digital twin of human hearts. The discrete cell model used in this study was developed by Dr. Charles Houston.

The hypotheses to be addressed were as follows:

1. Both the continuum propagation model and the discrete cell model can be used to simulate the electrical activity of virtual generated cell monolayers with gap junctional remodelling.

2. Virtual EGMs can be recorded and analysed.

For these purposes, the following studies described in this chapter were carried out:

1. Generate virtual cell monolayers using Virtual Cardiac Tissue Model (VCT).

2. Import the virtual cell monolayers into the simulation tool (Nektar++).

3. Add gap junctional remodelling to the cell monolayers.

4. Export EGMs and extract fratures from the recorded EGMs.

7.2 Methods

The in-silico tools used in the study were introduced in Section 2.7.2. The generation of the virtual cell monolayers, the simulations and the further analysis are introduced in detail in this Section.

7.2.1 Digital cell monolayer generation

VCT allows the user to create cell monolayers with required cell sizes, monolayer sizes, and shapes. By seeding the cells on preset fibres and providing the cells enough time to grow, the monolayer can be shaped in a format similar to the cell layers cultured in the lab. An example of virtual cell monolayer generation is shown in Figure 7.1.

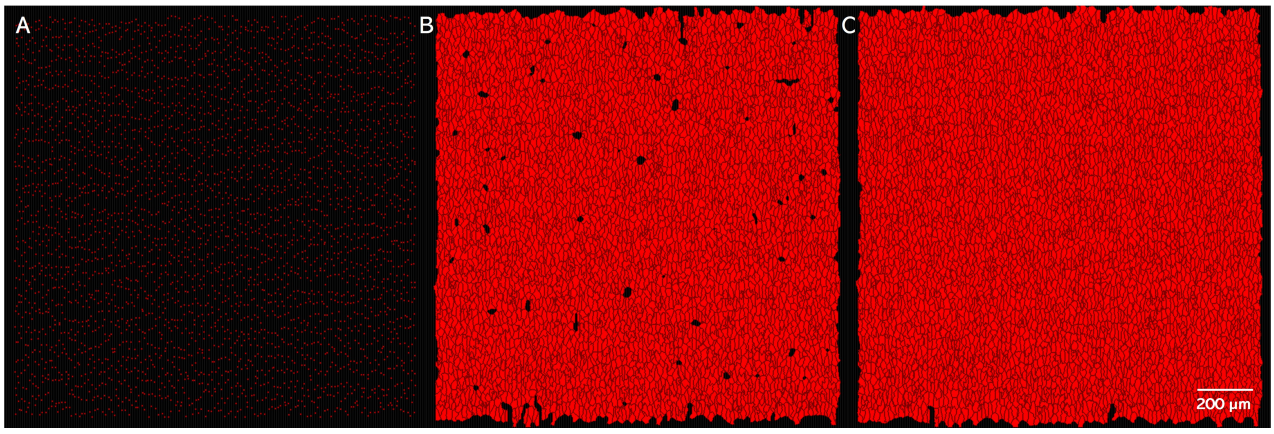


Figure 7.1: (A) Cells seeded in a 1.2 mm × 1.2 mm domain. (B) Cells in the "growing" process. (C) Final grown monolayer.

Codes were then developed to transfer the generated VCT file to the file that can be imported into Nektar++ for simulations. The transfer process is shown in Figure 7.2. The domains used for simulations with the continuum model were generated in Gmsh.

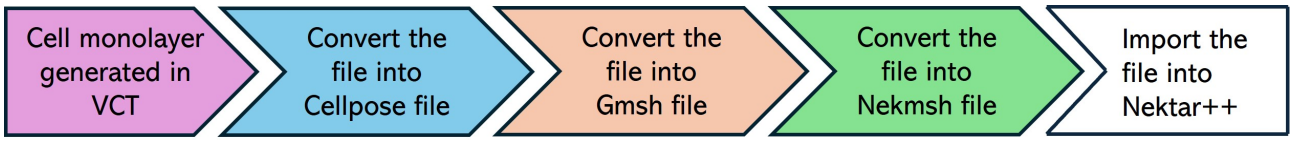


Figure 7.2: File format conversion process.

7.2.2 Simulation setup

The electrical propagation simulations were carried out using the CardiacEPSolver built on Nektar++. The Ten Tusscher human LV ion-channel model and in-house developed propagation models (both the continuum model and the discrete-cell model) were used.

For all simulations, the resting potential was set at -81 mV, the monolayers were stimulated from the right edge, creating a wavefront from right to left.

A 1.2mm × 1.2 mm domain is shown in Figure 7.1. A 0.2 mm × 0.2 mm area with abnormal gap junctions is introduced into the lower left corner by increasing the conduction resistance. To be more specific, the conductivities are set to 4 mS/mm in the healthy area and 20 mS/mm in the area with abnormal gap junctions for both the continuum model and the discrete-cell

model. In order to compare the propogation models and enable calibrating digital models with biological models in the future, 36 electrodes were placed on the same locations on each simulation domain and simulated EGMs were recorded during the simulations. The electrode locations and the abnormal gap junction area are shown in Figure 7.3.

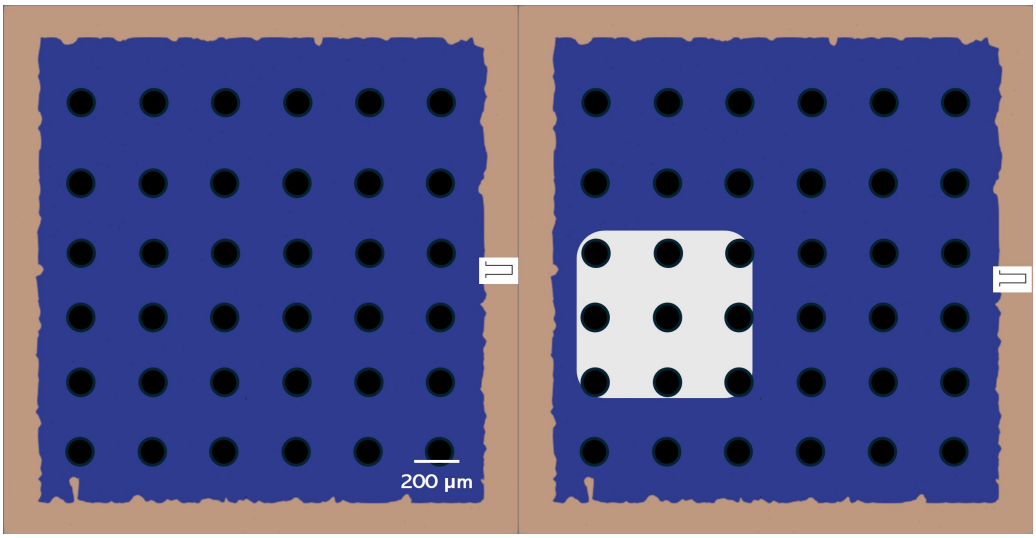


Figure 7.3: (A) A healthy 1.2 mm × 1.2 mm monolayer with electrodes. (B) Monolayer with an abnormal gap junction area, 9 electrodes are located in the abnormal area, the conductivity of the gap junctions within the abnormal area was set to 1/5 of it from the normal area.

7.3 Results

7.3.1 Feature extraction of simulated data

At current stage, the simulated EGM are much simpler than the real EGM obtained from the BMS. In that case, only three important time-domain features were extracted from the simulated EGM: EGM duration, EGM voltage, and conduction velocity. The example of simulated EGMs are shown in Figure 7.4 and Figure 7.5.

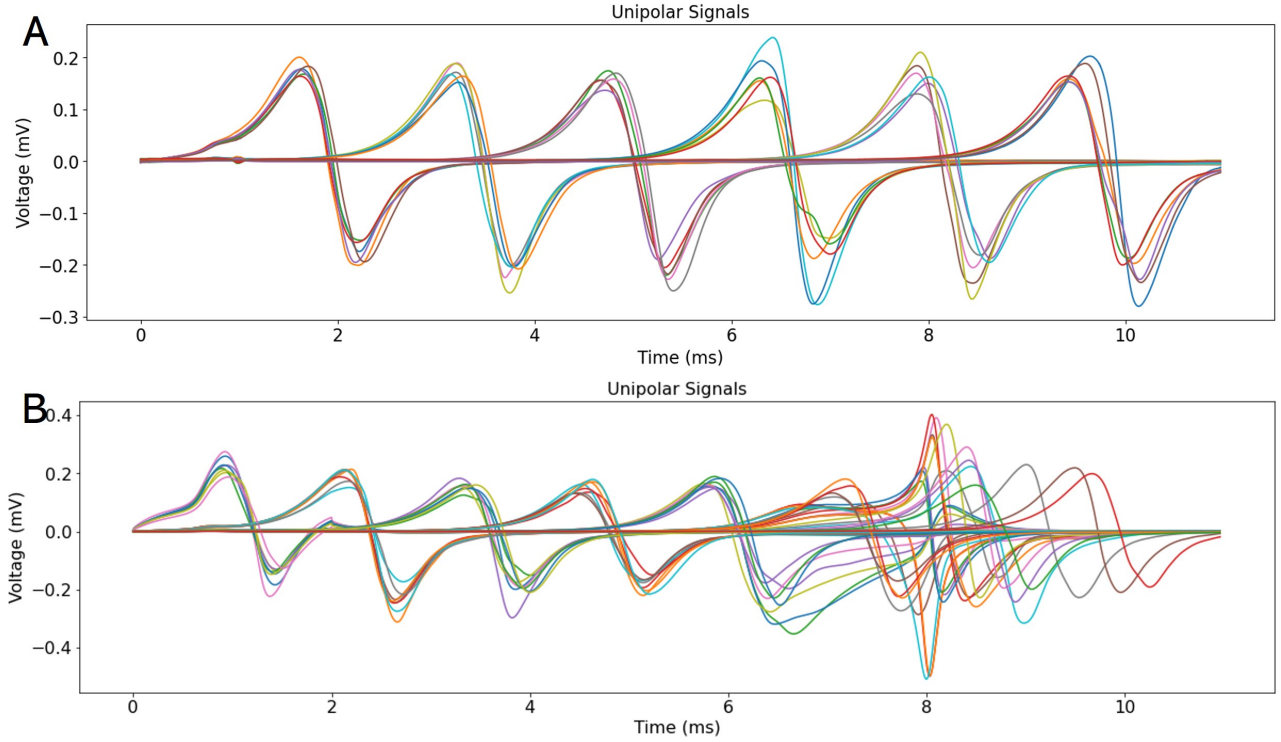


Figure 7.4: (A) EGMs recorded from the simulation with the discrete model and healthy monolayer. (B) EGMs recorded from the simulation with the discrete model and the monolayer with abnormal gap junction area.

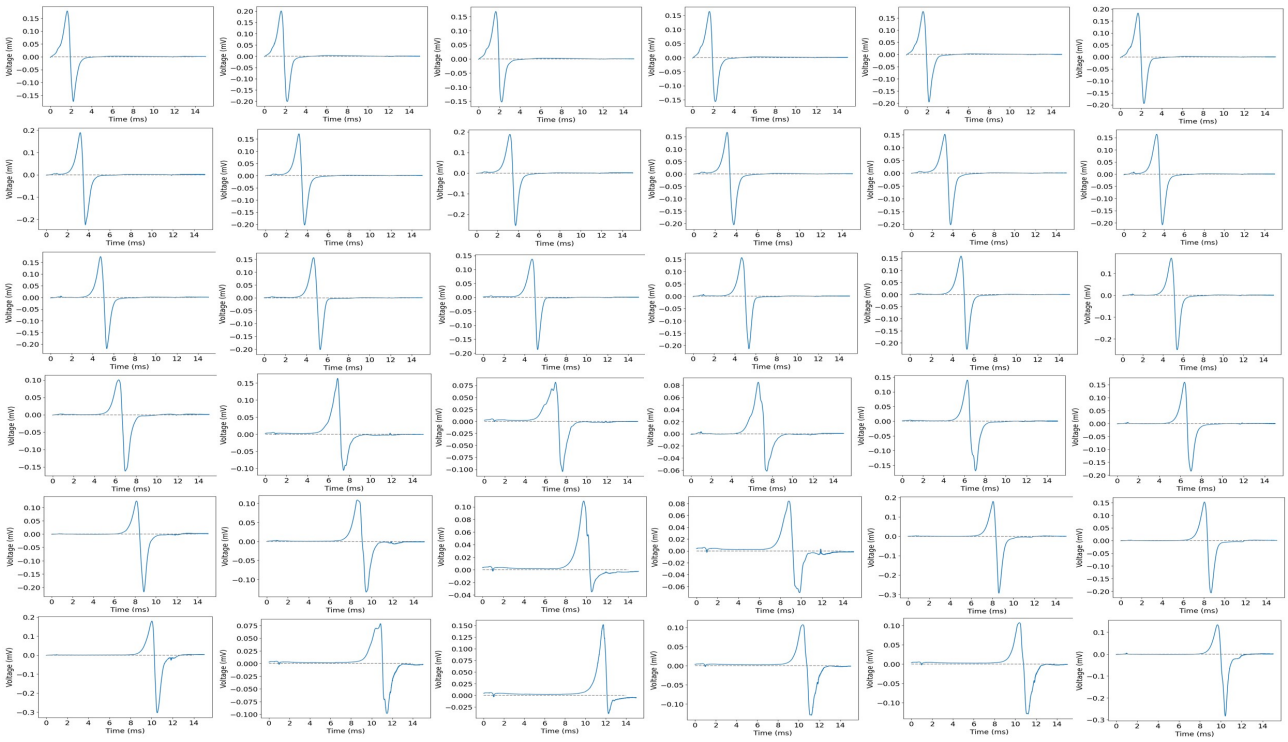


Figure 7.5: Simulated EGMs in relation with the locations of the electrodes.

7.3.2 Comparison between continuum model and discrete model

The simulation of a healthy monolayer using the discrete cell model took 19.5 hours, while the simulation of a monolayer containing an abnormal gap junction area took 32.1 hours. The simulation of a healthy monolayer using the continuous model took 29 minutes, while the simulation of an abnormal monolayer took 6.4 hours.

The features extracted from the example domains were used to compare the continuum model and the discrete model, the simulation results are shown in Figure 7.6, the comparation between the time domain features of simulated EGMs are shown in Figure 7.7.

The EGM duration increases significantly within the abnormal gap junction area (mean values of the discrete-cell model: 10.37 ± 2.33 ms; mean values of the continuum model model: 10.19 ± 1.57 ms) comparing to the healthy area (mean values of the discrete-cell model: 7.59 ± 0.85 ms; mean values of the continuum model: 7.73 ± 0.04 mV) for both models (p value of the discrete cell model: 0.0074; p value of the continuum model: 0.0001).

The EGM amplitude is also affected within the abnormal gap junction area. The EGM amplitude within the abnormal gap junction area (mean values of the discrete-cell model: 0.194 ± 0.045 mV; mean values of the continuum model model: 0.196 ± 0.02 mV) is decreased comparing to the healthy area(mean values of the discrete-cell model: 0.376 ± 0.05 mV; mean values of the continuum model: 0.378 ± 0.01 mV). The p value of the discrete cell model is less than 0.0001 and the p value of the continuum model is also less than 0.0001.

Visible slowing of the conduction velocity can be obtained on the activation map from the simulations using both models, but there is no significant quantified difference (p value for the discrete model: > 0.9999; p value for the continuum model: > 0.9999). For the discrete model, the mean value decreases from 0.15 ± 0.003 m/s in healthy area to 0.13 ± 0.01 m/s in abnormal gap junction area. For the continuum model, the mean value decreases from 0.25 ± 0.001 m/s in healthy area to 0.21 ± 0.0006 m/s in abnormal gap junction area.

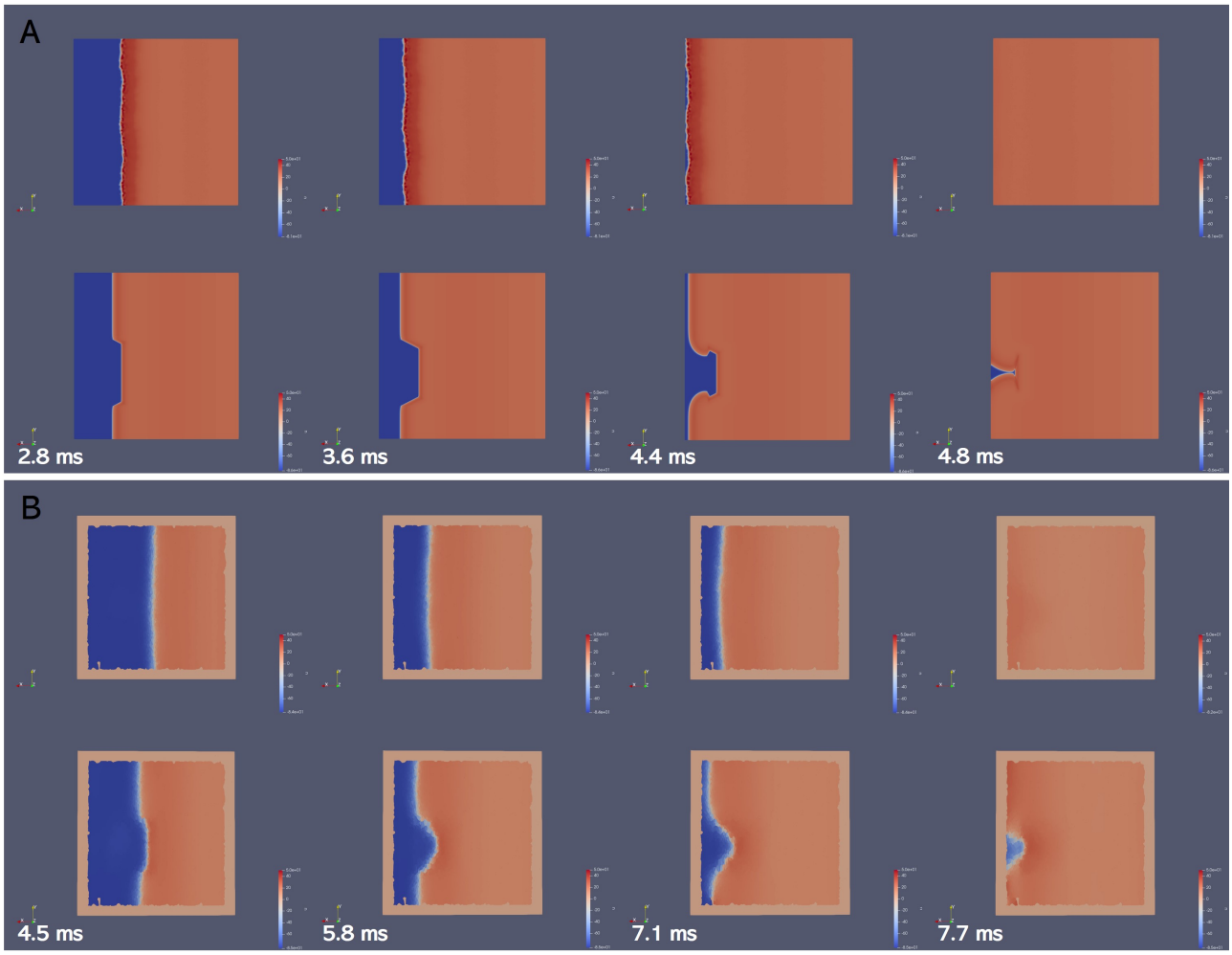


Figure 7.6: Simulated propagation in healthy monolayer and the monolayer with abnormal gap junction area. (A) The continuum model. (B) The discrete model.

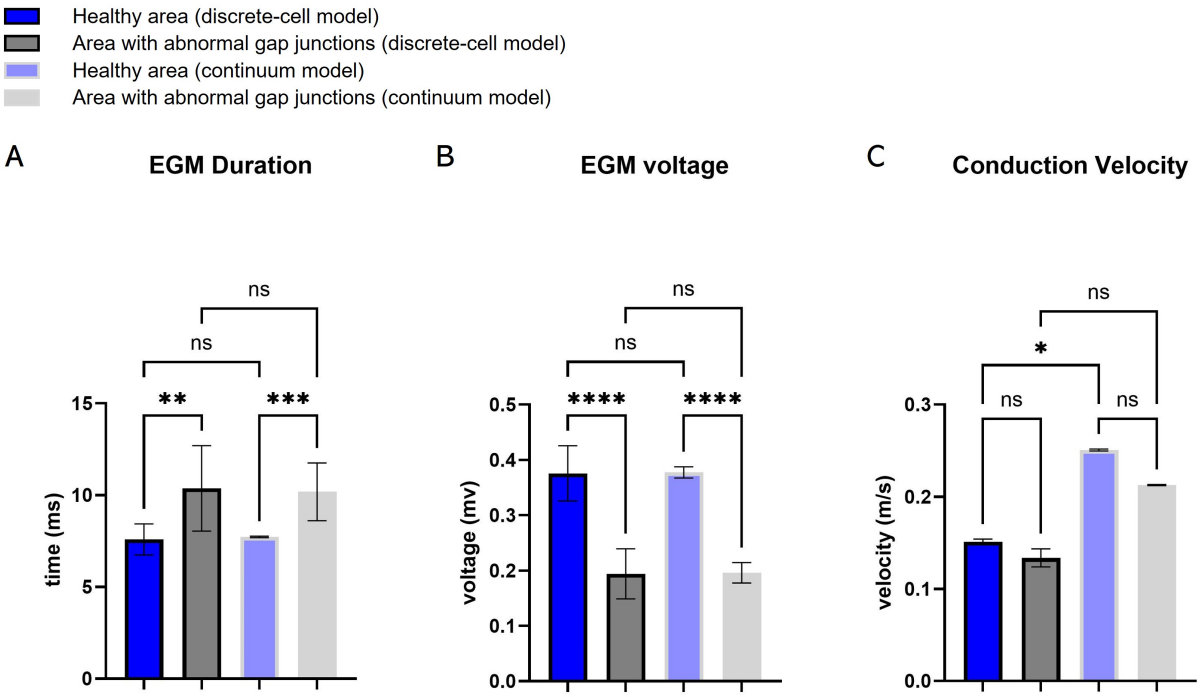


Figure 7.7: Comparison between time domain features of EGMs recorded from the simulations. (A) EGM duration. (B) EGM voltage. (C) conduction velocity. Grey error bars represent the standard deviation. All bar charts represent mean ± S.D.; ns $0.05 < p \leq 1$, *$p \leq 0.05$, **$p \leq 0.01$, ***$p \leq 0.001$, ****$p \leq 0.0001$.

Also, no significant differences were obtained from the comparisons between different models. For EGM duration, the p value between healthy area is more than 0.9999 and the p value between abnormal gap junction area is also more than 0.9999. For EGM voltage, the p value between healthy area is more than 0.9999 and the p value between abnormal gap junction area is also more than 0.9999. For conduction velocity, the p value between healthy area is 0.0210 and the p value between abnormal gap junction area is 0.2337.

7.4 Discussion

The existing literature on computational modelling has largely focused on action potential propagation, arrhythmia dynamics, and tissue-level conduction changes (Clayton and Panfilov; Vigmond et al.)[76, 77]. While these models have provided important insights into arrhythmia mechanisms, relatively few have attempted to reproduce EGM morphology in a manner that

can be directly compared with experimental data. This simulations therefore represent an advance by explicitly validating morphological features against experimental results.

7.4.1 The accuracy of different models

This study investigated how different propagation models affect the results of two-dimensional simulations of human left ventricle myocyte monolayers. The findings show that both models produce similar EGM features in the time domain when simulating a 1.2 mm $\times$ 1.2 mm monolayer. However, the conduction velocities differed between the models. This discrepancy could be attributed to the gap junctions included in the discrete-cell model, which adds more detailed interactions between cells, while the continuum model assumes a homogeneous tissue. The gap junction resistance in the discrete-cell model slows down conduction velocities, suggesting that it may provide a more accurate representation of conduction at the cellular level compared to the continuum model[213, 152].

7.4.2 The accuracy of the novel discrete model

Although the mean values of the time domain features are not significantly different, it is noticed from the standard deviations of the features that the distribution of feature values of the simulation using the discrete cell model is much wider than that using the continuous model, which may be due to the cell-level heterogeneity of the discrete cell model. This suggests that the discrete cell model may be more accurate in capturing cell-level heterogeneity despite similar group comparisons.

In addition, the simulation time of the simulations using the discrete cell model is much longer than that of the continuous model. This time will increase further if the size of the domain increases, potentially making such simulations intractable without extensive computational resources[214, 215].

7.5 Limitations

The simulation domains were created using the VCT, which means that the cell morphologies in the model do not perfectly match those of the BMS. While Cellpose[216] offers a function to generate virtual cell monolayers based on images of WGA staining, the BMS staining images contain an excessive number of cells, making it difficult to train Cellpose effectively for monolayer generation. The current version of Cellpose can accurately generate cell monolayers with fewer than 200 cells, but the BMS consists of over 5000 cells in a single layer, making it unsuitable for the monolayer generation process as currently designed.

Additionally, due to computational limitations, the simulations using the discrete model were restricted to smaller domains. This restriction prevents the accurate representation of certain features, such as conduction velocity, which could not be fully captured in these smaller simulations.

Moreover, the simulated EGM in these models is considerably simplified compared to a real EGM. As a result, many of the key features typically used for model calibration and validation are not present, limiting the ability to extract meaningful data from the simulations for further refinement or real-world comparison (digital-twin).

7.6 Conclusion

In this chapter, a computational framework capable of reproducing the effects of structural and functional remodelling on EGM morphology was developed. The significance of this work lies in demonstrating the capacity of in silico modelling not only to reproduce conduction abnormalities but also to generate EGM morphologies that closely resemble those recorded experimentally. This provides a powerful means of integrating mechanistic insights with experimental data, allowing for prediction, hypothesis testing, and validation across different scales of cardiac electrophysiology.

Although discrete cell models require more computational resources and time, they can more

accurately capture biophysical processes and simulate propagation in the presence of monolayer heterogeneity. Despite the simplifying assumptions of continuum models, their EGM features are still comparable to those produced by discrete cell models. While continuum models are important for organ-scale simulations, discrete cell models provide a more precise understanding of propagation at the microscopic level, offering better insights into the dynamics within monolayers and the myocardium.

The novelty of this chapter lies in integrating numerical simulation with the experimental framework established earlier in the thesis. By aligning in silico predictions with biological observations, a unique dual approach that reinforces the mechanistic interpretation of EGM features and establishes a platform for future predictive modelling of remodelling processes was provided.

Chapter 8

Conclusion

8.1 Summary of Key findings

This thesis aims to identify and characterise the underlying substrate changes in failing hearts and examine their impact on cardiac electrogram morphology. To achieve this, an advanced analysis tool was developed for extracting detailed features from unipolar cardiac EGMs. This tool was applied to data obtained from various experimental models, including rat LV BMS, human LV BMS, cultured cardiomyocytes, and porcine hearts in an ex vivo setup. The study investigates both structural and functional substrate changes, exploring their correlations with specific EGM features to better understand the electrophysiological manifestations of heart failure.

The central contributions of this work are as follow. The research expands the set of EGM features available for detailed analysis, incorporating novel morphological features of the electrograms that were previously underexplored. This expansion provides a more nuanced understanding of the electrical behaviour in the heart, particularly in pathological conditions. Apart from that, this research establishes significant correlations between EGM morphology and the structural and functional changes within the heart tissue. By correlating these electrogram features with alterations in the myocardial substrate—such as fibrosis and ion channel remodelling—this thesis contributes valuable insights into the electrophysiological mechanisms

that underlie heart failure. These findings not only deepen the understanding of the substrate changes in failing hearts but also have the potential to inform the development of more targeted diagnostic and therapeutic approaches for heart failure patients. Importantly, in addition to employing cell and animal models, this thesis also incorporated patient samples to characterise the pathology of heart failure (HF). This approach enhances the clinical relevance and robustness of the findings, as patient-derived data offer a more accurate reflection of human disease compared to simpler experimental models. Consequently, the conclusions drawn from this research are more reliable and more directly applicable to the human condition, providing valuable insights into the underlying mechanisms of HF.

8.1.1 Development of electrogram morphology analysis tool

In this thesis, a Python-based analysis tool was first developed to extract 34 distinct features from unipolar EGMs for the subsequent correlation of EGM morphology with underlying substrate changes. These features are categorised into four groups: 18 time-domain features, 7 frequency-domain features, 7 time-frequency features, and 2 entropy features. The tool utilises a range of signal processing techniques, such as applying filters without distorting the signal, detecting specific time points, and performing Fourier transforms, among others. It has been successfully tested on EGM data recorded from rat and human LV BMS, cultured cells, as well as from porcine ex vivo heart model. The newly developed tool fills a significant gap in the current research landscape, as no existing tool can accurately extract such a broad set of features from EGMs recorded during MEA experiments or those captured via LabChart. As such, this tool offers valuable support for researchers working with EGMs, enabling a more comprehensive analysis of electrophysiological data. To improve accessibility, a user-friendly graphical user interface (GUI) was also developed, facilitating use by non-computational researchers, including clinical and biological scientists.

Despite its notable advantages, the developed tool has certain limitations. A major challenge arises in detecting the T-wave due to the presence of unavoidable noise in the recorded signals. This noise not only hinders the detection of the T-wave but also affects the accuracy of several

frequency-domain and time-frequency features. As a result, time-domain features related to the T-wave were excluded from the analysis in this study, and the precision of their extraction remains unverified. Furthermore, an additional uncertainty exists regarding the scale corresponding to minimum energy, whether it is influenced by noise or if it is inherently unsuitable for evaluating EGM morphology. Currently, the tool is designed to process EGMs recorded in specific formats, limiting its broader applicability. However, there is substantial potential for future development, as expanding the compatibility of the tool with a wider range of EGM recording formats could significantly broaden its application scope, making it a more versatile tool for diverse electrophysiological studies.

8.1.2 Electrogram Morphology effects due to underlying substrate changes in BMS and cell models

This thesis investigates the EGM morphology, structural changes as well as functional changes in cultured cell, human heart BMS and rat heart BMS models. Additionally, the study explores the effects of these changes on the EGM morphology of these models. These findings have potential clinical implications for predicting and understanding cardiac arrhythmias and electrical disturbances in heart failure patients.

The results of this study reveal that human failing hearts exhibit significantly greater collagen expression compared to human donor hearts. In the context of heart failure, excessive collagen deposition leads to fibrosis, which can disrupt normal myocardial architecture and contribute to altered electrical conductivity. These findings are consistent with prior studies that have reported elevated collagen content and disorganised extracellular matrix as key contributors to conduction slowing and arrhythmogenesis in fibrotic hearts[217]. The increased collagen expression in failing hearts was found to directly correlate with a variety of electrogram features in both rat and human LV BMS. Specifically, 21 distinct EGM features were identified as being significantly influenced by collagen expression, which Significantly expands previous research on the correlation between collagen and EGM[218, 219]. This correlation suggests that collagen not only contributes to structural remodelling but also has a measurable impact on the electrical

activities within the heart. Importantly, traditional clinical features often prove inadequate for accurately detecting or quantifying collagen expression, thereby limiting their usefulness in guiding targeted interventions. In contrast, the observed correlations between EGM morphology and collagen expression suggest that EGM-based analysis could serve as a more sensitive and accessible approach for assessing fibrotic changes in cardiac tissue. Although the present study is constrained by a relatively small sample size, the results provide a compelling foundation for future research. Studies involving larger and more diverse cohorts will be essential to validate these findings and further explore their potential clinical applications.

Moreover, these results open the door to a reverse translational approach, in which specific EGM features associated with collagen may be traced back to underlying structural or cellular mechanisms. This could offer valuable insight into how fibrotic scar tissue alters electrophysiological properties, thereby deepening our understanding of the pathophysiological link between structural remodelling and electrical dysfunction in heart failure.

One of the key observations of this study is that the correlation between collagen expression and EGM features was stronger in rat LV BMS than in human LV BMS. This suggests that, while collagen plays a significant role in both models, additional factors in human hearts may contribute to a more complex relationship between the underlaying substrate and the EGM morphology. The pathological conditions may influence the ion channels within the cells and further affect the EGM morphology in human hearts. Therefore, further investigations are needed to fully comprehend the functional changes in human hearts and their correlation with the EGM features.

Immunohistochemical staining of human LV samples provided further insight into the molecular mechanisms underlying the changes in EGM morphology. The results indicated significant remodelling of two key channels: Cx43, a gap junction protein critical for cell-to-cell communication, and $Na_v1.5$, a sodium ion channel essential for action potential initiation. In human failing hearts, Cx43 expression was significantly reduced, and there was increased heterogeneity and lateralisation of its distribution. This is consistent with the literature[15], which has documented Cx43 downregulation and lateralisation in failing myocardium. Similarly, $Na_v1.5$

expression was diminished, and its distribution became more heterogeneous. These changes in ion channel expression and distribution were strongly correlated with alterations in EGM morphology, suggesting that the remodelling of these channels contributes significantly to the observed electrical disturbances in heart failure. This observation echoes findings from Akar et al., who showed that disrupted Cx43 expression can lead to conduction slowing and arrhythmia even in the absence of significant sodium current alterations[220]. In addition to the previous research, this thesis includes more features of the EGM which further explore the relationship between EGM morphology and channels. Notably, the remodelling of Cx43 exhibited a stronger correlation with the EGM features compared to $Na_v1.5$, indicating that changes in gap junction may play a more prominent role in the disruption of normal electrical conduction in the failing heart.

Despite the significant correlations observed between collagen expression, ion channel remodelling, and EGM morphology, it is important to note that the R^2 values of most correlations were low. This indicates that, while these relationships are significant, they may not fully explain the variability observed in the electrogram features. Several factors may contribute to this discrepancy. First, simple linear regression models may not adequately capture the complex, non-linear relationships between the structural and functional changes in the heart. More advanced statistical methods, such as machine learning or multi-variable modelling, could provide a more accurate representation of these relationships. Second, this study focused primarily on Cx43 and $Na_v1.5$ ion channels. Given the complexity of ion channel remodelling in heart failure, other ion channels and molecular pathways likely contribute to the observed changes in EGM morphology. Future research should explore the role of additional ion channels and other molecular factors that may influence electrical conduction and arrhythmogenesis in the failing heart.

An additional aspect of this study was the investigation of neuronal influence on EGM morphology. Neurons are known to contribute to the regulation of cardiac rhythm, and their role in the pathophysiology of heart failure has been increasingly recognised. However, due to the difficulty of detecting neurons in BMS and ex vivo heart models, this study used co-culture models with NRVMs and SNs to explore the effects of neuronal cells on EGM features. The

results demonstrated that the presence of neurons altered certain time-domain EGM features at the cellular level, further suggesting that neuronal activity may modulate the electrophysiological properties of the heart. It was found that co-culture with SNs enhance the growth of NRVMs and also increase the Cx43 expression in NRVMs. Previous comparative studies have similarly noted co-culture with SNs may have positive effects on cardiomyocyte growth rates[159, 160].

8.1.3 Electrogram Morphology effects due to functional changes in ex vivo porcine heart model

Although significant correlations between EGM features and underlying substrate changes have been demonstrated using cultured cells and BMS models, the translational relevance of these findings remains limited. This is primarily due to the inherent simplifications and assumptions within these models, which may not fully capture the complexity of human cardiac tissue in vivo.

In this thesis, the effects of functional changes induced by pharmacological modulation on EGM morphology were analysed in ex vivo porcine heart models. It is essential to determine whether the functional changes observed at the cellular and tissue levels translate to the organ level to validate the clinical applicability of the research.

Statistical analysis shows that changes in EGM features, similar to those observed in human donor and failing heart BMS, were observed between baseline EGM and post-pharmacological modulation in the ex vivo porcine heart models. This demonstrates that the functional changes have consistent effects on EGM morphology across different scales, providing strong evidence that the findings in this study may have clinical translational potential, which aligns with the literature[206]. By observing these changes at the organ level, this study further supports the potential to use EGM features as biomarkers for assessing the effects of therapeutic interventions in cardiac pathologies.

However, there are limitations inherent in the methodology, time constraints, and the costs

associated with the experiments, which prevented a thorough investigation of the influence of neurons and structural changes, such as collagen deposition, in the ex vivo heart models. Additionally, ion channel remodelling was simulated through pharmacological modulation rather than direct observation. As a result, it remains unclear whether the effects of neurons and collagen on the whole heart mirror those seen in the BMS and cell models. Furthermore, there is uncertainty as to whether the pharmacological modulation accurately reflects the functional changes occurring in vivo, making it challenging to fully extrapolate these findings to human clinical settings. Further studies incorporating a broader range of factors, such as neuronal influence and collagen deposition, would be necessary to confirm the full scope of the functional changes in the heart and their impact on EGM morphology at the organ level. Also the ex vivo model was built on porcine heart, the human data was not included in this thesis due to extreme low N number (N = 1), more human hearts are needed to test if the same results can be obtained from human ex vivo heart model.

8.1.4 Development of in-silico simulations

In this study, computational simulations were developed to model the electrical activities of human LV cell monolayers. Two different propagation models, the discrete cell model and the continuum model, were employed to simulate the electrical behaviour of these monolayers. To further enhance the realism of the simulation, regions with abnormal gap junctions were incorporated into the model domains. The monolayers, which were designed to replicate the morphology of human LV cardiomyocytes, were successfully generated and imported into the simulations. These simulations generated electrograms with time-domain features from both propagation models, applied to millimetre-scale monolayers, allowing for detailed analysis of electrical activity. The inclusion of an abnormal gap junction area in both models demonstrated their ability to replicate pathological changes in electrical conduction, further reinforcing the validity of these models for simulating arrhythmias and other electrical disturbances. The developed simulation method holds significant promise for generating digital twins of human BMS, which could eventually lead to more personalised approaches in understanding and treating

heart conditions.

At present, the simulations only incorporate simple gap junction abnormalities,additional functional changes and scars or more complex structural remodelling, need to be included to improve the accuracy and clinical relevance of the model. Moreover, the simulations rely on virtually generated cell monolayers, which may not fully capture the diversity and complexity of actual tissue structures. To address this limitation, further WGA staining should be conducted to build a more robust dataset for Cellpose, ensuring that cell monolayers can be accurately generated from high-resolution microscope images. By expanding the dataset and enhancing the simulation's input, the models can be calibrated more precisely. Once sufficient data is gathered from experimental setups, such as MEA experiments, the simulation parameters can be fine-tuned using the EGM features calculated from the real-world data. This calibration will allow for the creation of a more accurate digital twin, enhancing the potential of these computational models in understanding the complexities of cardiac arrhythmias and the effects of various interventions.

Through these advancements, the model could evolve into a more powerful tool for personalised medicine, where virtual simulations of a patient's cardiac tissue could be used to predict the impact of therapies and interventions, potentially improving clinical outcomes in heart disease management.

8.2 Clinical relevance of findings

The results of this study provide valuable insights into how to effectively evaluate the EGM morphology and assess the effects of both structural and functional changes on the EGM features in biological models at different scales. This research demonstrates that collagen deposition, ion channel remodelling, and neuronal activity have a significant impact on the EGM features and may serve as potential contributors to the development of arrhythmias. These findings suggest that, with a comprehensive understanding of these effects, it is possible to accurately predict the underlying conditions of the heart by interpreting and classifying the EGM signals during

catheter ablation procedures. By leveraging the morphology of collected EGMs, machine learning models can be trained to predict how the EGM might change under pathological conditions, further enhancing the diagnostic and prognostic capabilities of EGM-based analyses.

The ability to classify and predict arrhythmic conditions through the EGM morphology could be a key advancement in personalised cardiac care. In particular, it could lead to more precise and tailored interventions during catheter ablation, improving the success rate of procedures and reducing the risk of adverse outcomes. Furthermore, the study illustrates the potential for the EGM morphology to act as a non-invasive marker for identifying pro-arrhythmic conditions, which could pave the way for early detection and intervention in patients at risk of arrhythmias.

Overall, the results of this study underscore the promising potential of using EGM morphology as a predictive tool for identifying pro-arrhythmic conditions and enhancing the precision of treatments for arrhythmias. The findings also highlight the critical need for continued research in this area, as understanding the intricate relationship between structural and functional changes in the heart and their influence on electrical activity is essential to advance diagnostic and therapeutic strategies in cardiology.

8.3 Future directions

Looking forward, there are several potential avenues for future research that could further expand the understanding and application of the EGM morphology analysis. Currently, the feature extraction tool developed in this study is designed to analyse unipolar EGMs. However, additional functionality could be incorporated to enable the tool to also analyse bipolar and omnipolar EGMs. Bipolar EGMs are more commonly used in clinical practice, while omnipolar EGMs are gaining traction in research due to their ability to provide more comprehensive electrical mapping of the heart. Expanding the capabilities of the tool to analyse these types of EGMs would make it more versatile and applicable in both clinical and research settings. Additionally, investigating dynamic characteristics of EGMs could greatly enhance the feature dataset, providing a more nuanced understanding of the heart's electrical activity under differ-

ent conditions. Future work could also target more advanced noise reduction methodologies. While the current analysis tool is capable of extracting a broader range of EGM features than traditional clinical systems, residual noise may obscure subtle but clinically relevant signal components. Implementing more sophisticated denoising algorithms—potentially leveraging machine learning or adaptive filtering—could not only improve signal fidelity but also allow for the identification of additional features currently masked by artefacts such as T-wave[221, 222].

Furthermore, this study has demonstrated that collagen deposition can be correlated with EGM features at the electrode level. Expanding this analysis to encompass all the EGM features could yield even more detailed insights into the relationship between the structural changes including perivascular fibrosis and the EGM morphology within the heart. In addition, further investigation into more ion channel remodelling and its non-linear relationship with EGM morphology is crucial. Once a sufficient array of underlying substrates is identified, numerical equations could be developed to quantitatively describe the relationship between these substrates and the resulting EGM morphology. This would help in advancing predictive models for arrhythmias and other cardiac disorders. Additionally, extending this research to include more data from human ex vivo heart models would be important to confirm that the findings observed in porcine models are also applicable to human hearts, further strengthening the clinical relevance of the study[223].

Also, some studies show that it is possible to isolate a heart with the vagus nerve intact, which means Langendorff experiment can be carried out with neuronal input[224, 225]. Such model can be used to investigate the effect of the nerve on the EGM at the organ level, which can better verify clinical applicability than the cell model.

The development of computational simulations is still in its early stages, and there is considerable room for improvement. As computational power improves, more accurate and larger simulation domains can be generated, including models of the entire left ventricle or even the whole heart. Currently, simulations using the discrete cell model are limited to small domains due to computational constraints. However, with advancements in computer performance, it will be possible to create more comprehensive digital twins of the human heart, enabling sim-

ulations that more accurately reflect the complexities of heart function and pathology. These simulations could play a key role in personalised medicine by helping to model and predict individual patient responses to various treatments, ultimately improving the precision of therapeutic interventions for arrhythmias and other cardiac conditions.

In conclusion, the next steps of this research could expand the scope of both experimental and computational approaches. By broadening the capabilities of the tool, improving simulation models, and incorporating more comprehensive data, future research will provide a deeper understanding of the underlying mechanisms of cardiac arrhythmias and further contribute to the advancement of the clinical application of EGM-based diagnostics and treatments.

Bibliography

[1] Arnold M Katz. *Physiology of the Heart*. Lippincott Williams & Wilkins, 2010.

[2] Pingzhu Zhou and William T Pu. Recounting cardiac cellular composition, 2016.

[3] Marieke Rienks, Anna-Pia Papageorgiou, Nikolaos G. Frangogiannis, and Stephane Heymans. Myocardial extracellular matrix. *Circulation Research*, 114(5):872–888, 2014.

[4] Paul J Wang and NA Mark Estes III. Supraventricular tachycardia. *Circulation*, 106(25):e206–e208, 2002.

[5] Gernot Schram, Marc Pourrier, Peter Melnyk, and Stanley Nattel. Differential distribution of cardiac ion channel expression as a basis for regional specialization in electrical function. *Circulation Research*, 90(9):939–950, 2002.

[6] André G Kléber and Yoram Rudy. Basic mechanisms of cardiac impulse propagation and associated arrhythmias. *Physiological reviews*, 84(2):431–488, 2004.

[7] Bronagh Heath, Kevin Gingrich, and Robert S Kass. Ion channels in the heart: Cellular and molecular properties of cardiac na, ca, and k channels. *Comprehensive Physiology*, pages 548–567, 2011.

[8] Kim Christensen, Kishan A Manani, and Nicholas S Peters. A simple model for identifying critical structures in atrial fibrillation. *arXiv preprint arXiv:1403.3299*, 2014.

[9] Rengasayee Veeraraghavan, Robert G Gourdie, and Steven Poelzing. Mechanisms of cardiac conduction: a history of revisions. *American Journal of Physiology-Heart and Circulatory Physiology*, 306(5):H619–H627, 2014.

[10] Madison S Spach. Transition from a continuous to discontinuous understanding of cardiac conduction, 2003.

[11] Goran Söhl and Klaus Willecke. Gap junctions and the connexin protein family. *Cardiovascular research*, 62(2):228–232, 2004.

[12] John A Jansen, Toon AB van Veen, Jacques MT de Bakker, and Harold VM van Rijen. Cardiac connexins and impulse propagation. *Journal of molecular and cellular cardiology*, 48(1):76–82, 2010.

[13] H Lee Kanter, Jeffrey E Saffitz, and Eric C Beyer. Cardiac myocytes express multiple gap junction proteins. *Circulation research*, 70(2):438–444, 1992.

[14] Stephan B Danik, Gregg Rosner, Joshua Lader, David E Gutstein, Glenn I Fishman, and Gregory E Morley. Electrical remodeling contributes to complex tachyarrhythmias in connexin43-deficient mouse hearts. *The FASEB journal: official publication of the Federation of American Societies for Experimental Biology*, 22(4):1204, 2007.

[15] Nicholas J Severs, Alexandra F Bruce, Emmanuel Dupont, and Stephen Rothery. Remodelling of gap junctions and connexin expression in diseased myocardium. *Cardiovascular research*, 80(1):9–19, 2008.

[16] Jeffrey E Saffitz, H Lee Kanter, Karen G Green, Timothy K Tolley, and Eric C Beyer. Tissue-specific determinants of anisotropic conduction velocity in canine atrial and ventricular myocardium. *Circulation research*, 74(6):1065–1070, 1994.

[17] Stephan Rohr. Role of gap junctions in the propagation of the cardiac action potential. *Cardiovascular research*, 62(2):309–322, 2004.

[18] Jan P Kucera, Stephan Rohr, et al. Slow conduction in cardiac tissue: insights from optical mapping at the cellular level. *Journal of electrocardiology*, 34(4):57–64, 2001.

[19] Stephan Rohr and BM Salzberg. Characterization of impulse propagation at the microscopic level across geometrically defined expansions of excitable tissue: multiple site

optical recording of transmembrane voltage (msortv) in patterned growth heart cell cultures. *Journal of General Physiology*, 104(2):287–309, 1994.

[20] Nicholas J Severs. Gap junction remodeling in heart failure. *Journal of cardiac failure*, 8(6):S293–S299, 2002.

[21] Eric C Beyer, David L Paul, and Daniel A Goodenough. Connexin43: a protein from rat heart homologous to a gap junction protein from liver. *The Journal of cell biology*, 105(6):2621–2629, 1987.

[22] Nathalie Rouach, Annette Koulakoff, Veronica Abudara, Klaus Willecke, and Christian Giaume. Astroglial metabolic networks sustain hippocampal synaptic transmission. *science*, 322(5907):1551–1555, 2008.

[23] Xavier F Figueroa and Brian R Duling. Gap junctions in the control of vascular function. *Antioxidants & redox signaling*, 11(2):251–266, 2009.

[24] Sawa Kostin, Markus Rieger, Sebastian Dammer, Stefan Hein, Manfred Richter, Wölf-Peter Klövekorn, Erwin P Bauer, and Jutta Schaper. Gap junction remodeling and altered connexin43 expression in the failing human heart. *Molecular and cellular biochemistry*, 242(1):135–144, 2003.

[25] JH Smith, CR Green, NS Peters, S Rothery, and NJ1886321 Severs. Altered patterns of gap junction distribution in ischemic heart disease. an immunohistochemical study of human myocardium using laser scanning confocal microscopy. *The American journal of pathology*, 139(4):801, 1991.

[26] Michael A Beardslee, Deborah L Lerner, Peter N Tadros, James G Laing, Eric C Beyer, Kathryn A Yamada, André G Kléber, Richard B Schuessler, and Jeffrey E Saffitz. Dephosphorylation and intracellular redistribution of ventricular connexin43 during electrical uncoupling induced by ischemia. *Circulation research*, 87(8):656–662, 2000.

[27] David E Gutstein, Gregory E Morley, Houman Tamaddon, Dhananjay Vaidya, Michael D Schneider, Ju Chen, Kenneth R Chien, Heidi Stuhlmann, and Glenn I Fishman. Conduc-

tion slowing and sudden arrhythmic death in mice with cardiac-restricted inactivation of connexin43. *Circulation research*, 88(3):333–339, 2001.

[28] H Van Rijen, T Van Veen, Daniel Gros, Ronald Wilders, and J De Bakker. Connexins and cardiac arrhythmias. *Advances in cardiology*, 42(R):150, 2006.

[29] Nicholas S Peters, Nicholas J Severs, Stephen M Rothery, Christopher Lincoln, Magdi H Yacoub, and Colin R Green. Spatiotemporal relation between gap junctions and fascia adherens junctions during postnatal development of human ventricular myocardium. *Circulation*, 90(2):713–725, 1994.

[30] Fabien Kieken, Nancy Mutsaers, Elena Dolmatova, Kelly Virgil, Andrew L Wit, Admir Kellezi, Bethany J Hirst-Jensen, Heather S Duffy, and Paul L Sorgen. Structural and molecular mechanisms of gap junction remodeling in epicardial border zone myocytes following myocardial infarction. *Circulation research*, 104(9):1103–1112, 2009.

[31] Junko Shibayama, William Paznekas, Akiko Seki, Steven Taffet, Ethylin Wang Jabs, Mario Delmar, and Hassan Musa. Functional characterization of connexin43 mutations found in patients with oculodentodigital dysplasia. *Circulation research*, 96(10):e83–e91, 2005.

[32] Jan Heeringa, Deirdre AM van der Kuip, Albert Hofman, Jan A Kors, Gerard van Herpen, Bruno H Ch Stricker, Theo Stijnen, Gregory YH Lip, and Jacqueline CM Witteman. Prevalence, incidence and lifetime risk of atrial fibrillation: the rotterdam study. *European heart journal*, 27(8):949–953, 2006.

[33] Emelia J Benjamin, Paul Muntner, Alvaro Alonso, Marcio S Bittencourt, Clifton W Callaway, April P Carson, Alanna M Chamberlain, Alexander R Chang, Susan Cheng, Sandeep R Das, et al. Heart disease and stroke statistics—2019 update: a report from the american heart association. *Circulation*, 139(10):e56–e528, 2019.

[34] Richard JA Till and Martin R Cowie. Atrial fibrillation in heart failure: New directions in diagnosis, risk assessment and risk reduction. *Journal of atrial fibrillation*, 6(6):1036, 2014.

[35] Miguel Vaquero, David Calvo, and José Jalife. Cardiac fibrillation: from ion channels to rotors in the human heart. *Heart rhythm*, 5(6):872–879, 2008.

[36] Eugene Braunwald. Research advances in heart failure: a compendium. *Circulation research*, 113(6):633–645, 2013.

[37] William H Maisel and Lynne Warner Stevenson. Atrial fibrillation in heart failure: epidemiology, pathophysiology, and rationale for therapy. *The American journal of cardiology*, 91(6):2–8, 2003.

[38] Steven Poelzing and David S Rosenbaum. Altered connexin43 expression produces arrhythmia substrate in heart failure. *American Journal of Physiology-Heart and Circulatory Physiology*, 287(4):H1762–H1770, 2004.

[39] José Jalife, Omer Berenfeld, and Moussa Mansour. Mother rotors and fibrillatory conduction: a mechanism of atrial fibrillation. *Cardiovascular research*, 54(2):204–216, 2002.

[40] Rémi Peyronnet, Jeanne M Nerbonne, and Peter Kohl. Cardiac mechano-gated ion channels and arrhythmias. *Circulation research*, 118(2):311–329, 2016.

[41] Eva A Rog-Zielinska, Russell A Norris, Peter Kohl, and Roger Markwald. The living scar–cardiac fibroblasts and the injured heart. *Trends in molecular medicine*, 22(2):99–114, 2016.

[42] Yingrui Li, Jianlin Du, Songbai Deng, Bin Liu, Xiaodong Jing, Yuling Yan, Yajie Liu, Jing Wang, Xiaobo Zhou, and Qiang She. The molecular mechanisms of cardiac development and related diseases. *Signal Transduction and Targeted Therapy*, 9(1):368, 2024.

[43] Yao Sun and Karl T Weber. Infarct scar: a dynamic tissue. *Cardiovascular research*, 46(2):250–256, 2000.

[44] Paola Occhetta, Giuseppe Isu, Marta Lemme, Chiara Conficconi, Philipp Oertle, Christian Räz, Roberta Visone, Giulia Cerino, Marija Plodinec, Marco Rasponi, et al. A three-dimensional in vitro dynamic micro-tissue model of cardiac scar formation. *Integrative Biology*, 10(3):174–183, 2018.

[45] Amir Jadidi, Mark Nothstein, Juan Chen, Heiko Lehrmann, Olaf Dössel, Jürgen Allgeier, Dietmar Trenk, Franz-Josef Neumann, Axel Loewe, Björn Müller-Edenborn, et al. Specific electrogram characteristics identify the extra-pulmonary vein arrhythmogenic sources of persistent atrial fibrillation–characterization of the arrhythmogenic electrogram patterns during atrial fibrillation and sinus rhythm. *Scientific reports*, 10(1):9147, 2020.

[46] Mohammad Shenasa, Gerhard Hindricks, David J Callans, John M Miller, and Mark E Josephson. *Cardiac mapping*. John Wiley & Sons, 2019.

[47] Chris D Cantwell, Caroline H Roney, Fu Siong Ng, Jennifer H Siggers, Spencer J Sherwin, and Nicholas S Peters. Techniques for automated local activation time annotation and conduction velocity estimation in cardiac mapping. *Computers in biology and medicine*, 65:229–242, 2015.

[48] Mohammed Yusuf Ansari, Marwa Qaraqe, Fatme Charafeddine, Erchin Serpedin, Raffaella Righetti, and Khalid Qaraqe. Estimating age and gender from electrocardiogram signals: A comprehensive review of the past decade. *Artificial Intelligence in Medicine*, 146:102690, 2023.

[49] Madison S Spach and J Mailen Kootsey. Relating the sodium current and conductance to the shape of transmembrane and extracellular potentials by simulation: effects of propagation boundaries. *IEEE transactions on biomedical engineering*, (10):743–755, 1985.

[50] Ruben Coronel, Jacques MT de Bakker, Francien JG Wilms-Schopman, Tobias Opthof, André C Linnenbank, Charly N Belterman, and Michiel J Janse. Monophasic action potentials and activation recovery intervals as measures of ventricular action potential duration: experimental evidence to resolve some controversies. *Heart rhythm*, 3(9):1043–1050, 2006.

[51] Edward J Vigmond, Vincent Tsoi, Yalin Yin, Pierre Pagé, and Alain Vinet. Estimating atrial action potential duration from electrograms. *IEEE Transactions on Biomedical Engineering*, 56(5):1546–1555, 2009.

[52] Patrizia Camelliti, Sara A Al-Saud, Ryszard T Smolenski, Samha Al-Ayoubi, Nicholas R Banner, Christopher T Bowles, Magdi H Yacoub, and Cesare M Terracciano. Human heart slices-a novel multicellular system suitable for electrophysiological and pharmacological studies. *Biophysical Journal*, 100(3):575a, 2011.

[53] Rasheda A Chowdhury, Konstantinos N Tzortzis, Emmanuel Dupont, Shaun Selvadurai, Filippo Perbellini, Chris D Cantwell, Fu Siong Ng, Andre R Simon, Cesare M Terracciano, and Nicholas S Peters. Concurrent micro-to macro-cardiac electrophysiology in myocyte cultures and human heart slices. *Scientific reports*, 8(1):6947, 2018.

[54] Caroline Helen Roney. *Mathematical techniques for assessing cardiac wavefront dynamics*. PhD thesis, Imperial College London, 2015.

[55] Jacques MT De Bakker and Fred HM Wittkampf. The pathophysiologic basis of fractionated and complex electrograms and the impact of recording techniques on their detection and interpretation. *Circulation: Arrhythmia and Electrophysiology*, 3(2):204–213, 2010.

[56] Madison S Spach and Paul C Dolber. Relating extracellular potentials and their derivatives to anisotropic propagation at a microscopic level in human cardiac muscle. evidence for electrical uncoupling of side-to-side fiber connections with increasing age. *Circulation research*, 58(3):356–371, 1986.

[57] Madison S Spach, WT Miller 3rd, Elizabeth Miller-Jones, Robert B Warren, and Roger C Barr. Extracellular potentials related to intracellular action potentials during impulse conduction in anisotropic canine cardiac muscle. *Circulation Research*, 45(2):188–204, 1979.

[58] Madison S Spach, WT Miller 3rd, Paul C Dolber, J Mailen Kootsey, Joachim R Sommer, and CHARLES E Mosher Jr. The functional role of structural complexities in the propagation of depolarization in the atrium of the dog. cardiac conduction disturbances due to discontinuities of effective axial resistivity. *Circulation research*, 50(2):175–191, 1982.

[59] Michiel J Janse and Andre L Wit. Electrophysiological mechanisms of ventricular arrhythmias resulting from myocardial ischemia and infarction. *Physiological reviews*, 69(4):1049–1169, 1989.

[60] Thao P Nguyen, Zhilin Qu, and James N Weiss. Cardiac fibrosis and arrhythmogenesis: the road to repair is paved with perils. *Journal of molecular and cellular cardiology*, 70:83–91, 2014.

[61] JM De Bakker, FJ Van Capelle, Michiel J Janse, Sara Tasseron, Jessica T Vermeulen, Nicolaas de Jonge, and Jaap R Lahpor. Slow conduction in the infarcted human heart.'zigzag'course of activation. *Circulation*, 88(3):915–926, 1993.

[62] Kyoko Soejima, William G Stevenson, William H Maisel, John L Sapp, and Laurence M Epstein. Electrically unexcitable scar mapping based on pacing threshold for identification of the reentry circuit isthmus: feasibility for guiding ventricular tachycardia ablation. *Circulation*, 106(13):1678–1683, 2002.

[63] Koonlawee Nademanee, John McKenzie, Erol Kosar, Mark Schwab, Buncha Sunsaneewitayakul, Thaveekiat Vasavakul, Chotikorn Khunnawat, and Tachapong Ngarmukos. A new approach for catheter ablation of atrial fibrillation: mapping of the electrophysiologic substrate. *Journal of the American College of Cardiology*, 43(11):2044–2053, 2004.

[64] Sawa Kostin, Gabi Klein, Zoltan Szalay, Stefan Hein, Erwin P Bauer, and Jutta Schaper. Structural correlate of atrial fibrillation in human patients. *Cardiovascular research*, 54(2):361–379, 2002.

[65] M Tanaka, H Fujiwara, T Onodera, DJ Wu, Y Hamashima, and Ch Kawai. Quantitative analysis of myocardial fibrosis in normals, hypertensive hearts, and hypertrophic cardiomyopathy. *Heart*, 55(6):575–581, 1986.

[66] Nicholas J Severs, Steven R Coppen, Emmanuel Dupont, Hung-I Yeh, Yu-Shien Ko, and Tsutomu Matsushita. Gap junction alterations in human cardiac disease. *Cardiovascular research*, 62(2):368–377, 2004.

[67] Shigeto Kanno and Jeffrey E Saffitz. The role of myocardial gap junctions in electrical conduction and arrhythmogenesis. *Cardiovascular pathology*, 10(4):169–177, 2001.

[68] Sven Kaese and Sander Verheule. Cardiac electrophysiology in mice: a matter of size. *Frontiers in physiology*, 3:345, 2012.

[69] Natalia A Trayanova. Whole-heart modeling: applications to cardiac electrophysiology and electromechanics. *Circulation research*, 108(1):113–128, 2011.

[70] Alexandra Bussek, Erich Wettwer, Torsten Christ, Horst Lohmann, Patrizia Camelliti, and Ursula Ravens. Tissue slices from adult mammalian hearts as a model for pharmacological drug testing. *Cellular Physiology and Biochemistry*, 24(5-6):527–536, 2009.

[71] Samuel A Watson, Martina Scigliano, Ifigeneia Bardi, Raimondo Ascione, Cesare M Terracciano, and Filippo Perbellini. Preparation of viable adult ventricular myocardial slices from large and small mammals. *Nature protocols*, 12(12):2623–2639, 2017.

[72] Alan L Hodgkin and Andrew F Huxley. A quantitative description of membrane current and its application to conduction and excitation in nerve. *The Journal of physiology*, 117(4):500, 1952.

[73] Denis Noble. A modification of the hodgkin—huxley equations applicable to purkinje fibre action and pacemaker potentials. *The Journal of physiology*, 160(2):317, 1962.

[74] Ching-hsing Luo and Yoram Rudy. A dynamic model of the cardiac ventricular action potential. i. simulations of ionic currents and concentration changes. *Circulation research*, 74(6):1071–1096, 1994.

[75] Thomas O'Hara, László Virág, András Varró, and Yoram Rudy. Simulation of the undiseased human cardiac ventricular action potential: model formulation and experimental validation. *PLoS computational biology*, 7(5):e1002061, 2011.

[76] Richard H Clayton and Alexander V Panfilov. A guide to modelling cardiac electrical activity in anatomically detailed ventricles. *Progress in biophysics and molecular biology*, 96(1-3):19–43, 2008.

[77] EJ Vigmond, R Weber Dos Santos, AJ Prassl, M Deo, and G Plank. Solvers for the cardiac bidomain equations. *Progress in biophysics and molecular biology*, 96(1-3):3–18, 2008.

[78] Kirsten HWJ Ten Tusscher and Alexander V Panfilov. Alternans and spiral breakup in a human ventricular tissue model. *American Journal of Physiology-Heart and Circulatory Physiology*, 291(3):H1088–H1100, 2006.

[79] William G Stevenson, H Khan, Ph Sager, LA Saxon, HR Middlekauff, PD Natterson, and I Wiener. Identification of reentry circuit sites during catheter mapping and radiofrequency ablation of ventricular tachycardia late after myocardial infarction. *Circulation*, 88(4):1647–1670, 1993.

[80] Alan L Hodgkin and Andrew F Huxley. A quantitative description of membrane current and its application to conduction and excitation in nerve. *Bulletin of mathematical biology*, 52:25–71, 1990.

[81] Steven A Niederer, Martin Fink, Denis Noble, and Nicolas P Smith. A meta-analysis of cardiac electrophysiology computational models. *Experimental physiology*, 94(5):486–495, 2009.

[82] Elizabeth M Cherry, Harold M Hastings, and Steven J Evans. Dynamics of human atrial cell models: restitution, memory, and intracellular calcium dynamics in single cells. *Progress in biophysics and molecular biology*, 98(1):24–37, 2008.

[83] Olaf Dössel, Martin W Krueger, Frank M Weber, Mathias Wilhelms, and Gunnar Seemann. Computational modeling of the human atrial anatomy and electrophysiology. *Medical & biological engineering & computing*, 50:773–799, 2012.

[84] Denis Noble and Yoram Rudy. Models of cardiac ventricular action potentials: iterative interaction between experiment and simulation. *Philosophical Transactions of the Royal Society of London. Series A: Mathematical, Physical and Engineering Sciences*, 359(1783):1127–1142, 2001.

[85] Andreas Mayer, Philip Bittihn, and Stefan Luther. Complex restitution behavior and reentry in a cardiac tissue model for neonatal mice. *Physiological Reports*, 5(19):e13449, 2017.

[86] DS Lindblad, CR Murphey, JW Clark, and WR Giles. A model of the action potential and underlying membrane currents in a rabbit atrial cell. *American Journal of Physiology-Heart and Circulatory Physiology*, 271(4):H1666–H1696, 1996.

[87] Yasutaka Kurata, Ichiro Hisatome, Sunao Imanishi, and Toshishige Shibamoto. Dynamical description of sinoatrial node pacemaking: improved mathematical model for primary pacemaker cell. *American Journal of Physiology-Heart and Circulatory Physiology*, 283(5):H2074–H2101, 2002.

[88] Topi Korhonen, Sandra L Hänninen, and Pasi Tavi. Model of excitation-contraction coupling of rat neonatal ventricular myocytes. *Biophysical journal*, 96(3):1189–1209, 2009.

[89] Ching-hsing Luo and Yoram Rudy. A model of the ventricular cardiac action potential. depolarization, repolarization, and their interaction. *Circulation research*, 68(6):1501–1526, 1991.

[90] Chris D Cantwell, Sergey Yakovlev, Robert M Kirby, Nicholas S Peters, and Spencer J Sherwin. High-order spectral/hp element discretisation for reaction–diffusion problems on surfaces: Application to cardiac electrophysiology. *Journal of computational physics*, 257:813–829, 2014.

[91] Joseph Brook, Min-young Kim, Simos Koutsoftidis, David Pitcher, Danya Agha-Jaffar, Annam Sufi, Catherine Jenkins, Konstantinos Tzortzis, Suofeiya Ma, Richard J Jabbour, et al. Development of a pro-arrhythmic ex vivo intact human and porcine model: cardiac electrophysiological changes associated with cellular uncoupling. *Pflügers Archiv-European Journal of Physiology*, 472:1435–1446, 2020.

[92] Min-young Kim, James Nesbitt, Simos Koutsoftidis, Joseph Brook, David S Pitcher, Chris D Cantwell, Balvinder Handa, Catherine Jenkins, Charles Houston, Stephen Rothery, Anand Jothidasan, Justin Perkins, Poppy Bristow, Nick W F Linton, Emm Drakakis,

Nicholas S Peters, Rasheda A Chowdhury, Prapa Kanagaratnam, and Fu Siong Ng. Immunohistochemical characteristics of local sites that trigger atrial arrhythmias in response to high-frequency stimulation. *EP Europace*, 25(2):726–738, 10 2022.

[93] Kyuseok Im, Sergey Mareninov, M Fernando Palma Diaz, and William H Yong. *An introduction to performing immunofluorescence staining*. Springer, 2019.

[94] David M Miller and Diane C Shakes. Immunofluorescence microscopy. *Methods in cell biology*, 48:365–394, 1995.

[95] Riccardo Cicchi, Nadine Vogler, Dimitrios Kapsokalyvas, Benjamin Dietzek, Jürgen Popp, and Francesco Saverio Pavone. From molecular structure to tissue architecture: collagen organization probed by shg microscopy. *Journal of biophotonics*, 6(2):129–142, 2013.

[96] Guy Cox and Eleanor Kable. Second-harmonic imaging of collagen. *Cell Imaging Techniques: Methods and Protocols*, pages 15–35, 2006.

[97] George Karniadakis and Spencer J Sherwin. *Spectral/hp element methods for computational fluid dynamics*. Oxford University Press, USA, 2005.

[98] Chris D Cantwell, David Moxey, Andrew Comerford, Alessandro Bolis, Gabriele Rocco, Gianmarco Mengaldo, Daniele De Grazia, Sergey Yakovlev, J-E Lombard, Dirk Ekelschot, et al. Nektar++: An open-source spectral/hp element framework. *Computer physics communications*, 192:205–219, 2015.

[99] Kirsten HWJ Ten Tusscher, Denis Noble, Peter-John Noble, and Alexander V Panfilov. A model for human ventricular tissue. *American Journal of Physiology-Heart and Circulatory Physiology*, 286(4):H1573–H1589, 2004.

[100] Nina Kudryashova, Valeriya Tsvelaya, Konstantin Agladze, and Alexander Panfilov. Virtual cardiac monolayers for electrical wave propagation. *Scientific reports*, 7(1):7887, 2017.

[101] Konstantinos Nektarios Tzortzis. *Predicting cardiac functional and structural abnormalities from electrogram morphology using supervised machine learning*. PhD thesis, Imperial College London, 2020.

[102] Steven W Smith. The scientist and engineer's guide to digital signal processing. *California Technical Pub*, 1997.

[103] Li Tan and Jean Jiang. *Digital signal processing: fundamentals and applications*. Academic press, 2018.

[104] Laura A Unger, Tobias G Oesterlein, Axel Loewe, and Olaf Dössel. Noise quantification and noise reduction for unipolar and bipolar electrograms. In *2019 Computing in Cardiology (CinC)*, pages Page–1. IEEE, 2019.

[105] Michael Porter, William Spear, Joseph G Akar, RAY Helms, Neil Brysiewicz, Peter Santucci, and David J Wilber. Prospective study of atrial fibrillation termination during ablation guided by automated detection of fractionated electrograms. *Journal of cardiovascular electrophysiology*, 19(6):613–620, 2008.

[106] Claus Schmitt, Heidi Estner, Birgit Hecher, Armin Luik, Christof Kolb, Martin Karch, Gjin Ndrepepa, Bernhard Zrenner, Gabriele Hessling, and Isabel Deisenhofer. Radiofrequency ablation of complex fractionated atrial electrograms (cfae): preferential sites of acute termination and regularization in paroxysmal and persistent atrial fibrillation. *Journal of cardiovascular electrophysiology*, 18(10):1039–1046, 2007.

[107] Heidi L Estner, Gabriele Hessling, Gjin Ndrepepa, Armin Luik, Claus Schmitt, Agathe Konietzko, Ekrem Ücer, JinJin Wu, Christof Kolb, Andreas Pflaumer, et al. Acute effects and long-term outcome of pulmonary vein isolation in combination with electrogram-guided substrate ablation for persistent atrial fibrillation. *The American journal of cardiology*, 101(3):332–337, 2008.

[108] Hakan Oral, Aman Chugh, Eric Good, Alan Wimmer, Sujoya Dey, Nitesh Gadeela, Sundar Sankaran, Thomas Crawford, Jean F Sarrazin, Michael Kuhne, et al. Radiofrequency

catheter ablation of chronic atrial fibrillation guided by complex electrograms. *Circulation*, 115(20):2606–2612, 2007.

[109] Prashanthan Sanders, Omer Berenfeld, Mélèze Hocini, Pierre Jaïs, Ravi Vaidyanathan, Li-Fern Hsu, Stéphane Garrigue, Yoshihide Takahashi, Martin Rotter, Fréderic Sacher, et al. Spectral analysis identifies sites of high-frequency activity maintaining atrial fibrillation in humans. *Circulation*, 112(6):789–797, 2005.

[110] Yoshihide Takahashi, Prashanthan Sanders, Pierre Jais, Méleze Hocini, Rémi Dubois, Martin Rotter, Thomas Rostock, Chrishan J Nalliah, Frédéric Sacher, Jacques Clémenty, et al. Organization of frequency spectra of atrial fibrillation: relevance to radiofrequency catheter ablation. *Journal of cardiovascular electrophysiology*, 17(4):382–388, 2006.

[111] Yenn-Jiang Lin, Hsuan-Ming Tsao, Shih-Lin Chang, Li-Wei Lo, Yu-Feng Hu, Chien-Jung Chang, Wen-Chin Tsai, Kazuyoshi Suenari, Shih-Yu Huang, Hsing-Ya Chang, et al. Role of high dominant frequency sites in nonparoxysmal atrial fibrillation patients: insights from high-density frequency and fractionation mapping. *Heart Rhythm*, 7(9):1255–1262, 2010.

[112] Jason Ng and Jeffrey J Goldberger. Understanding and interpreting dominant frequency analysis of af electrograms. *Journal of cardiovascular electrophysiology*, 18(6):680–685, 2007.

[113] David S Rosenbaum, Lance E Jackson, Joseph M Smith, Hasan Garan, Jeremy N Ruskin, and Richard J Cohen. Electrical alternans and vulnerability to ventricular arrhythmias. *New England journal of medicine*, 330(4):235–241, 1994.

[114] NA Mark Estes III, Greg Michaud, Douglas P Zipes, Nabil El-Sherif, Ferdinand J Venditti, David S Rosenbaum, Paul J Wang, and Richard J Cohen. Electrical alternans during rest and exercise as predictors of vulnerability to ventricular arrhythmias. *The American journal of cardiology*, 80(10):1314–1318, 1997.

[115] Mahesh A. Nair. Ecg feature extraction using time frequency analysis. In *International Symposium on Symbolic Computation in Software Science*, 2009.

[116] Usik Lee. *Spectral element method in structural dynamics*. John Wiley & Sons, 2009.

[117] Peter Welch. The use of fast fourier transform for the estimation of power spectra: a method based on time averaging over short, modified periodograms. *IEEE Transactions on audio and electroacoustics*, 15(2):70–73, 1967.

[118] Paul S Addison. Wavelet transforms and the ecg: a review. *Physiological measurement*, 26(5):R155, 2005.

[119] Mourad Talbi, Akram Aouinet, Riadh Baazaoui, and Adnane Cherif. Ecg analysis based on wavelet transform and modulus maxima. *IJCSI International Journal of Computer Science Issues*, 9(3):427–435, 2012.

[120] Serap Aydın, Hamdi Melih Saraoğlu, and Sadık Kara. Log energy entropy-based eeg classification with multilayer neural networks in seizure. *Annals of biomedical engineering*, 37:2626–2630, 2009.

[121] Claude Elwood Shannon. A mathematical theory of communication. *The Bell system technical journal*, 27(3):379–423, 1948.

[122] James H King, Christopher L-H Huang, and James A Fraser. Determinants of myocardial conduction velocity: implications for arrhythmogenesis. *Frontiers in physiology*, 4:154, 2013.

[123] Bo Han, Mark L Trew, and Callum M Zgierski-Johnston. Cardiac conduction velocity, remodeling and arrhythmogenesis. *Cells*, 10(11):2923, 2021.

[124] Ross J Hunter, Ihab Diab, Muzahir Tayebjee, Laura Richmond, Simon Sporton, Mark J Earley, and Richard J Schilling. Characterization of fractionated atrial electrograms critical for maintenance of atrial fibrillation: a randomized, controlled trial of ablation strategies (the cfae af trial). *Circulation: Arrhythmia and Electrophysiology*, 4(5):622–629, 2011.

[125] Emmanuel C Ifeachor and Barrie W Jervis. *Digital signal processing: a practical approach*. Pearson Education, 2002.

[126] Philip De Chazal, Maria O'Dwyer, and Richard B Reilly. Automatic classification of heartbeats using ecg morphology and heartbeat interval features. *IEEE transactions on biomedical engineering*, 51(7):1196–1206, 2004.

[127] Moloy Das, Jonathan J Loveday, Gareth J Wynn, Sean Gomes, Yawer Saeed, Laura J Bonnett, Johan EP Waktare, Derick M Todd, Mark CS Hall, Richard L Snowdon, et al. Ablation index, a novel marker of ablation lesion quality: prediction of pulmonary vein reconnection at repeat electrophysiology study and regional differences in target values. *Europace*, 19(5):775–783, 2017.

[128] Andres Orozco-Duque, John Bustamante, and German Castellanos-Dominguez. Semi-supervised clustering of fractionated electrograms for electroanatomical atrial mapping. *Biomedical engineering online*, 15:1–19, 2016.

[129] Sara Isabel Duque, Andrés Orozco-Duque, Václav Kremen, Daniel Novak, Catalina Tobón, and John Bustamante. Feature subset selection and classification of intracardiac electrograms during atrial fibrillation. *Biomedical Signal Processing and Control*, 38:182–190, 2017.

[130] ADInstruments. Labchart pro (version 8.1.28), 2023. Multi-channel physiological recording and analysis software.

[131] Sanjiv M Narayan, David E Krummen, Kalyanam Shivkumar, Paul Clopton, Wouter-Jan Rappel, and John M Miller. Treatment of atrial fibrillation by the ablation of localized sources: Confirm (conventional ablation for atrial fibrillation with or without focal impulse and rotor modulation) trial. *Journal of the American College of Cardiology*, 60(7):628–636, 2012.

[132] Thomas Eschenhagen, Roberto Bolli, Thomas Braun, Loren J Field, Bernd K Fleischmann, Jonas Frisén, Mauro Giacca, Joshua M Hare, Steven Houser, Richard T Lee, et al. Cardiomyocyte regeneration: a consensus statement. *Circulation*, 136(7):680–686, 2017.

[133] Leila Mostaço-Guidolin, Nicole L Rosin, and Tillie-Louise Hackett. Imaging collagen in scar tissue: developments in second harmonic generation microscopy for biomedical applications. *International journal of molecular sciences*, 18(8):1772, 2017.

[134] Michael A Pinkert, Rebecca A Hortensius, Brenda M Ogle, and Kevin W Eliceiri. Imaging the cardiac extracellular matrix. *Cardiac Extracellular Matrix: Fundamental Science to Clinical Applications*, pages 21–44, 2018.

[135] Hee Ryung Lee, Ilyas Saytashev, Vinh Nguyen Du Le, Mala Mahendroo, Jessica Ramella-Roman, and Tatiana Novikova. Mueller matrix imaging for collagen scoring in mice model of pregnancy. *Scientific reports*, 11(1):15621, 2021.

[136] Iftikhar Ahmad, Adam Gribble, Masroor Ikram, Mihaela Pop, and Alex Vitkin. Polarimetric assessment of healthy and radiofrequency ablated porcine myocardial tissue. *Journal of Biophotonics*, 9(7):750–759, 2016.

[137] Alain Coulombe, Isabel A Lefevre, Edith Deroubaix, Dominique Thuringer, and Edouard Coraboeuf. Effect of 2, 3-butanedione 2-monoxime on slow inward and transient outward currents in rat ventricular myocytes. *Journal of molecular and cellular cardiology*, 22(8):921–932, 1990.

[138] JK Gwathmey, RJ Hajjar, and RJ Solaro. Contractile deactivation and uncoupling of crossbridges. effects of 2, 3-butanedione monoxime on mammalian myocardium. *Circulation research*, 69(5):1280–1292, 1991.

[139] LC Sellin and JJ McArdle. Multiple effects of 2, 3-butanedione monoxime. *Pharmacology & toxicology*, 74(4-5):305–313, 1994.

[140] RS Kirton, AJ Taberner, PMF Nielsen, AA Young, and DS Loiselle. Effects of bdm,[ca2+] o, and temperature on the dynamic stiffness of quiescent cardiac trabeculae from rat. *American Journal of Physiology-Heart and Circulatory Physiology*, 288(4):H1662–H1667, 2005.

[141] Vadim V Fedorov, Ilya T Lozinsky, Eugene A Sosunov, Evgeniy P Anyukhovsky, Michael R Rosen, C William Balke, and Igor R Efimov. Application of blebbistatin as

an excitation–contraction uncoupler for electrophysiologic study of rat and rabbit hearts. *Heart rhythm*, 4(5):619–626, 2007.

[142] Madison S Spach, WT Miller 3rd, David B Geselowitz, Roger C Barr, J Mailen Kootsey, and Edward A Johnson. The discontinuous nature of propagation in normal canine cardiac muscle. evidence for recurrent discontinuities of intracellular resistance that affect the membrane currents. *Circulation research*, 48(1):39–54, 1981.

[143] Madison S Spach and J Francis Heidlage. The stochastic nature of cardiac propagation at a microscopic level: electrical description of myocardial architecture and its application to conduction. *Circulation research*, 76(3):366–380, 1995.

[144] Margaret L Kirby and Karen L Waldo. Neural crest and cardiovascular patterning. *Circulation research*, 77(2):211–215, 1995.

[145] Viorel G Florea and Jay N Cohn. The autonomic nervous system and heart failure. *Circulation research*, 114(11):1815–1826, 2014.

[146] Marco Rebecchi, Germana Panattoni, Bressi Edoardo, Ermenegildo de Ruvo, Luigi Sciarra, Alessandro Politano, Marianna Sgueglia, Chiara Ricagni, Sara Verbena, Cinzia Crescenzi, et al. Atrial fibrillation and autonomic nervous system: a translational approach to guide therapeutic goals. *Journal of Arrhythmia*, 37(2):320–330, 2021.

[147] Sahar Avazzadeh, Shauna McBride, Barry O'Brien, Ken Coffey, Adnan Elahi, Martin O'Halloran, Alan Soo, and Leo R Quinlan. Ganglionated plexi ablation for the treatment of atrial fibrillation. *Journal of Clinical Medicine*, 9(10):3081, 2020.

[148] Warren M Jackman and Benjamin J Scherlag. Nature of electrogram fractionation during atrial fibrillation, 2012.

[149] Demosthenes Katritsis, Eleftherios Giazitzoglou, Demetrios Sougiannis, Eutychios Voridis, and Sunny S Po. Complex fractionated atrial electrograms at anatomic sites of ganglionated plexi in atrial fibrillation. *Europace*, 11(3):308–315, 2009.

[150] Norishige Morita, Takayuki Iida, Tomihisa Nanao, Akiko Ushijima, Akira Ueno, Yuji Ikari, and Yoshinori Kobayashi. Effect of ganglionated plexi ablation by high-density mapping on long-term suppression of paroxysmal atrial fibrillation–the first clinical survey on ablation of the dorsal right plexus. *Heart Rhythm O2*, 2(5):480–488, 2021.

[151] Nicholas J Severs, Emmanuel Dupont, Steven R Coppen, Deborah Halliday, Edward Inett, Daniel Baylis, and Stephen Rothery. Remodelling of gap junctions and connexin expression in heart disease. *Biochimica et Biophysica Acta (BBA)-Biomembranes*, 1662(1-2):138–148, 2004.

[152] Nicholas S Peters, James Coromilas, Nicholas J Severs, and Andrew L Wit. Disturbed connexin43 gap junction distribution correlates with the location of reentrant circuits in the epicardial border zone of healing canine infarcts that cause ventricular tachycardia. *Circulation*, 95(4):988–996, 1997.

[153] Daniel C Bartos, Eleonora Grandi, and Crystal M Ripplinger. Ion channels in the heart. *Comprehensive physiology*, 5(3):1423, 2015.

[154] Carol Ann Remme and Connie R Bezzina. Sodium channel (dys) function and cardiac arrhythmias. *Cardiovascular therapeutics*, 28(5):287–294, 2010.

[155] James Weiss, Thao Nguyen, and Zhilin Qu. Cardiac fibrosis and arrhythmogenesis: the road to repair is paved with perils. 2014.

[156] Amir Dehghani-Samani, Samin Madreseh-Ghahfarokhi, and Azam Dehghani-Samani. Mutations of voltage-gated ionic channels and risk of severe cardiac arrhythmias. *Acta Cardiologica Sinica*, 35(2):99, 2019.

[157] Robert D Nass, Takeshi Aiba, Gordon F Tomaselli, and Fadi G Akar. Mechanisms of disease: ion channel remodeling in the failing ventricle. *Nature Clinical Practice Cardiovascular Medicine*, 5(4):196–207, 2008.

[158] William J Richardson, Samantha A Clarke, T Alexander Quinn, and Jeffrey W Holmes. Physiological implications of myocardial scar structure. *Comprehensive Physiology*, 5(4):1877, 2015.

[159] Rongrong Liu, Xiaoting Meng, Xiyao Yu, Guoqiang Wang, Zhiyong Dong, Zhengjie Zhou, Mingran Qi, Xiao Yu, Tong Ji, and Fang Wang. From 2d to 3d co-culture systems: a review of co-culture models to study the neural cells interaction. *International journal of molecular sciences*, 23(21):13116, 2022.

[160] William J Kowalski, Iris H Garcia-Pak, Wenling Li, Hideki Uosaki, Emmanouil Tampakakis, Jizhong Zou, Yongshun Lin, Kira Patterson, Chulan Kwon, and Yoh-Suke Mukouyama. Sympathetic neurons regulate cardiomyocyte maturation in culture. *Frontiers in Cell and Developmental Biology*, 10:850645, 2022.

[161] Howard A Rockman, Walter J Koch, and Robert J Lefkowitz. Seven-transmembrane-spanning receptors and heart function. *Nature*, 415(6868):206–212, 2002.

[162] Aasakiran Madamanchi. β-adrenergic receptor signaling in cardiac function and heart failure. *McGill Journal of Medicine: MJM*, 10(2):99, 2007.

[163] Michael Grimm and Joan Heller Brown. β-adrenergic receptor signaling in the heart: role of camkii. *Journal of molecular and cellular cardiology*, 48(2):322–330, 2010.

[164] Nicola Pianca, Anna Di Bona, Erica Lazzeri, Irene Costantini, Mauro Franzoso, Valentina Prando, Andrea Armani, Stefania Rizzo, Marny Fedrigo, Annalisa Angelini, et al. Cardiac sympathetic innervation network shapes the myocardium by locally controlling cardiomyocyte size through the cellular proteolytic machinery. *The Journal of Physiology*, 597(14):3639–3656, 2019.

[165] AE West, P Pruunsild, and T Timmusk. Neurotrophins: transcription and translation. *Neurotrophic factors*, pages 67–100, 2014.

[166] Annabel S Campbell, Scott R Johnstone, George S Baillie, and Godfrey Smith. β-adrenergic modulation of myocardial conduction velocity: Connexins vs. sodium current. *Journal of molecular and cellular cardiology*, 77:147–154, 2014.

[167] Aida Salameh and Stefan Dhein. Adrenergic control of cardiac gap junction function and expression. *Naunyn-Schmiedeberg's archives of pharmacology*, 383:331–346, 2011.

[168] Teun P De Boer, Harold VM van Rijen, Marcel AG Van der Heyden, Bart Kok, Tobias Opthof, Marc A Vos, Habo J Jongsma, Jacques MT de Bakker, and Toon AB van Veen. Beta-, not alpha-adrenergic stimulation enhances conduction velocity in cultures of neonatal cardiomyocytes. *Circulation Journal*, 71(6):973–981, 2007.

[169] Graeme Eisenhofer, Peter Friberg, Bengt Rundqvist, Arshed A Quyyumi, Gavin Lambert, David M Kaye, Irwin J Kopin, David S Goldstein, and Murray D Esler. Cardiac sympathetic nerve function in congestive heart failure. *Circulation*, 93(9):1667–1676, 1996.

[170] Juan Manuel González-Rosa, Víctor Martín, Marina Peralta, Miguel Torres, and Nadia Mercader. Extensive scar formation and regression during heart regeneration after cryoinjury in zebrafish. *Development*, 138(9):1663–1674, 2011.

[171] Dong Fan, Abhijit Takawale, Jiwon Lee, and Zamaneh Kassiri. Cardiac fibroblasts, fibrosis and extracellular matrix remodeling in heart disease. *Fibrogenesis & tissue repair*, 5:1–13, 2012.

[172] Jutta Schaper, Albrecht Elsasser, and Sawa Kostin. The role of cell death in heart failure, 1999.

[173] Peter M Kang and Seigo Izumo. Apoptosis and heart failure: a critical review of the literature. *Circulation research*, 86(11):1107–1113, 2000.

[174] Magda SC Fontes, Toon AB van Veen, Jacques MT de Bakker, and Harold VM van Rijen. Functional consequences of abnormal cx43 expression in the heart. *Biochimica et Biophysica Acta (BBA)-Biomembranes*, 1818(8):2020–2029, 2012.

[175] Heather S Duffy, Anthony W Ashton, Phyllis O'Donnell, Wanda Coombs, Steve M Taffet, Mario Delmar, and David C Spray. Regulation of connexin43 protein complexes by intracellular acidification. *Circulation research*, 94(2):215–222, 2004.

[176] Borislav Dinov, Lukas Fiedler, Robert Schönbauer, Andreas Bollmann, Sascha Rolf, Christopher Piorkowski, Gerhard Hindricks, and Arash Arya. Outcomes in catheter ablation of ventricular tachycardia in dilated nonischemic cardiomyopathy compared with

ischemic cardiomyopathy: results from the prospective heart centre of leipzig vt (help-vt) study. *Circulation*, 129(7):728–736, 2014.

[177] PETERS NS. Reduced content of connexin43 gap junctions in ventricular myocardium from hypertrophied and ischemic human hearts. *Circulation*, 88:864–875, 1993.

[178] Nicholas J Severs. Gap junction remodeling and cardiac arrhythmogenesis: cause or coincidence? *Journal of cellular and molecular medicine*, 5(4):355–366, 2001.

[179] Habo J Jongsma and Ronald Wilders. Gap junctions in cardiovascular disease. *Circulation research*, 86(12):1193–1197, 2000.

[180] Stephan Rohr, Jan P Kucera, and André G Kléber. Slow conduction in cardiac tissue, i: effects of a reduction of excitability versus a reduction of electrical coupling on microconduction. *Circulation research*, 83(8):781–794, 1998.

[181] Ronald Wilders, E Etienne Verheijck, Ronald W Joyner, David A Golod, Rajiv Kumar, Antoni CG van Ginneken, Lennart N Bouman, and Habo J Jongsma. Effects of ischemia on discontinuous action potential conduction in hybrid pairs of ventricular cells. *Circulation*, 99(12):1623–1629, 1999.

[182] Mary B Wagner, Takao Namiki, Ronald Wilders, Ronald W Joyner, Habo J Jongsma, E Etienne Verheijck, Rajiv Kumar, David A Golod, William N Goolsby, and Antoni CG van Ginneken. Electrical interactions among real cardiac cells and cell models in a linear strand. *American Journal of Physiology-Heart and Circulatory Physiology*, 276(2):H391–H400, 1999.

[183] Dobromir Dobrev, Leif Carlsson, and Stanley Nattel. Novel molecular targets for atrial fibrillation therapy. *Nature reviews Drug discovery*, 11(4):275–291, 2012.

[184] Cristobal Guillermo Dos Remedios, Sean Lal, Amy Li, David Baddeley, David J Crossman, Yufeng Hou, Mia Jullig, Martin Middleditch, Michelle Munro, Peter Ruygrok, et al. Increased collagen within the transverse tubules in human heart failure. 2017.

[185] Emily L Ongstad and Robert G Gourdie. Can heart function lost to disease be regenerated by therapeutic targeting of cardiac scar tissue? In *Seminars in cell & developmental biology*, volume 58, pages 41–54. Elsevier, 2016.

[186] Stanley Nattel, Ange Maguy, Sabrina Le Bouter, and Yung-Hsin Yeh. Arrhythmogenic ion-channel remodeling in the heart: heart failure, myocardial infarction, and atrial fibrillation. *Physiological reviews*, 87(2):425–456, 2007.

[187] Raphael P Martins, Kuljeet Kaur, Elliot Hwang, Rafael J Ramirez, B Cicero Willis, David Filgueiras-Rama, Steven R Ennis, Yoshio Takemoto, Daniela Ponce-Balbuena, Manuel Zarzoso, et al. Dominant frequency increase rate predicts transition from paroxysmal to long-term persistent atrial fibrillation. *Circulation*, 129(14):1472–1482, 2014.

[188] Carol Ann Remme, Arie O Verkerk, WMH Hoogaars, WTJ Aanhaanen, Brendon P Scicluna, C Annink, Maurice JB van den Hoff, Arthur AM Wilde, TAB Van Veen, Marieke W Veldkamp, et al. The cardiac sodium channel displays differential distribution in the conduction system and transmural heterogeneity in the murine ventricular myocardium. *Basic research in cardiology*, 104:511–522, 2009.

[189] Nathalie Gaborit, Sabrina Le Bouter, Viktoria Szuts, Andras Varro, Denis Escande, Stanley Nattel, and Sophie Demolombe. Regional and tissue specific transcript signatures of ion channel genes in the non-diseased human heart. *The Journal of physiology*, 582(2):675–693, 2007.

[190] Yuri A Kuryshev, Gary M Brittenham, Hisashi Fujioka, Perry Kannan, Char-Chang Shieh, Sidney A Cohen, and Arthur M Brown. Decreased sodium and increased transient outward potassium currents in iron-loaded cardiac myocytes: implications for the arrhythmogenesis of human siderotic heart disease. *Circulation*, 100(6):675–683, 1999.

[191] Carmen A Ufret-Vincenty, Deborah J Baro, W Jonathan Lederer, Howard A Rockman, Luis E Quinones, and L Fernando Santana. Role of sodium channel deglycosylation in the genesis of cardiac arrhythmias in heart failure. *Journal of Biological Chemistry*, 276(30):28197–28203, 2001.

[192] Carmen R Valdivia, William W Chu, Jielin Pu, Jason D Foell, Robert A Haworth, Mathew R Wolff, Timothy J Kamp, and Jonathan C Makielski. Increased late sodium current in myocytes from a canine heart failure model and from failing human heart. *Journal of molecular and cellular cardiology*, 38(3):475–483, 2005.

[193] Stephen Zicha, Victor A Maltsev, Stanley Nattel, Hani N Sabbah, and Albertas I Undrovinas. Post-transcriptional alterations in the expression of cardiac na+ channel subunits in chronic heart failure. *Journal of molecular and cellular cardiology*, 37(1):91–100, 2004.

[194] Anthony W Herren, Donald M Bers, and Eleonora Grandi. Post-translational modifications of the cardiac na channel: contribution of camkii-dependent phosphorylation to acquired arrhythmias. *American Journal of Physiology-Heart and Circulatory Physiology*, 305(4):H431–H445, 2013.

[195] Lars S Maier, Tong Zhang, Lu Chen, Jaime DeSantiago, Joan Heller Brown, and Donald M Bers. Transgenic camkiiδc overexpression uniquely alters cardiac myocyte ca2+ handling: reduced sr ca2+ load and activated sr ca2+ release. *Circulation research*, 92(8):904–911, 2003.

[196] Stefan Wagner, Nataliya Dybkova, Eva CL Rasenack, Claudius Jacobshagen, Larissa Fabritz, Paulus Kirchhof, Sebastian KG Maier, Tong Zhang, Gerd Hasenfuss, Joan Heller Brown, et al. Ca 2+/calmodulin-dependent protein kinase ii regulates cardiac na+ channels. *The Journal of clinical investigation*, 116(12):3127–3138, 2006.

[197] Albertas I Undrovinas, Victor A Maltsev, John W Kyle, Norman Silverman, and Hani N Sabbah. Gating of the late na+ channel in normal and failing human myocardium. *Journal of molecular and cellular cardiology*, 34(11):1477–1489, 2002.

[198] AI Undrovinas, VA Maltsev, and HN Sabbah. Repolarization abnormalities in cardiomyocytes of dogs with chronic heart failure: role of sustained inward current. *Cellular and Molecular Life Sciences CMLS*, 55:494–505, 1999.

[199] Lior Gepstein. Cell and gene therapy strategies for the treatment of postmyocardial infarction ventricular arrhythmias. *Annals of the New York Academy of Sciences*, 1188(1):32–38, 2010.

[200] Daigo Yagishita, Olujimi A Ajijola, Marmar Vaseghi, Ali Nsair, Wei Zhou, Kentaro Yamakawa, Roderick Tung, Aman Mahajan, and Kalyanam Shivkumar. Electrical homogenization of ventricular scar by application of collagenase: a novel strategy for arrhythmia therapy. *Circulation: Arrhythmia and Electrophysiology*, 6(4):776–783, 2013.

[201] Jeanne M Nerbonne. Studying cardiac arrhythmias in the mouse—a reasonable model for probing mechanisms? *Trends in cardiovascular medicine*, 14(3):83–93, 2004.

[202] Luther M Swift, Rafael Jaimes III, Damon McCullough, Morgan Burke, Marissa Reilly, Takuya Maeda, Hanyu Zhang, Nobuyuki Ishibashi, Jack M Rogers, and Nikki Gillum Posnack. Optocardiography and electrophysiology studies of ex vivo langendorff-perfused hearts. *Journal of visualized experiments: JoVE*, (153):10–3791, 2019.

[203] Robert M Bell, Mihaela M Mocanu, and Derek M Yellon. Retrograde heart perfusion: the langendorff technique of isolated heart perfusion. *Journal of molecular and cellular cardiology*, 50(6):940–950, 2011.

[204] Shah Zahid Khan, Mujahid Mohsin, and Waseem Iqbal. On gps spoofing of aerial platforms: a review of threats, challenges, methodologies, and future research directions. *PeerJ Computer Science*, 7:e507, 2021.

[205] Rong Bing and Marc Richard Dweck. Myocardial fibrosis: why image, how to image and clinical implications. *Heart*, 105(23):1832–1840, 2019.

[206] Joseph Brook. *Predicting electrophysiological function of ex-vivo hearts using machine learning*. PhD thesis, Imperial College London, 2024.

[207] Pipin Kojodjojo, Prapa Kanagaratnam, Oliver R Segal, Wajid Hussain, and Nicholas S Peters. The effects of carbenoxolone on human myocardial conduction: a tool to investigate the role of gap junctional uncoupling in human arrhythmogenesis. *Journal of the American College of Cardiology*, 48(6):1242–1249, 2006.

[208] BRUCE P Bean, CHARLES J Cohen, and RICHARD W Tsien. Lidocaine block of cardiac sodium channels. *The Journal of general physiology*, 81(5):613, 1983.

[209] Keisuke Iguchi, Masao Saotome, Kanna Yamashita, Prottoy Hasan, Miyuki Sasaki, Yuichiro Maekawa, and Yasuhide Watanabe. Pinacidil, a katp channel opener, stimulates cardiac na+/ca2+ exchanger function through the no/cgmp/pkg signaling pathway in guinea pig cardiac ventricular myocytes. *Naunyn-Schmiedeberg's Archives of Pharmacology*, 392(8):949–959, 2019.

[210] B Weinkauf, O Obreja, M Schmelz, and R Rukwied. Differential effects of lidocaine on nerve growth factor (ngf)-evoked heat-and mechanical hyperalgesia in humans. *European journal of pain*, 16(4):543–549, 2012.

[211] Ryan Wade Selby, Anup Jonchhe, Chen Kaplan, Coeli M Lopes, and Behnaz Ghoraani. Development of data acquisition components for simultaneous recording of 3d epicardial and surface ecg signals in the langendorff perfusion apparatus. In *2016 38th Annual International Conference of the IEEE Engineering in Medicine and Biology Society (EMBC)*, pages 2733–2736. IEEE, 2016.

[212] Alexander Weymann, Sivakkanan Loganathan, Hiroaki Takahashi, Carsten Schies, Benjamin Claus, Kristóf Hirschberg, Pál Soós, Sevil Korkmaz, Bastian Schmack, Matthias Karck, et al. Development and evaluation of a perfusion decellularization porcine heart model–generation of 3-dimensional myocardial neoscaffolds–. *Circulation Journal*, 75(4):852–860, 2011.

[213] Daniel A Goodenough. Lens gap junctions: a structural hypothesis for nonregulated low-resistance intercellular pathways. *Investigative ophthalmology & visual science*, 18(11):1104–1122, 1979.

[214] Charles Houston, Konstantinos N Tzortzis, Caroline Roney, Andrea Saglietto, David S Pitcher, Chris D Cantwell, Rasheda A Chowdhury, Fu Siong Ng, Nicholas S Peters, and Emmanuel Dupont. Characterisation of re-entrant circuit (or rotational activity) in vitro

using the hl1-6 myocyte cell line. *Journal of Molecular and Cellular Cardiology*, 119:155–164, 2018.

[215] Balvinder S Handa, Caroline H Roney, Charles Houston, Norman A Qureshi, Xinyang Li, David S Pitcher, Rasheda A Chowdhury, Phang Boon Lim, Emmanuel Dupont, Steven A Niederer, et al. Analytical approaches for myocardial fibrillation signals. *Computers in biology and medicine*, 102:315–326, 2018.

[216] Carsen Stringer, Tim Wang, Michalis Michaelos, and Marius Pachitariu. Cellpose: a generalist algorithm for cellular segmentation. *Nature methods*, 18(1):100–106, 2021.

[217] Stanley Nattel. Molecular and cellular mechanisms of atrial fibrosis in atrial fibrillation. *JACC: Clinical Electrophysiology*, 3(5):425–435, 2017.

[218] John Whitaker, Taylor E Baum, Pierre Qian, Anton J Prassl, Gernot Plank, Ron Blankstein, Hubert Cochet, William H Sauer, Martin J Bishop, and Usha Tedrow. Frequency domain analysis of endocardial electrograms for detection of nontransmural myocardial fibrosis in nonischemic cardiomyopathy. *Clinical Electrophysiology*, 9(7_Part_1):923–935, 2023.

[219] Amir S Jadidi, Hubert Cochet, Ashok J Shah, Steven J Kim, Edward Duncan, Shinsuke Miyazaki, Maxime Sermesant, Heiko Lehrmann, Matthieu Lederlin, Nick Linton, et al. Inverse relationship between fractionated electrograms and atrial fibrosis in persistent atrial fibrillation: combined magnetic resonance imaging and high-density mapping. *Journal of the American College of Cardiology*, 62(9):802–812, 2013.

[220] Fadi G Akar, David D Spragg, Richard S Tunin, David A Kass, and Gordon F Tomaselli. Mechanisms underlying conduction slowing and arrhythmogenesis in nonischemic dilated cardiomyopathy. *Circulation research*, 95(7):717–725, 2004.

[221] Saeed V Vaseghi. *Advanced digital signal processing and noise reduction*. John Wiley & Sons, 2008.

[222] Antonis A Armoundas, Gordon F Tomaselli, and Hans D Esperer. Pathophysiological basis and clinical application of t-wave alternans. *Journal of the American College of Cardiology*, 40(2):207–217, 2002.

[223] Ewelina Kałużna, Agnieszka Nadel, Agnieszka Zimna, Natalia Rozwadowska, and Tomasz Kolanowski. Modeling the human heart ex vivo—current possibilities and strive for future applications. *Journal of Tissue Engineering and Regenerative Medicine*, 16(10):853–874, 2022.

[224] G André Ng, Kieran E Brack, and John H Coote. Effects of direct sympathetic and vagus nerve stimulation on the physiology of the whole heart–a novel model of isolated langendorff perfused rabbit heart with intact dual autonomic innervation. *Experimental physiology*, 86(3):319–329, 2001.

[225] Kieran E Brack, John H Coote, and G André Ng. Interaction between direct sympathetic and vagus nerve stimulation on heart rate in the isolated rabbit heart. *Experimental physiology*, 89(1):128–139, 2004.